Title
Modeling the mechanical behavior and microstructure evolutions of irradiated nuclear materials using the coupled kinetic rate theory and continuum crystal plasticity method

Author
Yu, Qianran

Publication Date
2022

Peer reviewed|Thesis/dissertation

UNIVERSITY OF CALIFORNIA

Los Angeles

Modeling the mechanical behavior and microstructure evolutions of irradiated nuclear materials using the coupled kinetic rate theory and continuum crystal plasticity method

A dissertation submitted in partial satisfaction
of the requirements for the degree
Doctor of Philosophy in Mechanical Engineering

by

Qianran Yu

2022

ABSTRACT OF THE DISSERTATION

Modeling the mechanical behavior and microstructure evolutions of irradiated nuclear materials using the coupled kinetic rate theory and continuum crystal plasticity method

by

Qianran Yu
Doctor of Philosophy in Mechanical Engineering
University of California, Los Angeles, 2022
Professor Jaime Marian, Chair

Microstructure evolution of structural materials under fission/fusion irradiaiton conditions lead to significant degradation to their mechanical properties. These effects include an increase in yield stress, plastic localization and accelerated creep rate, etc. Besides, damaged materials inevitably exposing to hydrogen or its isotopes would result in embrittlement and safety problem. Regarding these problems, we in this thesis developed three types of numerical models and attempted to solve each of those.

First, a previously developed kMC algorithm based 0-dimentional mean field rate theory model, the stochastic cluster dynamics (SCD), is extended to have 1-dimentional spatial resolution (SRSCD). The SRSCD method is then used to simulate: (1) Zr-hydride nucleation and growth processes under dynamic oxide layer growth conditions; (2) Hydrogen retention in heavy ion irrdiated tungsten.

Second, the SCD method is coupled with a general implicit crystal plasticity (CP) formulation (CP/SCD) using a bidirectional variable swap scheme. The CP/SCD model is capable of capturing concurrent irradiation/straining process in materials and is applied to study (1) Irradiation hardening of self-ion irradiated tungsten under tensile loading conditions; (2) Creep and swelling effects of DEMO neutron irradiated iron.

Finally, a stochastic solver based on residence time algorithm is developed for solving a typical explicit crystal plasticity (SCP) procedure. The stochasitc nature of SCP is seen to break the symmetry of dislocation slip, which shows potential in studying plastic localization problems.

The dissertation of Qianran Yu is approved.

Nasr M. Ghoniem

Lihua Jin

Richard E. Wirz

Jaime Marian, Committee Chair

University of California, Los Angeles

2022

To my grandmother and mother...

who—among many other things—

have always loved, supported and

encouraged me unconditionally.

Table of Contents

Acknowledgements

At the outset, I would like to thank my advisor, Dr. Jaime Marian for his support and guidance through my stay at UCLA. He has given me the freedom to pursue independent research, and at the same time nudging me in the right direction. Besides his vast knowledge of mechanics and materials, I have also immensely benefited from his editorial skills. I would like to thank Dr. Brian Wirth, Dr. George Tynan, Dr. Giacomo Po and their group members Dr. Michael Simmonds, Dr. Sabyasache Chatterjee, with whom I had the opportunity to work closely and who have always given constructive feedback regarding my research. I would also like to thank Dr. Kenneth Roche for his valuable comments and discussions regarding this work. I am grateful for funding received from DOE of Fusion Sciences project DE-SC0019157 to support my study at UCLA.

I am also grateful to Dr. Enrique Martinez for guiding me to explore the field of phase field modeling and as well many valuable discussions with him. I have always enjoyed the engrossing discussions (and procrastinations) with present and former group mates, Mr. Andrew Alvarado, Dr. Nicholas Julian, Dr. Weicheng Huang, Dr. Yufeng Dong, Dr. Shu Huang and Dr. Yujing Xiao. My Ph.D. life would most certainly have been very boring without them. I am grateful for the company of my "non-work" friends, Ms Ying Ma, Ms Xiao Li, Dr. Yao Chen, Ms Siyu Wei and Ms Boying Liu, who have invariably managed to lighten things up

Finally, this thesis would not have been possible without the patient support of my entire family. Though they do not quite understand the technicalities of my work, they have always appreciated its importance to me and kept encouraging me

throughout. I am sorry for not being with them in their many moments of joy and sorrow over the past few years. I hope that this work is commensurate with their innumerable sacrifices.

Curriculum Vitae

2014	B.S. (Material Science and Engineering), Beijing Institute of Technology.
2016	M.S. (Material Science and Engineering), UCLA.
2017 – present	Ph.D. student, Research Assistant, Mechanical and Engineering Department, UCLA.
2022 – 2024 (expected)	Postdoc Fellow, Mechanical Engineering Department, Clemson University.

Publications

1. Qianran Yu, Michael Reyes, Nachiket Shah and Jaime Marian, "Kinetic Model of Incipient Hydride Formation in Zr Clad under Dynamic Oxide Growth Conditions," Materials **13(5)**, 1088(2020).

2. Qianran Yu, Michael J. Simmonds, Russ. Doerner, George R. Tynan, Li Yang, Brian D. Wirth and Jaime Marian, "Understanding hydrogen retention in damaged tungsten using experimentally-guided models of complex multispecies evolution," Nucl. Fusion **60**, 096003 (2020).

3. Qianran Yu, Sabyasachi Chatterjee, Kenneth J. Roche, Giacomo Po and Jaime Marian, "Coupling crystal plasticity and stochastic cluster dynamics models of irradiation damage in tungsten," Modeling Simul. Mater. Sci. Eng. **29**, 055021 (2021).

4. Qianran Yu, Enrique Martinez, Javier Segurado, Jaime Marian, "A stochastic solver based on the residence time algorithm for crystal placticity models," Computational Mechanics **68**, 1369-1384 (2021).

5. Qianran Yu, Sabyasachi Chatterjee, Giacomo Po, Jaime Marian, "Simulations of irradiation creep in ferritic materials under DEMO first-wall operation condition," Journal of Nuclear Materials (under review).

Presentations

1. "Kinetic modeling of phase field precipitation and growth in binary system using SRSCD, " at The 19th International Conference on Fusion Reactor Materials (ICFRM19).

CHAPTER 1

Introduction

1.1 Motivation

Over decades, the nuclear fusion technology has gained great research interest mainly due to its demonstrated potential of supplying almost limitless energy through controllable, safer and environmentally friendly fusion reactions [327]. Among various fusion reactor designs [36, 178, 341], the Magnetic Confinement fusion (MFE) based tokamak facility is yet the most promising one. In a typical MFE reactor, plasma or energetic particles, i.e. e^-, neutron and hydrogen isotopes are confined by a donut-shaped electrical-magnetic field, in which those particles are enabled intensive collisions. While owing to the edge-localized-modes (ELM) instability, rapid transportation of energy and particle fluxes onto plasma facing materials (PFMs) surfaces leads to significant irradiation damage that degrades materials' mechanical properties [213, 336]. It is known that the change of mechanical properties in structural materials is in essence governed by dislocation-mediated crystallographic deformation, while dislocation motions is inevitably affected by its interaction with microstructures. Thus, understanding the effect of radiation-induced defects on the dislocation-mediated crystallographic deformation behavior holds the key for modeling and designing robust structural alloys for nuclear applications.

The present research focuses on developing a coupled modeling method, through which the irradiation-induced microstructure evolution on meso-scale, and the dislocation-mediated inelastic deformation can be concurrently simulated, to explore the mechanical behavior of irradiated fusion materials.

1.2 Irradiation damage in metallic systems

Microscopically, the irradiation damage process can be described as being initiated by the 'knock-on' event where an incident energetic particle interacts with a lattice atom and transfers a certain part of its kinetic energy to it. Such energy transfer results in the lattice atom excitation and departure from its original site. We call it the primary knock-on atom (PKA). The PKA atom traverses through the material matrix and subsequently creats more PKAs and accompanying defects. While the PKAs have exhausted all their energy, they finally stop in the matrix as interstitials (SIA). Details about the physics of irradiation damage can be found in Was [373].

During irradiation, formation of common material defects includes point defect and defect clusters (i.e. interstitial and vacancy clusters), dislocation loops and networks, precipitatation, solute segregation and transmutation, etc. Interaction of the plasticity-carrying dislocations with those irradiation-induced defects alters their mechanical properties. Predominant effects involve irradiation hardening, plastic flow localization, reduced ductility, and premature failure. Further, the irradiation creep and swelling rates are observed to be accelerated compared to thermal creep [279, 373], and would occur at homologous temperatures.

In fusion conditions such as ITER reactor, plasma facing components are known to be exposed to harsher environment ($\sim$ 14 MeV neutron irradiaiton) [222], in which

the materials' mechanical properties could be significantly degraded by the largely increased amount of irradiation-induced defects. Lacking of the proper neutron source that is comprable to fusion device, experimental works would use heavy ions as sorrogates [13], followed by post-mortem mechanical tests. Such routine gurantees the generation of similar amount of defects, but loses the accuracy of mimicing the same cluster size distributions as in neutron irradiation conditions. Further, neutron-induced elemental transmutation would be totally missing in heavy ion irradiation. Besides the above limits, though post-mortem tests is powerful tool in measuring irradiation hardening, it is not applicable to irradiation creep investigations.

Given by those considerations, multi-scale modeling techniques have emerged as useful method in predicting microstructure evolutions in ion/neutron irradiation conditions. Among those, the mean-field rate theory models is capable of simulating up to more than several thousand seconds of a multi-species system, which covers the time duration even for creep tests. In this thesis, we developed an alternative mean-field rate theory model, namely the stochastic cluster dynamices (SCD), and made it to handle all irradiation microstructure evolutions in each sub-topics.

1.3 Detrimental effects of hydrogen isotope retention in nuclear material

Hydrogen and its isotope have long been recognized as detrimental elements in nuclear devices. In fission reactors, the presence of hydrogen comes from merging fuel-cladding tubes into water, where decomposition of H_2O releases extra hydrogen atoms into materials, and then forming needle-shaped hydrides that result in material embrittlement. While in MFE fusion devices, deuterium and tritium are common

fusion reactants, and are transported onto PFMs along with neutrons through ELM phenomenon. These hydrogen isotopes are then trapped into neutron-induced vacancy (V) clusters, dislocations and grain boundaries, which leads to embrittlement and radioactive safety problems. Further, many experimental observations show that the existence of hydrogen facilitates the formation of extra vacancies, such that more vacancy clusters with larger size should have been observed. In the following context, we call this phenomenon as *super-abundant vacancy* or SAV. Recent reviews on hydrogen behavior in fission/fusion materials can be found in ref. [55, 223]. Here in this thesis, hydrogen permeation in the matrix material and its interaction with irradiation defects are also dipicted by SCD model.

1.4 Scope of the present research

This thesis is a collection of research projects that have done in the past few years. All of those studies are relavant to the theme of microstructure evolutions and their effects on mechanical properties change of nuclear materials during irradiation, while each sub-topic stands independent from others and aims at solving one specific aspect of irradiation-induced problem of structural materials.

Here, unified simulation methods are used. For microstructure evolutions of irradiated materials, meso-scale modeling method, SCD [239], has been previously developed that could simulate average cluster concentration evolutions in one material point. However, the current studies involve simulating long-distance migration of hydrogen atoms in target materials, which requires a spatial extension of SCD method into a 1-D space, thus the former part of the content is focusing on developing the spatially resolved SCD (SR-SCD) model and applied it to solve (1) hydride

nucleation and growth in Zr;(2) deuterium retention in tungsten materials. For mechanical properties, a general continuum crystal plasticity (CP) framework for bcc metals is implemented and it is then coupled with one-point SCD method, such that a real-time defect-dislocation interaction can be captured. The developed CP/SCD method is then used to simulate (1) post-moterm and concurrent irradiation-tensile tests of tungsten single crystals; (2) irradiation creep and swelling effects of DEMO neutron irradiated Fe materials. Finally, inspired by the SCD method, we remould the deterministic CP formulation into a stochastic solver based on residence time algorithm. Such stochastic crystal plasticity (SCP) model is seen to be the starting point of exploring plastic localization caused by asymmetrical plastic slips.

1.5 Organization of the thesis

This thesis is organized in the following fashion.

Chapter 2 serves as an introduction of method and theory for the whole thesis. First, it contains the general fundamentals of the stochastic cluster dymics model with and without spatial resolutions. The (SR-)SCD model is the key simulation method used through Chapter 3 to 7. Additional decorations and parameter determinations to SCD are specified in each chapter. Second, we provided a brief demonstration on the crystal plasticity formulation which is part of the main simulation method for Chapter 5,6 and 7.

Chapter 3 focuses on modeling hydride formation in Zr clad. Compared to previous studies, this work adds a dynamic oxide growth layer in front of the hydride nucleation region, which, for the first time, concurrently considers the full picture of Zr corrosion processes in water. The model follows the standard phase diagram of

Zr-H system that converts the intermediate"$\alpha+\delta$" phase into a formation probability using inverse lever rule. The limit of the study lies in the very little simulation time achieved which is far away from the sufficient hydride formation time of at least one month, such that it only studies hydride nucleation and initial stage of growth.

Chapter 4 is an interesting study about hydrogen/deuterium retention in tungsten which is for now the most promising plasma facing material. The simulation strictly follows a real experimental routine done by UCSD group, where a piece of tungsten coupon was firstly irradiated by 3.4 MeV Cu ion for 15 min, then deposited with deuterium flux for 2500 seconds, and finally analyzed by NRA and thermal desorption (TDS) analysis. The model is parameterized with latest data from first-principle studies, such as binding energies between H-V, V-V, etc., and migration energies of SIA, V and hydrogen, and is also docorated with a new self-invented mechanism for describing SAV processes. Our simulated TDS diagram was compared with the experimental TDS result. It was found that good agreement with experimental data could be gained when activation energy of SAV reaction is set to be 0.95 eV. This work managed to link the experimental research with those microscale atomistic studies

Chapter 5 develops the coupled CP/SCD approach that is capable of concurrently treating irradiation and deformation in irradiated materials. As in Chapter 2, SCD evolves the defect microstructure stochastically, providing parameters such as statistically-averaged defect spacing that could be used by CP calculations as extra shear stresses caused by defect obstacles. As return, CP updates dislocation densities which is actually sink strength for SCD. Therefore, the coupling of this model is realized by a bidirectional information exchange scheme. We applied the CP/SCD model to simulate post-mortem and in-situ tensile tests of tungsten single crystals

through various crystal orientations and found that drastic dislocation multiplication during concurrent irradiation/straining process serves as strong sinks that absorbs more irradiation defects than without straining conditions.

Chapter 6 develops a stochastic solver for crystal plasticity based on residence time algorithm. The motivation of this project lies in the phenomenon such as flow localization and geometriacally-necessary dislocation where slip systems in those regions are not homogeneously activated. While, current CP models asumes slip systems are independent of each other such that a homogeneous plastic response sounds mathematically reasonable but is at odds with observed material response.

Chapter 7 studied irradiation creep and swelling of DEMO neutron irradiated Fe materials using the CP/SCD method shown in Chapter 5. In this work, the CP formulation goes beyond the traditional settings in Chapter 2 and distinguised dislocation motions by types (edge or screw). The novalty of this work is mainly seen in three aspects: (1) New climb and climb assistant glide velocity for edge dislocation are derived; (2) Mathematical definition of creep and swelling strains are provided for the first time; (3) Correlation between irradiation creep and swelling is found under DEMO neutrion irradiation conditions.

Chapter 8 summarizes the novel contributions and major conclusions of this research.

Major findings of Chapter 3,4,5 and 6 have appeared in Ref. [401–404]. The work done in 8 is presently under review for publication.

CHAPTER 2

Theory and Method

2.1 The Stochastic Cluster Dynamics Method

2.1.1 Brief overview

In this thesis, the microstructure/defects evolution during irradiation is simulated using the stochastic cluster dynamics (SCD) model. SCD is a stochastic variant of the mean-field rate theory technique, that eliminates the need to solve exceedingly large sets of ODEs and relies instead on sparse stochastic sampling from the underlying kinetic master equation. Rather than dealing with coutinuously varying defect concentrations in an infinite volume, SCD evolves an integer-valued defect population N_i in a finite material volume Ω, thus avoiding exponential growth in the number of ODEs. This makes SCD ideal to treat problems where the dimensionality of the cluster size space is high, e.g., when multispecies simulations – for example involving energetic particles, transmutation products, alloy elements, etc., simultaneously– are of interest. Mathematically, SCD recasts the standard ODE system:

$$\frac{dC_i}{dt} = g_i + \sum_q \left(\sum_j s_{jq} C_j - s_{iq} C_i + \right) + \sum_j \left[\left(\sum_k \hbar_{jk} C_k - \hbar_{ij} C_i \right) C_j \right] \tag{2.1}$$

into stochastic equations of the form:

$$\frac{dN_i}{dt} = \tilde{g}_i + \sum_q \left(\sum_j \tilde{s}_{jq} N_j - \tilde{s}_{iq} N_i + \right) + \sum_j \left[\left(\sum_k \tilde{\hbar}_{jk} N_k - \tilde{\hbar}_{ij} N_i \right) N_j \right] \tag{2.2}$$

where the subindices i, j, and k refer to a given defect species, and q runs over all potential defect sinks. The set $\{\tilde{g}, \tilde{s}, \tilde{\hbar}\}$ represents the reaction rates of 0^{th} (insertion), 1^{st} (thermal dissociation, annihilation at sinks), and 2^{nd} (binary reactions) order kinetic processes taking place inside Ω, and is obtained directly from the standard coefficients $\{g, s, \hbar\}$ as:

$$\tilde{g} \equiv g\Omega, \;\; \tilde{s} \equiv s, \;\; \tilde{\hbar} \equiv \hbar\Omega^{-1}$$

The volume Ω is in principle arbitrary, although its minimum value is subjected to a Neumann stability criterion given by:

$$\Omega^{\frac{1}{3}} > \ell \tag{2.3}$$

with

$$\ell = \max_i \{l_i\} \tag{2.4}$$

$$l_i = \sqrt{\frac{D_i}{R_i}} \tag{2.5}$$

Where D_i and R_i are the diffusivity and the lifetime of a mobile species within Ω. From eq. (2.2), $R_i = \tilde{s} + \sum_j \tilde{\hbar}_{ij} N_j$. The system of equations (2.2) is then solved using the kinetic Monte Carlo (residence-time) algorithm by sampling from the set $\{\tilde{g}, \tilde{s}, \tilde{\hbar}\}$ with the correct probability and executing the selected events. Here in this section, we provide general expressions on each reaction rate, however, details of certain reaction types according to the cases being studied would be re-emphasized in subsequent chapters.

2.1.2 0th-order reactions

Due to the stochastic nature, SCD is capable of treating ion/neutron and gas implantation inflicted collision cascades as stochastic processes, thus dealing with the probabilistic aspects of irradiation damage. In current implementation, external particle implantation and cascade damage are modeled as sequences of discrete Poisson events with the neutron/ion insertion rates adjusted to the nominal damage dose rate in dpa s^{-1} and to the gas implantation rate in appm/dpa. Further, constructing suitable source term g_i involves the calculation of recoil energy distributions is of certain matrix material using the SRIM software package [423]. The recoil spectra are given as cumulative probability disctribution function (*cpdf*) $\mathrm{C}(E_{\mathrm{PKA}})$.

Once a particle insertion event is selected, this *cpdf* is used to obtain random samples of the primary knock-on atom (PKA) energies E_{PKA} by solving $E_{\mathrm{PKA}} = C^{-1}(\xi)$, where ξ is a random number uniformly distributed in (0,1], until the sum of those E_{PKA} reaches the total incident energy that is expended on lattice damage, E_D. Note that here $C(E) = \int_0^E P(E)dE$, where $P(E)$ is the normalized recoil energy spectrum. For each individual PKA, further randomization is performed to account for statistical variations in the number of defects and defect clusters generated in a collision cascade with a given recoil energy. Defect species are generated randomly *on demand* by sampling from discrete distributions parameterized to reproduce subcascade statistics, for instance, clustering fractions for SIA and vacancies, f_c^{SIA} and f_c^{V} respectively. In this fashion, the inserted defect populations originate from a rich statistical database constructed from hundreds of MD cascade simulations covering a wide range of recoil energies and temperatures.

2.1.3 1st-order reactions

1st-order reactions represent events of cluster dissociation, defect absorption and emission at sinks. First, for cluster dissociation reactions, the monomer emission rates should reflect the likelihood of the return of some emitted monomers to the emitting cluster even if there's no cluster-monomer attraction. In principle the effective dissociation/emission rate is written as:

$$R^{\text{diss}} = \frac{d}{d+r}\frac{4\pi r^2}{a_0^2}\nu_0 \exp\left(-\frac{E_b(n)+E_m}{k_B T}\right) \tag{2.6}$$

where d is the first nearest-neighbor jump diatance, r is the cluster radius and term $\frac{d}{d+r}$ represents the fraction of non-returning monomers. Term $\frac{4\pi r^2}{a_0^2}$ is an approximate count of all distinct locations on the cluster surface from which a monomer may be emitted, with a_0 as the lattice parameter. ν_0 is the attempt frequency, $E_b(n)$ is the binding energy of a monomer to a cluster of size n, E_m is the monomer migration barrier, k_B is Boltzmann's constant and T is the temperature

As for defect absorption reactions, intrinsic microstructural heterogeneities such as dislocations, grain boundatries, precipitates and free surfaces are defined as sinks that correspond to different sink strength. In this thesis, the only sink type being considered is dislocations, thus the respective sink strength is directly dislocation density ρ_d. The absorption rate of mobile defects i by dislocations is then:

$$R_i^{\text{abs}} = z_i \rho_{\text{d}} D_i N_i \tag{2.7}$$

where z_i is an appropriate bias factor that captures the increased propensity of some defects over other to be absorbed by dislocations (e.g. SIAs v.s. vacancies).

2.1.4 2nd-order reactions

2nd-order reaction term accounts for the various mechanisms involving collisions of two defect cluster species. These processes could be single SIA-vacancy annihilation, SIA absorption by an interstitial cluster, vacancy aggregation, etc. Such binary reactions are often described directly by Smoluchowski's stationary solution for the collision rate between two clusters [328] whose simplified version used in SCD is written as:

$$\tilde{k}_{jk} = \frac{4\pi \left(r_j + r_k\right)\left(D_j + D_k\right)}{\Omega} N_j N_k \tag{2.8}$$

where r_j and r_k are the reaction radii of the reacting species. Here, we assume vacancy cluster V_n as spheres with radius,

$$r_j = \left(\frac{m 3 \Omega_v}{4\pi}\right)^{\frac{1}{3}} \tag{2.9}$$

and interstitial clusters SIA_n as plates:

$$r_j = \sqrt{\frac{n\Omega_{\mathrm{SIA}}}{\pi d}} \tag{2.10}$$

2.1.5 Spatial resolution

SCD has been applied in a variety of scenarios not involving concentration gradients [239, 241]. However, for those cases involving long-range migration of defects, such as hydrogen penetrations in structural materials, eq. (2.1) must be expanded into a transport equation (i.e. a *partial differential equation*, or PDE) by adding a *F*ickian term of the type:

$$\frac{dC_i}{dt} = \nabla \left(D_i \cdot \nabla C_i\right) + f(t; C_1, C_2, C_3 \ldots) \tag{2.11}$$

where D_i is the diffusivity of species i, and $f(t; C_1, C_2, C_3 \ldots)$ is used for simplicity to represent all of the terms in the r.h.s. of eq. (2.1). To cast eq. (2.11) into a stochastic

form, the transport term must be converted to a reaction rate in the finite volume Ω. As several authors have shown, this can be readily done by applying the divergence theorem and approximating the gradient term in terms of the numbers of species in neighboring elements [98, 99]. In the most general 3D case:

$$\nabla \left(D_i \cdot \nabla C_i \right) \rightarrow D_i \sum_{\beta} A_{\alpha\beta} \frac{N_i^{\beta} - N_i^{\alpha}}{\Omega_{\alpha} l_{\alpha\beta}}$$

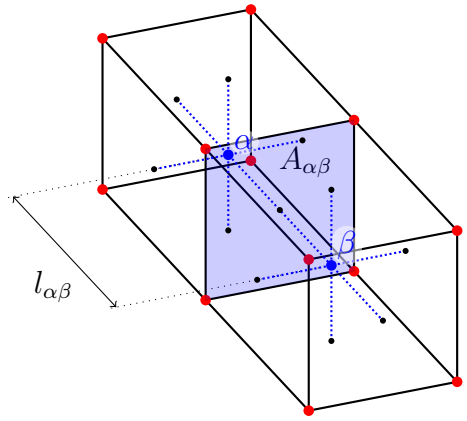

Figure 2.1: Schematic diagram of two volume elements of a 3D space discretization used to calculate spatial gradients within SCD.

where α is a subindex that represents the current element, and β represents the neighboring elements ($\beta = 1, \ldots, 6$ in 3D). $A_{\alpha\beta}$ is the dividing surface between neighboring elements α and β, $l_{\alpha\beta}$ is the distance between their centers, and Ω_{α} is the current element's volume. Figure 2.1 shows a schematic diagram of the geometry of two generic volume elements. In this fashion, each term of the above sum represents the rate of migration of species i from volume element α to β, which can be now added to the r.h.s. of eq. (2.2) and sampled stochastically as any other event using the residence-time algorithm.

The extension of eq. (2.2) from an ODE system into a PDE system can be written for species i in volume element m as:

$$\frac{dN_i^\alpha}{dt} = D_i \sum_\beta A_{\alpha\beta} \frac{N_i^\beta - N_i^\alpha}{\Omega_\alpha l_{\alpha\beta}} + \tilde{g}_i + \sum_q \left(\sum_j \tilde{s}_{jq} N_j^\alpha - \tilde{s}_{iq} N_i^\alpha \right) + \\ + \sum_j \left[\left(\sum_k \tilde{k}_{jk} N_k^\alpha - \tilde{k}_{ij} N_i^\alpha \right) N_j^\alpha \right] \tag{2.12}$$

For regular cubic meshes, or in 1D, the Fickian term simply reduces to $D_i \frac{N_i^\beta - N_i^\alpha}{l^2}$, where l is the element size. The spatial-resolved SCD model is employed in chapter 3 and 4.

2.2 The Crystal Plasticity Formulation

In this section we present a general crystal plasticity formulation that would be used in chapter 5 and 6, simply assuming bcc metals with only $1/2\langle 111 \rangle$ screw dislocation and dislocation glide as the only motion. A more comprehensive model based on dislocation climb & glide mechanism will be shown in chapter 7.

2.2.1 Kinematics.

For a deformable body occupying a volume Ω_0 bounded by a surface $\partial\Omega_0$, a one-to-one mapping $\boldsymbol{x}(\boldsymbol{X}, t)$ is assumed to exist between the position of material points in their reference position $\boldsymbol{X}$ and their current position $\boldsymbol{x}$. The deformation gradient of this mapping, $\boldsymbol{F} = \partial \boldsymbol{x} / \partial \boldsymbol{X}$ is typically decomposed multiplicatively into plastic and elastic contributions, $\boldsymbol{F}^{\mathrm{P}}$ and $\boldsymbol{F}^{\mathrm{E}}$ as [211]:

$$\boldsymbol{F} = \boldsymbol{F}^{\mathrm{E}} \boldsymbol{F}^{\mathrm{P}} = \boldsymbol{I} + \nabla \otimes \boldsymbol{u} \tag{2.13}$$

where $\boldsymbol{u}$ is the displacement vector. The rate of change of $\boldsymbol{F}$ can be written as:

$$\dot{\boldsymbol{F}} = \frac{\partial \dot{\boldsymbol{x}}}{\partial \boldsymbol{X}} = \frac{\partial \dot{\boldsymbol{x}}}{\partial \boldsymbol{x}} \frac{\partial \boldsymbol{x}}{\partial \boldsymbol{X}} = \boldsymbol{L}\boldsymbol{F} \tag{2.14}$$

where $\boldsymbol{L}$ is the velocity gradient. $\boldsymbol{L}$ additively decomposes into:

$$\boldsymbol{L} = \dot{\boldsymbol{F}}^{\mathrm{E}} \boldsymbol{F}^{\mathrm{E}-1} + \boldsymbol{F}^{\mathrm{E}} \left(\dot{\boldsymbol{F}}^{\mathrm{P}} \boldsymbol{F}^{\mathrm{P}-1} \right) \boldsymbol{F}^{\mathrm{E}-1} = \boldsymbol{L}^{\mathrm{E}} + \boldsymbol{L}^{\mathrm{P}} \tag{2.15}$$

where $\boldsymbol{L}^{\mathrm{E}}$ and $\boldsymbol{L}^{\mathrm{P}}$ are the elastic and plastic velocity gradients, respectively. In the small deformation limit (linearized kinematics),

$$\nabla \otimes \boldsymbol{u} = \boldsymbol{H}^{\mathrm{E}} + \boldsymbol{H}^{\mathrm{P}} \tag{2.16}$$

where $\boldsymbol{H}^{\mathrm{E}}$ and $\boldsymbol{H}^{\mathrm{P}}$ are the elastic and plastic *distortions*, respectively, such that, then, $\boldsymbol{L}^{\mathrm{E}} = \dot{\boldsymbol{H}}^{\mathrm{E}}$ and $\boldsymbol{L}^{\mathrm{P}} = \dot{\boldsymbol{H}}^{\mathrm{P}}$. If the only mechanism of plastic deformation at the crystal level is dislocation slip along specific crystallographic directions, then we can write [303]:

$$\dot{\boldsymbol{H}}^{\mathrm{P}} = \sum_{\alpha} \dot{\gamma}^{\alpha} \boldsymbol{s}^{\alpha} \otimes \boldsymbol{n}^{\alpha} \tag{2.17}$$

where $\dot{\gamma}^{\alpha}$ denotes the plastic slip rate of slip system α, $\boldsymbol{s}^{\alpha}$ and $\boldsymbol{n}^{\alpha}$ represent the corresponding slip and plane normal directions expressed in the original frame of reference, and $(\boldsymbol{s}^{\alpha} \otimes \boldsymbol{n}^{\alpha})$ is the *Schmid* tensor.

In isotropic linear elasticity, one can define a symmetric matrix $\mathbb{C} := (\kappa - {}^{2\mu}/_{3})\, \boldsymbol{I} \otimes \boldsymbol{I} + 2\mu \mathbf{1}$, where κ and μ are the bulk and shear modulus, and $\boldsymbol{I}$ and $\mathbf{1}$ are the second and fourth order identity matrices, such that the Cauchy stress can be expressed as a function of the elastic strain, i.e.:

$$\boldsymbol{\sigma} = \mathbb{C} : \boldsymbol{H}^{\mathrm{E}} = \mathbb{C} : \boldsymbol{\varepsilon}^{\mathrm{E}} \tag{2.18}$$

Assuming an instantaneous elastic response, the rate form of eq. (2.18) is:

$$\dot{\boldsymbol{\sigma}} = \mathbb{C} : \dot{\boldsymbol{\varepsilon}}^{\mathrm{E}} \tag{2.19}$$

The system is evolved in time subjected to the kinematic boundary condition:

$$\boldsymbol{L} = \dot{\boldsymbol{\varepsilon}}_0, \text{ in } \Omega_0$$

which combined with eq. (2.19) allows us to write:

$$\dot{\boldsymbol{\varepsilon}}^{\mathrm{E}} = \dot{\boldsymbol{\varepsilon}}_0 - \dot{\boldsymbol{H}}^{\mathrm{P}} \tag{2.20}$$

2.2.2 Flow rule.

The present CP model is rate dependent through the definition of $\dot{\boldsymbol{H}}^{\mathrm{P}}$ in eq. (2.17). The shear rates $\dot{\gamma}^\alpha$ are computed according to Orowan's equation:

$$\dot{\gamma}^\alpha = \rho^\alpha b^\alpha v^\alpha \tag{2.21}$$

where ρ^α, b^α and v^α are the dislocation density, Burger's vector modulus, and velocity in slip system α. Here, we consider bcc metals with only $1/2\langle 111\rangle$ screw dislocations, i.e., b is unique and equal to $a_0\sqrt{3}/2$, with a_0 the lattice parameter. In this thesis, we are interested in low and intermediate temperatures ($< 0.3T_m$, where T_m is the melting point), where thermally activated screw dislocation motion is represented by the following expression [57, 337]:

$$v^\alpha = \frac{\nu_0 h\left(\lambda^\alpha - w\right)}{b} \exp\left(-\frac{\Delta H_0}{kT}\left[1 - \left(\frac{\Delta\tau^\alpha}{\sigma_P}\right)^p\right]^q\right) \tag{2.22}$$

where ν_0, h, λ^α, and w are, respectively, the attempt frequency, the distance between Peierls valleys in the bcc lattice, the mean dislocation segment length for slip system α, and the kink-pair width. ΔH_0 and σ_P are the kink-pair formation energy and the Peierls stress. k is Boltzmann's constant, and p and q are fitting parameters. The term $\Delta\tau^\alpha$ in the equation is the available glide stress on slip plane α and will be discussed below.

The time evolution of the dislocation density is modeled using a rate equation of the type:

$$\dot{\rho}^{\alpha} = \dot{\rho}^{\alpha}_{\text{mult}} - \dot{\rho}^{\alpha}_{\text{ann}} \tag{2.23}$$

where $\rho^{\alpha}_{\text{mult}}$ and $\rho^{\alpha}_{\text{ann}}$ represent the net sources and sinks of dislocation line length. Each of these terms can be defined using a standard Kocks-Mecking model [57, 198]:

$$\dot{\rho}^{\alpha}_{\text{mult}} = \frac{|\dot{\gamma}^{\alpha}|}{b\lambda^{\alpha}} \tag{2.24}$$

$$\rho^{\alpha}_{\text{ann}} = \frac{2d_{\text{edge}}}{b}\rho^{\alpha}|\dot{\gamma}^{\alpha}| \approx 2\rho^{\alpha}|\dot{\gamma}^{\alpha}| \tag{2.25}$$

where it has been assumed that dislocation annihilation occurs spontaneously when dipoles meet within a critical spacing $d_{\text{edge}} \approx b$. λ^{α} is the available dislocation segment length, which is generally expressed as:

$$\frac{1}{\lambda^{\alpha}} = \frac{1}{d_g} + \sqrt{\rho^{\alpha}_f} \tag{2.26}$$

where d_g is the grain size and ρ^{α}_f is the *forest* dislocation density, which is obtained for each slip system α from contributions of all other systems β [303]:

$$\rho^{\alpha}_f = \sum_{\beta \neq \alpha} \rho^{\beta} |\boldsymbol{s}^{\beta} \cdot \boldsymbol{n}^{\alpha}| \tag{2.27}$$

The constitutive nature of ρ^{α} comes via its dependence on $\dot{\gamma}^{\alpha}$, which depends on the stress through the dislocation velocity. This is an implicit dependence that will have numerical implications as will be discussed below.

To close the model presented in eqs. (2.17)-(2.27), an expression for $\Delta\tau^{\alpha}$ needs to be provided. For this, we start by defining the *resolved shear stress* (RSS) from the Cauchy stress as:

$$\tau^{\alpha}_{\text{RSS}} = \boldsymbol{\sigma} : (\boldsymbol{s}^{\alpha} \otimes \boldsymbol{n}^{\alpha}) \tag{2.28}$$

which is also known as the Schmid stress[1]. The available glide stress is obtained by subtracting the forest hardening contribution from $\tau^{\alpha}_{\mathrm{RSS}}$:

$$\Delta\tau^{\alpha} = \tau^{\alpha}_{RSS} - \Delta\tau^{\alpha}_{f} \tag{2.29}$$

where

$$\Delta\tau^{\alpha}_{f} = \mu b \sqrt{\sum_{\beta} \xi_{\alpha\beta}\rho^{\beta}_{f}} \tag{2.30}$$

and $\xi_{\alpha\beta}$ is the hardening coefficient matrix [57, 118, 119]. This matrix, as well as the glide systems considered in the work are given in A and B.

[1]Although present in bcc materials [175], here we ignore non-Schmid effects.

CHAPTER 3

Kinetic Model of Incipient Hydride Formation in Zr Clad under Dynamic Oxide Growth Conditions

3.1 Literature Review

Corrosion of metallic structural materials is a pervasive phenomenon in industry and technology [72, 273, 314, 398]. In nuclear reactors, understanding the kinetics of corrosion of metallic components is grand materials science challenge due to the synergistic combination of high temperature, mechanical stresses, complex coolant and fuel chemistry, and irradiation [70, 182, 308]. In light-water nuclear reactors (LWR) zirconium alloys are used as cladding material in fuel elements to provide mechanical integrity between the coolant (water) and the fuel while keeping low levels of neutron absorption [10, 53, 111, 288]. In principle, Zr clad is subjected to corrosion from the coolant (water) and fuel sides, both by way of oxygen and hydrogen penetration. The oxidation and hydrogenation of zirconium fuel components in LWR may affect reactor safety and efficiency, which makes corrosion a critical design aspect of Zr materials response in nuclear environments [49, 56, 79, 162, 259, 262, 406].

While the majority of the focus of corrosion studies has centered on oxidation and oxygen transport and chemistry in the clad, in the corresponding tempera-

ture range, zirconium is known to absorb hydrogen and form hydrides once the critical concentration is reached in the interior of the clad. The accumulation of hydrides during operation plays an important role in fuel performance and safety during steady-state operation and transients, accident conditions, and temporary and permanent fuel storage [253, 425]. Examination of the Zr-H phase diagram below 810 K [100, 147, 333, 427] indicates that the first stable compound that appears after the metal solid solution (α-Zr) is a cubic phase with a nominal stoichiometry of 1:1.5 (atomic) known as δ-hydride. Generally, a range of stoichiometries between 1.52 and 1.66 is accepted experimentally as corresponding to this phase [149, 299].

While the presence of other metastable hydrides has been reported depending on temperature, aging time, or alloy composition [417], it is now well accepted that the needle-shaped structures that form in the metal region beneath the oxide layer are δ-hydride precipitates. Precipitation first starts when the hydrogen concentration reaches the terminal solubility limit, which ranges from zero at 523 K to approximately 7% at. at 810 K [427]. Although δ Zr_2H_3 displays good thermo-mechanical stability, it is also an exceedingly brittle phase [7, 64, 278, 422] that can compromise the clad's mechanical integrity [64, 71, 259, 353].

A key observation of the hydride microstructure is the elongated shape of the precipitates up to a few microns in length [39, 42, 68, 260], typically aligned along directions consistent with the stress distribution within the clad. Calculations and experiments point to the large misfit strains between the cubic δ-hydride and the host α-Zr as the reason behind such preferential alignment [29, 52, 105, 230, 260, 324], which may also impact the mechanical response of the clad. Indeed, the formation

of brittle hydride phases is a principal cause of delayed hydride cracking[1] in Zr clad [58, 212, 244, 253].

The phenomenology of corrosion is such that oxidation and hydrogenation are typically treated separately, despite some evidence suggesting that there might exist synergisms between oxygen and hydrogen pickup and transport that must be considered jointly in corrosion of Zr [1, 63, 75, 221, 332]. This is partially due to the formation of a clearly distinguishable outer oxide scale and and inner region where hydride platelets accumulate. In keeping with this distinction, existing models of hydrogen pickup and precipitation have been developed assuming no cooperative effects from oxygen on hydrogen transport and reaction [260, 290]. Models based on hydrogen supersaturation of the α-Zr metal [78, 243, 348] assume a binary partition of hydrogen in the clad, either as solid solution or as part of precipitates without specification of their size, number, or orientation. Detailed cluster dynamics (CD) modeling offers a more accurate alternative to obtain hydride size distributions and number densities by solving the complete set of differential balance equations with one-dimensional spatial resolution [22, 392]. Phase field methods can capture extra detail by furnishing the shape and orientation of hydrides in addition to concentrations and sizes [150, 232, 417].

An important aspect often overlooked in the models when studying hydrogen transport and hydride formation in the clad is that it occurs in a dynamic setting, with the oxide scale growing in time and hydrogen traversing an increasingly thicker layer before it can reach the interface. This is rationalized in terms of sluggish H diffusion through the oxide in the relevant temperature range ($< 300^{\circ}$C), suggesting

[1] A subcritical crack growth mechanism facilitated by precipitation of hydride platelets at the crack tips.

that this then would be the rate limiting step [40, 42]. This is the accepted picture during the *pre-transition* regime, as, after that, fast H transport then occurs through percolated crack networks formed in the oxide layer [21]. However, there is contradicting evidence in the literature about this [358,371], and it is not clear what effect a dynamic boundary condition might have on hydrogen precipitation in the metal substrate at higher temperatures, and what the evolution of the hydride microstructure will be in those conditions. With the objective of shedding new light on these and other issues by using new computational and experimental understanding, in this chapter, we present an comprehensive hydrogen transport and precipitation model in Zr formulated from first principles reaction kinetics and fundamental thermodynamics and mechanics. The model is parameterized using electronic structure calculations and experiments and captures both transport across the oxide layer growth and precipitation in the clad under dynamic hydrogen concentration profiles at the oxide/metal interface. First, we describe the fundamental chemistry and phenomenology of the hydrogen evolution in the clad followed by a mathematical formulation of the model. We then provide numerical results under a number of conditions relevant to LWR operation. We finalize with a discussion of the results and the implications of our modeling approach for zircalloy behavior.

3.2 Model Description

3.2.1 Zr-clad hydrogen chemistry

The formation of hydrides in the clad is predicated on exposure of its outer surface to bi-molecular hydrogen. This can occur as a consequence of exposure to water or

steam, from the reduction of water molecules as:

$$2H_2O + 4e^- \rightarrow 2O^{2-} + 2H_2 \tag{3.1}$$

or directly from exposure to hydrogen gas. It is well known that only a fraction of the hydrogen produced in this way is absorbed by the clad, ranging between 5 and 20% of the total hydrogen uptake (the total amount of hydrogen obtained stoichiometrically from reaction (3.1) [75, 77, 220, 260]. This, known as the *pickup* fraction, sets the boundary condition for the adsorption of hydrogen at the clad's surface. Adsorbed H_2 molecules can split into atomic hydrogen by a number of processes [167, 284], although whether this atomic H appears in a neutral or charged state in the metal is still an issue under debate [284,371]. Hydrogen atoms diffuse through the oxide layer and reach the oxide/metal interface, from which they can enter the α-Zr substrate and undergo a number of processes depending on temperature and concentration. Above the terminal solubility limit, hydrogen and zirconium react to form a hydride:

$$Zr + xH \rightarrow ZrH_x \tag{3.2}$$

where x is the atomic hydrogen concentration. By way of illustration, Figure 3.2 shows representative hydridized microstructures in Zirc-4 and Zirconioum.

In view of this picture, and to be consistent with our recent work on oxide layer growth modeling [295], we split our model into two connected elements: (i) a transport part involving H diffusion through an evolving oxide layer, and (ii) a kinetic model of hydride formation and growth in the metal with a dynamic boundary condition set by the first part (i). Figure 3.1 shows a schematic diagram of the geometry considered for this study and the principal chemical processes taking place in the material. Although it is well known that the Zr oxide layer is not monolithic,

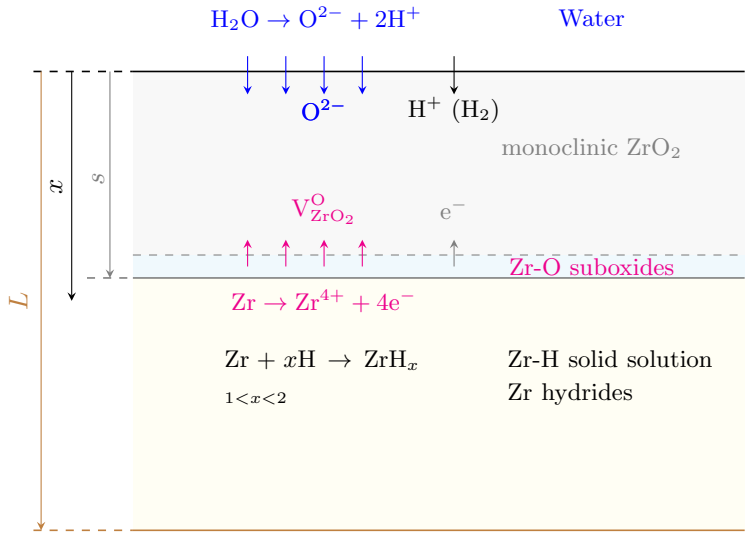

Figure 3.1: Schematic diagram (not to scale) of the geometry considered for the hydrogen penetration and hydride model developed in this work. x is the depth variable, s is the thickness of the oxide scale, and L is the total thickness of the clad. The chemical processes occurring at each interface are shown for reference.

containing various Zr-O phases depending on the external conditions and alloy composition [3, 138, 261, 295], here we consider a single phase (monoclinic) ZrO_2 with thickness defined by the variable $s(t)$. Hydrogen's diffusion through this layer is thought to occur mostly along grain boundaries, in microstructures ranging from columnar in out-of-pile [3] tests to roughly equiaxed for in-pile conditions [138]. This phenomenon takes place during the pre-transition regime, before the oxide layer cracks and/or develops porosity due to Pilling-Bedworth stresses developed during the metal-to-oxide transformation [65, 381]. Once cracking occurs, new diffusion avenues open up for hydrogen to reach the interface and diffusion is no longer seen as a rate limiting step. Our model applies only up to this transition point but not

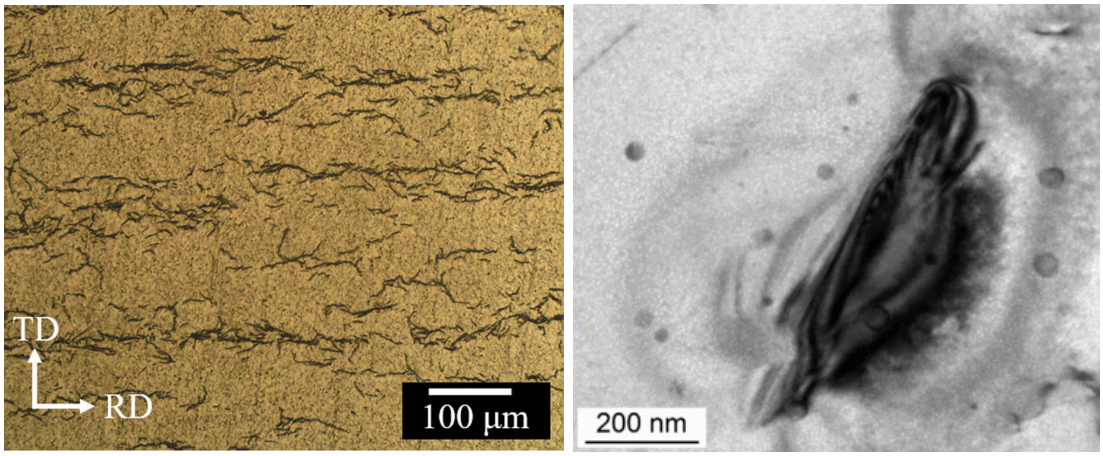

(a) (b)

Figure 3.2: (a) Optical micrographs of hydride morphologies in Zircaloy-4. 'TD' and 'RD' indicate the tangential and radial directions in the clad (reproduced with permission from ref. [161]). (b) Electron micrograph detail of a needle-like Zr hydride (reproduced with permission from ref. [418]).

beyond.

3.2.2 Diffusion model of hydrogen in ZrO_2

The goal of this part of the model is to determine the hydrogen concentration at the metal/oxide interface as a function of time. For this, a generalized drift-diffusion equation is solved:

$$\frac{\partial c_{\mathrm{H}}}{\partial t} = \nabla \left(D_{\mathrm{H}} \nabla c_{\mathrm{H}} \right) - \frac{U_{\mathrm{H}} D_{\mathrm{H}}}{kT^2} \nabla c_i \nabla T + \frac{q D_{\mathrm{H}}}{kT} \nabla \left(c_{\mathrm{H}} \nabla \phi \right) \tag{3.3}$$

This equation includes the following contributions:

- The first term is standard *Fickian* diffusion in the presence of a concentration gradient.

- The second term is the so-called *thermo-migration* contribution, which depends on the temperature gradient and where U_{H} is the activation energy for diffusion. The convention is for interstitial solutes to move in the direction opposing the gradient, i.e. a 'negative' drift contribution in the equation.

- The third term represents *electro-migration*, where q is the charge of the diffusing species (+1 for protons), and ϕ is the electrical potential, which can be determined by solving Poisson's equation:

$$\nabla^2 \phi = -\frac{\rho}{\varepsilon} \tag{3.4}$$

  where ρ is the charge density and ε is the dielectric permittivity.

Consistent with our previous work [295] and other studies [371], we assume the existence of a charge gradient across the oxide layer that originates from the onset of an electron density profile [76]. As well, in this work we consider autoclave conditions and thus neglect the thermomigration contribution.

Equation (3.3) is solved in one dimension (x) using the finite difference model with the following dynamic boundary conditions:

$$\begin{aligned} c_{\mathrm{H}}(x,0) &= 0 \\ J_{\mathrm{H}}(0,t) &= D_{\mathrm{H}} \frac{\partial c_{\mathrm{H}}(0,t)}{\partial x} = 2 f_{\mathrm{H}} C_0 \frac{\partial s}{\partial t} \end{aligned}$$

where C_0 is the amount of oxygen (per unit volume) absorbed into the clad to form Zr oxide.The first condition trivially states that the hydrogen content in the clad at the beginning of time is equal to zero, while the second one prescribes the flux of hydrogen at the water/oxide interface. This condition is time-varying as indicated by the growth rate of the oxide layer, $\dot{s}$. As well, it depends on the H pickup

fraction, f_{H}, which albeit may also be time dependent [77,220], we fix at 15% for the remainder of this work. The factor of '2' represents the fact that there are two atoms of hydrogen per oxygen atom available to penetrate the clad. Under homogeneous oxide formation conditions, $C_0 \approx 2\rho_{\mathrm{Zr}}$, with ρ_{Zr} the Zr atomic density.

Expressions for $s(t)$ have been provided in our previous study for a number of nuclear-grade Zr alloys [295]. In general, $s(t) = at^n$ such that the growth rate can be directly expressed as

$$\frac{\partial s}{\partial t} = ant^{n-1} \tag{3.5}$$

a values range between 0.33 (pure Zr) and 0.37 (Zirc-4), while $n = 0.34$ in both cases. These values give s in microns when t is entered in days. With this, $\dot{s} \approx 0.11t^{-0.66}$ (microns per day).

3.2.3 Stochastic cluster dynamics model with spatial resolution

In this work, we use the spatial-resolved stochastic cluster dynamics (SRSCD) to perform all simulations (see section 2.2). To solve eq. (2.12), the model assumes the following:

(i) The only mobile species considered are hydrogen atoms.

(ii) The source term $\tilde{g}_i$ only applies to element 0 (oxide/metal boundary) and is calculated from the hydrogen arrival flux calculated from the model in Section 3.2.2.

(iii) The only processes considered in the metal are:

  (a) H diffusion

(b) Immobilization of H atoms through formation of Zr_2H_3 molecules (equivalent to nucleation of hydride platelets).

(c) Growth of Zr_2H_3 clusters.

(d) Thermal dissolution of Zr_2H_3 clusters.

Next, we provide suitable expressions for each of the kinetic processes just listed.

3.2.4 H atom diffusion

The hydrogen diffusivity in both the oxide and the metal is assumed to follow an Arrhenius temperature dependence:

$$D_{\mathrm{H}}^{\alpha}(T) = D_0^{\alpha} \exp\left(-\frac{e_m^{\alpha}}{kT}\right) \tag{3.6}$$

where D_0 is the exponential pre-factor, e_m is the migration energy, k is Boltzmann's constant, and the superscript α can refer to the oxide ('ox') or the metal ('m'). The diffusivity of H in Zircaloy-4 oxides has been recently measured by Tupin *et* al. [354], which give values of 2.5×10^{-14} m·s^{-1} and 0.41 eV for D_0^{ox} and e_m^{ox}, respectively. Alloy composition, however, has been shown to have a significant impact on diffusion parameters. For example, values of e_m^{ox}=0.55 and 1.0 eV have been reported for Zr-2.5%Nb and pure Zr, respectively, with D_0 numbers in as high as 1.1×10^{-12} m·s^{-1} [80, 193]. Here, we use the parameters for Zirc-4 given by Tupin *et* al.

Similarly, the only mobile species in the metal is monoatomic hydrogen. The most widely used parameters for hydrogen diffusion in metal Zr, and Zircaloy-2 and -4 (D_i in eq. (2.12)) are those by Kearns [192] in the 200-to-700°C temperature range, with values of $D_0^{\mathrm{m}} = 7.90 \times 10^{-7}$ m·s^{-1} and $e_m^{\mathrm{m}} = 0.46$ eV. Earlier literature on these measurements [149, 312, 329] reveals pre-factors ranging from 7.00×10^{-8}

to 4.15×10^{-7} m·s^{-1} and migration energies between 0.3 and 0.5 eV, all in a similar temperature range. More recent experiments and molecular dynamics simulations are also consistent with these values [148, 325].

The values chosen here for each case (diffusion in the oxide and in the metal) are given un Table 3.1.

3.2.5 Nucleation of Zr_2H_3 hydride

As shown in Fig. 3.1, once hydrogen penetrates into the metal clad, the hydration reaction $\mathrm{Zr} + x\mathrm{H} \rightarrow \mathrm{ZrH}_x$ starts occurring. Although the formation of the δ-hydride is seen for a range of x values, here we assume a perfect stoichiometry of x=1.5. Consequently, the governing equilibrium constant for the reaction can be expressed as:

$$K_\delta = \frac{[\mathrm{ZrH}_{1.5}]}{[\mathrm{Zr}]\,[\mathrm{H}]^{1.5}}$$

However, it is more convenient to use an expression that is linear in the hydrogen concentration. From this, one can write the reaction rate as:

$$k_\delta = 4\pi\,(r_\mathrm{H} + r_\mathrm{Zr})\left(V^{-\frac{1}{3}}\rho_\mathrm{Zr}^{\frac{2}{3}}\right) D_\mathrm{H} N_\mathrm{H} p(x) \exp\left(-\frac{\Delta E_\delta}{kT}\right) \tag{3.7}$$

which is simply a coagulation rate for two species –H and Zr– in the proportions indicated by the exponents of ρ_Zr and N_H. ΔE_δ is the formation energy of a molecule of δ hydride ($\approx$ 0.52 eV at 350°C according to Blomqvist et al. [43]) and $p(x)$ represents the thermodynamic probability for this reaction to occur, which can be directly extracted from the Zr-H phase diagram using the lever rule:

$$p(x) = \frac{x - x_\mathrm{TTS}}{x_\delta - x_\mathrm{TTS}} \tag{3.8}$$

where x_{TTS} is the *terminal thermal solubility* at the temperature of interest, and x_δ is the phase boundary. A phase diagram of the Zr-H system in the temperature and concentration region relevant to the present study is shown in Figure 3.3. By way of example, at 660 K (horizontal dashed line in the figure) x_{TTS} is approximately 1.6% at. and $x_\delta \approx 60.0\%$ at. Equation (3.8) ensures that $p(x_{\mathrm{TTS}}) = 0$ and $p(x_\delta) = 1$, i.e. the

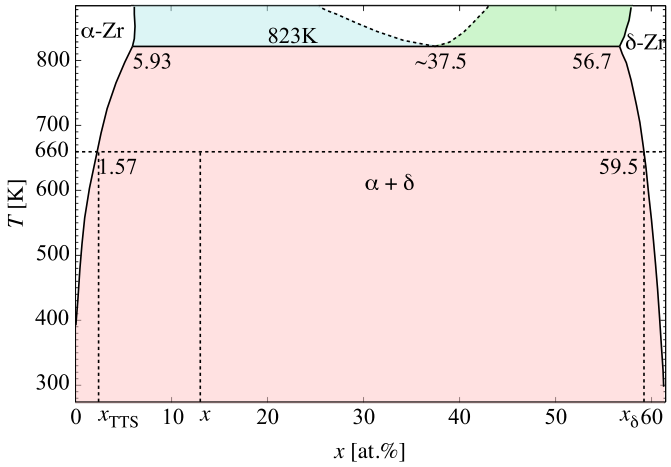

Figure 3.3: Phase diagram of the Zr-H system in the temperature and concentration region relevant to the present study (adapted from several sources [208, 255, 427]).

nucleation probability is zero at the phase boundary between the (α) and $(\alpha + \delta)$ regions, and unity at the $(\alpha + \delta)$ and (δ) boundary. This simple factor captures the thermodynamic propensity for the hydride reaction to take place, and thus ties the thermodynamics and kinetics of hydration together. r_{H} and r_{Zr} in eq. (3.7) are the interaction radii of H and Zr, respectively, their values given in Table 3.2. In the SCD calculations, the atomic fraction x is simply defined at any instant in time as:

$$x = \frac{N_{\mathrm{H}}}{N_{\mathrm{H}} + \rho_{\mathrm{Zr}} V}$$

3.2.6 Growth of Zr_2H_3 hydride

Once hydride nuclei appear in the clad, their growth is treated as a standard coagulation process in 3D with rate constant:

$$k_n = 4\pi V^{-1} \left(r_{\mathrm{H}} + r_\delta(n)\right) D_{\mathrm{H}} N_{\mathrm{H}} N_{(\mathrm{Zr}_{0.66n}\mathrm{H}_n)} \exp\left(-\frac{\Delta E_\delta}{kT}\right) \tag{3.9}$$

where r_δ is the interaction radius of the hydride clusters, and $N_{(\mathrm{Zr}_{0.66n}\mathrm{H}_n)}$ is the concentration of a hydride cluster containing n H atoms (which implies having $0.66n$ Zr atoms). It is assumed that hydride clusters are immobile. In accordance with previous works, hydrides grow as circular platelets whose size is directly related to the number of hydrogen monomers contained in it [392]:

$$r_\delta(n) = \sqrt{\frac{n\Omega_{\mathrm{H}}}{\pi d}}$$

with Ω_{H} and d the formation volume of hydrogen and the thickness of the platelet, respectively. This expression is the same as the pure interstitial cluster size in eq. (2.10). As given in Table 3.2, here we use $\Omega_{\mathrm{H}} = 2.8 \times 10^{-3}$ nm^3 per atom [377], and $d \approx 0.28$ nm [68].

The growth of hydride platelets is known to be highly directional, and influenced by stress and microstructure. Typically hydrides align themselves along the direction of the dominant axial stress components and grow preferentially in-plane on grain boundaries [39, 68, 348, 417]. These details are not captured in our model at present.

3.2.7 Dissolution of Zr_2H_3 hydride

The last process considered in our model is the thermal dissolution of the hydrides, as Fig. 3.3 shows, strictly speaking, hydrides are stable up to 550°C (eutectoid temperature), although there is ample evidence of their decomposition at much lower

temperatures, as well as the observation of thermal hysteresis during heating/cooling cycles [68, 274, 357, 409]. The dissociation rate is a first-order process that can be expressed as:

$$s_n = 4\pi r_\delta(n) D_{\mathrm{H}} N_{(\mathrm{Zr}_{0.66n}\mathrm{H}_n)} \exp\left(-\frac{e_b(n)}{kT}\right) \tag{3.10}$$

where e_b is the binding energy between a H monomer and a cluster containing n hydrogen atoms. Here, we assume a capillary approximation for e_b [22, 392]:

$$e_b(n) = e_s - 0.44\left[n^{\frac{2}{3}} - (n-1)^{\frac{2}{3}}\right]$$

with e_s being the heat of solution of H in the α-Zr matrix. This parameter has been found to be approximately 0.45 eV in electronic structure calculations [91, 268], compared to 0.66 eV in experiments [125].

3.2.8 Metal/oxide interface motion

Finally, the motion of the interface must also be considered as a viable stochastic event. To turn the interface velocity, eq. (3.5), into an event rate, r_i, one simply normalizes it by the interface thickness, s.

$$r_i = \left(\frac{1}{s}\right)\frac{ds}{dt} = \frac{ant^{n-1}}{at^n} = \frac{n}{t}$$

which results in the following expression for r_i:

$$r_i = 0.34t^{-1} \tag{3.11}$$

This is added to the event catalog and sampled with the corresponding probability as given by eq. (3.11). As the equation shows, this is a time-dependent rate that reflects the nonlinear growth of the oxide layer with time. In the context of the SCD model, it implies that the one-dimensional mesh shown in Fig. 3.4 must be

dynamically updated with time because the physical dimensions of the simulation domain are dynamically changed. To our knowledge, this has not been attempted in any prior models of hydride formation and buildup.

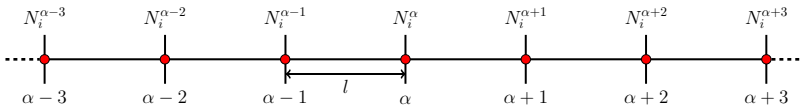

Figure 3.4: Schematic diagram of two volume elements of a 1D space discretization used to calculate spatial gradients within SCD. The superindex α refers to the physical element, while the subindex i refers to the cluster species.

3.2.9 Parameterization, physical dimensions, and boundary conditions

All the material constants used in the present model are given in Tables 3.1 and 3.2. External parameters representing the geometry and the boundary conditions are given in Table 3.3.

3.3 Results

We first show the time evolution of the hydrogen concentration at the oxide/metal interface. This results are from solving the diffusion equation in the the oxide layer subjected to a moving boundary as explained in Sec. 3.2.2. Figure 3.5 shows the buildup of hydrogen up to the first 580 hours. This represents a *dynamic* Dirichlet boundary condition for the spatially-resolved SCD calculations of hydride nucleation and growth in the metal substrate ($\tilde{g}$ term in eq. (2.12)). Second, we track the sampling rate r_i defined in Section 3.2.8 to confirm that it matches eq. (3.11). Figure 3.6

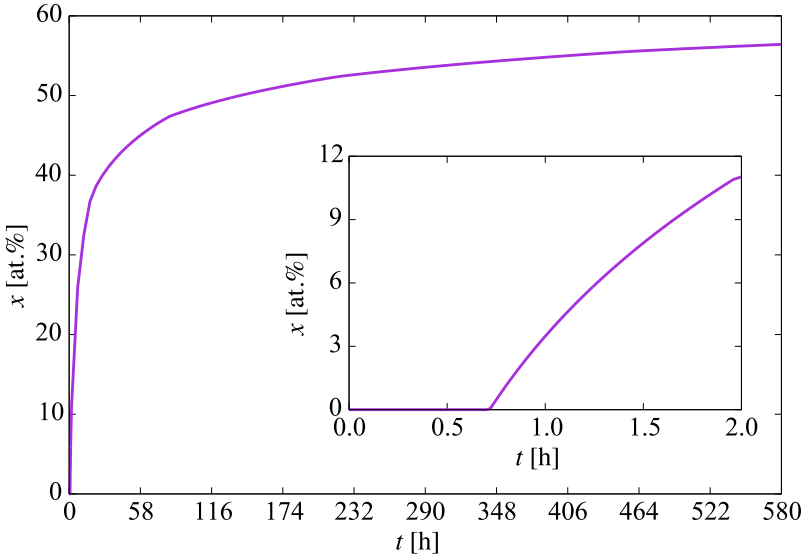

Figure 3.5: Evolution with time of the hydrogen concentration at the oxide/metal interface. This represents the boundary condition for the spatially-resolved SCD calculations of hydride nucleation and buildup.

shows a comparison between both, indeed demonstrating their equivalency and confirming the correctness of its implementation in the code. The effect of this interface motion is that, over the course of the time scale covered in the SCD simulations, the oxide layer effectively sweeps over the first mesh element of the metal depth profile (recall that we assume that such sweep results in dissolution of the hydrides existing within that element at that point, and re-solution of the immobilized hydrogen in the metal). In practice, this allows us to subsequently discard the first spatial element of the 1D mesh. That is the reason why in the figures shown next the spatial range shown spans 800 (as opposed to the original 900) nm.

Next, we study the generation of hydride molecules in the metal layer as a function of time and depth. The results are shown in Figure 3.7a, which shows a histogram

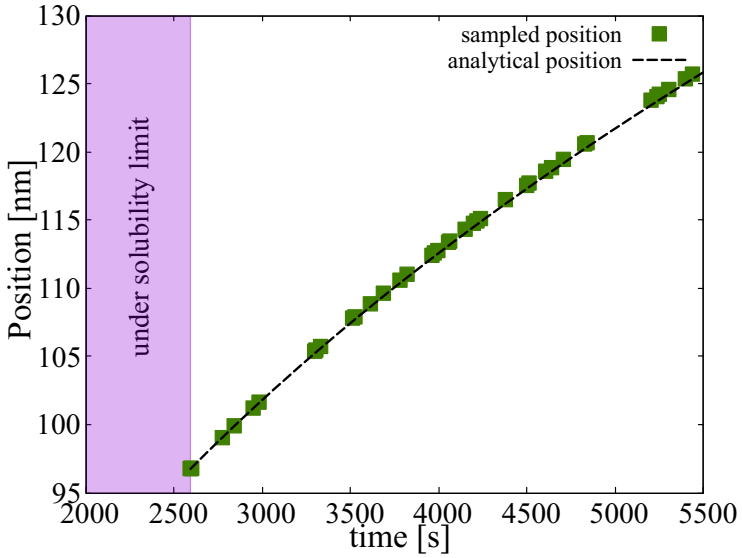

Figure 3.6: Comparison between the predictions of r_i and eq. (3.11) of the position of the oxide/metal interface as a function of time. We track the interface position only after the concentration of hydrogen has reached the solubility limit.

with the concentration of hydride molecules at several instants in time for each of the mesh elements of the metal region. As discussed in Section 3.2.5, the probability that a new hydride molecule will form depends primarily on the relative H concentration at the interface and the heat of formation of δ-hydride. With a probability per unit time k_δ (eq. (3.7)), freely-diffusing H atoms are immobilized to form $Zr_{2/3}H$ molecules that act as incipient hydride nuclei. The concentrations of such nuclei are strongly depth-dependent, as shown in the figure, ranging over two orders of magnitude over the entire specimen thickness L of 900 nm. As well, the nucleation rate, i.e. the derivative of the evolution curves shown in Fig. 3.7b (which display the same data as Fig. 3.7a but plotted as a function of time), can be seen to decrease gradually in time across the entire depth profile.

Subsequent growth of these embryos occurs at a rate given by the combination of the rates of H-atom absorption (eq. (3.9)) and dissolution (eq. (3.10)), i.e. $(k_n - s_n)$, as shown in Figure 3.8. Rapid net growth is seen in the initial stages of hydridization close to the oxide/metal interface. However, these rates gradually abate both in time and with increasing depth until almost no net growth is observed, particularly at depths greater than 700 nm after 1.4 hours of evolution.

The resulting hydride concentrations across the 900-nm metal layer at the end of the simulated time can be found in Figure 3.9a. As the graph indicates, the hydride number densities suffer almost a 100-fold decrease through the metal layer studied. In relative terms, these are large concentrations of small clusters, so it is to be expected that further time evolution of the hydride subpopulations will be dominated by growth, perhaps by way of some type of coarsening or ripening mechanism. The associated size distributions of the hydride clusters are shown in Figure 3.9b, where both the average and maximum cluster sizes are shown. We emphasize that, during the incipient nucleation of the hydrides, they grow as circular discs, and so the sizes simulated ($\approx$ 50 nm or less), correspond to the regime prior to the acicular growth of the hydrides.

3.4 Discussion

Several of the most important features of the model presented here are: (i) consideration of a moving interface representing the growth of the oxide scale during operation in corrosive conditions; (ii) using a hydride nucleation criterion that is consistent with the thermodynamics of the Zr-H system; (iii) using a mean-field growth/dissolution model that respects; (iv) a completely physics-based parameterization based on cal-

culated atomistic data. Some of these features were part of a comparable study [392], to which new ones have been added and existing ones augmented. All these features combined are the basis of a model that has been developed as an attempt to break the phenomenological vicious cycle in which models of materials degradation in nuclear environments are often found.

To study the nucleation of the hydride clusters, our method samples discrete kinetic processes defined by the corresponding energetics and thermodynamics. For example, hydride nucleation is simulated by considering the interplay between (i) aggregation, (ii) growth, and (iii) dissolution processes, which together determine the net nucleation and growth rates. Processes (i), (ii), and (iii) are embodied in eqs. (3.7), (3.9), and (3.10), respectively. Each one of these processes is treated as a stochastic event sampled with the probabilities given by each respective rate. If the conditions are such that dissolution would dominate over nucleation, the clusters would never form. If growth dominates over nucleation, the clusters would grow bigger, etc. All the energetics are given by the parameters in each of those equations.

As is often the case, the price paid for an increased physical fidelity in the simulations is computational efficiency. For this reason, our simulations can only extend to times of several thousand seconds (<2 hrs), which is of course only representative of the initial stages of hydridation in Zr clad (and, of course, part of the pre-transition corrosion regime)). In these relatively short time scales[2], one can only claim to faithfully study the incipient nucleation phase of the hydride microstructure. In this sense, our results do not include important features of the Zr hydride particles such as their elongated shape and/or their orientation. Excellent recent examples of ex-

[2]Note that these time scales are still orders of magnitude higher than what direct atomistic methods can cover

perimental characterization displaying all of these structure complexities exist now in the literature [38, 289, 369, 378]. They can act, however, as a good springboard from which to connect to other methods such as phase field simulations [27, 160, 417], or orientation-dependent precipitation models [349, 364]. Therefore, it is reasonable to assume that the time scale of the next phase of hydride formation/growth kinetics would be one dominated by coarsening/ripening, where population densities suffer a gradual decline at the expense of an increased average precipitate size. Thus, it is important to emphasize this aspect of the work: our results correspond to the incipient hydride nucleation and growth phase, before steady state populations are established. Steady state sizes and concentrations in corroded Zr specimens range from 100 nm to 1 μm [369] and $\sim 10^{24}$ m^{-3}. On this aspect, it is also difficult to reconcile calculated H-atom diffusivities in the clad with almost cross-clad uniform hydride distributions observed experimentally [41]. Calculated migration energies suggest a much more sluggish diffusion in the metal, and screening of the clad interior by hydrides formed near the oxide metal interface, as seen in this study, compared to experimental results. While validation on the time and length scales covered in this work is always difficult, it is encouraging to see reasonable qualitative agreement with experimental studies, e.g. hydride precipitation completion fractions in ref. [39] (Fig. 3) vs. Fig. 3.7b in this study. As well, our predictions for the size (long axis) of the precipitates in Fig. 3.9b are in good agreement with *in situ* SEM observations [317].

As reviewed in the Literature review, the formation of Zr hydrides in the metal clad is considered to be highly detrimental to reactor performance due to their embrittling effect. However, the high thermal stability of these hydride phases also makes them a matter of concern for reactor safety due to the potential for hydrogen storage and release during loss-of-coolant conditions and core meltdown. Palliative

measures such as increasing the enthalpy of formation of δ-ZrH by microstructure tailoring [203], or by hindering H diffusion in Zr oxide by selective alloying in the clad [326, 399], have been proposed for future candidate materials in novel nuclear fuel designs.

3.5 Summary

We end this chapter with a list of the most important conclusions:

- We have developed a spatially-resolved kinetic model of hydrogen transport/accumulation in Zr-metal clad. The model includes state-of-the-art hydride energetics data from atomistic calculations and is formulated as a stochastic version of the cluster dynamics method. Notably, boundary conditions are dynamically updated in time during the simulations, by accounting for oxide/metal interface motion due to the time-dependent growth of the oxide scale.

- In doing so, our model is consistent with the oxidation in the clad, as well as with the equilibrium thermodynamics of the Zr-H system.

- As most cluster dynamics models based on mean-field rate theory, our model does not capture the orientation dependence of elongated hydride platelets observed experimentally, and microstructural information such as grain sizes and dislocation densities is included only in an effective way. As such, our results are representative of the 'average' structure along the depth direction.

- Our results show that high concentrations of small hydride nuclei form across the entire metal clad. This results in a very fine microstructure that sets the

stage for the next kinetic phase, likely to be one of ripening and coarsening.

- Gaps in our knowledge identified in this work include, among others: (i) how to model the H dissolved from hydrides swept by the growing oxide layer, (ii) how to reconcile existing H-atom diffusion energies with almost cross-clad uniform hydride distributions, and (iii) the reasons for the acicular (or capsular) growth of the precipitates are still not clear and, while such geometries can be adopted in the models, a physical approach that yields these geometric features is still lacking.

Table 3.1: Zr-H energetics used in the model with the respective source.

Parameter	Unit	Symbol	Value	Source
Hydrogen diffusivity prefactor in Zr oxide	$m \cdot s^{-1}$	$D_{\mathrm{H}}^{\mathrm{ox}}$	2.50×10^{-14}	[354]
Hydrogen migration energy in Zr oxide	eV	e_m^{ox}	0.41	[354]
Hydrogen diffusivity prefactor in Zr metal	$m \cdot s^{-1}$	$D_{\mathrm{H}}^{\mathrm{m}}$	7.90×10^{-7}	[192]
Hydrogen migration energy in Zr metal	eV	e_m^{m}	0.46	[192]
δ-hydride formation energy	eV	ΔE_δ	0.88	[43]
H solution energy in Zr metal	eV	e_s	0.66	[125]

Table 3.2: Physical constants for the Zr-H system employed here. In actuality, the interaction radii of Zr and H atoms are extended by a distance equal to the Burgers vector $\langle$a$\rangle$ in α-Zr, which is equal to 3.23 Å.

Physical constant	Symbol	Unit	Value	Source
Zr atomic density	ρ_{Zr}	m^{-3}	4.31×10^{28}	-
H-atom interaction radius	r_{H}	Å	0.31	[74]
Zr-atom interaction radius	r_{Zr}	Å	1.75	[74]
H-atom formation volume	Ω_{H}	nm^3 per atom	2.8×10^{-3}	[377]
δ-hydride platelet thickness	d	nm	0.28	[68]

Table 3.3: Numerical parameters used in the model.

f_{H}	x_{TTS} [%]	x_{δ} [%]	T [K]	V [m^{-3}]	l [nm]	L [nm]
0.15	1.6	59.5	660	10^{-18}	100	900

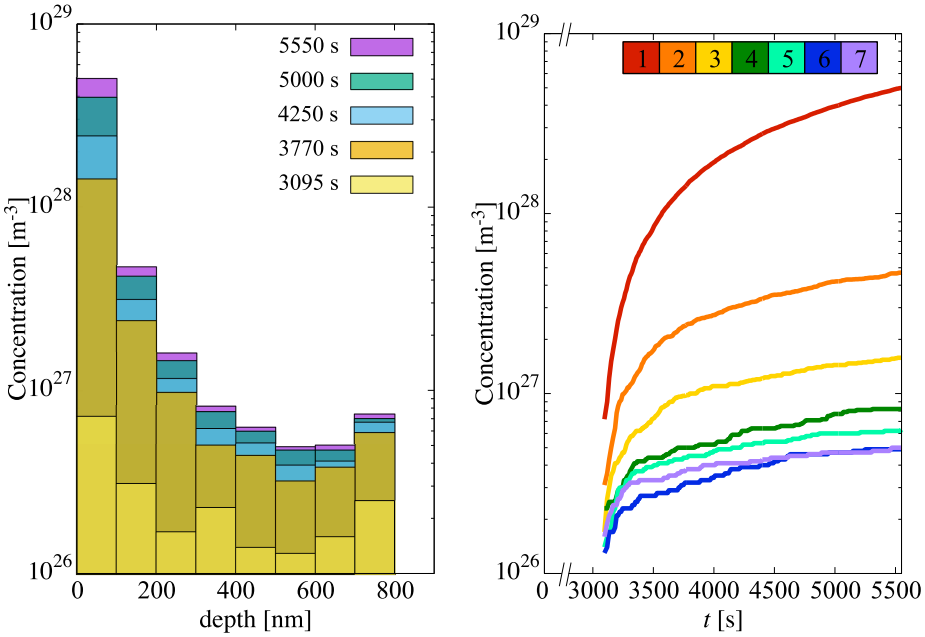

(a) (b)

Figure 3.7: (a) Concentration of incipient hydride nuclei in the metal layer as a function of depth for several time snapshots. (b) Hydride concentration buildup as a function of time for each depth element. Each curve is colored according to the key at the top of the figure (element 1 is closest to the oxide/metal interface). Per Table 3.3, each element is 100-nm thick.

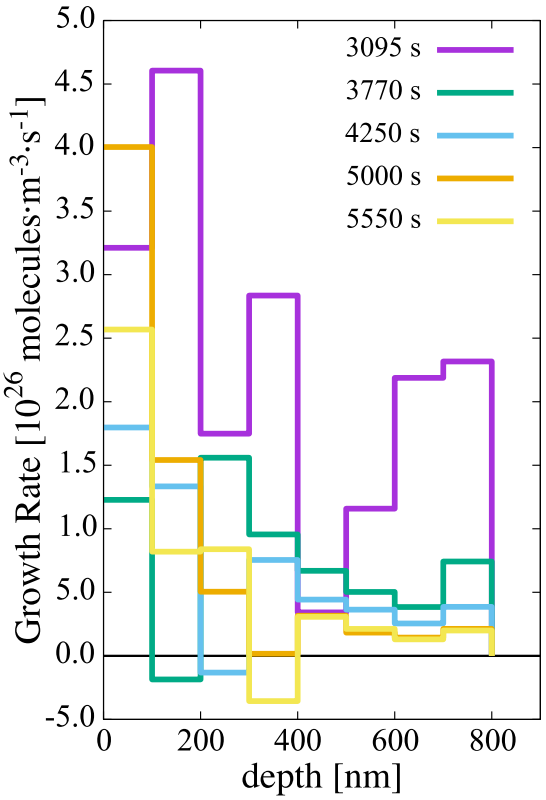

Figure 3.8: Growth rate of hydride clusters in the metal layer as a function of time and depth.

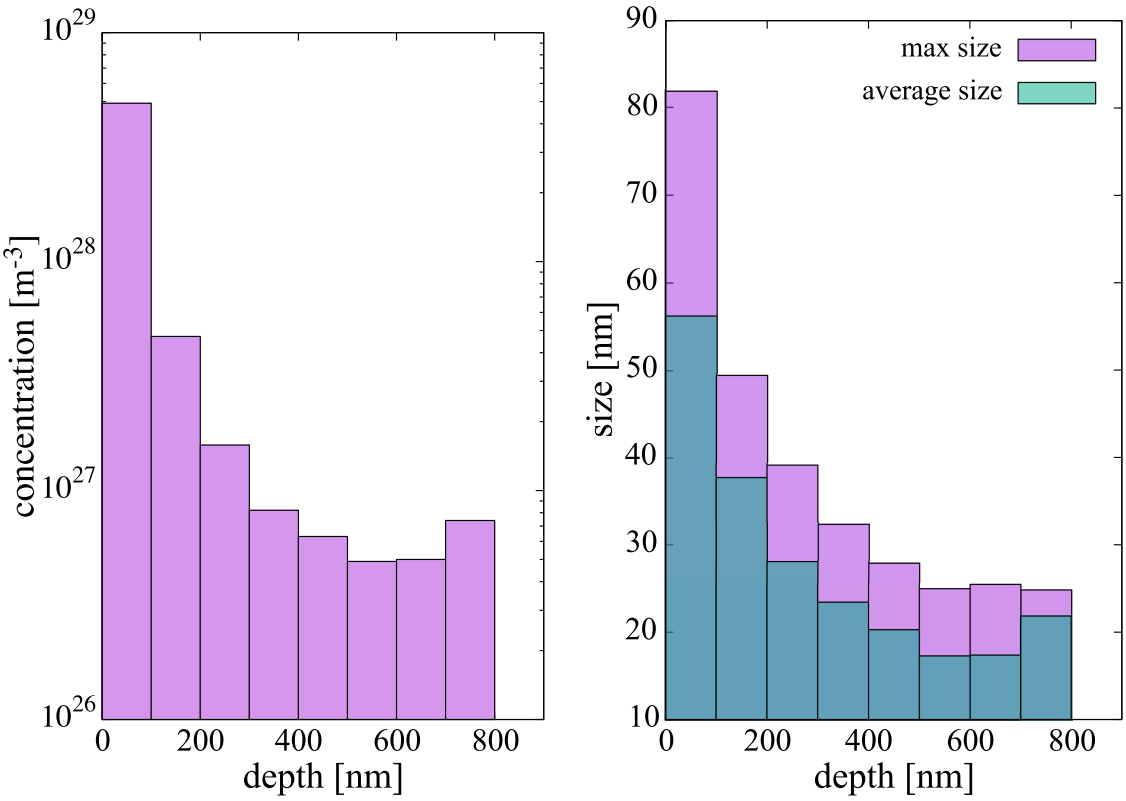

(a) (b)

Figure 3.9: (a) Concentration profile and (b) size distributions of the hydride cluster population after 1.53 hours of simulated evolution.

CHAPTER 4

Understanding hydrogen retention in damaged tungsten using experimentally-guided models of complex multispecies evolution

4.1 Literature Review

Tungsten (W) is being considered as a candidate plasma facing material (PFM) in magnetic fusion energy devices due, among others, to its high strength, high thermal conductivity, and low erosion/redeposition rates. Although W lacks the formation of stable hydrides, tritium fluxes as high as 10^{24} $m^{-2} \cdot s^{-1}$ are expected on the DEMO[1] [181, 343]. divertor, potentially leading to severe surface blistering [28, 231, 370, 393, 396], cracking [130], hydrogen embrittlement [104, 163], as well as creating safety and waste disposal concerns [426]. Retention of tritium (T), deuterium (D), or hydrogen (H) in as-fabricated W specimens is highly dependent on synthesis, thermal history, and intrinsic microstructure [8, 137, 236, 309, 419]. Understanding T/D/H retention in plasma-facing components is critical, as the viability of a D-T fusion energy source relies on the ability to breed sufficient T fuel for self-sustaining operation. For this, the allowable T retention probability limit must be

[1] DEMOnstration Fusion Reactor

very low (below $\sim 10^{-6}$) in the first wall and PFM's to achieve a tritium breeding ratio larger than unity [420]. Since the equilibrium vacancy concentration in the 500∼900 K temperature range is no higher than 10^{-9}, thermal retention of hydrogen is generally considered negligible [121, 202]. However, displacement damage at the level of 0.01 to 0.1 dpa introduced by energetic particle irradiation is known to lead to a significant (tenfold or more) increase in fuel retention [347, 366], making T inventory control more challenging during reactor operation subjected to neutron exposure. It is believed that defect clusters from irradiation can trap hydrogen atoms and contribute to the increase of fuel inventory in the material. Moreover, it is assumed that these clusters are primarily vacancy-hydrogen complexes (onwards referred to as V_mH_n defects containing m vacancies and n hydrogen atoms). Understanding the interplay between irradiation damage and T/D/H retention is thus of paramount importance to understand materials degradation and response, and to improve thermo-mechanical engineering and design.

Lack of suitable neutron sources has spurred the use of heavy ions as surrogates of neutron damage to study materials degradation under fusion conditions. Despite wide differences in dose rate and spatial penetration, heavy ions have proven an effective means to seed irradiation defects in materials subsequently exposed to hydrogen plasmas [13]. The amount of hydrogen trapped and the nature of the defect clusters present in the material is generally assessed by *a* posteriori thermal desorption spectroscopy (TDS), correlating hydrogen release with temperature to quantify detrapping energies of hydrogen from clusters [9, 16, 54, 127, 139, 300, 301, 305, 346, 356, 400]. TDS is an integrated measurement in the sense that it does not provide spatial information about the distribution and size of V_mH_n clusters. Insight into such properties of the defect cluster population can currently be gained from techniques such as elec-

tron microscopy (TEM) or nuclear reaction analysis (NRA) [69,168,191,233,376]. As well, X-ray diffuse scattering can provide information about the nature and size of the defects [338]. In all, the study of hydrogen retention in PFM's requires a multidimensional experimental effort involving heavy-particle irradiation, hydrogen plasma exposure, thermal desorption, and cross-characterization of defect populations and quantitative analysis of trapping energies using multiple techniques.

Given the inherent complexities discussed above, modeling has emerged as an effective option to contribute to our understanding of the fuel retention process at multiple levels. Kinetic transport methods such as rate theory (RT) or kinetic Monte Carlo (kMC) are natural choices to simulate the long-term kinetics of H penetration and trapping at length scales that capture surface and subsurface regions. As such, these methods must possess spatial resolution. While trivial for kMC calculations, this implies solving a system of partial differential equations (PDEs) formulated under the mean-field approximation for RT models[2]. This technique has been widely used to simulate H effects on W surfaces, partially owing to drastic advances in our capability to use first-principles atomistic methods based either on semi-empirical potentials –as in molecular dynamics (MD) simulations– or density functional theory (DFT) to account for the complex energy landscape of H penetration in the material and define the physical coefficients needed for kinetic transport simulations [46,186]. Indeed, atomistic calculations have provided and continue to provide fundamental kinetic parameters with unprecedented levels of physical accuracy. This includes energies for H adsorption, absorption, and desorption in W [164], migration energies [275], characterization of the bi-dimensional V_mH_n dissociation energy map [218,

[2]Also known as 'cluster dynamics' when based on classical nucleation theory.

276, 368], as well as –lately– He/H interaction energies [394]. Furthermore, our understanding of hydrogen retention processes has been enriched by consideration of yet-experimentally-unconfirmed physical processes such as the *t*rap mutation or the *s*uperabundant vacancy mechanisms [224, 291, 389], whose effect can be evaluated and tested using modeling and simulation in order to assess their applicability.

However, both RT and kMC suffer from intrinsic numerical limitations that hinder their application to the current problem. RT calculations cannot capture the full catalog of V_mH_n species due to the geometric growth in the number of PDEs to be considered for multispecies cases (vacancies, self-interstitials, hydrogen atoms, and clusters thereof) [5, 98, 199, 281, 334]. As well, they lack spatial correlations, a direct consequence of the mean-field approximation. For their part, direct kMC simulations are subjected to stiffness due to time scale separation of physical events and slow time evolution [33, 330]. In this work, we carry out spatially-resolved stochastic cluster dynamics (SR-SCD) simulations of a recent set of three-stage experiments performed by several of the co-authors involving (i) Cu-ion irradiation of single crystal W coupons, (ii) exposure to low-temperature H plasmas, and (iii) thermal desorption spectroscopy analysis [319, 320].

The chapter is organized as follows. A brief description of the experimental measurements is provided in Sec. 4.2.1. The physical processes considered as well as some additional reaction types within the SR-SCD model, and the parameterization employed are given in Sec. 4.2.2 and **??**. This is followed by the results in Sec. 4.3 and a brief technical discussion in Sec. 4.4. We end with summary.

4.2 Model Description

4.2.1 Experimental details and analysis

To avoid activated PFM samples, the experiments use deuterium and heavy ions as proxies for tritium and fusion neutrons, respectively. Polycrystalline tungsten (W) samples were dynamically annealed, each at a fixed temperature ranging from 300 to 1243 K (which is the expected temperature interval of PFM in ITER or DEMO), while irradiated with 3.4-MeV Cu ions to a dose of 1.82×10^{18} ions/m^2. The irradiated specimens were subsequently exposed to deuterium plasmas up to a fluence of 10^{24} D/m^2. During D exposure, samples were held to 383 K and biased to implant 110 eV D ions. Nuclear Reaction Analysis (NRA) and thermal desorption spectroscopy (TDS) measured the spatial D concentration profile and temperature dependent D release, respectively. The NRA-measured D profile correlated well with the defect profile calculated using SRIM. Total D retention measured by both NRA and TDS show a significant reduction with increased dynamic annealing temperature, approaching intrinsic D retention values when annealed at 1243 K. Detailed information about the experimental procedure and measurements can be found in ref. [319].

4.2.2 Theory and methods

Quantifying hydrogen transport and accumulation in plasma-exposed W necessitates understanding the pertinent energy landscape that H atoms encounter. Figure 4.1 shows a schematic diagram[3] of the near-surface region of the PFM divided into three

[3]After E.A. Hodille et al. [164].

zones. The 'vacuum', representing the plasma boundary region, the 'surface', representing the first few nanometers where material properties are significantly affected by their proximity to the material's edge, and the 'bulk', where hydrogen atoms do not feel the effect of the surface. The figure illustrates the rich variety of energy barriers experienced by hydrogen as it penetrates the solid from the plasma region. Starting with the vacuum region, E^{diss} is the dissolution energy of a H_2 molecule into two H atoms. In the surface region, H atoms must overcome an absorption energy barrier, E^{abs} to penetrate the bulk. This energy consists of a 're-absorption', energy E^r, a surface trapping energy, E^s, and the heat of solution of H in W, E^f_{H}. Once in the bulk, hydrogen atoms diffuse with a migration energy barrier, E^m. Deep traps in the bulk region are characterized by the binding energies, E^b, of H atoms to vacancy-hydrogen clusters. Each energy depicted in Figure 4.1 represents a kinetic process defined by an event rate. These rates control the time evolution of H in the system. As such, every one of these parameters must be obtained using a first-principles method (typically electronic structure calculations or semi-empirical potentials). We discuss this starting in Sec. 4.2.3.

4.2.3 Source term and determination of coefficients g_i

With respect to simulation method, all results are performed using the SR-SCD method that has been described in section 2.1. Here we provide some details that is only applicable to this study. For the damage source term g_i, W-recoil distribution for approximately 1000 Cu ions with the same incident energy of 3.4 MeV is obtained from the SRIM package. According to the calculations, only about 43.5% or ($E_D \sim$)1.48 MeV of the total incident energy is expended on lattice damage, with

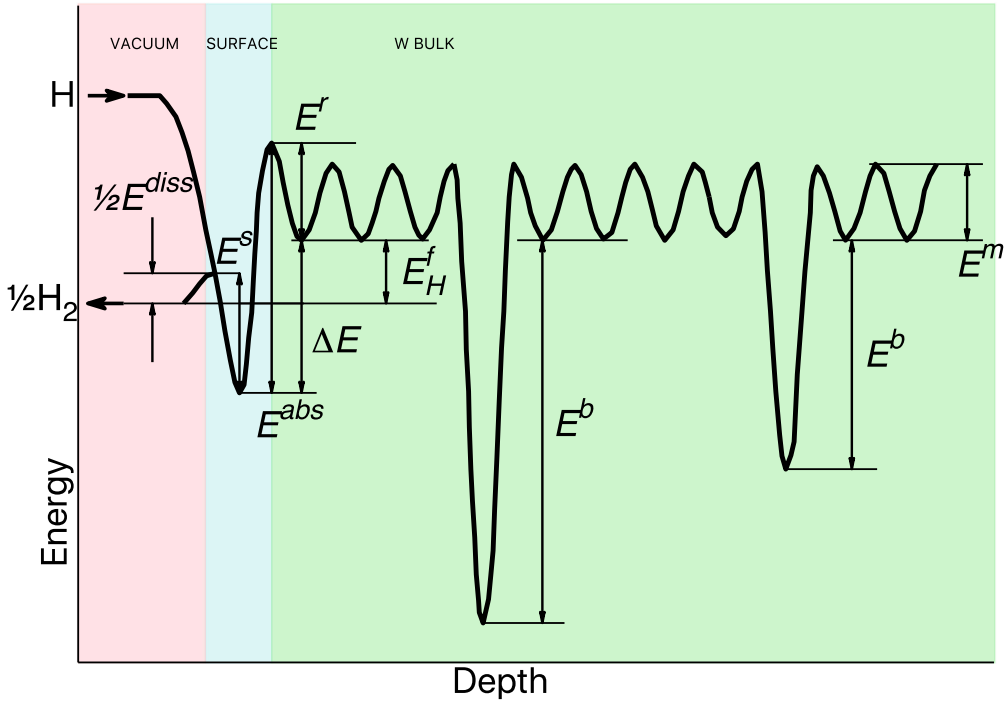

Figure 4.1: Schematic diagram of the energy landscape for H penetration and trapping in tungsten (adapted from ref. [164]). All energy barriers are defined in the text. Deep traps in the bulk region (shaded green) correspond to accumulation of H atoms at vacancy-hydrogen clusters.

the rest lost in ionization via electronic stopping. Since there is spatial resolution in this case, the corresponding cpdf profile mentioned in section 2.1.2 must also be a function of material depth which is shown in Fig. 4.2

The rate of Cu-ion insertion is calculated as:

$$r_{\text{ion}} = \rho_a^{-1} \phi \gamma \tag{4.1}$$

where ϕ is the ion flux, ρ_a is the atomic density of W, and γ is a damage function calculated within SRIM and measured in units of displacements per ion per unit length,

and corresponds to the dashed line shown in Fig. 4.2. Once an ion impact event is selected in the simulation volume, a sequence of PKA energies is obtained following the procedure just described until the sum of all sampled recoil energies reaches E_D. The insertion coefficients g are obtained by sampling from discrete distributions parameterized to reproduce sub-cascade statistics collected from hundreds of MD cascade simulations at different temperatures [234, 235]. Specifically, the number of Frenkel pairs produced as a function of PKA energy are:

$$N_F = \begin{cases} 1.15 \times 10^{-2} \left(E_{\mathrm{PKA}}\right)^{0.74}, & \text{if } E_{\mathrm{PKA}} < 43 \text{ keV} \\ 1.89 \times 10^{-5} \left(E_{\mathrm{PKA}}\right)^{1.34}, & \text{otherwise} \end{cases} \tag{4.2}$$

where E_{PKA} is given in eV. The dependence of N_F with temperature was seen to be weak and is not considered in this study. We set the minimum value of E_{PKA} to produce a stable Frenkel pair inside the material to be 620 eV [241]. For their part, the fractions of clustered SIAs and vacancies f_c^{SIA}, f_c^V depend strongly on, respectively, PKA energy and temperature [266]:

$$f_c^{SIA} = 0.0185 \left(E_{\mathrm{PKA}}\right)^{0.326} \tag{4.3}$$

$$f_c^V = 0.625 - 1.750 \times 10^{-4} T \tag{4.4}$$

where T is the absolute temperature.

4.2.4 Hydrogen dissociation from dislocation

The original SCD model discards defect dissociation from dislocations, while in this study we add this process for hydrogen monomers. While the absorption of mobile defects and H atoms by dislocations is spontaneous, the inverse process –i.e. emission– is thermally activated with a dissociation energy of E_d (for H atoms, it is ≈ 0.6 eV

according to several estimates [344])). After Friedel [2], this emission rate can be expressed as:

$$r_i^{\mathrm{em}} = \left(\frac{2\pi b \rho_{\mathrm{d}} \Omega}{a_0^2}\right) \nu_0 \exp\left(-\frac{E_d}{kT}\right) \left(N_i^d - N_i^0\right) \tag{4.5}$$

The first term (in parentheses) on the r.h.s. of the above expression is a geometric factor that gives the number of possible emission sites from a cylindrical 'tube' around dislocation segments, with a_0 the lattice parameter and $b = a_0\sqrt{3}/2$. ν_0 is an attempt frequency (e.g. the *Debye* frequency of the material), and N_i^0 is the equilibrium concentration of species i. Assuming thermal equilibrium,

$$N_i^0 = (\rho_a \Omega) \exp\left(-\frac{E_i^f}{kT}\right)$$

where E_i^f is the formation energy (for H atoms, this is equivalent to the heat of solution) of species i. After inserting the expression for N_{H}^0 into eq. (4.5) – the emission rate becomes:

$$r_{\mathrm{H}}^{\mathrm{em}} = \left(\frac{2\pi b \rho_{\mathrm{d}} \Omega}{a_0^2}\right) \nu_0 \exp\left(-\frac{E_d}{kT}\right) \left(N_{\mathrm{H}}^d - \rho_a \Omega \exp\left(-\frac{\Delta E_{\mathrm{H}}^f}{kT}\right)\right) \tag{4.6}$$

4.2.5 The 'super-abundant' vacancy model.

Broadly speaking, the *super abundant* vacancy (SAV) mechanism is a process by which hydrogen assists in the generation of vacancies in a metal. Numerous examples of the SAV effect exist in metals, e.g. Ni, Cr, Pd, Al, Mo, or Nb [73,124,126,229]. At the atomistic level, the fundamental idea is that as vacancies and vacancy clusters capture hydrogen atoms their internal pressure grows up to an unstable point, after which a vacancy-SIA pair is produced with the extra vacancy helping to relieve the pressure (i.e. decrease the H/V ratio) of the cluster, and a SIA emitted into the bulk. In such fashion, the system is in principle able to absorb an indefinite amount

of hydrogen, provided that the H/V ratio (n/m) is kept within the stability limits of the equation of state of the clusters. This is akin to the well-known 'trap-mutation' mechanism observed in W exposed to He plasmas [245]. For hydrogen in tungsten, several authors have introduced this mechanism and discussed the energetics of the process to determine the vacancy-to-hydrogen ratios that trigger the reaction [224, 291, 389].When the energetics of the reaction are favorable, the sequence goes as follows:

$$\mathrm{V}_m\mathrm{H}_n + \mathrm{H}_1 \rightarrow \mathrm{V}_m\mathrm{H}_{n+1} \rightarrow \mathrm{V}_{m+1}\mathrm{H}_{n+1} + \mathrm{I}_1 \tag{4.7}$$

such that the ratio changes from $\frac{n+1}{m}$ to $\frac{n+1}{m+1}$ and a SIA is inserted into the lattice. The stability of the reaction can be assessed in terms of the energies of each of the reactants and products:

$$E^f\left(\mathrm{V}_{m+1}\mathrm{H}_{n+1}\right) + E^f(\mathrm{I}_1) \leqslant E^f\left(\mathrm{V}_m\mathrm{H}_{n+1}\right) \tag{4.8}$$

such that reaction (4.7) will take place when the excess energy

$$\Delta E_{\mathrm{SAV}} = E^f\left(\mathrm{V}_{m+1}\mathrm{H}_{n+1}\right) + E^f(\mathrm{I}_1) - E^f\left(\mathrm{V}_m\mathrm{H}_{n+1}\right) \tag{4.9}$$

becomes negative. These formation energies can be calculated as:

$$E^f\left(\mathrm{V}_m\mathrm{H}_n\right) = nE^f(\mathrm{H}_1) + E^f(\mathrm{V}_m) - \left[E^b(\mathrm{V}_m\text{-}\mathrm{H}_n) + m\mu_{\mathrm{W}}\right]$$
$$E^f(\mathrm{V}_m) = E^f(\mathrm{V}_1) + E^f(\mathrm{V}_{m-1}) - E^b(\mathrm{V}_{m-1}\text{-}\mathrm{V}_1)$$

where $E^b(\mathrm{V}_m\text{-}\mathrm{H}_n)$ is the binding energy between a pure H aggregate with n atoms and a V_m vacancy cluster, and μ_{W} is the cohesive energy (eV/atom) of W. $E^f(\mathrm{H}_1)$, $E^f(\mathrm{I}_1)$, and $E^f(\mathrm{V}_1)$ are the heat of solution of H in W, and the vacancy and self-interstitial atom formation energies, respectively. Values for the required binding energies are given in Appendix C (Tables C.1 and C.3), while the rest of the parameters are:

$\mu_{\mathrm{W}} = 8.90$ eV [216], $E^f(\mathrm{H}_1) = 1.04$ eV [187], $E^f(\mathrm{I}_1) = 9.96$ eV [340], and $E^f(\mathrm{V}_1) = 3.23$ eV [363].

Figure 4.3 shows a color map of ΔE_{SAV}. The white solid line marks the limit of stability of the SAV mechanism. Above it, reaction (4.7) becomes energetically favorable and the SAV mechanism is in operation, while, below it, $\mathrm{V}_m\mathrm{H}_n$ clusters are stable. This criterion guides the behavior of the clusters and is an independent source of growth during the simulations.

This solid line can be approximated by a linear relation whose slope yields the critical $x = n/m$ ratio. For our model, this is equal to $x = 4.0$, represented as a white dashed line in the figure. However, while Fig. 4.3 indicates the thermodynamic stability region of the SAV mechanism, its occurrence may also be controlled by a kinetic barrier (in the manner of standard chemical reactions). Such an energy, which we term E_0^{SAV}, defines a transition rate that is enabled only when $\Delta E_{\mathrm{SAV}} < 0$:

$$r_{\mathrm{SAV}} = \nu_0 \exp\left(-\frac{E_0^{\mathrm{SAV}}}{kT}\right) \tag{4.10}$$

At present, there are no experimental or numerical estimates of E_0^{SAV}, and it thus must be obtained through other means. We will return to this point when we discuss the model results below.

4.2.6 Model parameterization

4.2.6.1 Simulation conditions

Table 4.1 gives all the numerical parameters and simulation conditions in accordance with the three experimental phases discussed in Sec. 4.2.1.

Table 4.1: Material and simulation parameters employed in the simulations.

W material parameters:	Symbol	Value	Units
Atomic density	ρ_a	6.31×10^{28}	[m^{-3}]
Lattice parameter	a_0	3.16	Å
Dislocation density	ρ_d	10^{10}	[m^{-2}]
Cu irradiation parameters:			
Irradiation temperatures	T	300, 573, 873, 1023, 1243	[K]
Ion flux	ϕ	1.34×10^{15}	[$m^{-2}s^{-1}$]
Ion energy	E_{ion}	3.4	[MeV]
Dose	(ϕt)	0.2	[dpa]
H plasma exposure parameters:			
Temperature	T	383	[K]
Flux	ϕ_{H}	4.0×10^{20}	[$m^{-2}s^{-1}$]
Time duration	Δt	2500	s
Deposition energy	E_{H}	113	[eV]
Thermal desorption parameters:			
Heating rate	β	0.5	[K·s^{-1}]
Temperature range	ΔT	300 ∼ 1300	[K]
Numerical parameters:			
Number of spatial elements	n	101	-
Element volume	Ω_i	10^{-23}	[m^3]
Top layer thickness	l_s	0.54	[nm]
Element thickness	l_i	20	[nm]

Table 4.2: Diffusion coefficients of the mobile species considered in this work.

Species	D_0 [m^2 s^{-1}]	E^m [eV]	Source
SIA clusters, I_m:			
I_1	8.74×10^{-8}	0.009	[108]
I_2	7.97×10^{-8}	0.024	[108]
I_3	3.92×10^{-8}	0.033	[108]
$m > 3$	$2.99 \times 10^{-7} m^{-0.5}$	0.013	[226]
Vacancy clusters, V_n:			
V_1	177×10^{-6}	1.29	[108]
V_2	2.91×10^{-9}	1.66	[226]
$n > 2$	$4.01 \times 10^{-(5+3n)}$	1.66	[226]
Hydrogen:			
H_1, H_2	1.58×10^{-7}	0.25	[275]

4.2.6.2 Defect and hydrogen atom energetics in W

The calculation of the transport energetics of defects and hydrogen atoms in tungsten has attracted a great deal of attention in recent years [88, 108, 113, 121, 121, 159, 165, 177, 186, 201, 210, 216, 217, 225–227, 242, 263, 269, 275, 283, 292, 395, 421]. Based on an extensive literature review, we have selected a set of parameters for the diffusivities and energetics of defects and hydrogen, summarized in Tables 4.2 and 4.3. The first table gives the values of the diffusivities of all mobile species assuming the standard Arrhenius expression for thermally-activated motion $D(T) = D_0 \exp\left(-\frac{E^m}{kT}\right)$. Table 4.3 gives additional values for the parameters used in Fig. 4.1.

Table 4.3: H-atom energetics in W (refer to Fig. 4.1 for details). All energies are given in eV (from ref. [164]).

Symbol	Value [eV]
E^{diss}	0.0
E^{abs}	1.44
E^{r}	0.25
E^{s}	0.79

4.3 Results

4.3.1 Cu-ion irradiation

Cu-ion irradiation, described in Sec. 4.2.1, to a total dose of 0.2 dpa at 300, 573, 873, 1023, and 1243 K results in the accumulation of point defect and defect clusters in the irradiated specimens. Figure 4.4a shows the concentration of vacancy-type defects[4] in the entire specimen as a function of dose calculated with SR-SCD. As the figure shows, the defect concentration experiences an incubation period of rapid increase characterized by a power law with scaling exponent 0.5 (which appears to be independent of temperature), followed by convergence to steady state. This steady state is reached more rapidly at elevated temperature, and its final value is indicative of the point at which vacancy and vacancy cluster production is balanced by absorption at sinks. At 300 K the system has not reached this steady state after 0.2 dpa. The accumulation of vacancy defects is substantial, with concentrations approaching 0.02 at.% at 300 and 573 K. The steady state concentrations roughly

[4]Without distinction as to whether they exist as monovacancies or as part of larger clusters

decrease linearly with temperature. The buildup of SIA clusters is seen to follow identical qualitative trends as vacancies, although with much lower concentrations.

The depth distributions at 0.2 dpa for each temperature are plotted in Figure 4.4b. Consistent with Fig. 4.2, defects are distributed uniformly into the material to a depth of approximately 1.4 microns. These initial vacancies and vacancy clusters become the seeds for the formation of larger hydrogen-trapping V_mH_n complexes during the plasma exposure phase.

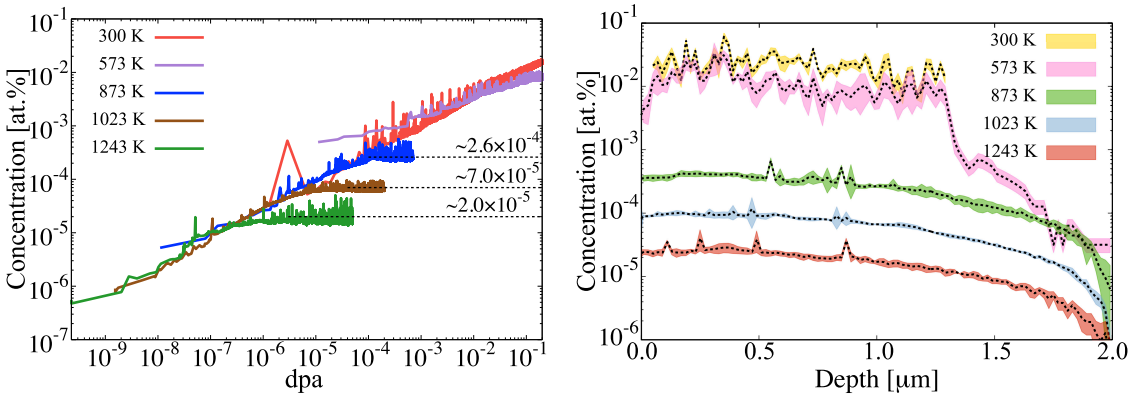

(a) (b)

Figure 4.4: Vacancy-type defect accumulation in W during Cu-ion irradiation at 300, 573, 873, 1023, and 1243 K, respectively. (a) Integrated defect accumulation as a function of dose. (b) Depth profiles at the end of the ion irradiations. The colored bands represent error bars from numerical fluctuations over five independent SR-SCD runs.

4.3.2 Determination of SAV reaction barrier by mapping to experimental results

Next, we simulate the next two phases, i.e. hydrogen plasma exposure and thermal desorption of all irradiated samples. First, however, as introduced in Sec. 4.2.5, a key parameter to be defined before entering a complete set of simulations of the H exposure phase is the energy barrier E_0^{SAV}. In the absence of direct measurements or calculations of E_0^{SAV}, here we take a backend approach to ascertain its value: we systematically vary it from zero to 1.5 eV and simulate plasma exposure and thermal desorption for each value. We then compare the simulated TDS to the experimental ones and select the value of E_0^{SAV} that produces the best match as evaluated using a least-squares error analysis. As an advance of more results to come, in Figure 4.5 we show results for six different scenarios: 0 (equivalent to a 'spontaneous' SAV mechanism), 0.90, 0.95, 1.00, and 1.20 eV. We also show results for simulations under no SAV mechanism. Our results suggest that the best match is obtained for $E_0^{\mathrm{SAV}} = 0.95$ eV, which is the value used hereafter to showcase the hydrogen exposure and thermal desorption phases.

4.3.3 Hydrogen exposure of irradiated specimens

In accordance with experimental conditions, the hydrogen exposure stage is simulated at a temperature of 383 K and a duration 2500 s under a constant hydrogen flux of 4.0×10^{20} $\mathrm{m^{-2}s^{-1}}$ (total fluence 10^{24} $\mathrm{m^{-2}}$). Figure 4.6 shows the distribution of hydrogen as a function of depth for each irradiation temperature at the end of the exposure period. Note that the concentrations shown include hydrogen in any form, i.e. free hydrogen monomers as well as H atoms trapped in vacancy clusters. Irradi-

ation temperature is seen to have a noticeable impact on the depth distribution of hydrogen, largely correlated with the distribution of vacancy clusters during the irradiation phase. In general, hydrogen is found deeper, albeit in lower concentrations, the larger T_{irr} is.

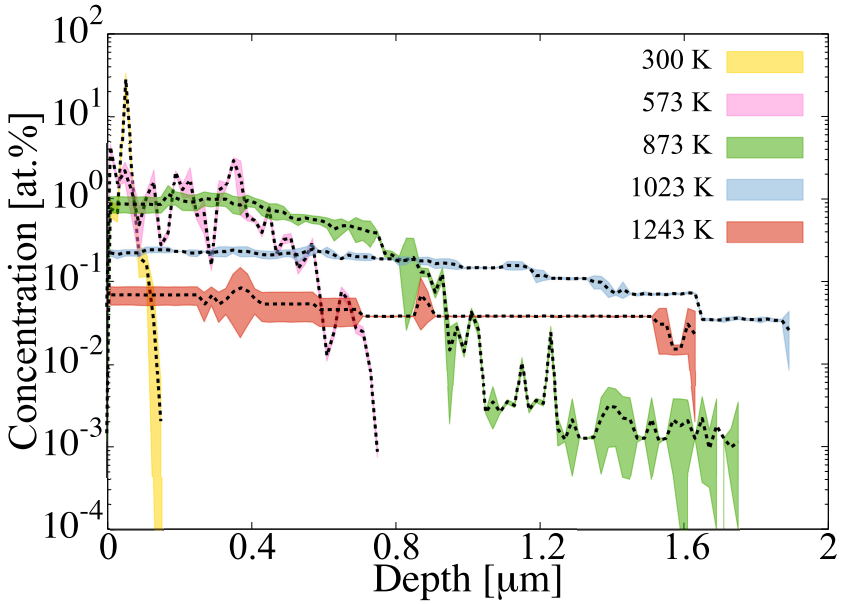

Figure 4.6: Depth profile of hydrogen in W after 2500 s of exposure to a flux of 4.0×10^{20} $\text{m}^{-2}\text{s}^{-1}$. The hydrogen considered in the graph includes both free hydrogen and hydrogen trapped at vacancy clusters. The colored bands represent error bars from numerical fluctuations over five independent SR-SCD runs.

The analysis of the V_mH_n populations displayed in Fig. 4.6 is critical, as it quantitatively establishes the trapping propensity of the material under the conditions explored here. There are two main aspects of this population that must be further studied. One is the relative partition of hydrogen-to-vacancy ratios, $x = n/m$ within the cluster subpopulation. The other is the absolute size of the clusters, which has

implications for both the total amount of H stored in the system and the visibility under the microscope of the defects. Next, we provide a detailed analysis of both of these aspects in an attempt to ascertain the fuel footprint in irradiated single-crystal W surfaces.

4.3.3.1 Stability of hydrogen-vacancy clusters and distribution of hydrogen-to-vacancy ratios.

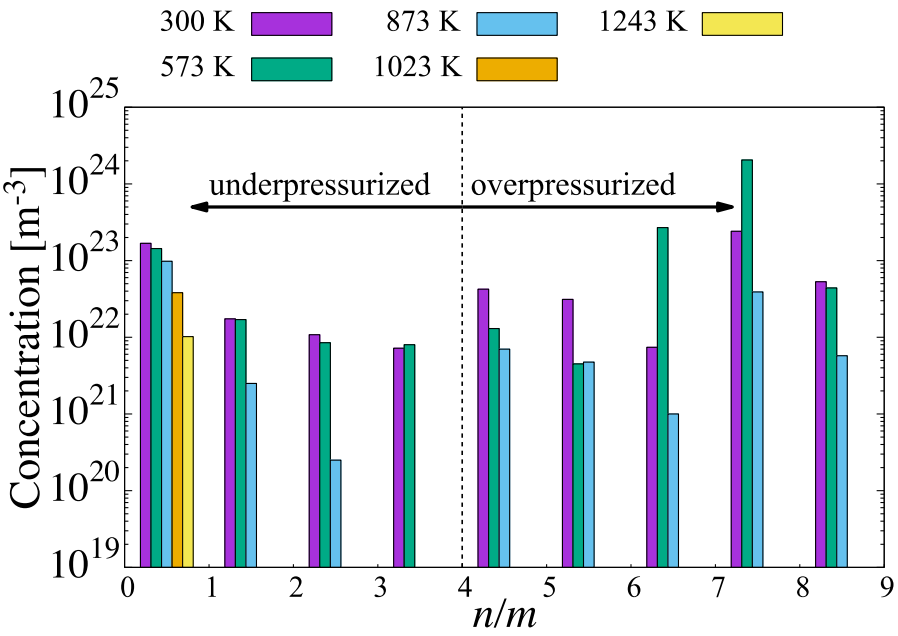

Figure 4.7: Histogram of the integrated concentration of vacancy-hydrogen clusters in terms of their hydrogen-to-vacancy ratio after 2500 s of exposure to a hydrogen flux of 4.0×10^{20} $\mathrm{m^{-2}s^{-1}}$.

Figure 4.7 shows the integrated concentration of V_mH_n clusters as a function of x for each irradiation temperature case. In keeping with the limits established in Fig.

4.3, a dashed line is drawn at $x = 4$ to show the relative stability of clusters based on their hydrogen-to-vacancy ratio. Clusters with $x < 4$ are generically deemed to be 'underpressurized', i.e. with a propensity to absorb more hydrogen atoms, while clusters with $x > 4$ are said to be 'overpressurized', i.e. with propensity to release hydrogen (or, when the SAV mechanism is active, to produce vacancies). On the basis of this partition, two things can be established about the different T_{irr} cases: (i) a higher irradiation temperature leads to preferentially underpressurized clusters, while lower temperatures result in an equipartition between under- and overpressurized bubbles; (ii) the range of x observed is 0 to 9.

Figure 4.8 shows the depth distribution of the V_mH_n clusters in terms of their x value as a function of T_{irr} at the end of the H-exposure phase. The colored bands around each curve represent error bars from numerical fluctuations over five independent SR-SCD runs. Generally, little correlation is observed between x and the depth at which each cluster type is found. Consistent with Fig. 4.6, the main effect of irradiation temperature is to result into deeper V_mH_n cluster penetration.

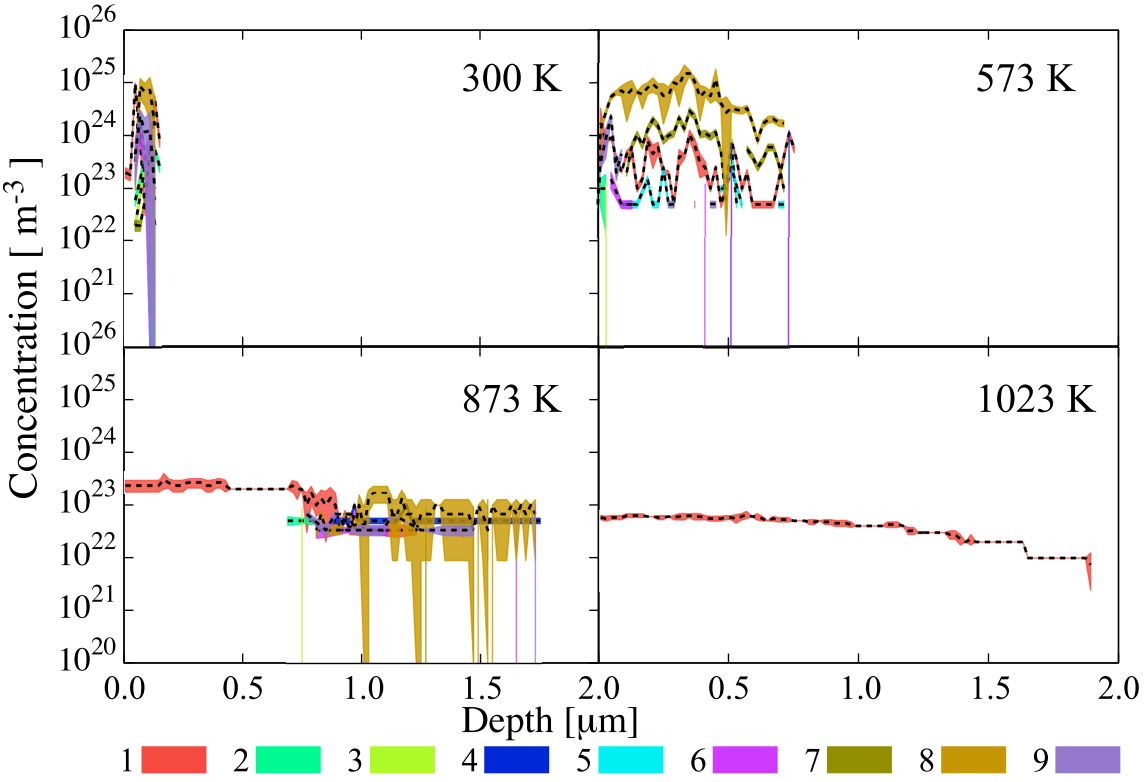

Figure 4.8: Depth distribution of the V_mH_n clusters after 2500 s of H exposure in terms of their hydrogen-to-vacancy ratio as a function of irradiation temperature. We omit the 1243-K case due to its similarity with the results at 1023 K. The colored bands represent error bars from numerical fluctuations over five independent SR-SCD runs.

Finally, it is useful to represent the cluster population not just in terms of their x ratios but also in terms of their absolute m and n numbers. Figure 4.9 shows three-dimensional plots of V_mH_n clusters as a function of m, n, and the depth at which they are found. Their concentration is given using the color key as specified in the figure. Each subplot corresponds to a specific irradiation temperature. In

a similar manner to the distribution of x ratios, key qualitative differences can be appreciated between the lower and higher temperature cases. At lower temperatures, Figs. 4.9a, 4.9b and 4.9c, most V_mH_n clusters are located within the first micron of depth, with m and n covering a large span between $V_{1\sim6}H_{10\sim30}$ to approximately $V_{7500\sim8000}H_{2200\sim2350}$ and relatively high concentrations. By contrast, at 1023 and 1243 K (Fig. 4.9d, the figure for $T_{\text{irr}} = 1243$ K is not shown due to its qualitative and quantitative similarity with the 1023-K case) only clusters composed of more than 5500 vacancies are observed at high depths. These large clusters appear in relatively low concentrations. We can synthesize the information contained in these figures into a global size distribution for the end of the exposure phase. This represent essential information to facilitate comparison with experimental distributions, which are limited on the low end by machine resolution. Our results are shown in Figure 4.10 in the form of temperature-smeared Gaussian distributions, with the raw data shown as a histogram in the background.

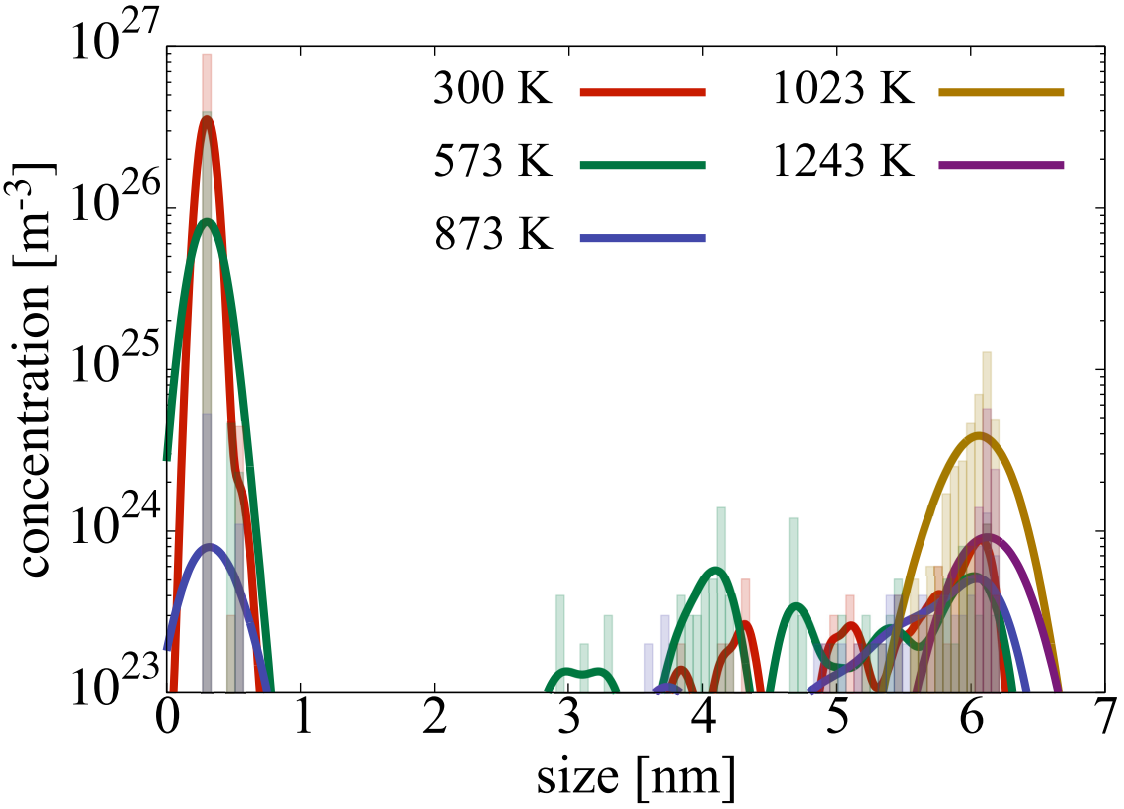

Figure 4.10: Vacancy-hydrogen cluster size distributions at the end of the hydrogen exposusre simulations. The raw data shown as a histogram with faint colors in the background..

While the figure clearly shows a bi-modal distribution with a peak within one nanometer sizes and another one centered around 6 nm, the standard resolution limit in microscopy of 0.5-to-1.0 nm may prevent revealing the former in experimental size distributions. Techniques such as X-Ray diffuse scattering can achieve sub-nanometer resolutions, thus enabling a better comparison with our results [338]. We discuss this further in Sec. 4.4.2.

4.3.4 Thermal desorption simulations

Thermal desorption processes are thought to be composed of a series of emission events characterized by Gaussian profiles [180, 397]. These Gaussians are centered at temperatures defined by characteristic binding energies representing specific hydrogen release events. It is therefore useful to decompose the desorption profiles shown in the figure into a set of overlapping Gaussian distributions that coincide with the most dominant peaks (or protuberances) in each TD spectrum. Doing this, however, may involve a certain degree of arbitrariness, as these peaks are not always evident (particularly at high temperatures). In any case, we believe that some clear mappings exist and some consistency among the different curves can be found.

Here we focus on the 0.95-eV case in Fig. 4.5. Figure 4.11 shows the decomposed thermal desorption spectra for each irradiation temperature. In performing each decomposition, Gaussians with like colors are used when they are centered at the same desorption temperature (horizontal axis), regardless of the irradiation temperature case. The width of the Gaussians is temperature dependent and has been adjusted so that the contribution to the TD spectrum from the overlap among them is consistent with the full curve. As such, the 300-K and 573-K temperature case (Fig. 4.11a and 4.11b) is composed of seven distinct Gaussians, each representing a specific desorption mechanism, centered at, respectively, 333, 425, 485, 527, 574, 623, and 836 K. Two of these are shared with the 873-K case, Fig. 4.11c, which is suggestive of identical H-release mechanisms in these two cases. However, the remaining spectra corresponding to the higher irradiation temperatures are characterized by different peaks, namely 310, 842 K (Fig. 4.11d).

As mentioned above, each one of the Gaussians shown in Fig. 4.11 represents a

distinct hydrogen emission mechanism. These mechanisms can be directly identified in the simulations from processes defined by eqs. (4.6) and (2.6)), so that we can ascribe a specific dissociation reaction to each emission temperature, T_p. Further, we characterize each Gaussian by a representative dissociation energy E^d_{TDS}, determined as [293]:

$$\frac{E^d_{\mathrm{TDS}}}{kT_p^2} = \frac{\nu_0}{\beta} \exp\left(-\frac{E^d_{\mathrm{TDS}}}{kT_p}\right) \tag{4.11}$$

where β is the heating rate. Each E^d_{TDS} can subsequently be compared with the corresponding dissociation energies corresponding to the specific reactions taking place in the simulations. Those ultimate originate from the data given in Table C.3. The results of such analyses are provided in Table 4.4.

The information contained in the table is the culmination of the simulation effort of the three-stage experimental study described in Sec. 4.2.1. The first column represents all the Gaussian peaks used in Fig. 4.11. Columns 2-5 specify the transitions suffered by the clusters during each emission process. With increasing desorption temperature, the emission events include hydrogen emission from dislocations, small overpressurized clusters gradually releasing hydrogen to reduce their hydrogen-to-vacancy ratio towards $x = 4$, and large underpressurized clusters emitting H atoms until all the hydrogen is evacuated from the system. Finally, the last column lists the corresponding dissociation energies of each dissociation event as calculated with eq. (4.11). We find that, in general, the discrepancy between the E^d_{TDS} given in Table 4.4 and the actual dissociation energies from Table C.3 is small. While this simply corroborates that the reactions identified in each temperature interval are consistent with the Gaussian emission peaks, it is an encouraging result that adds confidence to our results.

Table 4.4: Operative dissociation mechanisms at each thermal desorption peak temperature for each irradiation temperature. The symbol '⊥' represents 'dislocations'. The simulated dissociation energy, E^d_{sim} is obtained as $E^d_{\text{sim}} = E^b + E^m$. The values for E^b are extracted from Table C.3 for each specific reaction, while E^m comes from Table 4.2. The values for E^d_{TDS} were obtained from eq. (4.11).

T_p [K]	Irradiation temperature [K]					E^d_{sim} [eV]	E^d_{TDS} [eV]
	300	573	873	1023	1243		
310	–	–	–	⊥	⊥	0.85	0.70
333	⊥	⊥	⊥	–	–	0.85	0.75
425	$V_1H_8 \rightarrow V_1H_7$	$V_1H_8 \rightarrow V_1H_7$	–	–	–	0.88	0.97
485	$V_1H_7 \rightarrow V_1H_6$	$V_1H_7 \rightarrow V_1H_6$	–	–	–	1.05	1.11
	$V_6H_{23} \rightarrow V_6H_{22}$		–	–	–	1.06	
527	$V_1H_6 \rightarrow V_1H_5$	$V_1H_6 \rightarrow V_1H_5$	–	–	–	1.18	1.21
	$V_6H_{21} \rightarrow V_6H_{20}$	$V_6H_{22} \rightarrow V_6H_{21}$	–	–	–	1.18	
574	$V_1H_5 \rightarrow V_1H_3$	$V_1H_5 \rightarrow V_1H_3$	–	–	–	1.28	1.32
	$V_6H_{18} \rightarrow V_6H_{17}$	–	–	–	–	1.34	
623	$V_1H_3 \rightarrow V_1$	$V_1H_3 \rightarrow V_1$	–	–	–	1.49	1.44
	$V_6H_{16} \rightarrow V_6H_{12}$	$V_6H_{16} \rightarrow V_6H_{12}$	–	–	–	1.42	
836	$V_{202\sim818}H_{1\sim67} \rightarrow V_{202\sim818}H_{0\sim66}$	$V_{172\sim3593}H_{1\sim181} \rightarrow V_{172\sim3593}H_{0\sim181}$	$V_{145\sim2100}H_{1\sim109} \rightarrow V_{145\sim2100}H_{0\sim108}$	–	–	1.69∼1.96	1.96
842	–	–	–	$V_{563\sim840}H_{104\sim171} \rightarrow V_{563\sim840}H_{103\sim170}$	$V_{692\sim844}H_{1\sim51} \rightarrow V_{692\sim844}H_{0\sim50}$	1.94∼1.96	1.97

4.4 Discussion

4.4.1 Physical implications of the present results

Hydrogen thermal desorption in damaged crystals is an extremely complex problem involving numerous processes often co-occurring in a synergistic or nonlinear manner. Just listing those considered here gives an idea of this complexity: cascade damage, defect diffusion, hydrogen deposition and penetration, hydrogen passivation, internal hydrogen diffusion, hydrogen absorption and trapping at dislocations and grain boundaries, vacancy cluster-hydrogen reaction, production of vacancies from cluster internal overpressurization, and hydrogen dissociation from clusters, all of it captured with spatiotemporal resolution. The amount of physics needed to undertake simulations of such a challenging process can be staggering, both in terms of the kinetics and thermodynamics of the atomic species involved, as well as in terms of the detailed parameterization needed for physical accuracy and validation. As well, carefully-conducted experiments covering the above processes and in such a way as to facilitate comparison with the models are an invaluable tool to validate and refine the simulations. Fortunately, we believe that the fusion materials community has reached sufficient maturity in all of these fronts to enable the type of study presented here. For example, a systematic effort by researchers to map the energetics of the W-H system using electronic structure calculations and semi-empirical potentials, there are now very reliable data sets available. Thanks to advances in algorithms and computer power, there now exist powerful reaction-diffusion PDE models to study strongly-coupled multispecies problems in great detail. This, combined with several decades of 'know-how' in irradiation damage modeling has open the door to simulations such as those presented here which allow us to push the

physical accuracy/computational efficiency tradeoff to unprecedented levels.

In undertaking the present simulation effort, we must also be transparent about two key premises adopted here, namely the presumed infallibility of both experimental results and electronic structure calculations. It is beyond the scope of this work to comment in depth about the validity of such premises, the reader is simply referred to the pertinent sources, e.g. refs. [166,218,319,400] for details. Suffice it to say that, as has become common practice in the computational materials science community, both experimental characterization and *ab initio* calculations have reached a degree of reliability as it relates to PMI studies that allow us to confidently use them in our studies as the 'true' baseline against which to compare model predictions.

With this in mind, the main result of this work is presented in Figure 4.12 (subpanel in Fig. 4.5), which we use to discuss the main physical insights gained from the current exercise. Analysis of figures such as those points to two principal features that stand out from within the body of results obtained here:

(i) Our results conclusively show that, vis-à-vis the experiments, the superabundant vacancy mechanism is a key piece of physics needed to understand the accumulation of vacancy-hydrogen clusters in damaged W subjected to hydrogen exposure point to the existence of a transition barrier. Moreover, we find that the SAV mechanism is accompanied by a transition barrier that modulates changes in the cluster structure. Mapping the simulated TDS to the experimental ones points to a value of 0.95 eV for this transition energy.

(ii) The thermal desorption spectra of H-exposed damaged W surfaces can be broadly decomposed into three distinct emission temperature regions:

1. A low temperature region around room temperature where H atoms are released from intrinsic microstructural defects such as dislocations and grain boundaries.
2. An intermediate region between 400 and 700 K where smaller overpressurized V-H clusters dissolve giving rise to a series of overlapping release peaks.
3. A high temperature region > 800 K where larger underpressurized bubbles gradually emit all their hydrogen giving rise to clearly defined emission peaks.

These temperature regimes are schematically depicted in Figure 4.13, which are in strong qualitatively agreement with the experimental TDS obtained in ref. [319].

In this context, the SAV mechanism plays a fundamental role in the final accumulation and release of hydrogen from damaged tungsten surfaces. Going back to Fig. 4.5, the absence of a SAV-type mechanism overemphasizes smaller, overpressurized cluster populations, while an unabated[5] SAV mechanism leads to an abundance of larger, underpressurized bubbles. In view of these trends, the effect of the SAV activation barrier is clear. E_0^{SAV} modulates the two extremes (no SAV, spontaneous SAV) and bridges the temperature regions where overpressurized and underpressurized clusters dominate. This is clearly seen in Fig. 4.5 and in the experiments, where for $E_0^{\mathrm{SAV}} = 0.95$ eV our results show remarkable agreement with both the emission peaks and the emission fluxes measured experimentally.

[5] I.e. 'spontaneous', with E_0^{SAV}=0.

4.4.2 Validation

A first attempt at validation of our results can be made by comparing the Sun et al. [338] (Fig. 6 in their paper). At 300 K and 0.2 dpa with 5-MeV Cu ions, the measured vacancy defect concentration was 0.103±0.02 at. %, while our integrated value from Fig. 4.4b is 0.023±0.004 at. %. Part of this 5× difference is likely attributable to the difference in irradiation energy (5.0 vs 3.4 MeV), although we do not discount other factors related to more fundamental factors such as the model framework. Noteworthy is also the fact that the average cluster sizes in each case (measured vs. simulated) are 10 ± 3 Å and 8.32 ± 0.3 Å, in very close agreement with one another.

Second, related to the experimental effort discussed in Sec. 4.2.1, the desorption hydrogen fluence can be measured for each of the irradiation-temperature specimens and compared to the integrated hydrogen release in the simulations. The measurements are shown in Figure 4.14 for two Cu-ion irradiation energies together with the present results. A difference factor of about 2.5× is observed, which can be partially explained from the analysis of the difference in TDS features that we discuss next.

Analyses of the experimental peaks between 400 and 700 K (intermediate temperature range) suggests that our simulations underestimate the concentrations of clusters that give rise to the first set of emission peaks (between 400 and 550 K), while they slightly overestimate those in the range between 600 and 700 K. We can specifically point to the reactions that govern each subregime from among those listed in Table 4.4 to analyze this discrepancy. Between 400 and 550 K the peaks are due to the decomposition of V_1H_7, V_1H_8, V_6H_{21}, and V_6H_{22} clusters. The implication would thus be that the simulations are underestimating these populations relative

to the experimental observations. Conversely, between 600 and 700 K the relevant clusters are V_1H_3, V_1H_5, V_6H_{16}, and V_6H_{18}, whose populations would appear to be overestimated in the simulations. This could be due to a number of causes, although given how similar the clusters are in both subregimes, subtle changes in the binding energies would likely suffice to correct this. This is one way simulations such as these can inform the atomistic calculations of the energetics of the W-H system.

4.5 Summary

The main summary points and conclusions of this work are:

1. We have assembled a simulation methodology based on spatially-resolved stochastic cluster dynamics calculations to simulate a set of experiments involving sequences of ion-irradiations, hydrogen plasma exposure, and hydrogen thermal desorption.

2. The models are parameterized using atomistic calculations only (a combination of DFT and semi-empirical potentials) of hydrogen-vacancy cluster energetics. We find that these calculations provide a high degree of numerical accuracy vis-à-vis the experimental results.

3. To facilitate comparison, the simulated thermal desorption spectra are analyzed using similar tools to the experiments revealing a set of Gaussian peaks characterizing specific desorption events. In general, these events are different manifestations of the reduction of the hydrogen-to-vacancy ratio from their highest values down to zero. This is achieved by the sequential emission of H monomers at different temperatures, from which the critical binding energies

are extracted.

4. A principal conclusion of our study is that the thermal desorption spectra are broadly composed of three temperature regions: one below room temperature characterized by emissions from dislocations and grain boundaries, and intermediate one characterized by emissions from small overpressurized V-H clusters, and a high temperature one governed by release from large underpressurized bubbles.

5. We conclude that the super-abundant vacancy (SAV) formation mechanism (which is equivalent to the so-called 'trap mutation' mechanism in the context of W-He evolution simulations) plays a key role during exposure of tungsten to H plasmas. Under such mechanism, V_mH_n clusters may absorb H more or less indefinitely provided they can emit self-interstitial atoms. The SAV mechanism acts to shift clusters between the populations belonging to the intermediate and high temperature regimes. We find that a value of 0.95 eV for the SAV activation energy barrier fits the experimental data best.

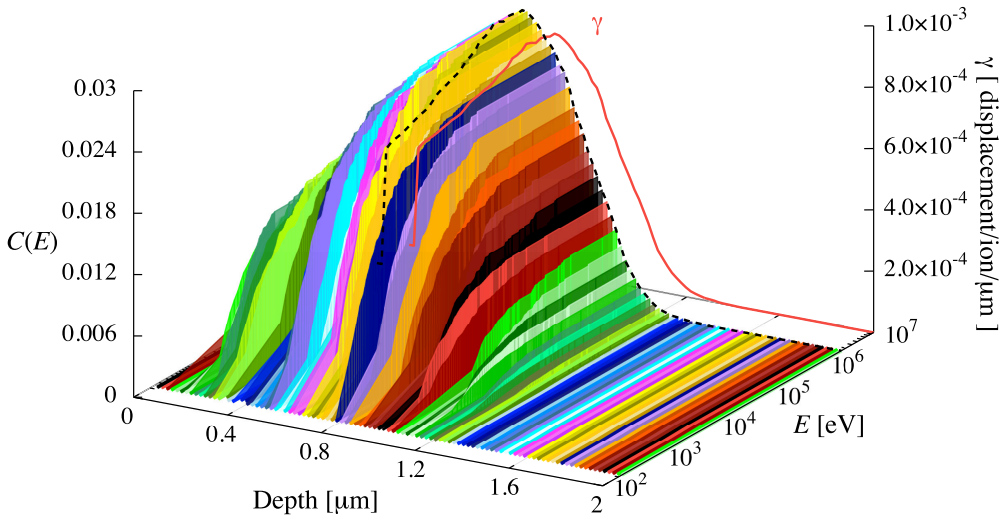

Figure 4.2: Cumulative Cu recoil distribution obtained from SRIM for 3.4-MeV ion irradiations of W surfaces as a function of target depth. The area contained by the dashed line – representing the cumulative value of in each depth bin – amounts to unity to maintain the cumulative probabilistic nature of $C(E)$. The dashed line also represents the damage function γ in eq. (7.6), which peaks with a value of 1.2×10^{-3} displacements per ion per micron at a depth of approximately 0.9 μm.

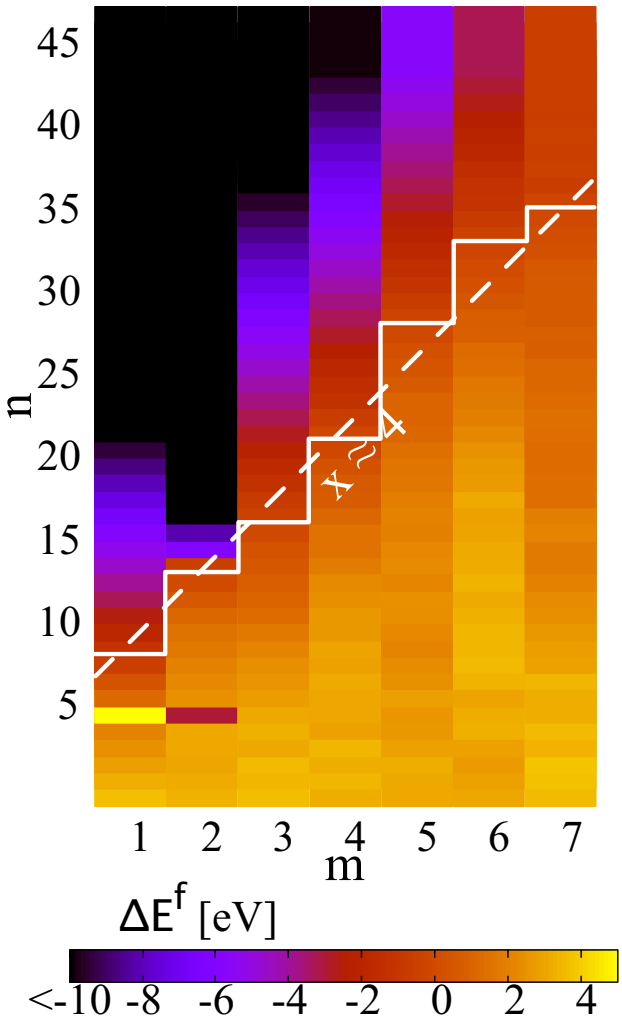

Figure 4.3: Color map of excess energies according to eq. (4.9). The white solid line marks the limit of stability of the SAV mechanism. Above it, reaction (4.7) becomes energetically favorable and the SAV mechanism is in operation. Below it, V_mH_n clusters are stable. The dashed line represents a linear fit yielding the optimum hydrogen-to-vacancy ratio.

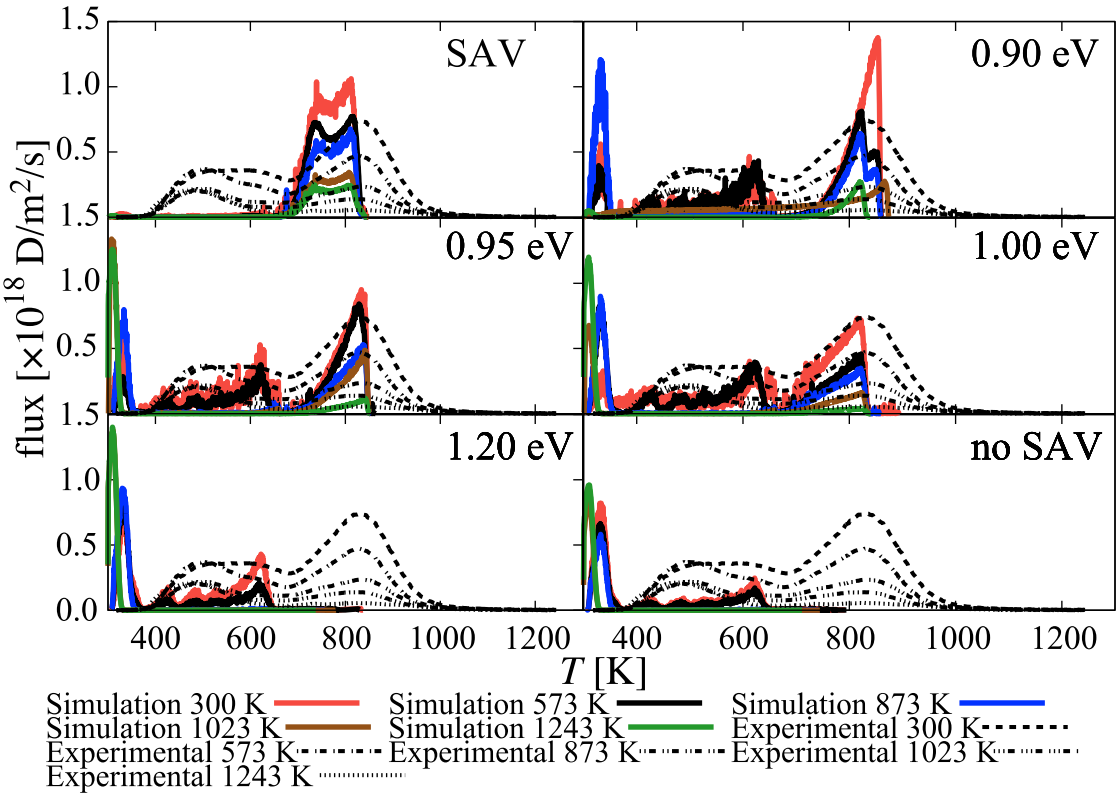

Figure 4.5: Simulated and experimental hydrogen thermal desorption spectra for the five irradiation temperatures considered in this work under different values of E_0^{SAV}.

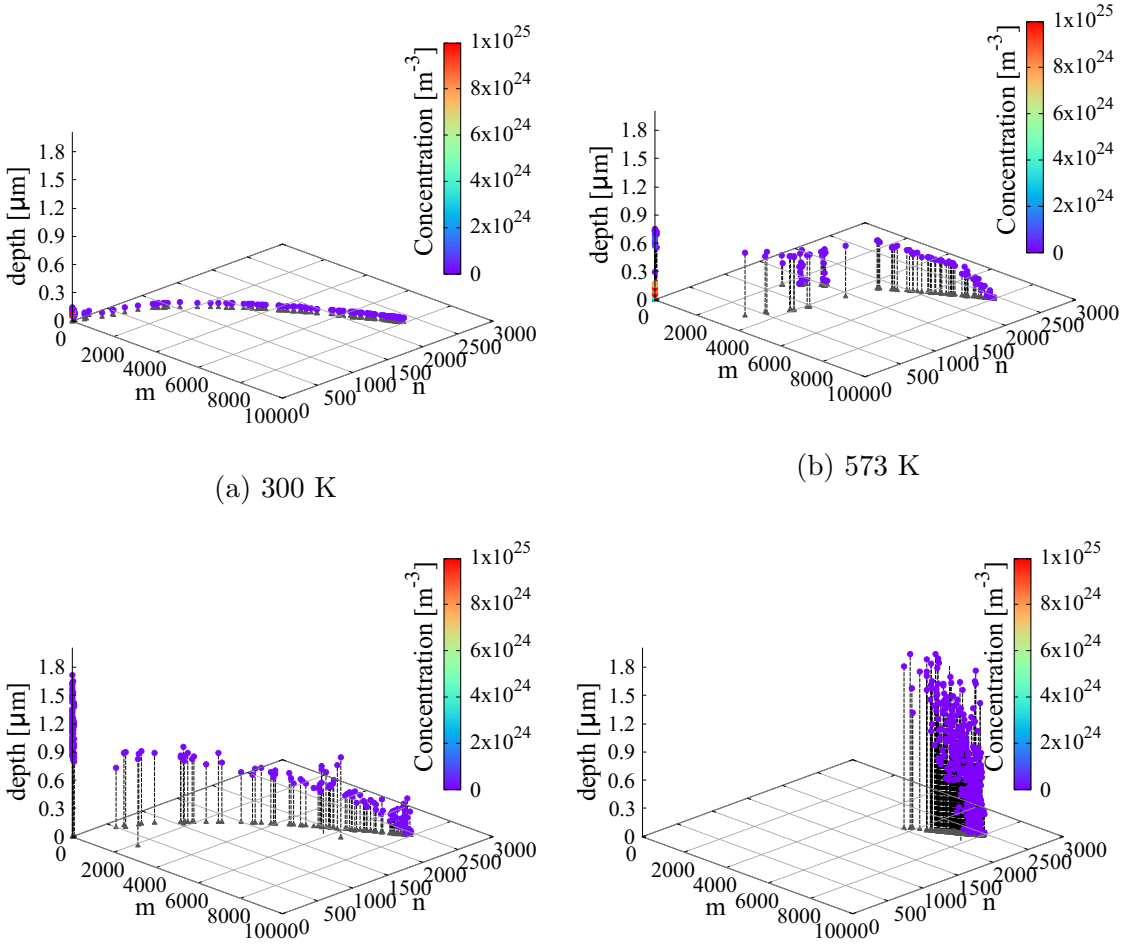

(a) 300 K

(b) 573 K

(c) 873 K

(d) 1023 K

Figure 4.9: V_mH_n cluster size distributions as a function of m, n, depth, and irradiation temperature. Cluster concentrations are described by a color key. Dashed vertical lines are projections of each data point on he m-n plane for ease of visualization. We omit the 1243-K case due to its similarity with the results at 1023 K.

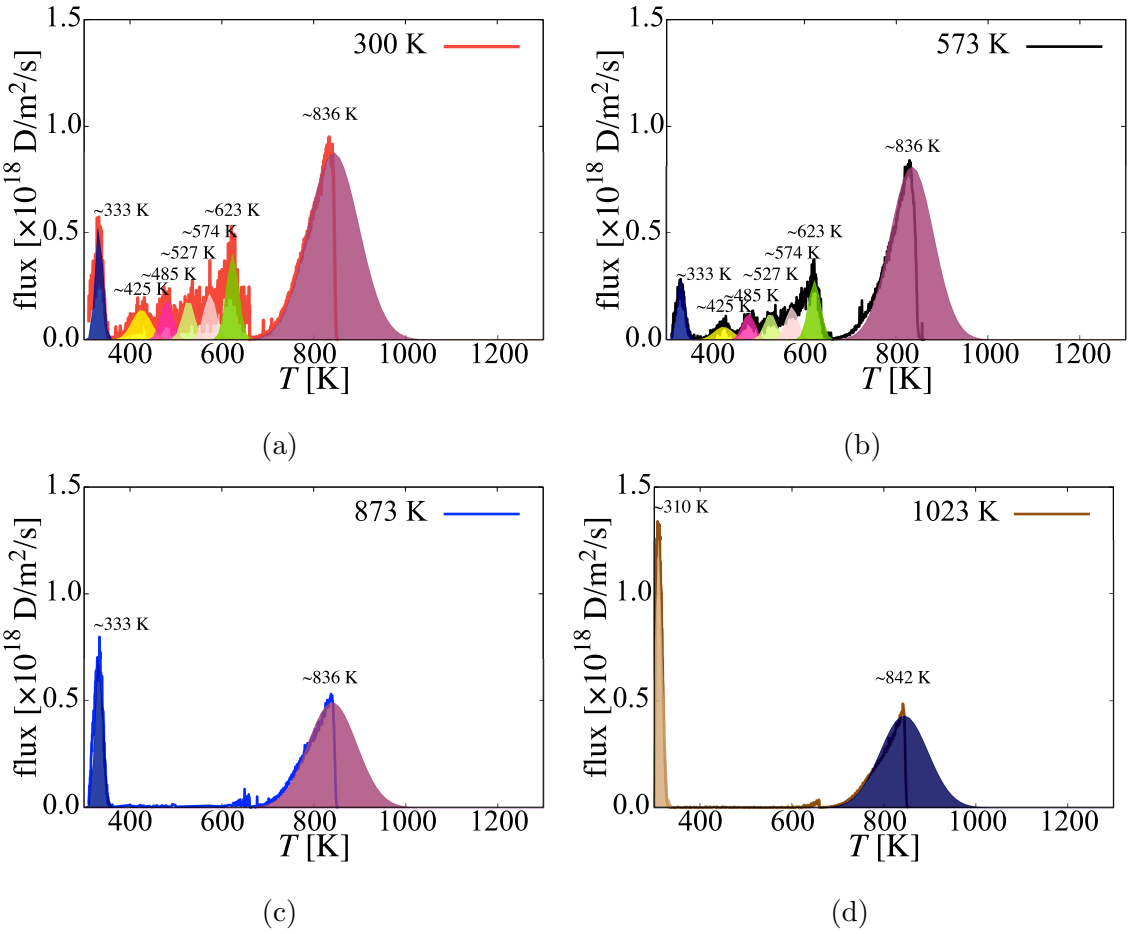

Figure 4.11: Thermal desorption spectra for each irradiation temperature case decomposed into their constituent Gaussian emission profiles. Each Gaussian is expected to represent a distinct emission mechanism, to be discussed in Table 4.4.

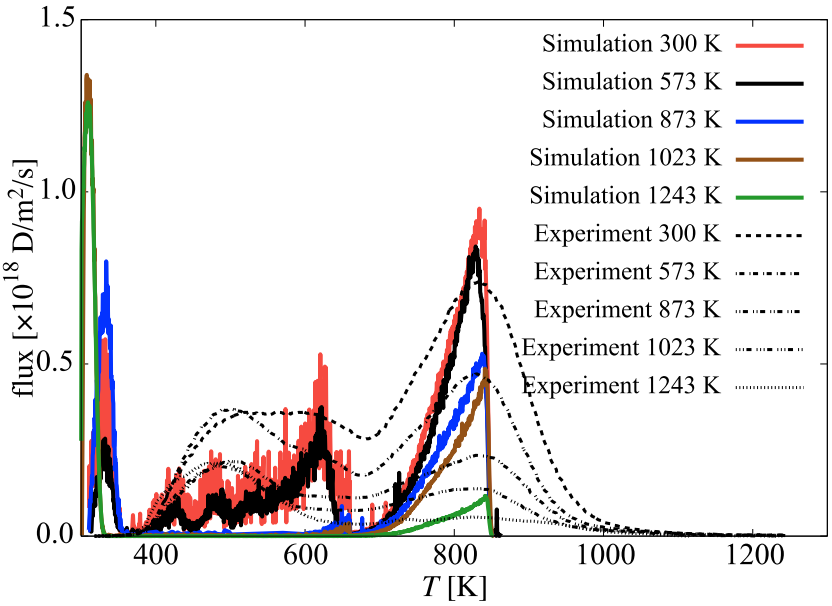

Figure 4.12: Thermal desorption spectrum for $E_0^{\mathrm{SAV}} = 0.95\ eV$.

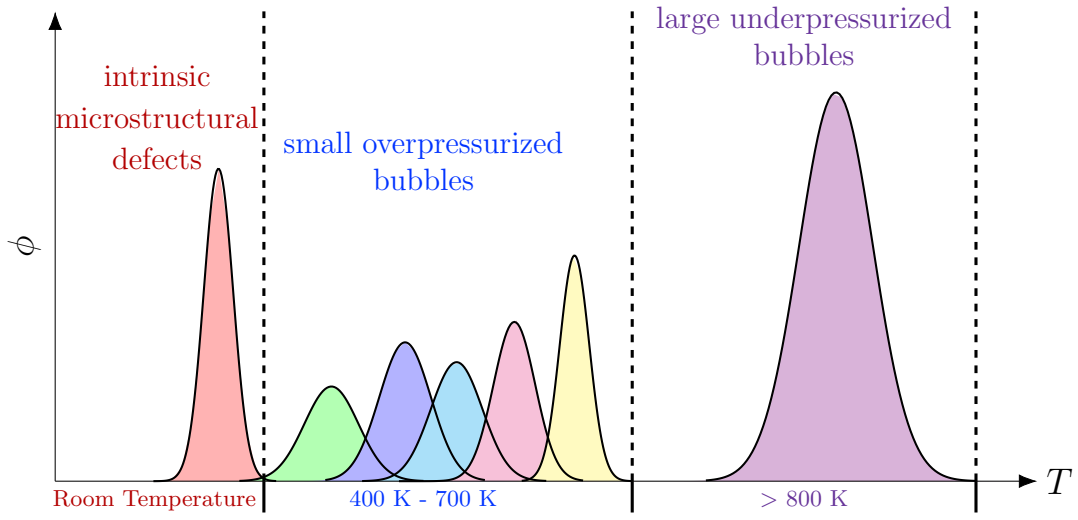

Figure 4.13: Schematic diagram of the TDS peak distribution. ϕ represents the desorbed hydrogen flux in arbitrary units.

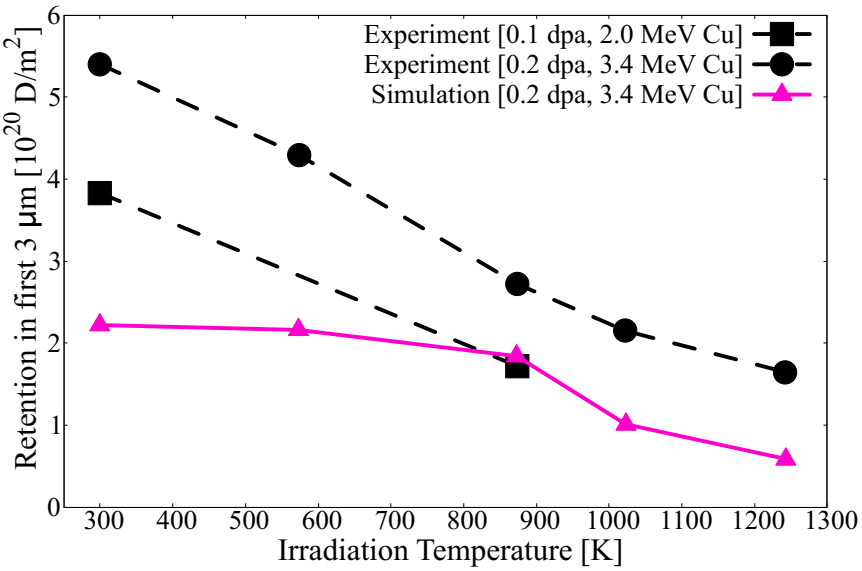

Figure 4.14: Comparison between experiments and model results of the total hydrogen fluence integrated from the TDS spectra as a function of T_{irr}. Dashed lines are experimental measurements while the continuous curve represents the model predictions.

CHAPTER 5

Coupling crystal plasticity and stochastic cluster dynamics models of irradiation damage in tungsten

5.1 Literature Review

Irradiation of structural materials in nuclear environments is known to result in mechanical property degradation and premature failure [336]. Prolonged exposure to energetic particle radiation leads to a variety of far-from-equilibrium effects, such as point defect and defect cluster accumulation, solute segregation, precipitation, transmutation, etc, potentially leading to microstructural evolution and macroscale changes such as hardening, embrittlement, swelling [25, 66, 107], and, depending on temperature, creep and/or accelerated corrosion [154, 321, 375].

In some scenarios, such as for fusion materials, the lack of suitable materials testing facilities with the appropriate neutron energy spectra calls for the development of physics-based numerical tools to simulate irradiation damage in candidate materials [214, 361]. On their path to becoming predictive, such tools must be carefully verified with *f*irst-principles techniques and validated with detailed experimental data. While much progress has been achieved by the irradiation damage

community over the last few decades [26, 60, 272], our renewed understanding of irradiation damage processes and increasingly more powerful numerical resources make the development of new and improved computational methods an imperative. As a subtopic within the wide array of issues related to irradiation of materials [85, 86, 109, 194, 296, 307], the problem of mechanical property degradation has received much attention since the beginning of radiation damage studies due to its complexity and importance. Much has been learned from experimental studies going back several decades [106, 136, 136, 153, 169, 331], including basic relations between irradiation variables such as particle energy, irradiation dose and dose rate, temperature, and/or initial microstructure, and the mechanical response in a wide range of materials. From a theoretical/simulation perspective, models that capture materials deformation must be used in conjunction with damage accumulation methods. Among the former, *c*rystal plasticity (CP) simulations have established themselves as the preferred option to determine a crystal's internal plastic response to external arbitrary loads [179, 184, 294, 303, 318] (and, more specifically, *finite-element* based CP, or CP-FEM [302]). In terms of irradiation defect accumulation techniques, kinetic reaction-diffusion models based on the *m*ean-field rate theory (MFRT) approach have long been the work-horse of the irradiation damage community [142, 334, 339].

While enjoying wide applicability in a multitude of scenarios, MFRT suffers from certain limitations that restrict its application to multispecies situations such as those found in nuclear materials subjected to a variable transmutation inventory. Techniques such as *s*tochastic cluster dynamics (SCD) were developed with the aim to overcome these limitations due to intrinsic advantages in their mathematical formulation [239, 241, 404]. As well, much work has been done to modify CP and adapt it to irradiation scenarios, including sequential linkages of CP and MFRT [59, 170, 372]. A

combined CP-FEM/SCD model has also been proposed [97]. However, a formal coupling of these two techniques is still lacking, which is the objective of this chapter. We attempt this by way of a bidirectional assemblage where, in one direction, the dislocation density evolution model in CP informs the defect sink term in SCD, while the defect concentration and size distribution from SCD feeds back into the calculation of the resolved stress in CP. In addition to the standard *p*ost mortem deformation tests of irradiated specimens, our coupled model enables *i*n situ irradiation-straining tests, which may be helpful in interpreting in-service conditions where materials are subjected concurrently to irradiation and loading.

The chapter is organized as follows. In Section 5.2 we discuss the details of the CP-SCD coupling, the integration algorithm, and the numerical stability. Then, we present our results in Section 5.3, including simulations of post-irradiation straining tests and *i*n situ irradiation/deformation. We end with a discussion in Section 5.4 and the main conclusions.

5.2 Model Description

5.2.1 The coupling procedure and the CP-SCD algorithm

The simulation method used in this chapter is called the coupling CP-SCD model. Readers are referred to section 2.1 and 2.2 for details of CP and 0-dimentional SCD models separately. Here, we focus on describing how these two methods are linked. The purpose of coupling CP and SCD is to realize real-time connection between material deformation and irradiation microstructure evolutions. Irradiation introduces defects that interact with networked dislocations, leading to changes in

dislocation density that –in turn– modify the sink strength for defect absorption. As such, the coupling between SCD and CP is bidirectional, which makes the model self-consistent. The effects of each model on the formulation of the other are discussed next.

5.2.1.1 SCD→CP

Irradiation damage introduces a new class of dislocation obstacles, i.e., irradiation defects, in the microstructure that must now be accounted for in the CP formulation. This is done by considering a new length scale d_{irr} that reflects the irradiation defect spacing [204, 391]:

$$\frac{1}{d_{\text{irr}}} = \sum_i \eta_i \sqrt{\frac{N_i^{\text{im}} r_i}{\Omega}} \tag{5.1}$$

where N_i^{im} is the subset of immobile species among all N_i, η_i is a dimensionless coefficient representing the strength of dislocation-defects interactions, and r_i is the size of the defects (assumed to be represented by the radius of disc-like SIA clusters or spheres for vacancy clusters, precipitates, and gas bubbles). Determination about the mobility of the defects is primarily based on defect nature and size. Only vacancy clusters with less than three vacancies and SIA clusters with less than 10 self-interstitials are considered mobile.

Connection with the CP model is done via eq. (2.26), which is now modified as:

$$\frac{1}{\lambda^\alpha} = \frac{1}{d_g} + \sqrt{\rho_f^\alpha} + \frac{1}{d_{\text{irr}}} \tag{5.2}$$

As well, the effect of irradiation defects on hardening is introduced into eq. (2.29) as:

$$\Delta\tau^\alpha = \tau_{RSS}^\alpha - \Delta\tau_f^\alpha - \Delta\tau_{\text{irr}} \tag{5.3}$$

with:

$$\Delta\tau_{\text{irr}} = \frac{\mu b}{d_{\text{irr}}}$$

For the coefficients η_i we simply use 0.2 for SIA clusters and loops and 0.6 for vacancy clusters and voids [176].

5.2.1.2 CP→SCD

After the crystal plasticity update, the total dislocation density is calculated as:

$$\rho_{\text{tot}} = \sum_{\alpha} \rho^{\alpha}$$

and is then transferred to SCD as the updated sink strength for defect absorption, $S_d \equiv \rho_{\text{tot}}$. In this fashion, defect production, dislocation multiplication and hardening are all linked during the course of a simulation iteration. Next, we discuss the numerical algorithm employed to integrate the time evolution of the state variables $\boldsymbol{\sigma}$, $\boldsymbol{\varepsilon}$, and the set of $\{N_i\}$ for the coupled CP-SCD model.

5.2.2 Numerical solution procedure

As is commonly the case in CP methods, the system of equations (7.5)-(2.30) is indeterminate and has to be solved iteratively. While very robust implicit integration algorithms exist for crystal plasticity problems [11, 188], here the focus is on the coupling of methods and, for simplicity, we simply use the backward Euler method to integrate the CP equations. The detailed algorithm as well as the working flowchart is given in Appendix D and is discussed here briefly. For a prescribed applied strain rate tensor $\dot{\boldsymbol{\varepsilon}}_0$, the total strain increment $\Delta\boldsymbol{\varepsilon}_{\text{t}} = \dot{\boldsymbol{\varepsilon}}_0 \delta t$ is split into elastic and plastic parts (δt is a fixed time step). The stress $\boldsymbol{\sigma}$ is calculated from the elastic strain, which

is then used to determine the plastic strain increment $\Delta \boldsymbol{H}^{\mathrm{P}}$, integrating Orowan's equation over all slip systems α. The calculated plastic strain is compared with the initial one, and convergence is achieved if their difference is within a prescribed numerical tolerance. If the difference is too large, a new elastic-plastic partition is generated and a new iteration starts. As part of the main calculation loop, dislocation densities and resolved stresses are updated with every iteration.

For its part SCD advances in time using variable time steps as given by the kinetic Monte Carlo algorithm [365]. In the present implementation, we always ensure that the mean defect lifetime R_i (cf. 2.2) is well below δt from the CP calculation. This is generally not a problem, as time steps associated with SCD events range between 10^{-12} to 10^{-6} s. As such, the SCD simulation is subordinated to the CP time update in such a way that the defect microstructure is evolved for as long a time as that dictated by δt. To that effect, the number of iterations in SCD in each CP time step is determined as the integer n_{SCD}, such that:

$$\sum_{i}^{n_{SCD}} \delta t_i^{SCD} < \delta t < \sum_{i}^{n_{SCD}+1} \delta t_i^{SCD}$$

Note that, due to the stochastic nature of δt_i^{SCD} (which is distributed as a Poisson variable), n_{SCD} may change in each CP iteration.

With this approach, the deformed and irradiated microstructures evolve concurrently, and mutually affect one another. At the end of each CP step, the total strain and total irradiation fluence are advanced by the corresponding amount dictated by δt. Without loss of generality, in this work we concentrate on uniaxial loading conditions, such that going forward we work only with the axial component along the z direction of $\dot{\boldsymbol{\varepsilon}}_0$, which we simply denote by the scalar quantity $\dot{\varepsilon}_0$.

5.2.3 Numerical stability criterion

During quasistatic deformation conditions, i.e.. with the axial strain rate $\dot{\varepsilon}_0 < 10^{-2}$ s^{-1}, unconditional stability is defined by the following relation (specified in instruction 6 of Algorithm 4):

$$\Delta H^{\mathrm{P}} \leqslant \Delta\varepsilon_{\mathrm{t}} - \Delta\varepsilon^{\mathrm{E}}$$

This simply implies that the tangent modulus (i.e., the hardening rate in the flow stress region) must be nonnegative. In terms of slip rates, this condition is expressed as:

$$\sum_{\alpha} \dot{\gamma}^{\alpha} \boldsymbol{s}^{\alpha} \otimes \boldsymbol{n}^{\alpha} \leqslant \dot{\varepsilon}_0 \tag{5.4}$$

Using eq. (2.21) and assuming a Schmid factor of 0.5 (most conservative scenario) for all slip systems considered here (given in Table A.1), eq. (5.4) can be written as:

$$6b\rho^{\alpha} v^{\alpha}\left(\tau^{\alpha}_{\mathrm{RSS}}\right) \leqslant \dot{\varepsilon}_0 \tag{5.5}$$

where ρ^{α} and $v^{\alpha}\left(\tau^{\alpha}_{\mathrm{RSS}}\right)$ will be the dislocation density and dislocation velocities in the slip system that is most restrictive to the application of the stability criterion. Plugging eq. (2.22) into the above expression and operating, we arrive at:

$$\Delta\tau^{\alpha} \leqslant \left(\frac{kT}{\Delta H_0}\log\left\{\frac{\dot{\varepsilon}_0}{6h\nu_0\sqrt{\rho^{\alpha}}}\right\} + 1\right)^2 \sigma_P \tag{5.6}$$

or, in terms of the RSS:

$$\underbrace{\tau^{\alpha}_{\mathrm{RSS}}}_{F^{\alpha}(\dot{\varepsilon}_0,\rho^{\alpha},L)} \leqslant \underbrace{\left(\frac{kT}{\Delta H_0}\log\left\{\frac{\dot{\varepsilon}_0}{6h\nu_0\sqrt{\rho^{\alpha}}}\right\} + 1\right)^2 \sigma_P}_{G^{\alpha}(T,\dot{\varepsilon}_0,\rho^{\alpha})} + \underbrace{\mu b\left(\sqrt{\sum_{\beta\neq\alpha}\xi_{\alpha\beta}\rho^{\beta}} + \frac{1}{d_{\mathrm{irr}}}\right)}_{H^{\alpha}(\rho^{\alpha},L)} \tag{5.7}$$

The two terms in the r.h.s. of above equation (5.7) represent the thermal and athermal contributions to the material's strength, respectively, which going forward we denote by the two functionals G^{α} and H^{α} (shown in the equation). Making $\tau^{\alpha}_{\mathrm{RSS}} \equiv F^{\alpha}$,

the stability criterion is simplified to: $F^\alpha < G^\alpha + H^\alpha$. Inequality (5.7) essentially gauges whether dislocation-mediated slip is moderated by the algorithm [282].

During the course of a simulation, F^α, G^α, and H^α are calculated for each slip system α and the stability criterion is applied to each one independently. Note that, while the time does not appear in inequality (5.7), it does enter the criterion via G^α and H^α, which are nonlinear functions of δt and change by different amounts when the time step is modified. As well, one can see that adding irradiation defects makes the criterion more restrictive, since adding the term $\mu b/d_{\text{irr}}$ always increases the value of H^α. Furthermore, increasing the irradiation dose also increases H^α, because d_{irr} always decreases with dose. If the criterion is not satisfied in a given slip system at any given time, the time step is reduced and the iteration is repeated. At the beginning of Section 5.3, we perform a preemptive stability analysis to set bounds on reasonable values of δt, F^α, G^α, and H^α in anticipation of more detailed simulations.

5.2.4 Model parameterization

The values of the most important parameters used in this work are given in Table 5.1. Parameters such as diffusion and dissociation energetics of irradiation defects are found in ref. [241]. Dislocation slip parameters and material physical parameters are found in refs. [57, 337].

Table 5.1: Material and simulation parameters employed in the simulations (from refs. [57, 241, 337].

W material parameters:	Symbol	Value	Units
Atomic density	ρ_a	6.31×10^{28}	$[\mathrm{m}^{-3}]$
Lattice parameter	a_0	3.16	[Å]
Initial dislocation density per slip system	ρ_0	8.3×10^{12}	$[\mathrm{m}^{-2}]$
SCD-relevant parameters:			
Ion energy	E_{ion}	18.0	[MeV]
Dose rate	ϕ	4.3×10^{-5}	$[\mathrm{dpa \cdot s}^{-1}]$
Dose	(ϕt)	0.2, 1.0, 5.0	[dpa]
Bulk volume	Ω	10^{-19}	$[\mathrm{m}^3]$
CP-relevant parameters:			
Burgers vector	b	2.72	[Å]
Kink length	h	$\frac{\sqrt{6}}{3}$	$[a_0]$
Kink pair separation	w	11	$[b]$
Knk pair activation enthalpy	ΔH_0	1.63	[eV]
Exponents	$p,\ q$	0.68, 1.69	[-]
Peierls stress	σ_P	2.03	[GPa]
Shear modulus	μ	151	[GPa]
Young's modulus	E	340	[GPa]
Poisson's ratio	ν	0.27	[-]
Attempt frequency	ν_0	10^{11}	$[\mathrm{s}^{-1}]$

5.3 Results

5.3.1 Stability analysis of the CP model

As dictated by eq. (5.7), numerical stability is guaranteed by $F < G + H$. Accordingly, we plot G, $G + H$, and the function $F' = (G + H)/(\boldsymbol{s} \cdot \boldsymbol{n})|_{\max}$ in Figure 5.1 at four different temperatures. The analysis has been done for reference values of $\dot{\varepsilon}_0 = 10^{-3}$ s^{-1} and $\rho_0 = 8.33 \times 10^{12}$ m^{-2}. $G + H$ represents the surface of stability of the algorithm, while F' represents the maximum axial stress at each orientation that satisfies the criterion. $(\boldsymbol{s} \cdot \boldsymbol{n})|_{\max}$ is the *maximum* Schmid factor of any slip system given in Table A.1 for each loading orientation considered in the stereographic triangle, shown in Figure 5.1e. Robust stability is illustrated by a high value of the function F', which is highest among all the figures shown at 1200 K. Note that, because function G is quadratic in temperature, there is a nonlinear correlation between temperature and stability. Indeed, the minimum of the parabola $G(T^2)$ is reached at a temperature of 705 K, which is thus the temperature around which the most restrictive numerical conditions for the application of the CP method are displayed. As well, it can be seen that G, makes up most of the $G + H$ combination, i.e., the athermal part H is small compared with the thermal part of the slip resistance G.

Informed by this analysis, we proceed to calculate yield strengths of unirradiated and irradiated W in the subsections below.

5.3.2 Yield strength of unirradiated W

We first calculate the yield stress of unirradiated W as function of temperature, strain rate and loading orientation. Representative stress-strain curves at different

loading directions for a strain rate of 10^{-3} s^{-1} at 600 K are plotted in Figure 5.2a. The figure shows the evolution of the flow stress under multi-slip ([100] and [111]) and single-slip ([110] and [213]) conditions, with various degrees of work hardening being observed.

From these results, the yield strength is extracted using the 0.2%-strain offset method and its dependence on temperature is plotted in Figure 5.2b. Results from a comprehensive study of the orientation, temperature, strain rate dependence of σ_Y are plotted in Figure 5.3. Based on the color differential in the plots, the temperature dependence is seen to be the most pronounced, with weaker orientation and strain rate sensitivities. These results are consistent with past studies published in the literature [57, 287].

5.3.3 Yield strength of irradiated W

Next we study the effect of irradiation on single crystal W with the results shown in Sec. 5.3.2 as a baseline reference. Two types of studies can be envisaged: (i) a standard *p*ost-mortem test, where the material is irradiated in the absence of deformation, and then evaluated in a tensile test to study the effect of irradiation conditions on yield stress, and (ii) a less common but important *i*n situ test where irradiation and deformation take place in unison, sharing temperature and crystal orientation. These therefore represent *sequential* and *concurrent* irradiation/deformation scenarios. First we study the former case, starting with standalone SCD simulations of irradiation damage in undeformed W materials, followed by tensile tests of the type carried out in the previous section.

5.3.3.1 Standalone irradiation simulations

SCD simulations were carried out mimicking self-ion irradiation experiments in single crystal W specimens [176]. The irradiations consisted of 18-MeV W^{6+} ions with a dose rate of 4.3×10^{-5} dpa s^{-1} at temperatures of 300, 373, and 573 K. The primary knock-off atom (PKA) probability distribution function obtained from SRIM [424] using best practices [335] is shown in Figure 5.4. Dislocations are the only defect sinks considered with a density equal to ρ_0. We track the evolution of vacancy and self-interstitial atom (SIA) clusters as a function of dose and temperature. A cluster is defined as containing three or more point defects. Other details pertaining to the simulations are given in refs. [171, 404]. Additionally, the simulations comprise a 14-hour annealing down to 300 K of the configurations obtained after 0.2, 1.0, and 5.0 dpa. This is consistent with *p*ost mortem tests where the irradiated specimens undergo a cooling period to room temperature after irradiation. We will use these annealed defect distributions in the loading tests to be described in the next subsection.

Defect clusters concentrations and sizes are shown in Figure 5.5 for all irradiation temperatures as a function of dose. The values obtained after annealing the configurations irradiated to 0.2, 1.0, and 5.0 dpa are shown as isolated markers in each plot. Selected data from the experiments by Hwang et al. [176] at 1073 K are also provided for comparison.

Finally, we track the evolution of the inverse mean defect spacing $1/d_{\text{irr}}$ –calculated using eq. (5.1)– as a function of dose at all temperatures. The results are plotted in Figure 5.6, clearly showing a steady increase with dose at all temperatures evaluated. This behavior is indicative of the potential for hardening of the irradiated

microstructure, whose effect will be analyzed in more detail in the next subsection.

5.3.3.2 Tensile tests of irradiated W single crystals

Tensile tests of the irradiated systems were simulated using the CP model described in Sec. 2.2. The effect of irradiation dose on the flow stress of [100] and [213] oriented crystals is illustrated in Figure 5.7a. As the figure shows, the materials suffers a considerable amount of hardening with dose, which results in large increases in the yield strength of the material. The full dependence of σ_{Y} with orientation, temperature, and dose (for a fixed strain rate of 10^{-4} s^{-1}) is provided in Figure 5.8. By way of comparison, the ideal tensile strength of [100] W crystals computed using electronic structure methods is in the 27∼29-GPa range (attained at strains of 11∼14 %) [146, 228], while the experimental tensile strength of high-purity W crystals at low temperature (77 K) is on the order of 2∼10 GPa (depending on loading orientation) [15, 31, 45]. These values are marked in the figure in terms of color shaded regions indicating the failure zone as defined by the ideal and experimental tensile strength values. The variation of the irradiation-induced hardening $\Delta\sigma_{\mathrm{Y}}$ (defined as the yield strength at a given dose relative to the yield strength of the unirradiated material) with dose is given in Figure 5.7b. Square-root fits to the data are included as dashed lines in the figure showing very good agreement with the numerical values. Such behavior is consistent with a dispersed barrier hardening model [322,345], with the square root dependence being provided by $1/d_{\mathrm{irr}}$ (see Fig. 5.6). The implications of these results will be discussed further in Sec. 5.4.

5.3.4 In-situ irradiation/straining tests

The final set of simulations involves cases of *in situ* irradiation/deformation tests. These correspond to true coupled SCD/CP simulations as described in Sec. 5.2.1. The irradiations are performed under the same parameters as in Sec. 5.3.3.1, while the tensile tests are made to reach a total strain of 3%. With a strain rate of 10^{-4} s^{-1}, this amounts to 300 s, which for a dose rate of 4.3×10^{-5} dpa s^{-1} results in 0.013 dpa of total dose. Thus, due to the relatively short duration of the tensile test, the accumulated *i*n situ irradiation doses are low.

Similar to the results shown in Fig. 5.6, we first study the evolution with strain/dose of the inverse average defect spacing $1/d_{\text{irr}}$. Contrary to the pre-irradiation tests, however, d_{irr} is intimately linked to the evolving crystal dislocation density, and, as such, it displays a crystal orientation dependence. Figure 5.9a shows results at 600 K for several crystal directions as well as the reference case at 600 K from Fig. 5.6. The associated dislocation density evolution is shown in Figure 5.9b. The stark differences between the *i*n situ and *p*ost mortem data in Fig. 5.9a is due to the fact that dislocations are strong defect sinks, and thus remove defects from the irradiated volume as they evolve during deformation. Interestingly, the crystal orientation dependence on $1/d_{\text{irr}}$ is quite weak, suggesting that a critical absorption efficiency is achieved even for slow-evolving dislocation density orientations.

Several representative stress-strain curves at 10^{-4} s^{-1} and 600 K are shown for various crystal orientations in Figure 5.10. It can be seen that the level of extra hardening is fairly limited due to the low doses accumulated and the extra defect sink strength due to dislocation multiplication. Results showing the differential yield strength ($\sigma_{\text{Y}}|_{\text{in-situ}} - \sigma_{\text{Y}}|_{\text{unirr}}$) are given in Figure 5.11. As expected from Fig. 5.10,

the plots reveal only a marginal hardening increase in the *in situ* tests compared to the unirradiated specimens.

5.4 Discussion

5.4.1 Utility of the coupled SCD/CP method

Since its designation as first-wall candidate material for fusion energy, the response of tungsten to irradiation has attracted a great deal of attention [6, 83, 238]. Models to simulate damage accumulation in the dpa range have been developed and/or improved [34, 171, 185, 241, 250], including complex multispecies scenarios involving He, H, and transmutation element cases [44, 171, 209, 404]. For their part, CP models of irradiated W have been developed to capture a number of different scenarios [84, 246, 316, 390]. However, these methods are generally constructed with some degree of phenomenology and fitting parameters that must be adjusted with experimental data. As well, work on coupling kinetic transport models of irradiation damage accumulation with crystal deformation methods is much more scarce.

The contributions of this work to the existing literature lie in two main aspects. First, the coupling strategy proposed here to link stochastic cluster dynamics with the crystal plasticity model relies on a bidirectional update of state variables. SCD evolves both the mean defect spacing and the resistance stress due to damage accumulation in CP, while CP updates the dislocation density in response to SCD-furnished information. The dislocation density is transferred back to SCD, providing a renewed sink strength for defect cluster evolution. This approach is different from existing implementations where the defect subpopulation follows a separate evolution law,

which is typically linked to the plastic slip rates in CP [30, 285, 323]. The calculation of the mean defect separation d_{irr} (in eq. (5.1)) is also original, and specifically tailored to the stochastic nature of the SCD method.

Second, this implementation of the SCD and CP approaches enables a natural way to carry out simultaneous (i.e., *in situ*) irradiation/deformation tests. While accumulated doses (even in ion-beam experiments) are small due to the relative short duration of a standard tensile test, such simulations could be extremely useful to study scenarios where the irradiation and deformation rates are comparable, e.g., during high-temperature creep tests at low stresses (see comments on the characteristic time constants in Sec. 5.4.3 below). We leave these simulations to future studies.

5.4.2 Physical findings

While the main purpose of this work is to focus on the development of a coupled SCD/CP method, our demonstration calculations have resulted in several interesting physical findings. Our simulations cover two aspects of irradiation in materials: (i) post-mortem irradiation tensile tests and (ii) concurrent irradiation/deformation situations. In the former case, our work involves SCD simulations of self-ion irradiation replicating actual ion-beam experiments in W, and CP simulations of tensile deformation after exposure to several different total doses.

Standalone SCD simulations reveal a marked temperature effect on defect accumulation and cluster formation (Fig. 5.5), and have been partially validated against the results by Hwang et al. [176], which adds confidence to the results. For their part, the CP calculations display extremely elevated levels of irradiation harden-

ing, 5∼25 GPa, even after only 0.2 dpa of damage accumulation (see Figs. 5.7a and 5.8). While this is not inconsistent with past experimental studies in both ion and neutron irradiated single-crystal W, where levels in excess of 5 GPa have been measured [17, 157, 169, 171, 416], these hardening values amply surpass the tensile strength of W single crystals, likely leading to premature failure. It is now recognized that transmutation element precipitates (whether introduced by design as alloy elements or generated chemically by nuclear transmutation) are responsible for large fractions of the measured hardening, although existing studies suggest that SIA loops can be as effective as these precipitates [176, 416]. Note that dislocations are known to absorb some defects during plastic deformation –sometimes leading to dislocation channeling and flow localization [20, 30] (although not commonly seen in W)– but this is not captured in these simulations and the material is assumed to deform uniformly at all times. However, part of the hardening calculated from the simulations could probably be discounted due to this mechanism. Finally, while we have spent considerable effort accounting for non-Schmid effects in dislocation slip in W [57, 287, 337], the present simulations have been run using standard Schmid plasticity. Non-Schmid effects are known to reduce the computed yield stresses by up to a factor of four [57, 90].

For their part, simulations involving the concurrent irradiation and deformation of tensile specimens reveal two interesting findings. The first is that strain hardening is a powerful damage inhibitor. As deformation proceeds and the dislocation density increases, the fraction of defects absorbed by dislocations grows commensurably. This results in very limited levels of hardening at the end of the tests. While it is expected that the defect absorption strength of dislocations would become saturated at some dose level, the irradiation doses reached in our *in situ* simulations (≈0.013 dpa) are far

too low for this effect to occur. The second effect, related to the first just described, is that irradiation hardening in *i*n situ irradiation/deformation simulations do not display any appreciable crystal orientation dependence (Fig. 5.11). The evidence for this is in Fig. 5.10, which show that modest hardening levels occur even for crystal orientations for which dislocation multiplication is limited, suggesting that the dislocation density threshold needed to absorb most of the defect population is probably not very high.

5.4.3 Computational performance

There are several challenges associated with the coupling of the SCD and CP methods. First, CP requires a robust implicit solver to achieve self-consistent solutions. That implies lack of knowledge of the duration of δt *a* priori during each iteration. Second, SCD is intrinsically a stochastic method based on the residence time algorithm, such as time steps throughout a simulation are an output in each iteration, not an input parameter. Thus, coupling SCD and CP to run concurrent simulations requires devising ways to keep both approaches synchronized during each iteration. Our approach is to use a *m*aster-slave scheme, with the SCD compute cycle subordinated to the iterative CP solver. With this, once convergence is attained during the CP cycle, the SCD simulation is run until the accumulated time reaches the converged CP time step. From a numerical point of view, this is justified also because the time constants that characterize CP and SCD simulations are such that $\tau_{\mathrm{SCD}} \ll \tau_{\mathrm{CP}}$, with $\tau_{\mathrm{CP}} = \varepsilon_0^{-1}$ and $\tau_{\mathrm{SCD}} = 1/\max_i \{R_i\}$ respectively (recall from Sec. 2.2 that, for species i, $R_i = \tilde{s}_i + \sum_j \tilde{k}_{ij} N_j$).

The extra computational overhead associated with the inner SCD loop in CP is

illustrated in Figure 5.12a. The figure shows the required CPU time to run different physical times in three different scenarios: CP only, SCD only, and coupled SCD/CP (the aggregate of the CPU times of the isolated SCD and CP runs is also shown for reference). The results show that the SCD simulations are about 15× more costly than CP calculations. They also show that the coupled methodology results in slower simulations compared to the simple sum of SCD and CP runs. This convincingly points to the need to synchronize and subordinate the SCD compute cycles to the CP iterative scheme as the culprit behind the extra overhead incurred. The CPU cost per crystal plasticity time step in the same three cases is shown in Figure 5.12b. After an initial transient, the CPU cost reaches constant values in all instances, with the coupled CP/SCD again displaying an extra overhead compared to CP-only and SCD-CP cases.

The present approach provides results at the level of a material point, i.e., at integration points in finite element (FE) calculations of spatial domains. Ultimately, the coupled SCD/CP method will have to be integrated into nonlinear FE solvers of boundary-valued problems that carry their own CPU overhead demands. For that reason, it is important to understand and estimate the computational overheads associated with the proposed coupled methodology. We conclude by noting the parallelization potential of the approach, which could be amenable to the implementation of suitable algorithms to accelerate the SCD calculations [248, 249] as well as the CP simulations [195, 215].

5.5 Summary

We finalize the work with the following main conclusions:

- We have developed a model linking a kinetic transport model of irradiation damage accumulation (SCD) and crystal plasticity simulations (CP). The coupling is bidirectional, with state variables from one method updating and informing state variables of the other method and vice versa.

- The SCD method provides statistically averaged defect cluster spacing that informs the dislocation density evolution model and resistance stresses in CP. Updated dislocation densities are transferred back from CP to SCD for updating the defect sink concentration and strength.

- We have tested the coupled methodology both sequentially and concurrently, simulating tensile tests of pre-irradiated W specimens and *in situ* irradiation/deformation tests.

- Our results on pre-irradiated W tensile tests suggest multi GPa-level irradiation hardening associated with <5 dpa irradiations with 18-MeV self-ions, consistent with past modeling and experimental studies.

- In the *in situ* tests, dislocation multiplication acts as potent defect accumulation inhibitor, leading to a weak crystal orientation dependence and modest levels of defect hardening.

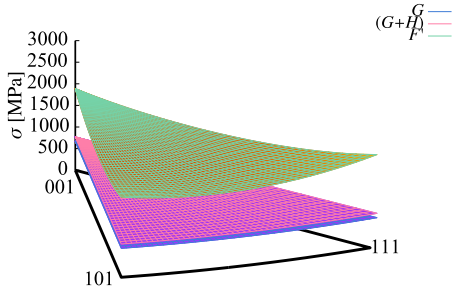

(a) 300 K

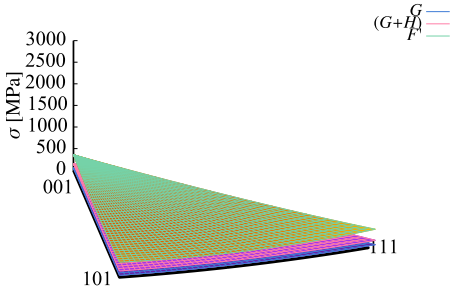

(b) 600 K

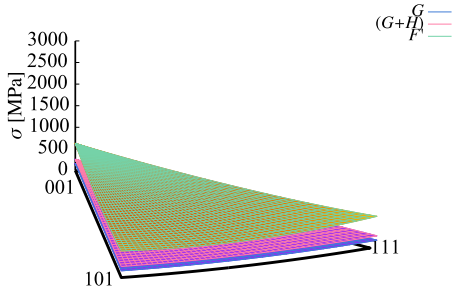

(c) 900 K

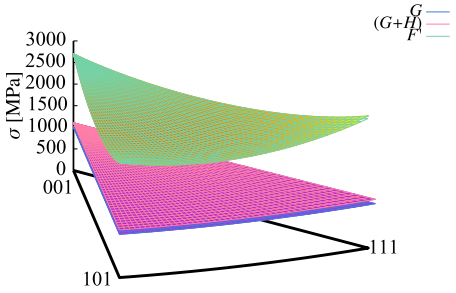

(d) 1200 K

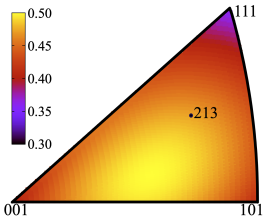

(e) Maximum Schmid factor

Figure 5.1: (a)-(d) Orientation dependence of the different terms in eq. (5.7) at four different temperatures. The function F' plotted shows the axial stress corresponding to the most highly activated slip system for each orientation. The $G + H$ surface delineates the stability space of the CP method. (e) Maximum Schmid factor for each orientation in the stereographic triangle.

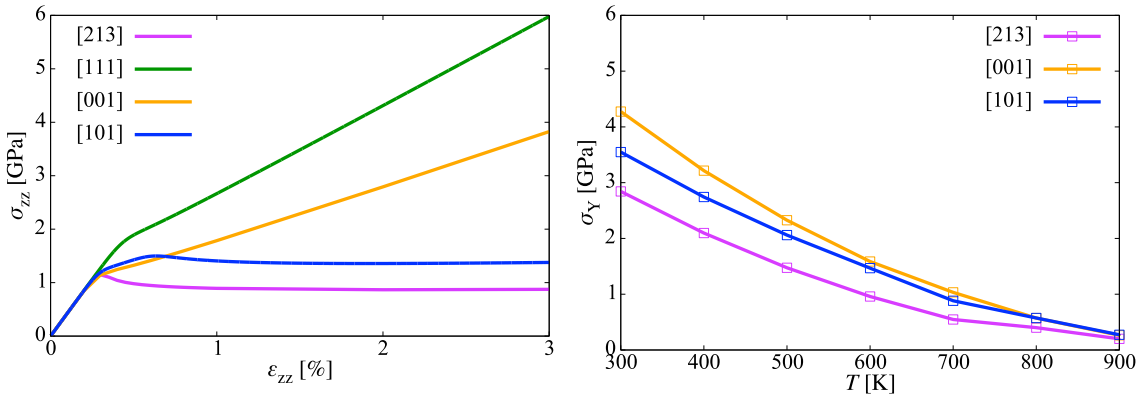

(a) (b)

Figure 5.2: (a) σ_{zz}-ε_{zz} curves of unirradiated single-crystal W at different loading directions for a strain rate of 10^{-3} s^{-1} at 600 K. (b) Temperature dependence of the yield strength for three of the orientations in (a) at 10^{-3} s^{-1}.

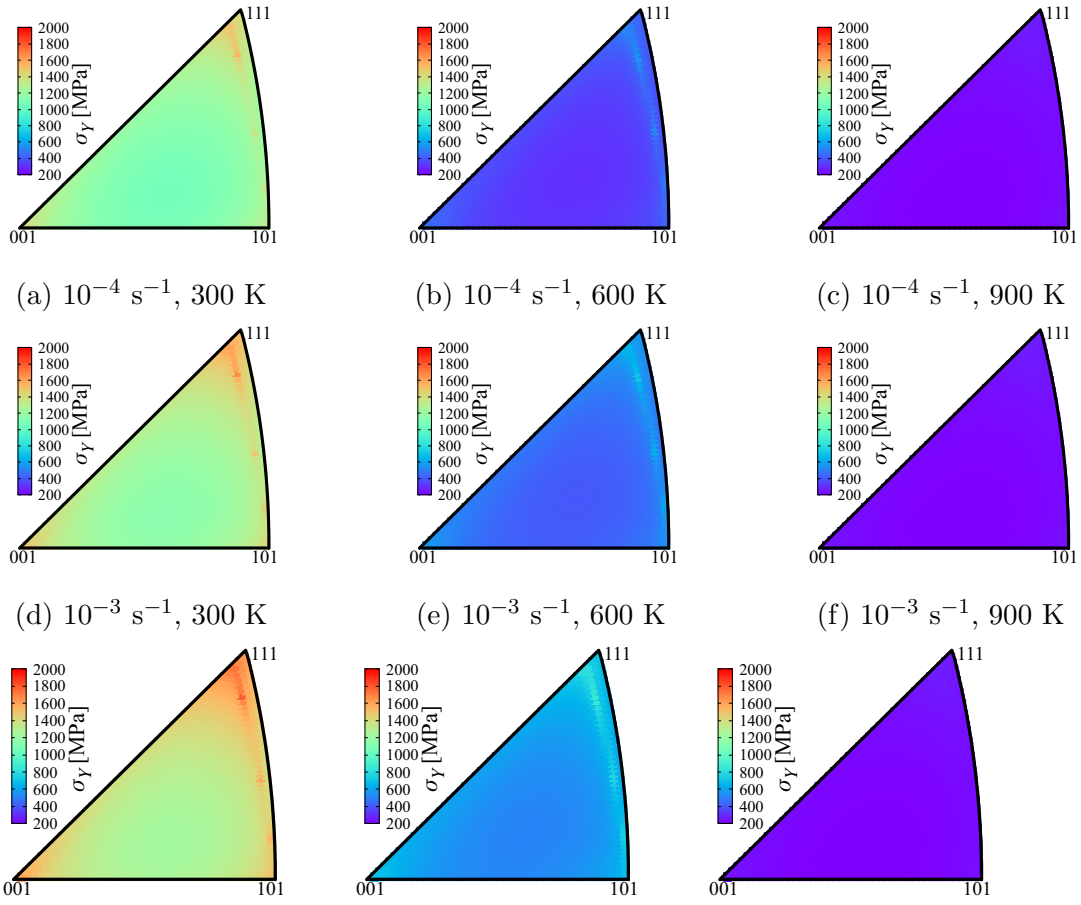

(a) 10^{-4} s^{-1}, 300 K (b) 10^{-4} s^{-1}, 600 K (c) 10^{-4} s^{-1}, 900 K

(d) 10^{-3} s^{-1}, 300 K (e) 10^{-3} s^{-1}, 600 K (f) 10^{-3} s^{-1}, 900 K

(g) 10^{-2} s^{-1}, 300 K (h) 10^{-2} s^{-1}, 600 K (i) 10^{-2} s^{-1}, 900 K

Figure 5.3: Yield stress of unirradiated W as a function of loading orientation at strain rates of 10^{-4}, 10^{-3}, and 10^{-2} s^{-1}, and temperatures of 300, 600, and 900 K.

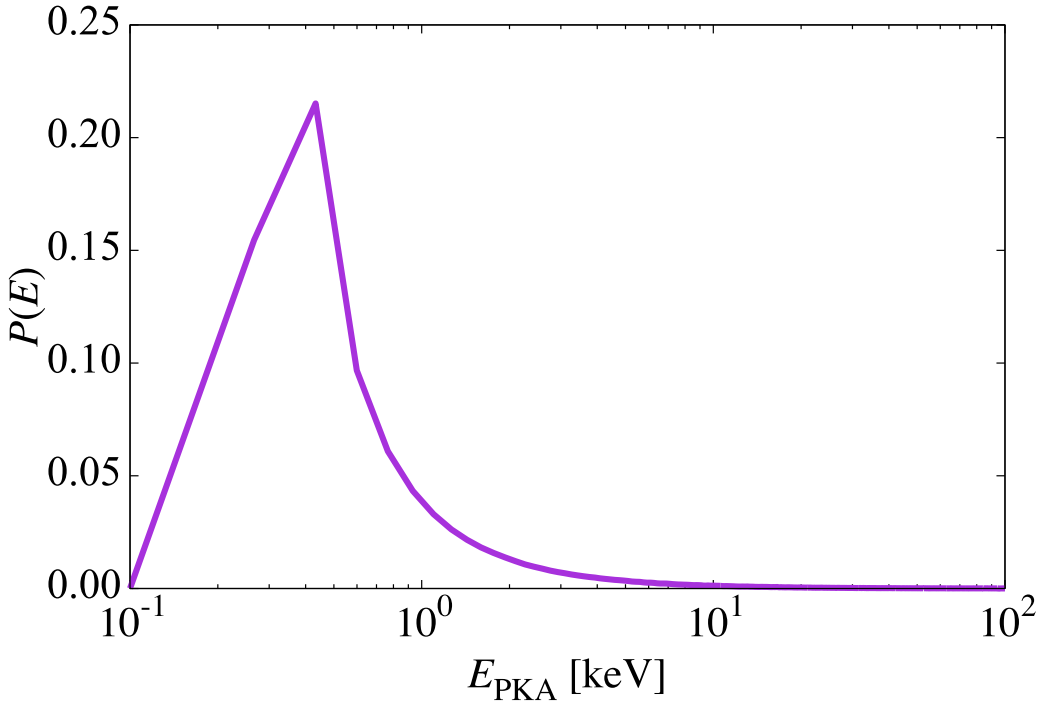

Figure 5.4: Normalized PKA distribution obtained from SRIM simulations of 18-MeV W ions on W.

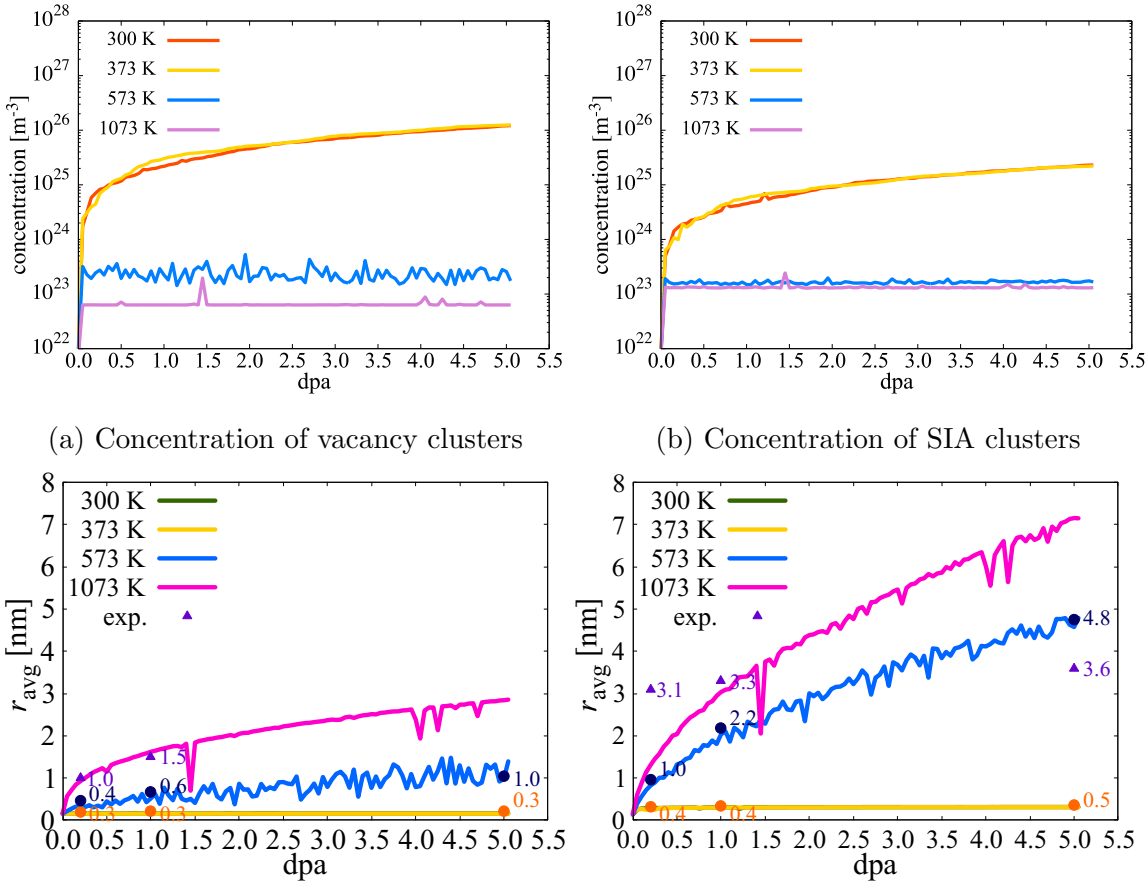

(a) Concentration of vacancy clusters

(b) Concentration of SIA clusters

(c) Average size of vacancy clusters

(d) Average size of SIA clusters

Figure 5.5: Evolution with dose and temperature of defect cluster concentrations and average sizes. Clusters are defined as containing three or more point defects. Separate markers indicate the results after annealing down to 300 K of the defect distributions after 0.2, 1.0, and 5.0 dpa. Selected data from experiments are also provided for comparison. The cluster sizes at 300 and 373 K are indistinguishable from one another.

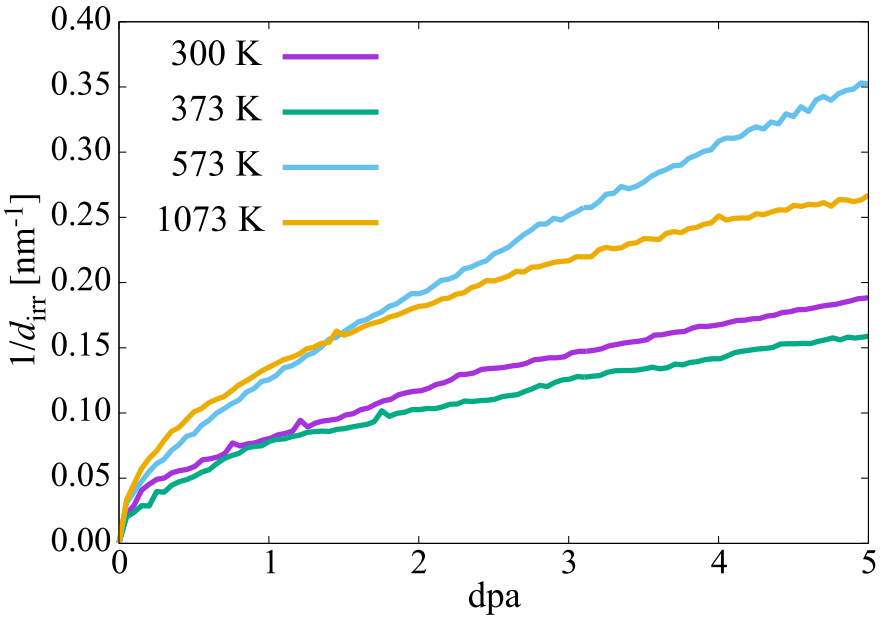

Figure 5.6: Evolution with dose of the inverse average defect spacing d_{irr} as obtained using eq. (7.23).

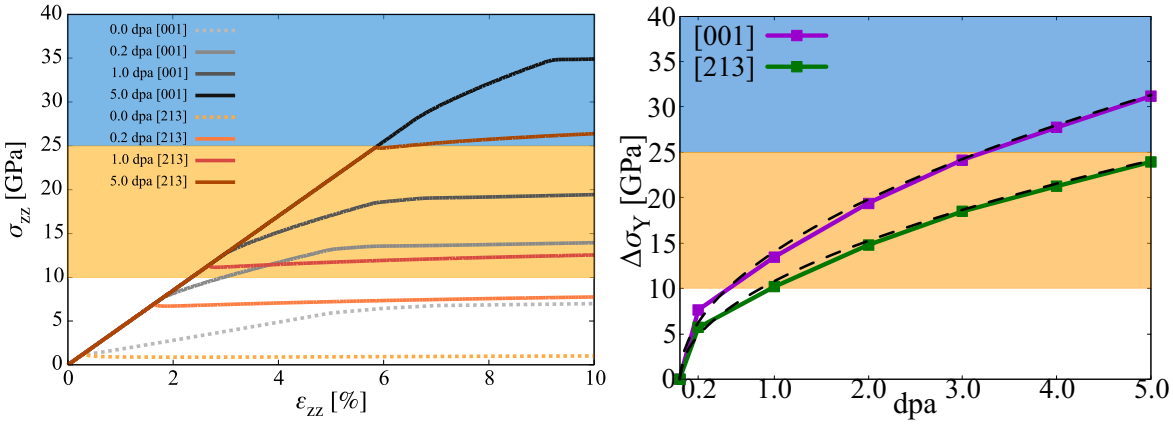

(a) (b)

Figure 5.7: (a) σ_{zz}-ε_{zz} curves for unirradiated and irradiated (at the three doses: 0.2, 1.0, and 5.0 dpa) tungsten for [100] and [213]-oriented crystals for a strain rate of 10^{-3} s^{-1} at 600 K. (b) Variation of the magnitude of irradiation hardening $\Delta\sigma_Y$ with irradiation dose for the cases at 10^{-3} s^{-1}. The dashed lines are visual guides based on a square-root dependence of the hardening with dose. The shaded areas indicate regions of the stress-strain space where the tensile strength would be surpassed (see text).

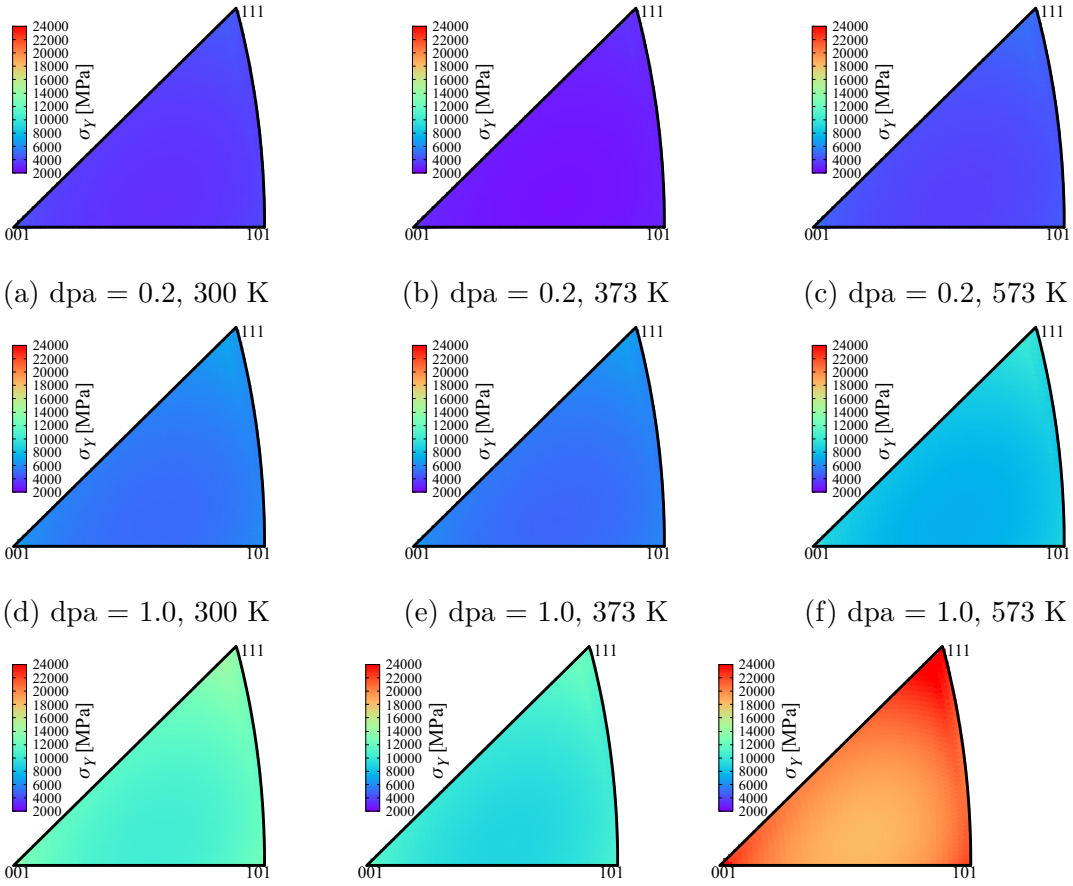

(a) dpa = 0.2, 300 K (b) dpa = 0.2, 373 K (c) dpa = 0.2, 573 K

(d) dpa = 1.0, 300 K (e) dpa = 1.0, 373 K (f) dpa = 1.0, 573 K

(g) dpa = 5.0, 300 K (h) dpa = 5.0, 373 K (i) dpa = 5.0, 573 K

Figure 5.8: Yield stresses of pre-irradiated W samples as a function of irradiation dose, irradiation temperature, and crystal orientation. All tests were performed at 300 K and ε_0 =10^{-4} s^{-1}.

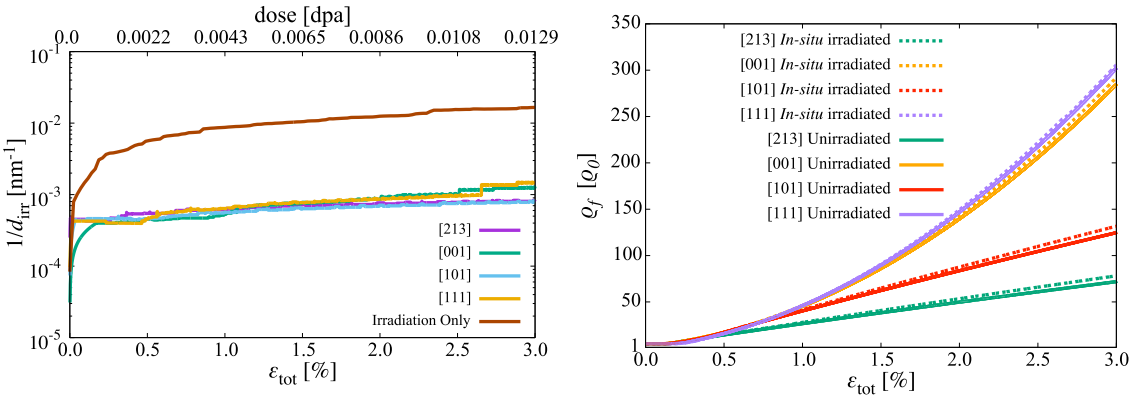

(a) (b)

Figure 5.9: Evolution of microstructural parameters during *in-situ* irradiation/deformation simulations for four crystal orientations deformed at 600 K and 10^{-4} s^{-1}. (a) Inverse mean defect spacing $1/d_{\mathrm{irr}}$, including a reference standalone irradiation case at 600 K. (b) Total forest dislocation density, including comparison with deformation-only tests.

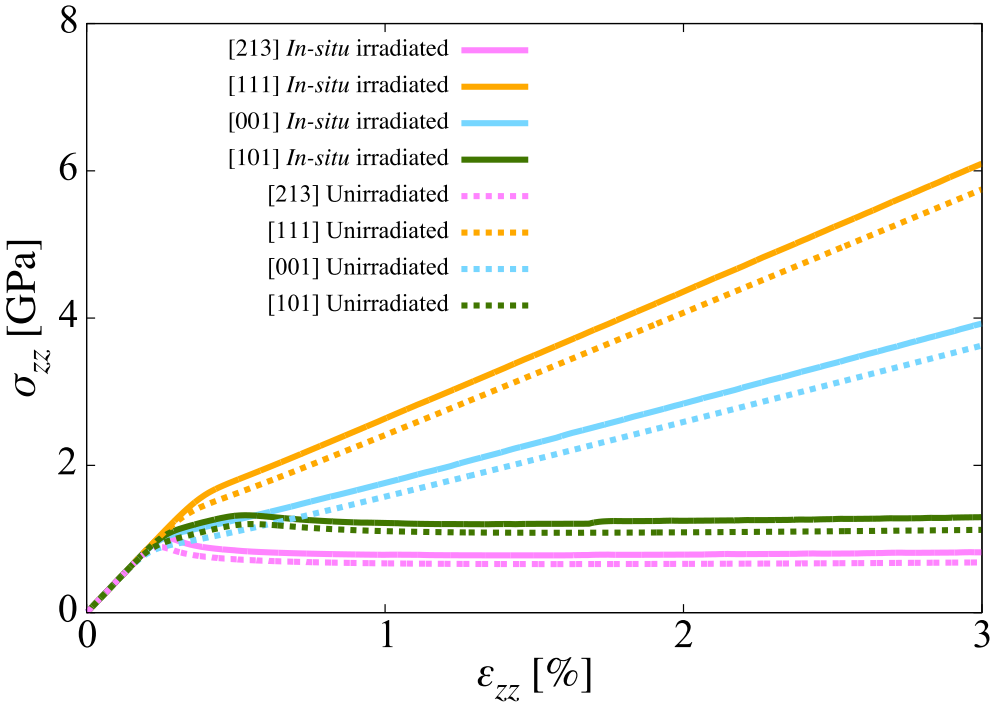

Figure 5.10: σ_{zz}-ε_{zz} curves for *in-situ* irradiated tungsten for various crystal orientations at a strain rate of 10^{-4} s^{-1} and 600 K.

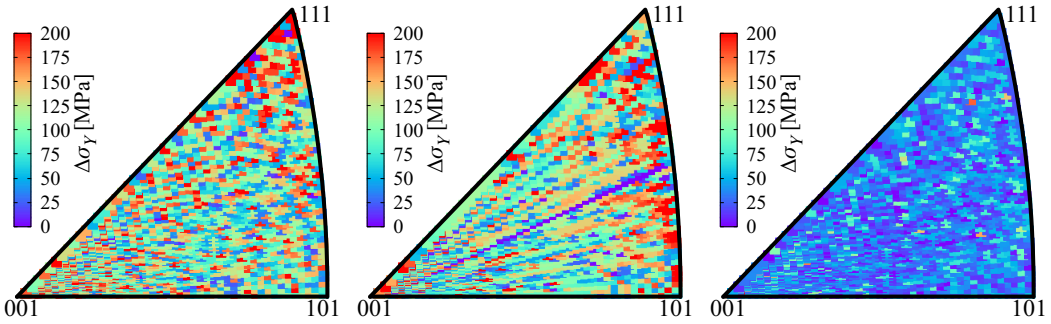

(a) 300 K (b) 600 K (c) 900 K

Figure 5.11: Differential yield stresses $\Delta\sigma_{\mathrm{Y}} = \sigma_{\mathrm{Y}}|_{\textit{in-situ}} - \sigma_{\mathrm{Y}}|_{\mathrm{unirr}}$ at a strain rate $\varepsilon_0 = 10^{-4}$ s^{-1}, and $T = 300$, 600, and 900 K, respectively.

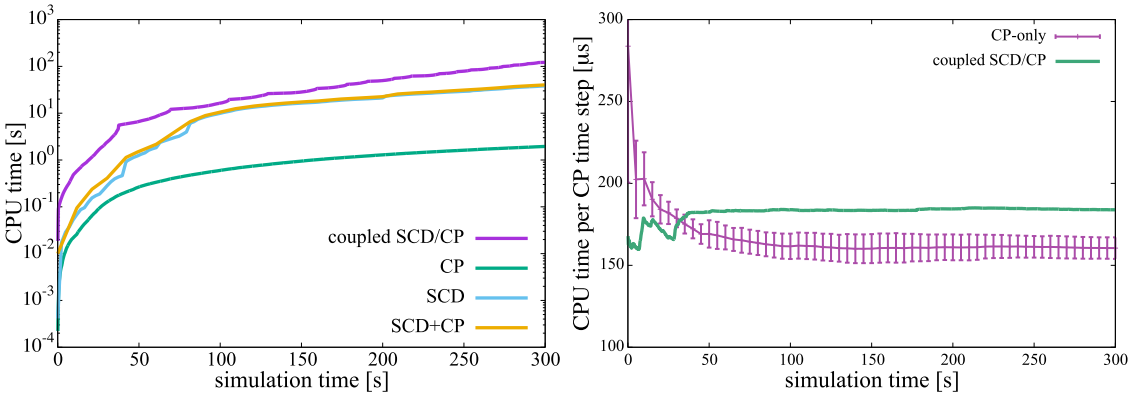

(a) (b)

Figure 5.12: (a) Total wall-clock computational time vs. simulated time for coupled CP-SCD, CP-only, and SCD-only simulations. (b) CPU cost of one converged crystal plasticity time step under the three cases in (a). Error bars correspond to the standard deviation from five independent tests.

CHAPTER 6

A stochastic solver based on the residence time algorithm for crystal plasticity models

6.1 Literature Review

Plastic deformation in single crystals can generally be construed as a process in which slip on a set of well-defined crystallographic planes results in irreversible shape changes in a material [23,87]. Through its various forms, the crystal plasticity method (CP) has proven extremely successful in predicting crystalline materials deformation thanks to (i) the existence of a robust mathematical theory [23, 151, 152, 313], (ii) a strong connection between the physics of slip and the geometry of deformation [14], and (iii) the development of accurate and efficient integration algorithms [**?**, 11, 156, 414]. While some challenges still remain, such as the indetermination of the active slip systems under a prescribed set of conditions [19], or the distinction between stored and geometrically-necessary dislocation density evolutions [18, 115], suitable approximations exist that are generally valid and give accurate results in most applications.

However, the standard implementation in CP models of crystallographic slip as a linear combination of plastic shear on a finite set of slip systems assumes that

these slip systems are independent of each other [81, 114, 197]. Such notion is generally grounded on an adiabatic interpretation of dislocation-mediated shear[1], which is often questionable and leads to an homogeneous plastic response even in cases where valid localized deformation pathways exist [30, 115]. Such homogenization is mathematically not problematic, as the underlying constitutive models intrinsically ensure stability in the solutions. However, it is often at odds physically with the observed material response [190, 252, 410] in which symmetry in the evolution of plastic slip can naturally break and lead to a non-homogeneous distribution of plastic shear. Accounting for symmetry-breaking modalities in the slip response has typically been done by adding external probabilistic descriptors of certain internal variables [24, 110, 379, 408, 413]. Alternatively, stochasticity can be introduced intrinsically, via the integration algorithm itself, a practice widely used for integrating differential equation systems [131, 145, 239, 248]. As such, stochastic fluctuations are an intrinsic part of the solution, not just an externally added variable. When suitably adapted for CP models, such solvers could lead to fluctuations in plastic shear that can numerically break the symmetry in slip systems with identical Schmid factors. These fluctuations can also be regarded as reflecting the natural intrinsic variability of certain internal variables, i.e., they can be justified as 'physical' in many cases.

The main objective of this chapter is to develop a stochastic solver based on the residence time algorithm [48, 189] for standard single crystal plasticity problems. Under our approach, the mathematical formulation of the CP problem remains unchanged, which makes the algorithm completely general and independent of the

[1]The process is adiabatic in the sense that, during a small time interval, slip in a given slip system is assumed to evolve without being affected by slip in the remaining slip systems, i.e., the time step is sufficiently short to justify a lack of interaction among the operative slip systems.

constitutive framework and material model chosen. For proof of principle, here we focus on single-point material cases with no associated boundary-value problem. The chapter is organized as follows. First, in Sec. 6.2 we provide an essential review of the theory and methods used here, including brief descriptions of the residence time algorithm and crystal plasticity approach. In Sec. 6.3, we present results of CP simulations of uniaxial deformation in single crystal tungsten using the proposed stochastic algorithm under a variety of different scenarios. Section 6.4 contains a detailed discussion of the main results as well as of the potential usage of the method. We finalize with the summary.

6.2 Model Description

6.2.1 The residence time algorithm

The starting point is a (continuous) transition function $P_{ij}(t)$ representing the probability that a random variable $\xi_1(t)$ describing the state of a continuous-time Markov chain is X_j at time t having originated from an initial state X_i at time $t = 0$, i.e.[2]:

$$P_{ij}(t) = \Pr\left(\xi_1(t) = X_j |\ \xi(0) = X_i\right)$$

As such, all the $p_i(t) = \sum_{j \neq i} P_{ij}(t)$ conform a vector $\boldsymbol{p}$ of probabilities of dimension N equal to the total number of states accessible to the system. A square positive-definite $N \times N$ matrix $\boldsymbol{Q} = \{q_{ij}\}$ satisfying $\sum_{j \neq i} q_{ij} = r_i$ (where r_i is the *exit* rate from state X_i) gives the transition rates connecting all states X_i with all states X_j

[2]We use the standard notation $\Pr(\xi_1 = X)$ to denote the probability that a random variable ξ assumes a particular value X. $\Pr(\xi_1 = X|\xi_1 = Y)$ represents the (conditional) probability of finding the system in state X *p*rovided that it originated from state Y earlier in time.

($q_{ij} = 0$ when $i = j$). To preserve the Markovian structure of the process, all the coefficients q_{ij} are considered to be time-invariant.

The continuous-time master equation associated with $\boldsymbol{p}$ and $\boldsymbol{Q}$ is [132, 247, 315]:

$$\frac{dp_i(t)}{dt} = \sum_{j \neq i} [q_{ji} p_j(t) - q_{ij} p_i(t)] \tag{6.1}$$

The Markov chain representing this process generates a sequence of state transitions $X_i \rightarrow X_j$ with probabilities $P_{ij} = 0$ (if $i = j$) or $P_{ij} = q_{ij}/r_i$ (if $i \neq j$). Time reversibility of eq. (6.1) results in the *detailed balance* condition: $q_{ij} p_j = q_{ji} p_i$ (in matrix form, $\boldsymbol{Q}\boldsymbol{p}^T = \boldsymbol{Q}^T\boldsymbol{p}$), which allow us to express the above equation in matrix form as:

$$\dot{\boldsymbol{p}} = (\boldsymbol{Q} - \boldsymbol{R})\,\boldsymbol{p} \tag{6.2}$$

where $R_{ij} = r_i \delta_{ij}$ is a diagonal matrix (as a matter of notation, here summation is explicitly indicated by the symbol '$\sum$' and the corresponding indices).

The *residence* time in state X_i, δt_i can be shown to follow an exponential distribution with mean $1/r_i$ [145,362], which allows us to define a probability $\Pr(\delta t_i > t | \xi_1(0) = X_i) = r_i \exp\{-r_i \delta t_i\}$ from which to sample the residence time using a uniform random variable ξ_2: $\delta t_i = r_i^{-1} \log(1 - \xi_2)$.

Solving the master equation (6.1) (or (6.2)) fully characterizes the evolution of the system in time. However, in most applications of interest the total number N of states accessible to the system (dimension of the Markov space) is not known, resulting in undetermined $\boldsymbol{Q}$ matrices and thus precluding the use of analytical or deterministic methods to solve the master equation. In such cases, the problem is characterized by a discrete Markov chain with infinite dimension, and approximate methods must be used. When the following two conditions are met, discrete event

methods can be used to solve the master equation: (i) the probability of each event depends only on the state reached in the previous event (i.e., the system is defined by a 1^{st} order Markov process), and (ii) the system remains unchanged during a transition between two states (i.e., the time spent during a transition is negligible compared to the residence time).

This is where the utility of the residence-time algorithm (also known as the kinetic Monte Carlo (kMC) method) resides. In particular, in rejection-free kMC (also known as 'BKL' after its original proponents [48]), once a transition between two states $n \rightarrow m$ is selected with the corresponding probability $q_{nm}/\sum_m q_{nm}$, it is executed and time is advanced by an amount equal to either $1/\sum_m q_{nm}$ or obtained by sampling a uniform random number $\chi \in (0, 1]$ as $\delta t_n = -\log(1-\chi)/\sum_m q_{nm}$. In this fashion, the system evolves in discrete time increments as the state space $\{X\}$ is sampled, leading to a significant computational gain over standard Monte Carlo methods. The reader is referred to recent reviews for more information on the topic [82, 247].

6.2.2 Casting the crystal plasticity model as a stochastic process

The crystal plasticity formulation has been described in section 2.2. Here we introduce the method of solving this formulation with stochastic process. The Markov chain representing the process described by the master equation (6.1), (6.2) evolves the system forward in time by following a sequence of transitions whose rates depend solely on the initial and final states. As such, eq. (6.1) is akin to an explicit time discretization of the crystal plasticity model, in which the properties of the system at time $t + \delta t$ are obtained solely as a function of those at time t. With this, eq.

(2.19) can be recast as:

$$\dot{\boldsymbol{\sigma}} = \mathbb{C} : \left(\dot{\boldsymbol{\varepsilon}}_0 - \dot{\boldsymbol{H}}^{\mathrm{P}} \right) \tag{6.3}$$

The constitutive framework for the explicit form of the model remains unchanged. Additionally, the unknowns of the crystal plasticity problem remain the same. However, instead of solving iteratively for the ensemble of slip rates, the shear rates are determined in a sequential manner. The evaluation at time $t + \delta t$ is based on the calculation of the available glide stress $\tau^{\alpha}_{\mathrm{RSS}}$ and the dislocation velocities at time t [96, 205, 412].

By analogy with (6.2), the above equation can be trivially written as a stochastic equation:

$$\dot{\boldsymbol{\varepsilon}}^{\mathrm{E}} = \dot{\boldsymbol{\varepsilon}}_0 - \dot{\boldsymbol{H}}^{\mathrm{P}} \tag{6.4}$$

In essence, this equation yields the time rate of the probability of finding the system under a given stress state. In the r.h.s. of the equation, $\dot{\boldsymbol{\varepsilon}}_0$ can be regarded as an external source term that is independent of the current stress state, while $\dot{\boldsymbol{H}}^{\mathrm{P}}$ acts as a stress absorber through conversion to plastic deformation. From eqs. (2.21) and (6.3), eq. (6.4) can be expanded to:

$$\dot{\boldsymbol{\varepsilon}}^{\mathrm{E}} = \dot{\boldsymbol{\varepsilon}}_0 - \sum_{\alpha} \rho^{\alpha} b^{\alpha} v^{\alpha} \left(\boldsymbol{s}^{\alpha} \otimes \boldsymbol{n}^{\alpha} \right) \tag{6.5}$$

While this equation is not strictly a master equation, i.e., one of the type $\dot{\boldsymbol{p}} = \boldsymbol{Q}'\boldsymbol{p}$, as in eq. (6.2), a set of event rates can be extracted from eq. (6.5) that govern the evolution of the elastic strain in time. The total rate to 'exit' a given stress state defined by a total elastic strain ε^{E} at time t^n can be written as:

$$r^n = \sum_{\alpha=1}^{N} q^n_{\alpha} + q_0 \tag{6.6}$$

with $q_0 = \sum_i \sum_j (\dot{\boldsymbol{\varepsilon}}_0)_{ij}$, $q_\alpha = \rho^\alpha b^\alpha v^\alpha$, and N is the number of independent slip systems.

In rejection-free kMC, the next event to be executed is selected as the k^{th} process that satisfies:

$$q_{k-1}^n < \xi_1 r^n < q_k^n \tag{6.7}$$

where $k = 0, \ldots, N$. If the event selected corresponds to the rate q_0, further sampling is carried out among the different nonzero components of $\dot{\boldsymbol{\varepsilon}}_0$ to determine which deformation to impose. The total time is then advanced as:

$$t^{n+1} = t^n + \delta t^n \tag{6.8}$$

$$\delta t^n = -\frac{\log \xi_2}{r^n} \tag{6.9}$$

where ξ_1 and ξ_2 are uniform random numbers in $(0, 1]$. Once an event is executed, the elastic strain is updated and, with it, the stress state. From the new stress state, resolved shear stresses are calculated, from which in turn plastic slip rates and dislocation densities are updated, thus closing the cycle.

A schematic diagram showing the sampling of event rates and the total rate is given in Figure 6.1. A complete algorithm suitable for solving eq. (6.5) based on the above procedure is provided next.

6.2.3 A residence-time algorithm for elasto-viscoplastic CP problems

The crystal is defined by its dislocation density content, ρ^α, in each of its N slip systems α and the grain size d_g. Deformation conditions are given by the applied strain rate (tensor) $\dot{\boldsymbol{\varepsilon}}_0$, the temperature T and the loading orientation $\boldsymbol{o}$ (generally aligned with a given crystal axis corresponding to the z direction). Thus our simu-

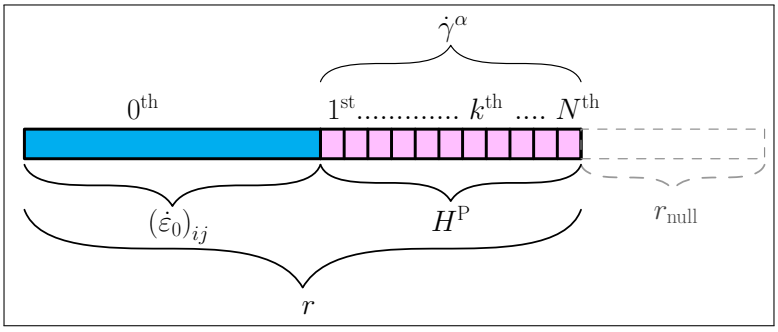

Figure 6.1: Sampling array of event rates in the SCP algorithm. The total rate r is partitioned between the prescribed applied strain rate $\dot{\varepsilon}_0$ and the total plastic distortion H^{P}. In turn, H^{P} is composed of N independent shear rates γ^{α}. As such, there are always $N+1$ different possible event rates to sample from, contained in an array whose index k runs from 0 to N. Note that, in general, the value of each shear rate γ^{α} may be different to the rest of the shear rates during each time step. The dashed section refers to the possibility of using $n$ull events, discussed in Sec. 6.4.1.

lations are carried out with only one nonzero component of the imposed strain rate tensor, such that $q_0 \equiv (\varepsilon_0)_{zz}$. The algorithm proceeds as a standard crystal plasticity algorithm until the calculation of the slip rates is completed. The stochastic part of the algorithm that serves as integrator is captured in lines 30 to 32.

For comparison, the equivalent deterministic (explicit) algorithm is given in algorithm 3 in Appendix E.

6.2.4 Physical bounds on problem time scale

Figure 6.2 shows the raw time step distributions sampled from three independent SCP runs at three different strain rates for [100] loading at 500 K. The averages of the distributions are 4500, 517, and 52 s for $\dot{\varepsilon}_0 = 10^{-4}$, 10^{-3}, and 10^{-2} s^{-1},

respectively. These results illustrate the absolute time scales that emanate from the direct sampling of eq. (6.5). Strictly speaking, the time increments shown in the figure represent the maximum time steps compatible with the rate equation being solved. However, one may use an arbitrarily smaller set of δt without sacrificing the numerical validity of the method, which may be advantageous when, e.g., there are other constraints on the time scales of the problem besides purely numerical ones. Indeed, such is the case here, where deformation tests performed at quasistatic strain rates ($10^{-5} \sim 10^{-2}$ s^{-1}) result in total strains that are almost always < 1, and which are thus reached in much shorter times than those indicated in Fig. 6.2 .

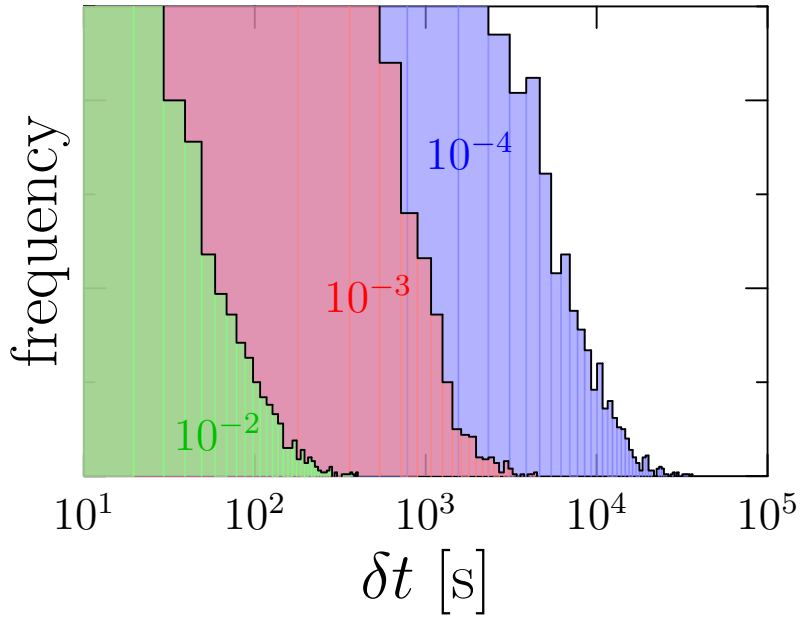

Figure 6.2: Time step distributions sampled from eq. (6.6) for crystal plasticity simulations at 500 K under [100] loading at three different strain rates of 10^{-4}, 10^{-3}, and 10^{-2} s^{-1}. The averages of the distributions are 4500, 517, and 52 s, respectively. All three histograms are given in arbitrary units

One way of establishing meaningful boundaries for δt may be by considering the physical validity range of the present algorithm, which is set by the condition $\left(\frac{\tau^{\alpha}_{\mathrm{RSS}}-\tau^{\alpha}_{h}}{\sigma_{\mathrm{P}}}\right) < 1$ (from eq. (2.22)), i.e.:

$$\tau^{\alpha}_{\mathrm{RSS}} < \tau^{\alpha}_{h} + \sigma_{\mathrm{P}} \tag{6.10}$$

Taking time increments, the above expression becomes (σ_{P} is constant):

$$\frac{d\tau^{\alpha}_{\mathrm{RSS}}}{dt} < \frac{d\tau^{\alpha}_{h}}{dt} \tag{6.11}$$

Implicit in this relation there is a time step condition that must be satisfied such that the time scale of the problem is reflective of the physical processes that participate in the evolution of the deformation of the material. As shown in Alg. 1, $\tau^{\alpha}_{\mathrm{RSS}}$ displays a linear dependence on δt, while τ_h scales as $\mathcal{O}(\delta t^{1/2})$ (through its dependence on the term $\sqrt{\sum_{\beta}\rho^{\beta}}$, $\beta = 1 \ldots N$). As such, one can rewrite the above inequality generically as:

$$\frac{d\left(\mathcal{C}_1 \delta t\right)}{dt} < \frac{d\left(\mathcal{C}_2 \delta t^{1/2}\right)}{dt}$$

which results in the condition:

$$\mathcal{C}_1 < \frac{\mathcal{C}_2}{2\delta t^{1/2}}$$

or

$$\delta t < \left(\frac{\mathcal{C}_2}{2\mathcal{C}_1}\right)^2 \tag{6.12}$$

where $\mathcal{C}_1$ and $\mathcal{C}_2$ are constants representing, respectively, the (elastic) stress rate, $\mathcal{C}_1 \approx E\left(\dot{\varepsilon}_0 - \dot{\gamma}_p\right)$ and the forest hardening rate $\mathcal{C}_2 \approx \mu\sqrt{\dot{\gamma}_p}$, where $\dot{\gamma}_p$ is again a generic plastic shear rate, i.e.:

$$\delta t < \left[\frac{\mu\sqrt{\dot{\gamma}_p}}{E\left(\dot{\varepsilon}_0 - \dot{\gamma}_p\right)}\right]^2 \tag{6.13}$$

where $E = \frac{9\kappa\mu}{3\kappa+\mu}$ is the Young's modulus. For simplicity, it is assumed that the shear rates are well captured by the term $\rho_0 bv$, where v is a temperature dependent dislocation velocity, set by eq. (2.22). With this, the above expression becomes:

$$\delta t < \left[\frac{\mu\sqrt{\rho_0 bv}}{E\left(\dot{\varepsilon}_0 - \rho_0 bv\right)}\right]^2 = \left(\frac{\mu}{E}\right)^2 \frac{\rho_0 bv}{\left(\dot{\varepsilon}_0 - \rho_0 bv\right)^2} = \delta t^* \tag{6.14}$$

This expression is fundamentally equivalent to that derived by Van der Giessen et al. [360] using a slightly different constitutive model. In the present model, for the 300-to-1000-K temperature range, v varies between 10^{-7} and 10^{-3} m·s^{-1}. By way of example, using material constants from Table 6.1, this results in critical time steps δt^* between 0.05 to 100 s when $\dot{\varepsilon}_0 = 10^{-3}$ s^{-1}.

As such, the physical time scale symbolized by δt^* and the results from Fig. 6.2 (defined by the value $1/r^n$) must be reconciled. While there are rigorous ways to connect both (discussed in Sec. 6.4), here we adopt the practical approach of defining a normalization factor $\Delta\varepsilon^* \ll 1$, which is used to scale eq. (6.9):

$$\delta t^n = -\log \xi_2 \left(\frac{\Delta\varepsilon^*}{r^n}\right)$$

The impact of the choice of $\Delta\varepsilon^*$ will be evaluated in the next section.

6.3 Results

6.3.1 Verification of algorithm capabilities

In this section, we verify that the stochastic solver in Alg. 1 is capable of reproducing the results of deterministic CP calculations under generic loading and temperature conditions. We first consider uniaxial loading along the [001] crystal orientation at 500 K and 10^{-3} s^{-1}. [001] loading results in eight active slip systems each with

Table 6.1: Values for the material parameters employed in this work.

Property	Symbol	Value	Unit
Burgers vector's modulus	b	$\sqrt{3}/2$	a_0
Lattice parameter	a_0	3.16	Å
Bulk modulus	κ	310	GPa
Shear modulus	μ	160	GPa
Young's modulus	E	409	GPa
Peierls stress	σ_{P}	2.0	GPa
Initial dislocation density	ρ_0	8.3×10^{12}	m^{-2}

a Schmid factor of 0.409 and four inactive ones. As such, it is representative of multi-slip conditions conducive to latent hardening. In this work we consider single crystal deformation only, i.e., $1/d_g \approx 0$. Values for the material parameters used in the calculations are given in Table 6.1.

6.3.1.1 Stress-strain response

Figure 6.3 shows stress-strain curves for several $\Delta\varepsilon^*$. The shaded area represents the reference deterministic result (forward Euler method with $dt = 0.1$ s) for comparison. A prescribed strain rate of $(\dot{\varepsilon}_0)_{zz} \equiv \dot{\varepsilon}_0 = 10^{-3}\ \mathrm{s}^{-1}$ was used. As the figure shows, the value of $\Delta\varepsilon^*$ determines the magnitude of the stochastic oscillations, but not its steady state value, which is seen to consistently reproduce the deterministic solution. In particular, the hardening modulus – assumed to remain constant during plastic flow – is seen to be virtually identical in all cases, 0.96 GPa, irrespective of the value of $\Delta\varepsilon^*$. The average yield strength, $\bar{\sigma}_{\mathrm{Y}}$, obtained from all the different $\Delta\varepsilon^*$ cases

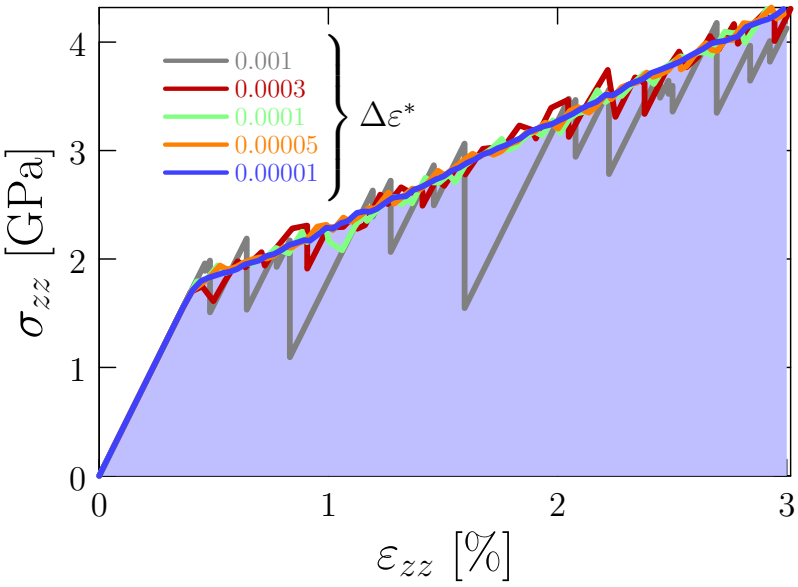

Figure 6.3: Stress-strain response at 500 K under [001] axial loading. The shaded area represents the reference deterministic result (forward Euler method with $dt = 0.1$ s). Results for several $\Delta\varepsilon^*$ inside the stability range are given for comparison.

is seen to slightly exceed the deterministic value, 1.9 vs. 1.8 GPa, respectively. The standard deviation of $\bar{\sigma}_Y$ scales linearly with $\Delta\varepsilon^*$, with a proportionality constant on the order of the Young's modulus E. This is consistent with having elastic strain increments that may 'overshoot' the true (deterministic) yield stress, which is then immediately followed by a plastic event.

6.3.1.2 Dislocation densities and fluxes

Figure 6.4 shows the evolution of the total dislocation density with strain corresponding to the cases shown in Fig. 6.3. The values shown in the curves are normalized to the initial dislocation density value ρ_0 (cf. Table 6.1). The dislocation density is seen

to evolve in bursts of a magnitude commensurate with the value of $\Delta\varepsilon^*$. Although a small drift at high strains can be appreciated for the two cases with the largest scaling factor, the steady state value of ρ_{tot} is in excellent agreement with the solution furnished by the deterministic solver.

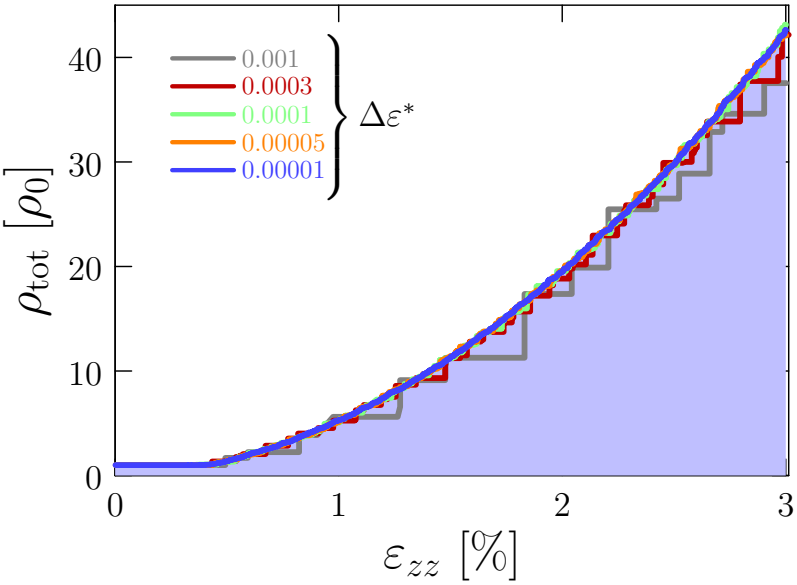

Figure 6.4: Total dislocation density evolution as a function of axial strain at 500 K under [001] loading. The shaded area represents the reference deterministic result (forward Euler method with $dt = 0.1$ s). Results for several $\Delta\varepsilon^*$ inside the stability range are given for comparison.

ρ_{tot} is an integrated measure of the overall performance of the algorithm during plastic deformation. However, it is also of interest to look at the evolution at the level of the slip systems. Figure 6.5 shows results for the average shear rates under [001] axial loading at 500 K, defined as:

$$\bar{\dot{\gamma}} = \frac{1}{N_{\text{act}}} \sum_{\alpha}^{N_{\text{act}}} \dot{\gamma}^{\alpha}$$

where $N_{\text{act}} < N$ is the number of slip systems with nonzero Schmid factor (8 out of 12, all with an identical Schmid factor of 0.409 under these conditions). The average shear plastic rates shown in the figure are normalized to $\dot{\varepsilon}_0$. The error bars shown represent the standard deviation associated with the stochastic sampling. As in Figs. 6.3 and 6.4, the deterministic solution is shown in the background as a shaded area. Clearly, the values associated with larger $\Delta\varepsilon^*$ show much larger average plastic shear rates and more pronounced deviations from the mean value.

6.3.1.3 Exploring the parametric space

For generalization purposes, next we apply the method changing the three external variables in the simulations, i.e., temperature, strain rate, and loading orientation. Figure 6.6 shows a set of stress-strain curves at temperatures ranging from 300 to 800 K at $\dot{\varepsilon}_0 = 10^{-2}$ s^{-1} under [001] loading. All curves are for $\Delta\varepsilon^* = 5.0 \times 10^{-5}$. The temperature dependence of the yield strength (obtained as the 0.2%-offset stress) is given in the inset to the figure.

Figure 6.7 shows the stress-strain response of the system as a function of $\dot{\varepsilon}_0$ at 500 K under [001] loading. All curves are for $\Delta\varepsilon^* = 5.0 \times 10^{-5}$. The inset shows the strain-rate sensitivity (SRS) of the yield strength (obtained as in Fig. 6.6), including the SRS exponent m from the fit $\sigma_{\text{Y}} = C\dot{\varepsilon}_0^m$. The fit (dashed line in the inset) yields values of $C = 2.83$ GPa and $m = 0.059$.

Finally, we explore several different loading orientations with $T = 500$ K, $\dot{\varepsilon}_0 = 10^{-2}$ s^{-1}, and $\Delta\varepsilon^* = 5.0 \times 10^{-5}$. Figure 6.8 shows stress-strain curves for several loading directions in the standard triangle, shown on the right. The deterministic solutions for each case are shown as black dashed lines.

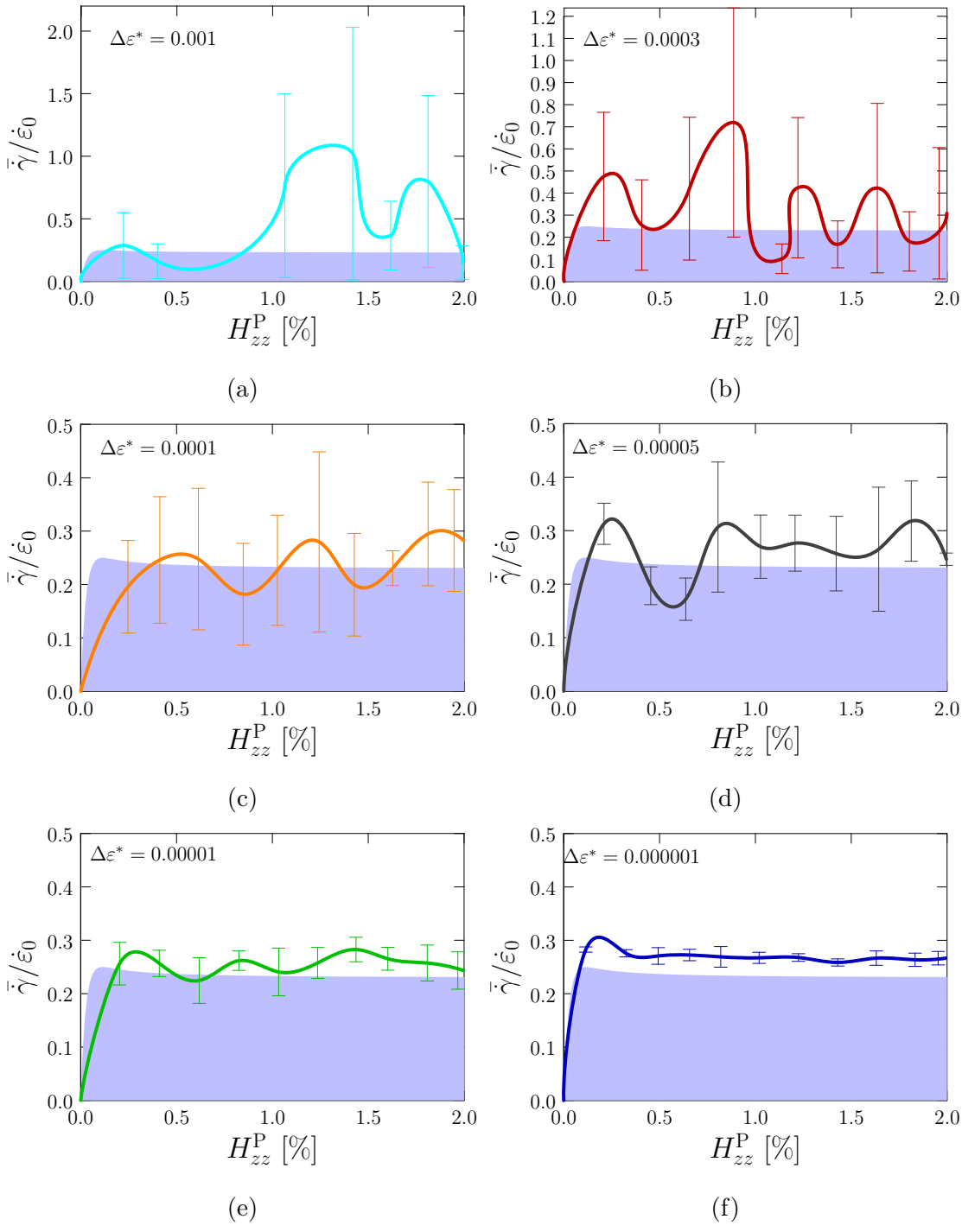

Figure 6.5: Evolution of the normalized shear slip rate with plastic strain for several values of $\Delta\varepsilon^*$ at 500 K under axial loading along the [001] direction. Results are given as averages and standard deviations for all active systems under these loading conditions (8 out of 12, all with an identical Schmid factor of 0.4091). The shaded area in the background corresponds to the reference deterministic result (forward Euler method with $dt = 0.1$ s).

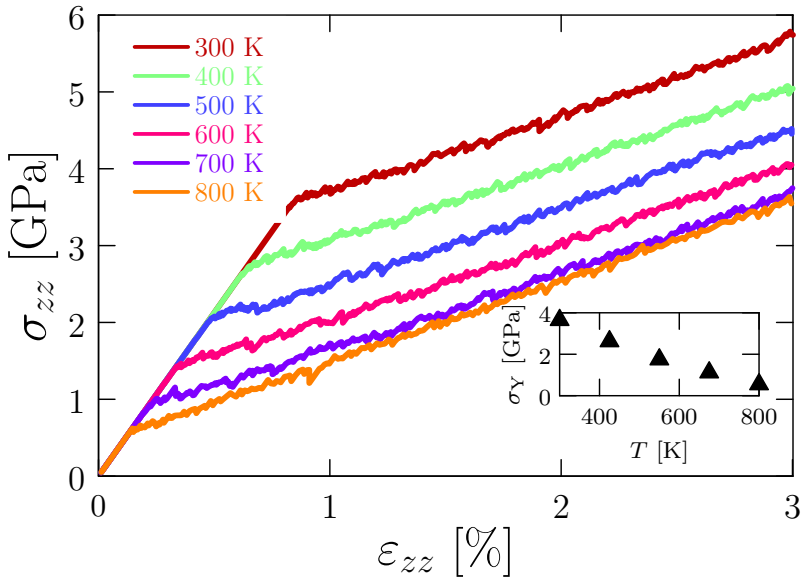

Figure 6.6: Axial stress-strain curves as a function of temperature under $\dot{\varepsilon}_0 = 10^{-2}$ s^{-1} and [001] loading. All curves are for $\Delta\varepsilon^* = 5.0 \times 10^{-5}$. The inset gives the temperature dependence of the yield stress (0.2%-strain offset stress).

6.3.2 Natural evolution of slip under heterogeneous conditions

The above subsections unequivocally show that the stochastic crystal plasticity (SCP) algorithm is capable of solving the same mathematical problem as standard crystal plasticity. However, as indicated in the introduction, this is not the main point of SCP. Stochasticity represents an intrinsic numerical element that can promote plastic shear heterogeneously across different slip systems, i.e., SCP can capture natural fluctuations in the underlying plastic rates without the need for *a*d-hoc probabilistic treatments.

To showcase this feature of the model, here we study again uniaxial tests at 500 K, 10^{-2} s^{-1}, and several orientations using the SCP method sampling one single

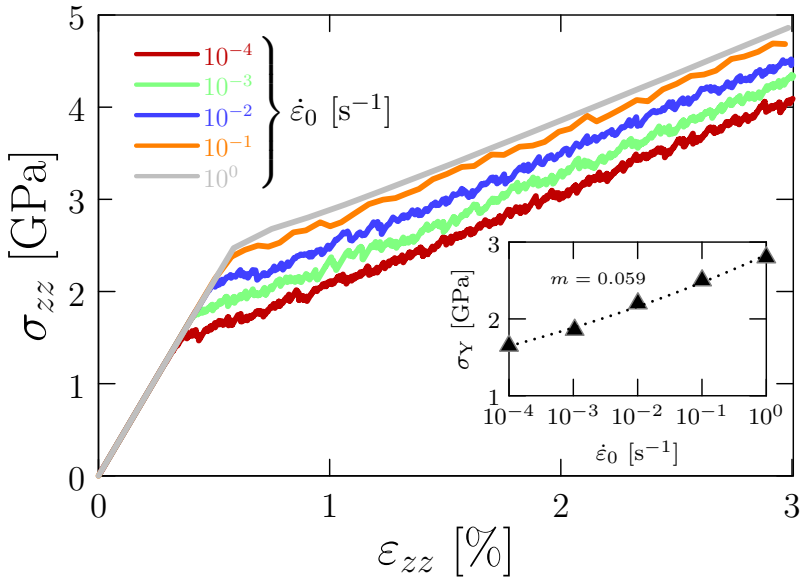

Figure 6.7: Axial stress-strain curves as a function of strain rate at 500 K and [001] loading. All curves are for $\Delta\varepsilon^* = 5.0\times10^{-5}$. The inset gives the strain rate sensitivity (SRS) of the yield stress (0.2%-strain offset stress). The SRS exponent is $m = 0.059$.

slip event per time step. Our curves are compared to results obtained using the CP explicit solver by Kuchnicki et al. [205], which is also designed to induce asymmetric plastic flow by using a sequential cycle that prioritizes slip in systems with the highest excess stress (i.e., what the quantity $\Delta\tau^\alpha$ used in eq. (2.22) represents here).

To demonstrate slip anisotropy, we take the [101] direction as representative of multislip conditions (four slip systems with a Schmid factor of 0.408 and eight inactive slip systems) to compare the deterministic approach by Kuchnicki et al. and the SCP method. In Figure 6.10 we plot the plastic shear rates in all 12 slip systems for the [101] loading case shown in Fig. 6.9. As shown, the plastic slip that leads to the stress-strain curves for the [101] loading orientation in Fig. 6.9 is carried by a single slip system ($\alpha = 7$ in Table A.1) in the SCP case, and by two of them ($\alpha = 6,\ 9$) in the

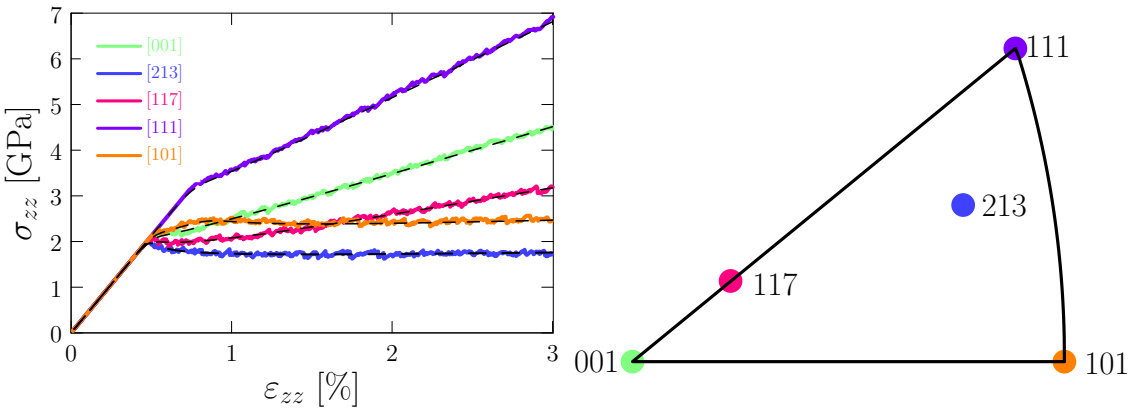

Figure 6.8: Axial stress-strain curves as a function of loading direction at 500 K and [001] loading and 10^{-2} s^{-1}. All curves are for $\Delta\varepsilon^* = 5.0 \times 10^{-5}$. The corresponding deterministic solutions are provided as black dashed lines. The loading directions are marked in the stereographic triangle for reference.

deterministic case. We have confirmed that in each SCP simulation the probability that any one of the four active slip systems is activated is indeed the same (25%).

6.3.3 Computational performance

In general terms, the efficiency of the residence time algorithm is tied to the event search encoded in eq. (6.7). When the dimension, n, of the sampling array is large, binary searches with a $\mathcal{O}(\log(n))$ nominal overhead are more efficient than simple $\mathcal{O}(n)$ linear searches. However, this is not a factor in the present calculations, where, at most, $n = N + 2$ with $N = 12$. Instead, the computational overhead may be defined as the CPU time invested in advancing a CP simulation by some amount of

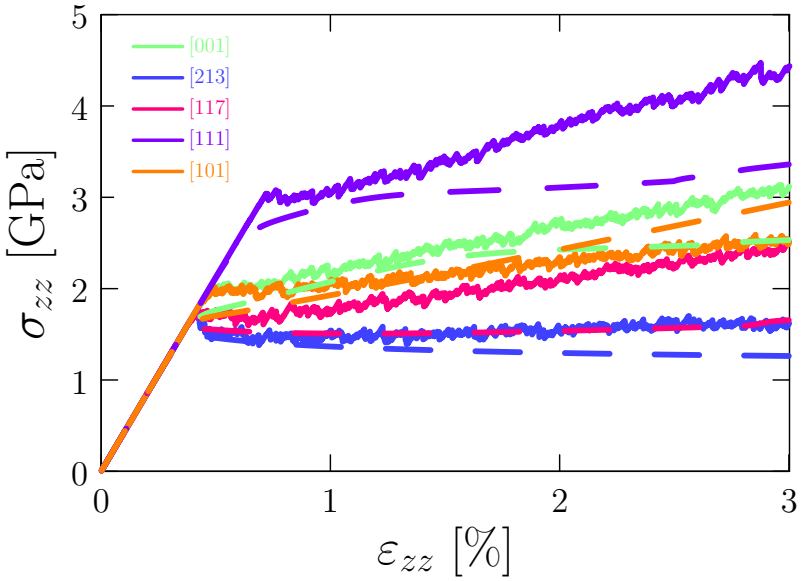

Figure 6.9: Axial stress-strain curves as a function of loading orientation at 500 K and 10^{-2} s^{-1} using two methods that break the symmetry of slip: the stochastic algorithm evolving shear one event at each time (solid lines) and the explicit method by Kuchnicki et al. [205] (discontinuous lines with like colors). The SCP curves are for $\Delta\varepsilon^* = 5.0 \times 10^{-5}$.

strain. Figure 6.11a shows the CPU cost per 1% strain[3] for the implementation of Alg. 1 on a 1.4GHz Intel Core i5 processor tested as a function of $\Delta\varepsilon^*$ for a number of SCP simulations at 500 K under [101] loading at 10^{-3} s^{-1}. As the figure clearly shows, an inverse correlation between the CPU time and $\Delta\varepsilon^*$ is found. For the results shown in the figure, $t_{\text{CPU}} = 3.43 \times 10^{-5} x^{-0.97}$ [s per 1% strain]. This is not unexpected, since, as we showed above, there is a direct equivalence between $\Delta\varepsilon^*$

[3]It should be noted that, while the CPU cost of the SCP method in the elastic and plastic regions is virtually identical, this is not the case for a deterministic integrator, where the initial buildup in elastic strain is practically instantaneous compared to the plastic flow region.

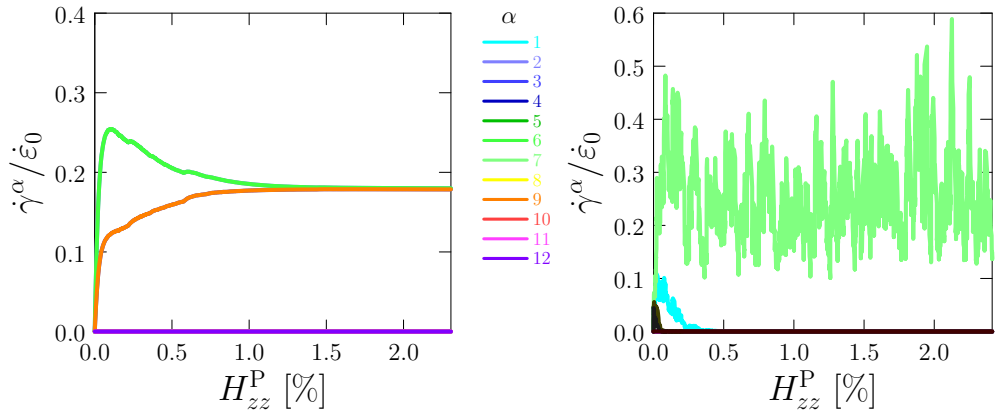

(a) Deterministic [205]. (b) Stochastic (this work).

Figure 6.10: Normalized plastic shear rates as a function of plastic strain for symmetry-breaking slip evolution modes of the SCP algorithm and an explicit deterministic model [205].

and the effective time step used in the simulations. Using such correlations can be helpful in estimating the *a priori* CPU overhead of a SCP simulation.

For its part, Figure 6.11b gives the same metric as a function of applied strain rate for a fixed value of $\Delta\varepsilon^* = 10^{-4}$. A sharp drop is observed between $\dot{\varepsilon}_0 = 10^{-3}$ and 10^{-2} s^{-1}, although this is likely to be somewhat dependent on the value of $\Delta\varepsilon^*$ chosen in each case.

6.4 Discussion

In essence, the present method provides a new approach for time integration of crystal plasticity models. The solver itself is the well-known residence time algorithm, which relies on stochastic sampling of a set of transition rates that determine the

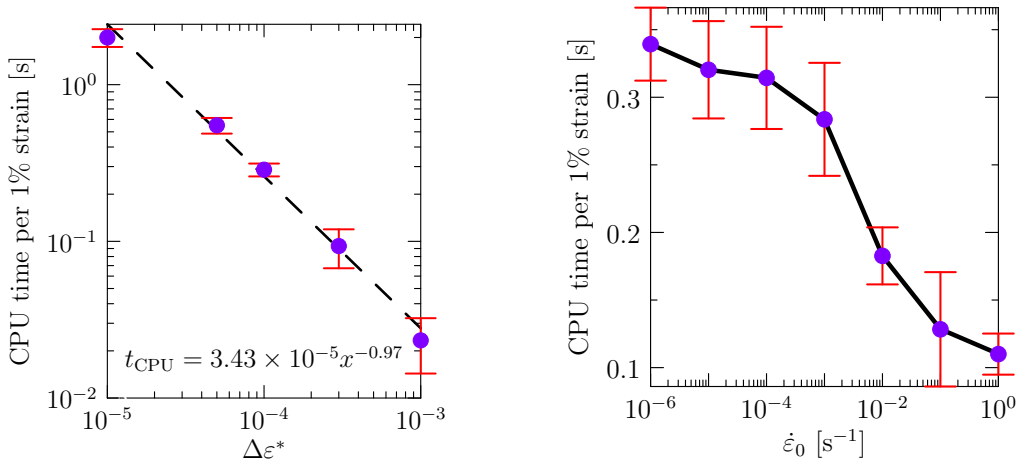

Figure 6.11: Computational cost of SCP simulations at 500 K under [101] loading. (a) CPU time per 1% strain for at 10^{-3} s^{-1} as a function of $\Delta\varepsilon^*$. A power law fit to the data is shown as a dashed line, represented by the expression $t_{\mathrm{CPU}} = 3.43 \times 10^{-5} x^{-0.97}$. (b) CPU time per 1% strain for $\Delta\varepsilon^* = 10^{-4}$ as a function of strain rate. In both cases, the error bars correspond to the variability of the results from 10 independent runs.

evolution of the system through a sequence of states with the correct probability. KMC methods require concurrent sampling of all event rates, and thus the method is suited for explicit time discretizations of the crystal plasticity equations (when $\dot{\varepsilon}_0$ and the different $\dot{\gamma}_\alpha$ are strictly independent of one another). However, this is more a technicality in the definition than a limitation in the computational sense, as the SCP approach is not constrained by the same stability considerations of standard (deterministic) methods.

The discrete nature of the method naturally leads to oscillations in the plastic response of the system. It is worth emphasizing that, while numerical in origin, these

oscillations are physical and can be ultimately linked to the discreteness of dislocation slip at the lattice level, by way of integer Burgers vector amounts. The magnitude of the oscillations is encoded in a parameter $\Delta\varepsilon^*$, which here is user-defined under certain physical restrictions (Sec. 6.2.4). A way to quantitatively interpret these oscillations may be by considering $\Delta\varepsilon^*$ to scale with the ratio b/L, where b and L are the Burgers vector's modulus and a generic specimen's dimension, respectively. In bulk materials, this ratio becomes extremely small, leading to smooth stress-strain responses as shown in Figs. 6.3 and 6.7, while for higher values of $\Delta\varepsilon^*$, a highly oscillatory behavior is seen, in accordance with what is seen in small-scale specimens such as free-standing nano-pillars or cantilever nano-beams [101, 172, 183, 407].

This, and other features of the model, including several potential advantages over standard explicit CP approaches, are further elaborated on below.

6.4.1 Physical time scale defined through $\Delta\varepsilon^*$

In Sec. 6.2.4, a parameter $\Delta\varepsilon^*$ is introduced to restrict the time steps that would naturally emanate from eq. (6.6), graphically represented in Fig. 6.2. However, a formal connection between $\Delta\varepsilon^*$ and δt^*, in eq. (6.14), was not established at the time.

A rigorous way to demonstrate this connection can be by adding an extra rate to r^n in eq. (6.6) to extend the exit rate of the system with an event that does not alter its state at a given time. This 'null' event process, which has been applied successfully in the context of parallel kMC algorithms [248, 249], is characterized by a rate r_{null} that can be used at will to 'slow' down the evolution of the system while

preserving the correct kinetics. Mathematically:

$$\frac{1}{r^n + r_{\text{null}}} < \delta t^* \tag{6.15}$$

which leads to the condition: $r_{\text{null}} > \frac{1}{\delta t^*} - r^n$. The pictorial representation of r_{null} is shown in Fig. 6.1 as an extra entry (dashed gray line) in the array. It is trivial to show that the relationship among $\Delta\varepsilon^*$, r^n, and r_{null} is:

$$\Delta\varepsilon^* = \frac{r^n}{r^n + r_{\text{null}}}$$

or, alternatively, $\Delta\epsilon^*/r^n < \delta t^*$, i.e., $\Delta\varepsilon^*$, r_{null}, and δt^* can be thought of as being interchangeable parameters. In any case, these relationships show that one can rigorously connect the mathematical representation of the system's kinetics to the physical time evolution under deformation.

6.4.2 Potential advantages of the present method over deterministic integrators

6.4.2.1 Asymmetry in slip rates with identical orientation

It is well known that from a purely geometric point view, there is a redundancy in establishing the number of active slip systems that contribute to deformation under highly-symmetric loading conditions. Mathematically, this problem of slip indeterminacy is intrinsically found in rate-independent CP formulations, and can be partially addressed by, e.g., imposing additional constraints on the internal variables or the stress space of the system [18, 117, 270]. While the non-uniqueness of the solution is no longer an issue in viscoplastic (rate-dependent) crystal plasticity models, the plastic response still displays symmetries in slip that are not observed in real materials' deformation [103, 116, 359].

The SCP model presented here offers the potential to introduce variability in the solution in a natural way, thus intrinsically enabling the possibility for non-symmetric activation of slip systems according to just the Schmid criterion. This symmetry-breaking capability emanates directly from the solver, i.e., without the need to add it externally, which means that it can lead to inhomogeneous plastic deformation naturally. This inhomogeneity emerges from the inherent stochastic treatment of the plastic shear rates, and thus may be seen as having a direct correlation to real deformation situations.

From a thermodynamic standpoint, several works have established a link between the heterogeneity of plastic deformation and the system's entropy production based on maximum-dissipation criteria [35, 415]. Indeed, stochastic approaches have the potential to access an increased number of states. While beyond the scope of the present work, it would be of interest to augment the current model by introducing quantitative metrics of entropy production directly connected to the stochastic variability and the symmetry-breaking features of the SCP model.

6.4.2.2 Numerical stability and computational cost

While the computational overhead of the SCP method has been assessed in Sec. 6.3.3 and Fig. 6.11, any meaningful discussion of the CPU cost of the SCP method must necessarily involve a comparison with a standard explicit (forward Euler) integrator for CP problems in equivalent conditions. Figure 6.12 shows the computational cost (in seconds per 1% strain) of a reference crystal plasticity problem ([101] loading direction at $\dot{\varepsilon}_0 = 10^{-3}$ s^{-1}) as a function of temperature simulated both with the SCP model using several values of $\Delta\varepsilon^*$ and a standard deterministic CP model based

on a forward Euler integrator. The numbers associated with each data point of the deterministic calculations (in blue) indicate the maximum dt attainable to maintain numerical stability[4].

There are several remarkable features that emerge from the analysis presented in the figure. We start by noting that the SCP method is intrinsically stable under all conditions, a virtue of the residence-time algorithm, while the numerical stability of the deterministic solver is highly dependent on temperature and strain rate. Second, the CPU cost of the stochastic algorithm is practically independent of temperature. Third, and most important for the purposes of this discussion, the deterministic solver's numerical stability requires increasingly smaller time steps (labeled as '$\delta t_{\max}$' in the figure) as the temperature increases. For this reason, at 600 K we see a sharp upturn in the CPU cost, which drives its computational overhead far above that of the SCP model. The fact that the algorithm samples one event per time step helps stabilize the numerical solution and allows for longer time steps at high temperature compared to a standard forward Euler approach. While it is common practice to add modifications to the Euler method to improve its stability [360,411], we consider this a very attractive potential advantage of SCP over standard explicit solvers.

We close Section 6.4.2 reiterating the potential advantages of SCP over deterministic (both explicit and implicit) approaches. One obvious advantage of using our method at all temperatures (including room temperature and below) is the added benefit of capturing plastic fluctuations naturally. Thus, in cases where those are of interest (cf. Section 6.4.2.1), our approach is useful from a physical point of view. Numerically, at low temperatures our method is consistent with the be-

[4]Here stability is guaranteed by limiting the deviation of the solution using a given time step compared to the solution using $dt = 10^{-5}$ s to no more than 10%.

havior of kinetic Monte Carlo models versus deterministic solvers in other fields of physics [219, 334, 367]. Rather than being attributable to stochastic solvers being slow, the advantages of deterministic solvers have to do more with their ability to be stable using large time steps. In general, the consensus is that for simple models (with low physical complexity) deterministic models will always outperform stochastic ones. However, as the physical model (so-called 'material model' in crystal plasticity) grows in complexity, stochastic solvers become relatively more efficient. Note that such complexity may be introduced also via the external conditions, as is the case in this work, when thermally activated mechanisms become dominant at higher temperatures.

6.5 Summary

We conclude this chapter with a list of our most important findings:

- We have developed a stochastic solver for crystal plasticity models based on the residence-time algorithm. The method strictly works for explicit problems, when the total strain rate and the individual plastic shear rates can be considered independent from one another.

- The SCP model is intrinsically numerically stable without the need of any extra procedures. Changes in the values of the external variables manifest themselves in terms of the magnitude of the oscillations of the solution, not on its stability.

- The SCP model naturally breaks the symmetry of plastic slip by sampling among the active plastic shear rates with the correct probability. This can lead to phenomena such as plastic localization without needing to add any *a*d hoc

treatments to the model.

- All variables kept the same, the computational overhead of the SCP method scales inversely with $\Delta\varepsilon^*$ (as $\sim 1/\Delta\varepsilon^*$) and $\dot{\varepsilon}_0$. The CPU cost is insensitive to temperature for the crystal plasticity model employed here.

- For a fixed prescribed total strain rate and loading direction, the SCP model becomes more efficient than a standard forward Euler approach at $T > 600$ K. It is expected that similar transitions exist for other crystal orientations and strain rates.

Algorithm 1 Residence-time algorithm for crystal plasticity models

Initialize: $\dot{\boldsymbol{\varepsilon}}_0$, T, TOL, `maxiter`, N, t_{TOT}, $t = 0$, $\{\rho^\alpha\} = \rho_0$, $\boldsymbol{q}(0, \ldots, N)$

while $(t < t_{\mathrm{TOT}})$ **do**

  Calculate: stress (tensor) increment $\Delta\boldsymbol{\sigma} = \mathbb{C} : \Delta\boldsymbol{\varepsilon}^{\mathrm{E}}$

  Update: stress tensor $\boldsymbol{\sigma} = \boldsymbol{\sigma} + \Delta\boldsymbol{\sigma}$

  Initialize: $q_0 = \dot{\varepsilon}_0$

  Get: random numbers $\xi_1,\ \xi_2 \in (0, 1]$

  for $\alpha = 1, N$ **do**

    Calculate: modulus: $b = \|\boldsymbol{b}^\alpha\|$

    Get: slip direction $\boldsymbol{s}^\alpha = b^{-1}\boldsymbol{b}^\alpha$, plane normal $\boldsymbol{n}^\alpha$

    Calculate: resolved shear stress $\tau^\alpha_{\mathrm{RSS}} = \boldsymbol{s}^\alpha \cdot \boldsymbol{\sigma} \cdot \boldsymbol{n}^\alpha$

    Initialize: $r_t = \dot{\varepsilon}_0$

    for $\beta = 1, N$ **do**

      Calculate: forest dislocation density $\rho^\alpha_f = \rho^\alpha_f + \rho^\beta |\boldsymbol{s}^\beta \cdot \boldsymbol{n}^\alpha|$.

      Calculate: forest dislocation hardening $g^\alpha = g^\alpha + \xi_{\alpha\beta}\rho^\beta |\boldsymbol{s}^\beta \cdot \boldsymbol{n}^\alpha|$

    end for

    Get: dislocation hardening $\tau^\alpha_h = \mu b \sqrt{g^\alpha + \xi_{\alpha\alpha}\rho^\alpha}$

    Calculate: $\lambda^\alpha = \left(\sqrt{\rho^\alpha_f} + \frac{1}{d_g}\right)^{-1}$

    Calculate velocity:

    if $((\lambda^\alpha - w > 0)$ **and** $(\tau^\alpha_{\mathrm{RSS}} - \tau^\alpha_h > 0))$ **then**

      $v^\alpha_0 = \mathrm{sgn}(\tau^\alpha_{\mathrm{RSS}})\nu_0 \frac{h}{b}\,(\lambda^\alpha - w)$

      $v^\alpha = v^\alpha_0 \exp\left\{-\frac{\Delta H_0}{kT}\left(1 - \left|\frac{\tau^\alpha_{\mathrm{RSS}} - \tau^\alpha_h}{\sigma_{\mathrm{P}}}\right|^p\right)^q\right\}$

    else

      $v^\alpha = 0$

    end if

Algorithm 1 (continued)

Calculate: $q_\alpha = \rho^\alpha b v^\alpha$

Calculate: $r_t = r_t + q_\alpha$

end for

Calculate: $\delta t = -\frac{\log \xi_2}{r_t}$

Update: $t = t + \delta t$

Select: event k such that $q_k < \xi_1 r_t < q_{k+1},\ k = 0, \ldots, N$

Initialize: $\Delta\boldsymbol{\varepsilon}^{\mathrm{P}} = \Delta\boldsymbol{\varepsilon}_{\mathrm{tot}} = 0$

if $\left(\xi_1 < \frac{q_0}{r_t}\right)$ **then**

Calculate: $\Delta\boldsymbol{\varepsilon}_{\mathrm{tot}} = \dot{\boldsymbol{\varepsilon}}_0 \delta t$

Update: $\boldsymbol{\varepsilon}_{\mathrm{tot}} = \boldsymbol{\varepsilon}_{\mathrm{tot}} + \Delta\boldsymbol{\varepsilon}_{\mathrm{tot}}$

else

for $\alpha = 1, N$ **do**

Update: dislocation density $\rho^\alpha = \rho^\alpha + \frac{|q_\alpha|}{\lambda^\alpha}\left(1 - 2b\lambda^\alpha \rho^\alpha\right)\frac{\delta t}{b}$

Calculate: $\Delta\boldsymbol{\varepsilon}^{\mathrm{P}} = \Delta\boldsymbol{\varepsilon}^{\mathrm{P}} + q_\alpha\left(\boldsymbol{s}^\alpha \otimes \boldsymbol{n}^\alpha\right)\delta t$

end for

end if

Calculate: $\Delta\boldsymbol{\varepsilon}^{\mathrm{E}} = \Delta\boldsymbol{\varepsilon}_{\mathrm{tot}} - \Delta\boldsymbol{\varepsilon}^{\mathrm{P}}$

end while

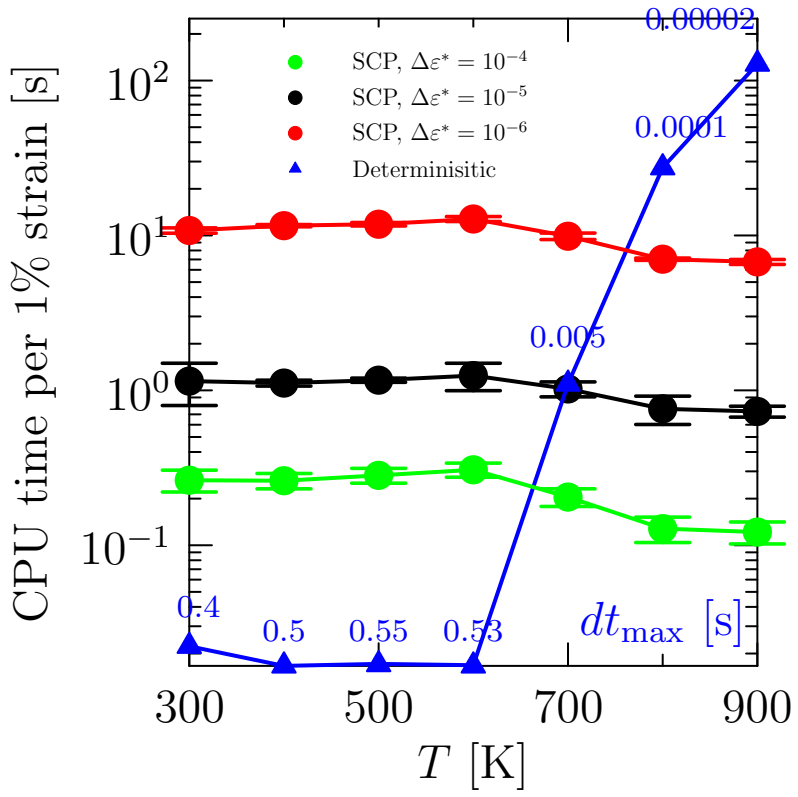

Figure 6.12: Computational overhead of a reference crystal plasticity simulation ([101] loading direction at $\dot{\varepsilon}_0 = 10^{-3}$ s^{-1}) as a function of temperature for both the SCP model and a standard CP model using an explicit forward Euler integrator (deterministic). The numbers associated with each data point of the deterministic calculations (in blue) indicate the maximum dt attainable to maintain numerical stability.

CHAPTER 7

Physics-based model of irradiation creep for ferritic materials under DEMO first-wall operation conditions

7.1 Literature Review

Irradiation creep is a very important factor in structural materials evolution in nuclear reactors [4,112,374]. In light-water reactors, both stainless steels and zirconium alloys are known to exhibit substantial irradiation creep under conditions where thermal creep is generally negligible [4, 112, 120, 134, 256, 264, 271, 306]. Irradiation effectively removes the strong temperature dependence of diffusional and power-law creep, providing defects in large amounts that activate creep mechanisms without the need for thermal assistance. As such, irradiation creep may be considered one more associated effect of irradiation damage [279, 373], rather than an accelerated version of thermal creep.

Much like its thermal counterpart at high temperatures and moderate stresses, steady state irradiation creep is mediated by coupled dislocation climb/glide processes at stresses below the elastic limit. The complexity associated with irradiated microstructures makes it difficult to isolate the governing mechanisms with

certainty, but it is believed that a variety of processes play a role during creep, all of whom are directly or indirectly associated with the preferential absorption of self-interstitial atoms (SIA) and SIA clusters by dislocations relative to that of vacancies. Among these are the mechanism known as *stress induced preferential absorption* (SIPA), *preferential absorption glide* (PAG), or *stress-induced preferential nucleation* (SIPN) [374,387]. While, these mechanisms are somewhat arbitrary in that they apportion different degrees of importance to dislocation climb and glide processes, they are all united by their common origin based on the biased absorption of SIA defects over vacancies. This bias is directly attributable to elastic forces between long-ranged dislocation elastic fields and large local distortion (high dielastic interaction) around SIA defects (including the re-orientation of SIA clusters under SIPN) [89,94]. Low dose-rate (and total dose) and low neutron energy irradiation generally permits the separation of the contributions due to these mechanisms in terms of a linear (additive) creep law. However, fusion energy brings a new paradigm by introducing doses and neutron energies several orders of magnitude larger than in conventional reactors. Under such conditions, such a *a priori* decomposition of creep mechanisms may not be sufficient or adequate.

Unfortunately, neutron energies of 14 MeV and doses in the tens of dpa (displacements per atom) are beyond the reach of existing reactors and irradiation facilities at present. Consequently, direct creep studies under fusion conditions are not currently attainable. Our lack of a fusion neutron source for advanced materials testing has been partially addressed by recurring to fast neutron flux testing reactors [67,304]. Indeed, early studies of irradiation creep in fusion energy candidate materials were carried out in fast neutron flux conditions over the period between the 1970s and 80s. A principal finding in these experiments was the confirmation of a direct correlation

between swelling and creep [102, 133, 174, 258, 385], a conclusion that solidified the viewpoint that both irradiation creep and swelling can be seen as different manifestations of the same microscopic processes that govern dislocation glide and climb in irradiated materials [374, 385]. Subsequent experiments in FFTF and BOR-60 carried out from the early 90s into the 2000s were partially aimed to understanding the effects on materials of fusion reactor-like conditions [135, 200, 351], including the effect of He and H on irradiation creep. A primary goal in these studies was to quantify the creep compliance, B_0, and creep-swelling coupling, D, coefficients in low-activation ferritic/martensitic steels to characterize a generalized steady-state creep law of the type $\epsilon_{\text{irr}} = B\phi + DS$, where ϕ is the irradiation dose and S is the amount of swelling.

While data-fitted correlations can be useful tools for reactor design, however, phenomenological models based on empirically-calibrated formulations often fail to provide a physical understanding of the main irradiation creep mechanisms. However, despite this and the large volume of experimental literature devoted to it, irradiation creep has been comparatively much less studied using physics-based modeling. To address this, starting in the 1980s several efforts were directed to develop models primarily based on a mean-field approach, including more recent ones coupling irradiation damage models to a crystal plasticity description of material deformation [251, 285, 355, 380, 388]. While these approaches have enabled the self-consistent consideration of mechanical and chemical driving forces controlling climb, creep, and swelling, no irradiation creep modeling studies yet exist for fusion reactor conditions.

An added motivation to pursue such studies is also the lack of suitable fusion neutron irradiation facilities mentioned above. Physics-based models can help bridge the gap existing between current fast neutron test reactors, heavy-ion irradiation

facilities and fusion conditions, thus helping researchers understand irradiation creep in fusion materials at a conceptual and mechanistic level. Indeed, we believe that an important aspect of such models must be a 'first-principles' definition of creep mechanisms, i.e., where creep correlations are not assumed *a priori* but derived from fundamental physical principles instead. This is the main objective of the present paper, where a stochastic defect transport method based on the mean-field approximation is integrated into a crystal plasticity model that includes slip and creep as fundamental plastic processes in an irradiated microstructure setting. Our study pertains to pure Fe as the basis for low-activation ferritic steels although without consideration of H or He effects at the moment. The paper is organized as follows. In Section 7.2 we provide a detailed description of the physical theory behind our models. The model and material parameters are all given in Section 7.3. Section 7.4 contains all the results of this work, including irradiation creep under a wide range of conditions. In Section 7.5, an extensive discussion of the simulation results is given, followed by our most important conclusions in Section 7.6.

7.2 Model Description

In this study, we again use the coupled CP/SCD model to simulate the whole irradiation/deformation processes. Although there are already much demonstrations on CP, SCD and the coupling scheme of the two in Chapter 2 and 5, the whole CP formulation needs to be upgraded with edge dislocation climb associated motions and correspondingly the variables exchanged between SCD and CP are also different from those in section 5.2. In this chapter, we first introduce the renewed CP/SCD model that captures dislocation climb-mediated creep, and then apply it to simula-

tions of irradiation creep under representative fusion (DEMO) operation conditions in Fe-based first walls.

7.2.1 Crystal plasticity model

7.2.1.1 Kinematics

For a deformable body occupying a volume Ω_0 bounded by a surface $\partial\Omega_0$, a one-to-one mapping $\boldsymbol{x}(\boldsymbol{X}, t)$ is assumed to exist between the position of material points in their reference position $\boldsymbol{X}$ and their current position $\boldsymbol{x}$. The deformation gradient of this mapping, $\boldsymbol{F} = \partial\boldsymbol{x}/\partial\boldsymbol{X}$ is typically decomposed multiplicatively into plastic and elastic contributions, $\boldsymbol{F}^{\mathrm{P}}$ and $\boldsymbol{F}^{\mathrm{E}}$ as [211]:

$$\boldsymbol{F} = \boldsymbol{F}^{\mathrm{E}}\boldsymbol{F}^{\mathrm{P}} = \boldsymbol{I} + \nabla \otimes \boldsymbol{u} \tag{7.1}$$

where $\boldsymbol{u}$ is the displacement vector. The rate of change of $\boldsymbol{F}$ can be written as:

$$\dot{\boldsymbol{F}} = \frac{\partial \dot{\boldsymbol{x}}}{\partial \boldsymbol{X}} = \frac{\partial \dot{\boldsymbol{x}}}{\partial \boldsymbol{x}} \frac{\partial \boldsymbol{x}}{\partial \boldsymbol{X}} = \boldsymbol{L}\boldsymbol{F} \tag{7.2}$$

where $\boldsymbol{L}$ is the velocity gradient. $\boldsymbol{L}$ additively decomposes into:

$$\boldsymbol{L} = \dot{\boldsymbol{F}}^{\mathrm{E}}\boldsymbol{F}^{\mathrm{E}-1} + \boldsymbol{F}^{\mathrm{E}}\left(\dot{\boldsymbol{F}}^{\mathrm{P}}\boldsymbol{F}^{\mathrm{P}-1}\right)\boldsymbol{F}^{\mathrm{E}-1} = \boldsymbol{L}^{\mathrm{E}} + \boldsymbol{L}^{\mathrm{P}} \tag{7.3}$$

where $\boldsymbol{L}^{\mathrm{E}}$ and $\boldsymbol{L}^{\mathrm{P}}$ are the elastic and plastic velocity gradients, respectively. In the small deformation limit (linearized kinematics), the total strain, $\boldsymbol{\varepsilon}_{\mathrm{t}} = \nabla \otimes \boldsymbol{u}$, can be defined as:

$$\nabla \otimes \boldsymbol{u} = \boldsymbol{H}^{\mathrm{E}} + \boldsymbol{H}^{\mathrm{P}} \tag{7.4}$$

where $\boldsymbol{H}^{\mathrm{E}}$ and $\boldsymbol{H}^{\mathrm{P}}$ are the elastic and plastic *distortions*, i.e., $\boldsymbol{L}^{\mathrm{E}} = \dot{\boldsymbol{H}}^{\mathrm{E}}$ and $\boldsymbol{L}^{\mathrm{P}} = \dot{\boldsymbol{H}}^{\mathrm{P}}$. The present model captures contributions to plastic deformation from

dislocation slip and climb as:

$$\dot{\boldsymbol{H}}^{\mathrm{P}} = \sum_{\alpha} \left[\dot{\boldsymbol{\varepsilon}}^{\alpha}_{\mathrm{slip}} + \dot{\boldsymbol{\varepsilon}}^{\alpha}_{\mathrm{climb}} \right] \tag{7.5}$$

$$\dot{\boldsymbol{\varepsilon}}^{\alpha}_{\mathrm{slip}} = \dot{\gamma}^{\alpha} \left(\boldsymbol{s}^{\alpha} \otimes \boldsymbol{n}^{\alpha} \right) \tag{7.6}$$

$$\dot{\boldsymbol{\varepsilon}}^{\alpha}_{\mathrm{climb}} = \dot{\beta}^{\alpha} \left(\boldsymbol{s}^{\alpha} \otimes \boldsymbol{s}^{\alpha} \right) \tag{7.7}$$

$\dot{\gamma}^{\alpha}$ denotes the plastic slip rate of slip system α, $\boldsymbol{s}^{\alpha}$ and $\boldsymbol{n}^{\alpha}$ represent the corresponding slip and plane normal directions expressed in the original frame of reference, and $(\boldsymbol{s}^{\alpha} \otimes \boldsymbol{n}^{\alpha})$ is the *Schmid* tensor. For its part, $\dot{\beta}^{\alpha}$ represents the climb rate and $(\boldsymbol{s}^{\alpha} \otimes \boldsymbol{s}^{\alpha})$ is the climb projection tensor [140, 254, 405]. All sums with the α index are assumed to run up to the total number of slip systems in the material, N_{α}.

For cubic crystals one can define a fourth-order symmetric tensor $\mathbb{C}$ defined by just three independent elastic constants E, μ, and ν (respectively, the Young's modulus, the shear modulus, and the Poisson ratio). Further, under linear elastic assumptions, the Cauchy stress can be expressed as a function of the elastic strain as:

$$\boldsymbol{\sigma} = \mathbb{C} : \boldsymbol{H}^{\mathrm{E}} = \mathbb{C} : \boldsymbol{\varepsilon}^{\mathrm{E}} \tag{7.8}$$

Assuming an instantaneous elastic response, the rate form of eq. (7.8) is:

$$\dot{\boldsymbol{\sigma}} = \mathbb{C} : \dot{\boldsymbol{\varepsilon}}^{\mathrm{E}} \tag{7.9}$$

where $\boldsymbol{\varepsilon}^{\mathrm{E}}$ is the symmetric part of $\boldsymbol{H}^{\mathrm{E}}$,

Creep conditions are generally prescribed by imposing a constant stress tensor $\boldsymbol{\sigma}_0$ uniformly in Ω_0. From eqs. (7.3) and (7.9), this results in the trivial condition:

$$\boldsymbol{L} = \dot{\boldsymbol{H}}^{\mathrm{P}}$$

i.e.,

$$\boldsymbol{\varepsilon}_{\mathrm{t}} = \mathbb{S} : \boldsymbol{\sigma}_0 + \boldsymbol{H}^{\mathrm{P}} \tag{7.10}$$

where $\mathbb{S} = \mathbb{C}^{-1}$ is the *compliance* tensor.

7.2.1.2 Flow rule

The present CP model separates the total dislocation density into screw and edge dislocation contributions[1]. The shear rates $\dot{\gamma}^\alpha$ in eq. (7.6) are computed according to Orowan's equation:

$$\dot{\gamma}^\alpha = b^\alpha \left(\rho_{\mathrm{s}}^\alpha v_{\mathrm{s}}^\alpha + \rho_{\mathrm{e}}^\alpha v_{\mathrm{e}}^\alpha\right) \tag{7.11}$$

where b^α is the Burger's vector modulus, ρ_{s}^α and ρ_{e}^α are the screw and edge dislocation densities in slip system α, and v_{s}^α and v_{e}^α are the corresponding dislocation velocities. Here, we consider bcc metals with only $\frac{1}{2}\langle 111\rangle$-type dislocations, i.e., there is only one Burgers vector with $b = a_0\sqrt{3}/2$, where a_0 the lattice parameter. Screw dislocation glide is assumed to be thermally activated according to the following expression [57, 337]:

$$v_{\mathrm{s}}^\alpha = \begin{cases} \dfrac{\nu_0 h\left(\lambda^\alpha - w\right)}{b} \exp\left(-\dfrac{\Delta H_0}{kT}\left[1 - \left(\dfrac{\Delta\tau^\alpha}{\sigma_{\mathrm{P}}}\right)^p\right]^q\right), & \lambda^\alpha > w \\ 0, & \lambda^\alpha \leqslant w \end{cases} \tag{7.12}$$

where ν_0, h, λ^α, w, and ΔH_0 are, respectively, the attempt frequency, the distance between Peierls valleys in the bcc lattice, the mean dislocation segment length for slip system α, the kink-pair width, and the kink-pair formation energy. σ_{P} is the Peierls stress. Ordinarily, slip due to edge dislocation glide is governed by a viscous law described by a linear dependence on stress.

$$v_{\mathrm{e}}^\alpha = \frac{b\Delta\tau^\alpha}{\Gamma}, \quad \Delta\tau^\alpha > 0 \tag{7.13}$$

[1] Or, more precisely, into pure screw and non-screw dislocation subpopulations.

where Γ is a temperature-dependent viscosity constant.

In equations (7.12) and (7.13), $\Delta\tau^\alpha$ is the *e*xcess stress, obtained as the difference between the *resolved shear stress* (RSS) and the slip resistance, g^α, i.e., $\Delta\tau^\alpha = \tau^\alpha_{\text{RSS}} - g^\alpha$. The RSS is obtained from the Cauchy stress as:

$$\tau^\alpha_{\text{RSS}} = \boldsymbol{\sigma} : (\boldsymbol{s}^\alpha \otimes \boldsymbol{n}^\alpha) \tag{7.14}$$

which is also known as the Schmid stress[2], while g^α includes all *a*thermal sources of stress opposing dislocation motion.

For its part, $\dot{\beta}^\alpha$ in eq. (7.7) is due solely to edge dislocation climb:

$$\dot{\beta}^\alpha = b^\alpha \rho^\alpha_{\text{e}} v^\alpha_{\text{climb}} \tag{7.15}$$

When climb is operational, however, eq. (7.13) must be modified to account for the possibility of climb-assisted obstacle bypassing even when τ^α_{RSS} is smaller than the resistance stress g^α. In such situations, edge dislocations may glide unimpeded from obstacle to obstacle but then must climb over them in order to continue their motion. This process is characterized by an effective glide velocity $\bar{v}^\alpha_{\text{e}}$, derived in F (eq. (F.4)):

$$\bar{v}^\alpha_{\text{e}} = \frac{b\tau^\alpha_{\text{RSS}} \left(\lambda^\alpha + 2\Delta_{\text{obs}}\right) v^\alpha_{\text{climb}}}{\Gamma v^\alpha_{\text{climb}} \left(\lambda^\alpha + 2\Delta_{\text{obs}}\right) + b\tau^\alpha_{\text{RSS}}\Delta_{\text{obs}}}$$

where Δ_{obs} is a characteristic obstacle size. In this work, the climb velocity, v^α_{climb}, depends on the defect absorption rates during irradiation. The rest of the parameters are defined in Sec. 7.2.2.

With both glide options available –direct glide or climb-assisted glide–, edge

[2]Although present in bcc materials [57, 95, 286], here we ignore non-Schmid effects.

dislocations move at a velocity given by:

$$v_{\mathrm{e}}^{\alpha} = \begin{cases} \frac{b\Delta\tau^{\alpha}}{\Gamma}, & \Delta\tau^{\alpha} > 0 \\ \bar{v}_{\mathrm{e}}^{\alpha}, & \Delta\tau^{\alpha} \leqslant 0 \end{cases} \tag{7.16}$$

7.2.1.3 Dislocation density evolution model

In general, a minimal model of crystal deformation by glide and climb requires four types of dislocation densities: positive/negative edge dislocations, and positive/negative screw dislocations for each slip system [19]. For simplicity, in this work the net polarity of the total dislocation density is ignored, so the densities of positive and negative dislocations of edge and screw type are considered to be always balanced (i.e., $\rho_{\mathrm{e,s}}^{-} = \rho_{\mathrm{e,s}}^{+} = 1/2\ \rho_{\mathrm{e,s}}$). After, Yuan et al. [405], we use the following evolution equation for ρ_{s}:

$$\dot{\rho}_{\mathrm{s}}^{\alpha} = \frac{2\rho_{\mathrm{e}}^{\alpha}}{\lambda^{\alpha}}|v_{\mathrm{e}}^{\alpha}| - \frac{b\left(\rho_{\mathrm{s}}^{\alpha}\right)^{2}}{4}|v_{\mathrm{s}}^{\alpha}| \tag{7.17}$$

where λ^{α} is the available dislocation segment length, which is generally expressed as:

$$\frac{1}{\lambda^{\alpha}} = \frac{1}{d_g} + \frac{1}{d_{\mathrm{irr}}} + \sqrt{\rho_f^{\alpha}} \tag{7.18}$$

where d_g is the grain size and ρ_f^{α} is the *forest* dislocation density, which is obtained for each slip system α from contributions from all other systems κ [19]

$$\rho_f^{\alpha} = 2\sum_{\kappa\neq\alpha}\left(\rho_{\mathrm{e}}^{\kappa}\left|\boldsymbol{n}^{\alpha}\cdot\left(\boldsymbol{s}^{\kappa}\times\boldsymbol{n}^{\kappa}\right)\right| + \rho_{\mathrm{s}}^{\kappa}\left|\boldsymbol{n}^{\alpha}\cdot\boldsymbol{s}^{\kappa}\right|\right) \tag{7.19}$$

The first term in eq. (7.17) reflects the formation of screw dislocation dipoles when edge dislocations curve around obstacles separated by a distance λ^{α} during plastic flow. By contrast, the second term is quadratic in $\rho_{\mathrm{s}}^{\alpha}$ reflecting dislocation removal

due to mutual annihilation of canceling segments. For its part, ρ_{e} increases owing to the formation of curved segments around dislocation obstacles that merge into the network before closing into Orowan loops (known as *areal glide* model [196,297]). As in eq. (7.20), edge dislocations are removed due to the canceling of opposite-Burgers vector segments via glide (same glide plane) and/or climb (different glide plane):

$$\dot{\rho}_{\mathrm{e}}^{\alpha} = \frac{\sqrt{\rho_{\mathrm{e}}^{\alpha}}}{\lambda^{\alpha} b} |v_{\mathrm{e}}^{\alpha}| - \left(\rho_{\mathrm{e}}^{\alpha}\right)^{2} b \left(|v_{\mathrm{e}}^{\alpha}| + |v_{\mathrm{climb}}^{\alpha}|\right) \tag{7.20}$$

In both equations, the edge dislocation velocity is defined as $v_{\mathrm{e}}^{\alpha} = b\Delta\tau^{\alpha}/\Gamma$ when $\Delta\tau^{\alpha} > 0$. Under irradiation, the absorption of prismatic loops by dislocations results in direct dislocation density increases due to the formation of helical turns (by screw dislocations) or multiply-jogged segments in edge dislocations. As discussed by Was [374], this is the main mechanism behind *preferred absorption glide* (PAG) [237], which in reality is another manifestation of SIPA, but with a direct impact on glide rather than climb. This source term will be discussed and added to the dislocation density evolution equations in Section 7.2.2.1.

To close the model, an expression for g^{α} must be provided. In the present case, we consider forest hardening, τ_h^{α}, and irradiation hardening, τ_{irr}, i.e.:

$$g^{\alpha} = \tau_h^{\alpha} + \tau_{\mathrm{irr}}$$

with:

$$\tau_h^{\alpha} = \mu b \sqrt{2 \left(\sum_{\kappa \neq \alpha} \xi_{\alpha\kappa} \ \rho^{\kappa} + \xi_{\alpha\alpha} \rho^{\alpha} \right)} \tag{7.21}$$

$$\tau_{\mathrm{irr}} = \frac{\mu b}{d_{\mathrm{irr}}} \tag{7.22}$$

The first term inside the square root on the r.h.s. in eq. (7.21) represents the amount of latent hardening, while the second one reflects the amount of self-hardening. $\xi_{\alpha\beta}$

are the elements of the hardening coefficient matrix, $\boldsymbol{\xi}$ [57, 118, 119], whose values, as well as the glide systems considered in the work, are given in Tables B.1 and A.1. Here we focus on single crystals, when the term $1/d_g$ vanishes. The calculation of d_{irr} will be discussed in Section 7.2.2.1.

7.2.2 CP/SCD coupling

We still use the SCD method to simulate the microstructure evolution procedure. The coupling between the SCD and CP approaches is bidirectional, with information in terms of state variable updates being passed from one to the other and both advancing in lockstep. This section discusses the details of the coupling in both directions.

7.2.2.1 SCD→CP

During the course of a SCD simulation step, the variables $\bar{r}$, used in eq. (7.16), d_{irr}, in eqs. (7.18) and (7.22), and $v^{\alpha}_{\text{climb}}$, in eqs. (7.15), (7.16), and (7.20) are computed (updated) and passed to the CP module. The mean obstacle spacing d_{irr} is computed assuming a dispersed-barrier hardening model for irradiation defect clusters [204,391, 401]:

$$\frac{1}{d_{\text{irr}}} = \sum_i \eta_i \sqrt{\frac{N_i^{\text{im}} r_i}{\Omega}} \tag{7.23}$$

where N_i^{im} is the subset of immobile species among all N_i, η_i is a dimensionless coefficient representing the strength of dislocation-defects interactions, and r_i is the size of the defects (assumed to be represented by the radius of disc-like SIA clusters or spheres for vacancy clusters, precipitates, and gas bubbles). Determinations about the mobility of the defects are made on the basis of the defects' nature and size. Only

vacancy clusters with less than three vacancies and SIA clusters with less than 10 self-interstitials are considered mobile. For the coefficients η_i we simply use 0.2 for SIA clusters and loops and 0.6 for vacancy clusters and voids [176]. The characteristic defect cluster size $\bar{r}$ is obtained as the weighted average size of the immobile species:

$$\bar{r} = \frac{\sum_i N_i^{\mathrm{im}} r_i}{\sum_i N_i^{\mathrm{im}}} \tag{7.24}$$

In an irradiation setting, climb is mediated by point defect production and migration to dislocations. Vacancies and self-interstitial atoms have opposite effects on climb and thus it is the excess point defect concentration absorbed at dislocations that determines the direction and rate of climb. Here, we make the assumption that point defects are uniformly absorbed along edge dislocation lines. With this, the climb velocity is linked to the number of point defects absorbed by the total dislocation network per unit time, $\dot{N}_{abs}$, as:

$$v_{\mathrm{climb}}^{\alpha} = \left(\frac{\dot{N}_{abs}}{b\ \rho_{\mathrm{tot}}}\right)\left(\frac{\Omega_a}{\Omega}\right)\left(\frac{\rho_{\mathrm{e}}^{\alpha}}{\rho_{\mathrm{tot}}}\right) \tag{7.25}$$

where Ω_a is the atomic volume. The first term in parentheses in the above equation represents the excess defect concentration absorbed per unit dislocation length, the second gives the number of lattice sites in the simulation volume, and the third is the fraction of defect absorptions assigned to each slip system. During a time interval δt, $\dot{N}^{abs}$ is approximated by

$$\dot{N}_{abs} \approx \frac{\delta N_{abs}}{\delta t} = \frac{N_{abs}(t+\delta t) - N_{abs}(t)}{\delta t} \tag{7.26}$$

In actuality, N_{abs} represents the net imbalance between defects of self-interstitial and of vacancy type (in that order). The absorption rate for a defect cluster N_i of SIA or vacancy character designated by the superindex x (x='V', 'SIA') is:

$$\dot{N}_{abs}^{x} = \sum_i S_d^x D_i^x N_i^x = \rho_{\mathrm{e}} \sum_i Z_d^x D_i^x N_i^x \tag{7.27}$$

where $\rho_{\mathrm{e}} = \sum_{\beta} \rho_{\mathrm{e}}^{\beta}$. As indicated in Sec. 2.1.3, the sink strength is characterized by a bias factor Z_d^x that reflects the higher propensity of dislocations to absorb interstitials compared to vacancies. These factors can be modified to capture SIPA (see Sec. 7.1) by introducing a stress dependence that reflects this preferential absorption. While a number of different models of SIPA exist [51, 311, 382–384, 387], here we use the compact expression proposed by Kuramoto for bcc Fe based on matching elasticity theory with atomistic results [207]:

$$Z_d^{\mathrm{SIA}}(\boldsymbol{\sigma}_0) = Z_0^{\mathrm{SIA}} \left(1 + 1.6 \times 10^{-3}\ \mathrm{Tr}\left(\boldsymbol{\sigma}_0\right)\right) \tag{7.28}$$

where the stress is expressed in MPa. By contrast, the value of Z_d^{V} is kept unchanged. In this work, only mono-, di-, and tri-interstitial and vacancy clusters contribute to climb. As indicated in Section 7.2.1.3, when mobile clusters with more than three defects (I_4 and above) are absorbed directly into dislocation lines, the dislocation network experiences a net length density increase in a time interval δt quantified by the term:

$$\delta\rho_{\mathrm{e}}^{+\mathrm{irr}} = \delta\rho_{\mathrm{s}}^{+\mathrm{irr}} = \frac{1}{2\Omega} \sum_j 2\pi r_j^{abs} \tag{7.29}$$

where

$$r_j = \sqrt{\frac{n_j \Omega_a}{\pi b}}$$

and n_j is the number of SIA atoms forming part of the absorbed cluster (e.g., $n = 4$, for a I_4 cluster). The sum in eq. (7.29) runs over all SIA clusters, N_j, with $n > 3$ absorbed in a time interval δt. With this, during irradiation, eqs. (7.17) and (7.20) become:

$$\dot{\rho}_{\mathrm{s}}^{\alpha} = \left[\frac{\dot{\rho}_{\mathrm{s}}^{+\mathrm{irr}}}{N_\alpha} + \frac{2\rho_{\mathrm{e}}^{\alpha}}{\lambda^{\alpha}} |v_{\mathrm{e}}^{\alpha}|\right] - \frac{b\left(\rho_{\mathrm{s}}^{\alpha}\right)^2}{4} |v_{\mathrm{s}}^{\alpha}| \tag{7.30}$$

$$\dot{\rho}_{\mathrm{e}}^{\alpha} = \left[\frac{\dot{\rho}_{\mathrm{e}}^{+\mathrm{irr}}}{N_\alpha} + \frac{\sqrt{\rho_{\mathrm{e}}^{\alpha}}}{\lambda^{\alpha} b} |v_{\mathrm{e}}^{\alpha}|\right] - b\left(\rho_{\mathrm{e}}^{\alpha}\right)^2 \left(|v_{\mathrm{e}}^{\alpha}| + |v_{\mathrm{climb}}^{\alpha}|\right) \tag{7.31}$$

where $\dot{\rho}_{\mathrm{s,e}}^{+\mathrm{irr}} = \delta\rho_{\mathrm{s,e}}^{+\mathrm{irr}}/\delta t$. By the definition given in the above equations, the climb velocity and the dislocation evolution model are directly connected to the applied stress and to irradiation defect production.

7.2.2.2 CP→SCD

After the crystal plasticity update, the total dislocation density is calculated as:

$$\rho_{\mathrm{tot}} = 2\sum_{\alpha}(\rho_{\mathrm{e}}^{\alpha} + \rho_{\mathrm{s}}^{\alpha})$$

which is then transferred to SCD as the updated sink strength for defect absorption, $S_d \equiv \rho_{\mathrm{tot}}$. In this fashion, defect production, dislocation multiplication and hardening are all linked during the course of a simulation iteration. The numerical algorithm employed to integrate the time evolution of the state variables $\boldsymbol{H}^{\mathrm{P}}$, $\boldsymbol{\varepsilon}_{\mathrm{t}}$, and the set of $\{N_i\}$ for the coupled CP-SCD model is provided in G.

7.2.3 Mathematical definition of swelling and creep strain

Swelling and creep are nothing more than hydrostatic and deviatoric manifestations of the total plastic strain tensor $\boldsymbol{H}^{\mathrm{P}}$. Each of these is expressed as:

$$\boldsymbol{H}^{\mathrm{P}} = \boldsymbol{H}_{\mathrm{hyd}}^{\mathrm{P}} + \boldsymbol{H}_{\mathrm{dev}}^{\mathrm{P}} \tag{7.32}$$

where

$$\boldsymbol{H}^{\mathrm{P}}_{\mathrm{hyd}} = \begin{pmatrix} \frac{\mathrm{Tr}\left(\boldsymbol{H}^{\mathrm{P}}\right)}{3} & 0 & 0 \\ 0 & \frac{\mathrm{Tr}\left(\boldsymbol{H}^{\mathrm{P}}\right)}{3} & 0 \\ 0 & 0 & \frac{\mathrm{Tr}\left(\boldsymbol{H}^{\mathrm{P}}\right)}{3} \end{pmatrix} \tag{7.33}$$

$$\boldsymbol{H}^{\mathrm{P}}_{\mathrm{dev}} = \begin{pmatrix} H^{\mathrm{P}}_{xx} - \frac{\mathrm{Tr}\left(\boldsymbol{H}^{\mathrm{P}}\right)}{3} & H^{\mathrm{P}}_{xy} & H^{\mathrm{P}}_{xz} \\ H^{\mathrm{P}}_{yx} & H^{\mathrm{P}}_{yy} - \frac{\mathrm{Tr}\left(\boldsymbol{H}^{\mathrm{P}}\right)}{3} & H^{\mathrm{P}}_{yz} \\ H^{\mathrm{P}}_{zx} & H^{\mathrm{P}}_{zx} & H^{\mathrm{P}}_{zz} - \frac{\mathrm{Tr}\left(\boldsymbol{H}^{\mathrm{P}}\right)}{3} \end{pmatrix} \tag{7.34}$$

where $\mathrm{Tr}\left(\boldsymbol{H}^{\mathrm{P}}\right) = H^{\mathrm{P}}_{kk}$ (Einstein notation used). Swelling and creep are taken as scalar invariants of the above tensors, the volumetric strain θ for swelling, and the von Mises effective strain ϵ_{eff} for creep. Both of the metrics correspond to inelastic deformations, i.e., irreversible changes in the volume and shape of the material.

In the general case of finite deformations, the volumetric strain is obtained as:

$$\theta = \left(1 + H^{\mathrm{P}}_{xx}\right)\left(1 + H^{\mathrm{P}}_{yy}\right)\left(1 + H^{\mathrm{P}}_{zz}\right) - 1 = \det\left(\boldsymbol{F}^{\mathrm{P}}\right) \tag{7.35}$$

However, in the small deformation limit, θ is directly equal to $\mathrm{Tr}\left(\boldsymbol{H}^{\mathrm{P}}\right) = H^{\mathrm{P}}_{xx} + H^{\mathrm{P}}_{yy} + H^{\mathrm{P}}_{zz}$, from which the amount of swelling can be obtained. For its part, the effective strain is obtained as [92].

$$\epsilon_{\mathrm{eff}} = \sqrt{\frac{2}{3}\boldsymbol{H}^{\mathrm{P}}_{\mathrm{dev}} : \boldsymbol{H}^{\mathrm{P}}_{\mathrm{dev}}} \tag{7.36}$$

Note that ϵ_{eff} may generally contain contributions from pure dislocation slip as well as creep. The distinction made here is that creep is the umbrella term used to refer to inelastic deformation at stresses below the corresponding yield stress, regardless of its source.

In the foregoing we use the variables $S \equiv \theta$ and $\epsilon_{\mathrm{cr}} \equiv \epsilon_{\mathrm{eff}}$ as defined above to refer to the amount of swelling and creep, respectively.

7.3 Model inputs and material parameters

In this work, we study irradiation creep in Fe under neutron irradiation conditions representative of a DEMO helium-cooled pebble bed first wall (FW) as described by Gilbert et al. [143]. The equivalent NRT dose rate is 2.91×10^{-7} dpa/s. Neutron damage cross section databases are used to extract the primary knock-on atom (PKA) energy distribution in Fe from the corresponding neutron energy spectrum at the FW. In the current example, recoils are introduced at a rate of $r_{\mathrm{PKA}} = 4.33 \times 10^{14}$ s^{-1} cm^{-3} with energies E_{PKA} sampled from the cumulative PKA distribution function ($c$pdf) provided in Fig. 7.1. This $c$pdf is characterized by a mean PKA energy of 20 keV [144]. Following Malerba [234], each PKA generates a number of Frenkel pairs established by the correlation:

$$N_{\mathrm{FP}} = \eta \frac{0.8 E_{\mathrm{PKA}}}{2 E_{\mathrm{th}}} \tag{7.37}$$

where N_{FP} is an integer number, η is a defect survival efficiency, and $E_{\mathrm{th}} \approx 40$ eV is a threshold displacement energy. η is seen to be a decreasing function of PKA energy, Based on Malerba's data compilation in ref. [234], we use the following correlation:

$$\eta = 0.75 \left(\exp\left(-0.3 E_{\mathrm{PKA}} \right) + 0.4 \right) \tag{7.38}$$

which sets η close to 100% for very low PKA energies, declining to a saturation value of $\eta \approx 30\%$ above $E_{\mathrm{PKA}} > 5$ keV. Note that the condition $N_{\mathrm{FP}} > 1$ is not always met upon sampling the $c$pdf, which results in no damage being inserted[3].

For recoil impacts with $N_{\mathrm{FP}} > 2$, defects are generated as determined by the

[3]However, time is advanced regardless of the value of N_{FP}.

corresponding clustering fractions for SIA and vacancies, respectively [234]:

$$f_c^{\mathrm{SIA}} = 0.226 + 0.0319 E_{\mathrm{PKA}}$$

$$f_c^{\mathrm{V}} = 0.011 \ln\left(E_{\mathrm{PKA}}\right) + 0.2$$

where E_{PKA} is given in keV. The combination of the above equations defines the source term $\tilde{g}_i$ in the system of eqs. (2.2). The rest of the parameters and material

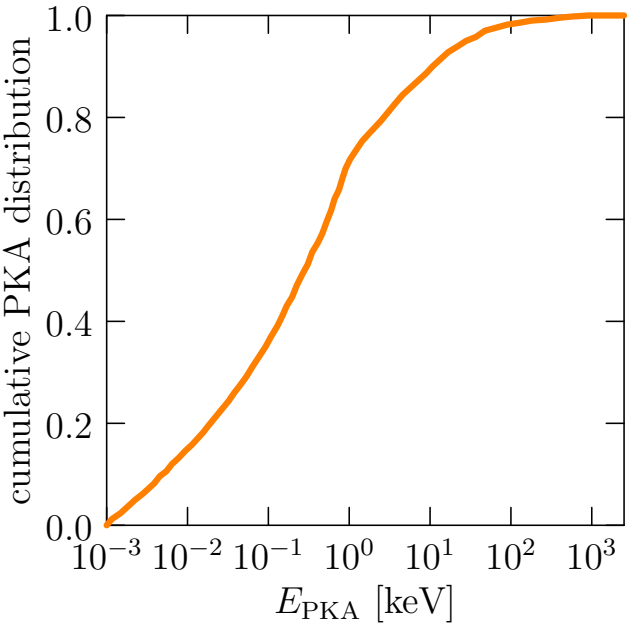

Figure 7.1: Cumulative PKA distributions for Fe under the DEMO hcpb FW conditions, reproduced after [143].

constants used in this work are given in Tables 7.1 and 7.2.

7.4 Results

All simulations presented here have been done for single crystal Fe under [001] crystallographic loading. Each case has been run up to 15 dpa, corresponding to 1.6

Table 7.1: Material and simulation parameters employed in this work [239, 267, 342].

Fe material parameters:	Symbol	Value	Units
Lattice parameter	a_0	2.9	[Å]
Atomic density	ρ_a	2.0	$[a_0^{-3}]$
Atomic volume	Ω_a	ρ_a^{-1}	$[a_0^3]$
Magnitude of Burgers vector	b	$\sqrt{3}/2$	$[a_0]$
Kink height	h	$\sqrt{\frac{3}{2}}$	$[a_0]$
Kink pair separation	w	11	$[b]$
Activation enthalpy at 0 K	ΔH_0	0.57	[eV]
Kocks-Ashby-Argon exponents	$p,\ q$	0.67, 1.18	[-]
Peierls barrier	σ_P	1.04	[GPa]
Shear modulus	μ	78	[GPa]
Young's modulus	E	204	[GPa]
Poisson's ratio	ν	0.29	[-]
Attempt frequenct	ν_0	10^{11}	$[\mathrm{s}^{-1}]$
Vacancy formation energy	E_f^{V}	1.7	[eV]
SIA formation energy	E_f^{SIA}	3.8	[eV]
Viscosity constant	Γ	$6.7 \times 10^{-7} T$	[Pa·s]
Initial total dislocation density	ρ_0	10^{14}	$[\mathrm{m}^{-2}]$
Neutron dose rate	$\dot{\phi}$	2.91×10^{-7}	[dpa/s]

Table 7.2: Migration energies (in eV) of vacancy and SIA clusters used in this work [239]. Vacancy clusters larger than V_3 are considered immobile.

n	SIA defects	Vacancy defects
1	0.25	0.60
2	0.36	0.66
3	0.14	0.66
4	0.15	–
>4	$0.06 + 0.07n^{-1.3}$	

years of DEMO operation. This amounts to about 50 million CP/SCD iterations, taking about 10 full days of CPU time.

7.4.1 Creep and swelling of simulated neutron irradiated Fe

We first present the evolution of the accumulated creep and the creep rate as a function of all the variables considered in this study. This constitutes our 'raw' data from which all correlations will be extracted. We choose to plot the results as a function of dose in Figures 7.2a to 7.2c for the creep strain and 7.2d to 7.2f for the creep rates. The simulations cover four temperatures, 300, 450, 600, and 800 K, and four stress points, 0, 100, 200, and 300 MPa. However, the behavior of the creep strain and the creep rate at 800 K is virtually identical to that at 600 K and it is not shown in the figures for compactness. The figures also show a shaded band around each curve representing the standard deviation obtained from five statistically independent runs for each condition. Likewise, the swelling and swelling rate as a function of accumulated dose are shown in Figures 7.2g to 7.2i and 7.2j to 7.2l.

In terms of the accumulated creep strain shown in Figs. 7.2a to 7.2c, a monotonically-increasing dependence with dose is observed in all cases, well represented by a concave function of dose. Here, stress has a noticeable effect on the curves at all temperatures (this will be analyzed further below). After 15 dpa of irradiation, the creep strain reaches values close to or exceeding 0.02 % at low temperatures (300 and 450 K), and 0.001 % at 600 and 800 K. A transition from what could be construed as primary (transient) creep to secondary (steady-state) can be appreciated in all cases. The dose at which this transition takes place varies with stress and temperature but it takes place at doses no less than 3 dpa in all cases. This is best appreciated in the creep rate curves, discussed next.

At 300 and 450 K (Figs. 7.2d to 7.2f), the creep rates at zero stress are seen to follow a rapid drop from approximately 10^{-5} %/s upon the onset of irradiation to 10^{-6} %/s at 6 dpa, or at 3 dpa for the other stresses. After these dose levels, the creep rates suffer a slow decline to values ranging from 10^{-8} %/s at 0 MPa to 10^{-7} %/s at 100, 200, and 300 MPa. At 600 and 800 K, the qualitative behavior displayed by the creep rates is equivalent to that at lower temperatures, except that their calculated values are reduced by roughly one order of magnitude. In all cases, there is a sharp increase from 0 to 100 MPa, while a much more moderated dependence on stress is seen afterwards.

Broadly speaking, the swelling levels and swelling rates calculated in Figs. 7.2g to 7.2i and 7.2j to 7.2l qualitatively behave in a similar manner to their creep counterparts, with similar rates although with a weaker stress response. Swelling levels are very small, reaching less than 0.01 percent at the lowest temperatures and the highest stresses after 15 dpa of neutron exposure. Unlike for creep, swelling rates display no appreciable stress dependence, ranging between 10^{-8} to 10^{-7} %/s.

7.4.2 Dependence of creep and swelling rates on stress

Plotting the steady-state $\dot{\epsilon}_{\text{cr}}$ and $\dot{S}$ data as a function of stress leads to the graphs given in Figure 7.3. We then fit each temperature data in Fig. 7.3a to a standard power law of the type

$$\dot{\epsilon}_{\text{cr}} = B\sigma^m \tag{7.39}$$

and tabulate the results for the creep compliance B and the stress exponent m in Table 7.3.

Table 7.3: Fitting coefficients for power law fits to the $\dot{\epsilon}_{\text{eff}}$-$\sigma$ data in Fig. 7.3a. The units of B are such that $\dot{\epsilon}_{\text{cr}}$ is given in %/s when the stress is in MPa.

T [K]	B [% s^{-1} MPa^{-m}]	m
300	3.02×10^{-8}	0.20
450	1.74×10^{-8}	0.18
600	6.1×10^{-9}	0.13
800	5.12×10^{-9}	0.17

B is only moderately temperature-dependent, as seen from the values in the table (B varies by a factor of six in the $300 < T < 800$ temperature interval). The temperature dependence of B is adequately captured by an exponential expression,

$$B(T) = B_0 \exp\left(-B_1 T\right)$$

with $B_0 = 8.6 \times 10^{-8}$ [% s^{-1} MPa^{-m}] and $B_1 = 0.004$ [K^{-1}]. The data points and the fit are shown in Figure 7.4.

For its part, the swelling rate is independent of stress and so swelling simply accumulates linearly with dose or time. The rate of swelling is low, ranging from

6×10^{-4} %/dpa at 300 K, to 5×10^{-5} %/dpa at 800 K. Consistent with swelling data for pure Fe irradiated with fast neutron spectra [50], $\dot{S}$ decreases with temperature as shown in Figure 7.4. This indicates that vacancy clusters remain unstable down to 300 K, suggesting either that the peak swelling temperature for Fe is below room temperature, which runs counter to most studies [37], or that the scatter in the data is too large to identify a clear peak. For consistency with the creep rate temperature dependence, we attempt an exponential fit to the data, $\dot{S} = D_0 \exp(-D_1 T)$, which yields $D_0 = 2.3 \times 10^{-7}$ [%/s] and $D_1 = 0.004$ [K^{-1}]. It is interesting to note that both B and $\dot{S}$ display the same exponential coefficient ($B_1 \approx D_1$). These constants are inverse temperatures corresponding to a temperature value of 250 K.

At this point it is important to note that some amount of stress-independent creep can be appreciated at all temperatures. Interestingly, the swelling rates, which are all insensitive to stress, and the creep rates at 0 MPa, display a very consistent relationship characterized by a temperature-independent constant ratio of approximately 31 (shown in Table 7.4). This suggests the existence of a creep/swelling coupling at zero stress, as indicated in many studies, defined mathematically simply by:

$$\dot{\epsilon}_{\text{cr}} = G\dot{S}$$

where $G = 31.4$ is the coupling constant. We will return to this issue in Sec. 7.5.1.

7.4.3 Evolution of the microstructure during creep deformation

In the context of the present model, the evolution of the microstructure is defined by two main effects: the accumulation of irradiation defect clusters in the material and the growth of the dislocation density from interactions with defects. These are

Table 7.4: Ratio of creep rates to swelling rates at zero stress in steady-state as a function of temperature. A constant value between 31.4 and 31.6 is consistently found for all temperatures.

T [K]	300	450	600	800
$\dot{\epsilon}_{\text{cr}}$ [% s^{-1}]	1.18×10^{-8}	7.51×10^{-9}	2.78×10^{-9}	2.63×10^{-9}
$\dot{S}$ [% s^{-1}]	3.74×10^{-10}	2.39×10^{-10}	8.85×10^{-11}	8.37×10^{-11}
$\dot{\epsilon}_{\text{cr}}/\dot{S}$	31.6	31.4	31.4	31.4

studied in depth next.

1. The first factor controlling microstructural evolution is the proliferation and accumulation of defect clusters in the material under irradiation. The parameter that embodies such accumulation as an integrated quantity is the mean obstacle spacing d_{irr} (refer to eq. (7.23)). Figures 7.5a to 7.5c show the evolution of $1/d_{\text{irr}}$ as a function of dose, stress, and temperature. Several trends can be clearly identified in the figures. First, at 300 K, $1/d_{\text{irr}}$ increases to values of 0.006 to 0.007 b^{-1} (i.e., $120 < d_{\text{irr}} < 150b$) between 0 and 300 MPa. At 450 K, $1/d_{\text{irr}}$ only increases at 200 and 300 MPa, taking values of 0.001 and 0.006 b^{-1}, respectively, while it remains unchanged from its original value at low stresses. Finally, at 600 K and above, the inverse obstacle spacing remains small, and oscillates in an uncorrelated manner with neutron dose. This suggest a weak accumulation of defect clusters in the material, i.e., a sink-dominated scenario enabled by defect diffusion over defect reactions.

2. The network dislocation density evolves with irradiation dose in the manner shown in Figures 7.6a to 7.6c, increasing almost linearly with dose at all tem-

peratures and stresses. ρ_{tot} grows directly as a consequence of the PAG process, and indirectly via dislocation-dislocation interactions through defect-induced climb processes. The proportionality constant is quite large, resulting in total dislocation density increases of up to three orders of magnitude larger than the original dislocation density ρ_0 at the highest temperatures. It is likely that the only way the system can accommodate such a drastic increase in total dislocation density is by creating dislocation substructures where dislocations group in bundles. This is beyond the scope of this work, as the CP model does not capture the formation of substructures at this point. For dislocation network growth, temperature leads to a faster accumulation, while stress also has a proportional effect.

In summary, irradiation creep results in appreciable accumulation of both defect clusters and network dislocations as the dose increases. The validity and implications of these results will be discussed below, in Sec. 7.5.

7.4.4 Irradiation defects controlling the evolution of the creep microstructure

It is well established that swelling and irradiation creep are due to the biased absorption of point defects at dislocations. In the present model, the 'dislocation bias model' is assumed, i.e., SIA and SIA clusters undergo a preferential absorption at dislocations, represented by eq. (7.28). Next we quantitatively analyze the evolution of the excess defect absorption with dose as a function of temperature and stress. The results are shown in Figure 7.7 for all four temperatures and stresses with N_{abs} in terms of atomic percentages. We recall that, in accordance with eq. (7.27), N_{abs} is

defined as the difference between SIAs and vacancies absorbed by the dislocations, and –consequently– dictate the direction of climb. However, we note that the instantaneous evolution of N_{abs} is not smooth, and what is plotted are splines capturing the overall evolution of otherwise highly-oscillatory data. These fluctuations result in rapid bursts of the value of $\dot{N}_{\text{abs}}$ that goes in eq. (7.25), and, as such, a net 'positive' or 'negative'[4] N_{abs} cannot be interpreted as implying positive or negative climb, respectively.

However, the overall values give an idea of the imbalance in point defect absorption in each case. At 300 K the net amount of absorbed point defects is clearly positive for all stresses, indicating a stronger bias for SIA absorption and a 'positive' direction of climb. At 450 K, stress is needed to maintain the same sense of climb, with 0 and 100 MPa giving slightly negative or negligible climb. At 600 and 800 K, there is a weak net effect at all stresses, with all values being close to zero or very small negatives.

7.5 Discussion

7.5.1 Creep and swelling correlations

Our final expression for the effective shear strain rate follows the expression:

$$\dot{\epsilon}_{\text{cr}} = B_0 \exp\left(-\frac{T}{T_0}\right)\sigma^m + G\dot{S} \tag{7.40}$$

with:

[4]Although arbitrary, we define positive climb as that contributing to positive swelling, i.e., volumetric expansion.

B_0 [% s^{-1} $MPa^{-0.20}$]	T_0 [K]	m	G
8.6×10^{-8}	250	0.20	31.5

Likewise, for the swelling rate:

$$\dot{S} = D_0 \exp\left(-\frac{T}{T_0}\right) \tag{7.41}$$

with:

D_0 [% s^{-1}]	T_0 [K]
2.3×10^{-7}	250

Combining eqs. (7.40) and (7.41) results in:

$$\dot{\epsilon}_{\text{cr}} = \exp\left(-\frac{T}{T_0}\right)\left(B_0\sigma^m + D_0 G\right) \tag{7.42}$$

Note that, strictly speaking, the correlations for creep and swelling can only be added by tensorial operations, not scalarly. As such, care must be exercised when using eq. (7.42). From a mechanistic point of view, creep is a volume-preserving irreversible deformation mode that should in principle be inactive in the absence of stress. However, as is apparent from eqs. (7.7) and (7.15), climb induced deformation triggered by irradiation can result in nonzero off-diagonal components of the strain tensor as a consequence of the orientation-dependent differences in dislocation activity across different slip systems. In other words, while the coupling constant G does not depend on temperature, it is likely dependent on crystal orientation (we recall that the present simulations have been done for [001] loading). In any case, it is clear that the absorption of point defects under no stress leads to plastic deformation that is partitioned between creep and swelling, with approximately a 31 times higher creep rate than swelling rate.

It is worth emphasizing that swelling and creep display an almost identical temperature dependence, characterized by a common temperature decay constant of 250 K. As a point of reference, stage III (monovacancy migration) during isochronal annealing has been estimated to occur at temperatures between 215 and 275 K in Fe [122]. This might suggest that creep and swelling are modulated by stage III kinetics, i.e., that steady state is achieved only once both vacancies and interstitials (which become mobilized at much lower temperatures) are capable of diffusing.

In closing this subsection, we also note that one of the great interests of extracting irradiation creep correlations is to determine the dependence with irradiation dose rate. Here we focus only on fusion (DEMO) conditions and so this study represents only one dose rate point. It is reasonable to believe that not only dose rate effects must be considered, but also spectral effects due to 14-MeV fusion neutrons and the associated transmutation rates, as such effects lead to time-dependent recoil energy distributions [144].

7.5.2 Additional physical elements to be captured by the present model

The main two pieces of physics that are not currently captured by the model are (i) dose rate effects, and (ii) He and H effects due to threshold reaction gas atoms production in Fe. Other effects such as material chemistry changes due to transmutation inventory evolution, or are considered to be second order effects as far as irradiation creep is concerned.

Regarding point (i), data show that the creep strain rate is directly proportional to neutron dose rate, as $\dot{\epsilon}_{\mathrm{cr}} \propto \phi$, where ϕ is the irradiation dose rate. With this, one

could speculate that such dependence can be trivially added to our correlation, i.e.:

$$\dot{\epsilon}_{\mathrm{cr}}(T,\phi) = B_0 \exp\left(-\frac{T}{T_0}\right)\phi^n \sigma^m$$

where $n = 1$. However, most of the experimental data point in the direction of $m = 1$ [12, 61, 62], whereas here we find a value of 0.2. This may suggest that the dose rate dependence may be nonlinear as well, and so dose rate effects should be explicitly studied with the model. In fact, nothing in principle precludes our model from being used at a different dose rate, provided that the appropriate PKA damage spectrum (in the form of a *c*pdf, Fig. 7.1) be supplied as well if needed. We, however, leave this for future studies.

In terms of He/H effects, the main effect attributable to the accumulation of gas atoms during irradiation/transmutation is the stabilization of small vacancy clusters [47, 123, 158, 257, 310]. Such effect enhances the biasing of the point defect absorption rates by immobilizing vacancies and contributing to delayed or suppressed recombination processes leading to enhanced creep and swelling, as shown in numerous studies [12, 206, 277, 350]. Indeed, the exceedingly low levels of swelling and creep calculated in this study are a reflection of the fact that vacancies and SIAs undergo delayed recombination at sinks due to their vast mobility difference. Such recombination processes are suppressed due to the trapping of vacancies by He atoms. Although less abundant, similar observations have been made in studies of H-irradiated ferritic materials [280, 352].

As for dose rate effects, the combined CP-SCD model developed here is suited to capture these effects, as the SCD module has been developed as a multispecies cluster dynamics method that has been used in the past to study He-metal and He-H-metal co-implantation [239–241, 404]. This is another aspect that would be

interesting investigating in future studies.

7.5.3 Advantages and shortcomings of the present model

As mentioned in Sec. 7.1, the number of existing irradiation creep models for structural alloys is remarkably low. The present approach attempts to take advantage of the existence of mature crystal plasticity formulations and irradiation damage evolution models to link them in a self-consistent manner and gain insight into complex microstructural processes leading to creep. However, our model incorporates some advantageous features missing in other approaches:

1. The model takes into account the whole cluster dimensionality space, without restricting it to just point defects or small clusters, or without employing grouping methods to reduce the damage species' complexity. Among the added benefits of such feature is the incorporation into the dislocation density evolution models of a growth term ascribed to direct SIA cluster/loop absorption, eqs. (7.30) and (7.31). This is not typically captured in other models [311,380,386], and indeed is what allows net creep and swelling to take place even in high temperature situations when the excess absorbed point defect concentration becomes zero or slightly negative.

2. The prior point enables the present model to take into account full cascade and neutron spectrum information. Damage is introduced directly by sampling cascade databases obtained in molecular dynamics simulations, which include point defects and their clusters as a function of PKA energy. Moreover, this clusters display the correct diffusivity characteristics of vacancy and SIA-type defects, including one-dimensional migration [173].

3. The creep and swelling strain constitutive relations are obtained, not pre-specified. Our model includes a flow rule purely based on dislocation-mediated processes driven by the imposed stress. In fact, there is no *a* priori strain rate prescribed for the material. The system responds to the prescribed stress (see procedure in eqs. (7.1) to (7.10)) and the creep strain rate and swelling rate are the outcome of the simulation process.

By contrast, our model does not take into account the formation of dislocation cells [141, 380], which known to be an important aspect of the evolution of the microstructure. Neglecting this effect may have two immediate effects. One is the modification the defect mean free path, which changes from $\sim \rho_{\text{tot}}^{-1/2}$ to the characteristic length scale of the dislocation cell microstructure. Such microstructural length scale is generally larger than the mean dislocation spacing, which could ultimately lead to enhanced recombination and/or larger cluster formation. The second one pertains more to defect damage theory: the sink strength of dislocations is obtained assuming a uniform dislocation density. The existence of subcells results in alterations in the absorption characteristics of defects due to the spatially heterogeneous nature of dislocations [128].

Finally, our approach does not capture loop alignment due to stress [129,298,382], which could attribute to the non-linear correlation between creep rate and stress. While we believe this is a second-order effect (in fact some irradiation studies report no effective dislocation loop orientation during creep studies [12,155]), its true impact on microstructural evolution for ferritic materials may merit additional attention via modeling and experimentation.

7.6 Summary

We finalize the chapter with our most important conclusions:

1. We have extended the coupled SCD/CP model for irradiation scenarios described in ref. [401] to simulate irradiation creep in fusion energy conditions. The model takes advantage of SCD features, including capturing the entire cluster dimensionality space, and being suited for multi-species conditions. Likewise, through CP, latent hardening and irradiation hardening are naturally included in the simulations.

2. The SCD and CP modules are bidirectionally coupled by a transfer of variables that produces (i) changes in the sink concentrations and strength for irradiation defects, and (ii) changes in the density evolution and hardening terms for dislocations.

3. The dislocation density evolution model accounts for the absorption of interstitial loops (PAG) and the preferential absorption of SIA small clusters and single SIAs (SIPA).

4. We have applied the creep model to single-crystal iron under first wall DEMO conditions, up to a total dose of 15 dpa, during which both stage I and II creep were observed. Our results qualitatively show monotonic increases in creep and swelling strains with dose, a decreasing dependence with temperature, and a relatively weak correlation with stress.

5. Neutron irradiation leads to a drastically linear increase in dislocation density, which is predominantly resulted from PAG processes. At present, the

approach lacks a dislocation patterning model which may limit the dislocation sink strength against unbounded dislocation density increases.

6. A coupling between swelling and creep is found at zero stress, with a coupling constant of 31.

7. A principal result of our study are the creep and swelling rate correlations provided in eqs. (7.41) and (7.42).

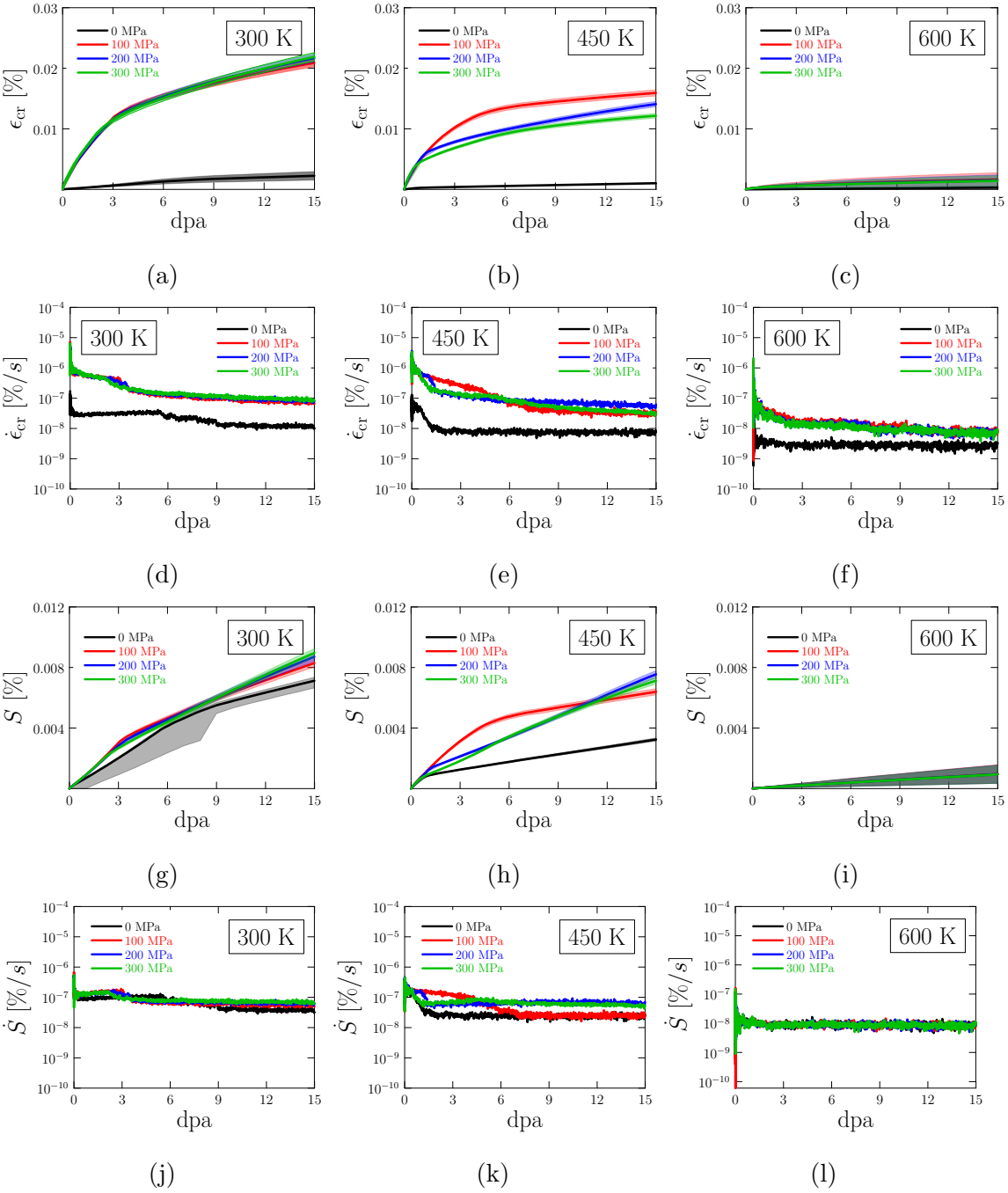

Figure 7.2: Evolution of the accumulated creep (figs. (a) to (c)) and swelling (figs. (g) to (i)) and their rates ((d) to (f)) and (j) to (l), respectively) with neutron dose at different temperatures and stresses (from five statistically independent runs). The results at 800 K (not shown) for all four variables are virtually the same as for 600 K.

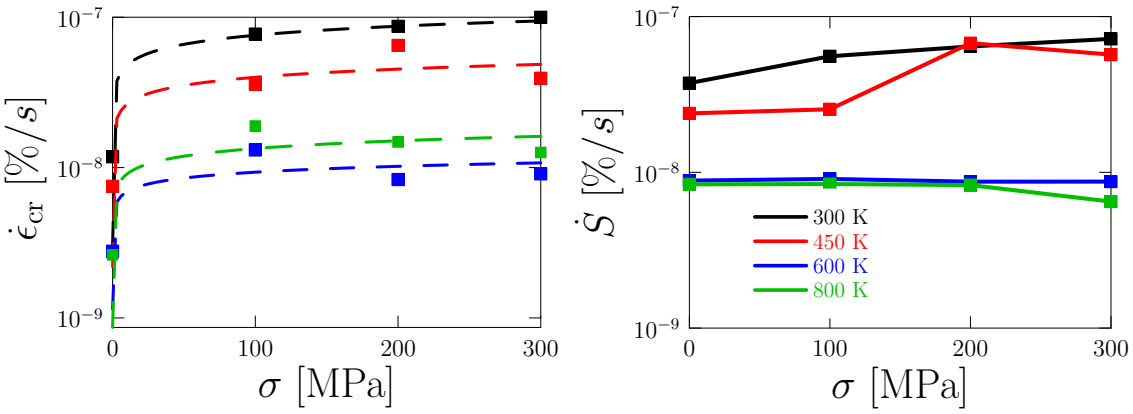

Figure 7.3: Averaged steady-state neutron irradiation (a) creep rate, and (b) swelling rate, as function of stress and temperature through five separate runs. The dashed lines with polygons in (a) are the fitted data from eq. (7.39).

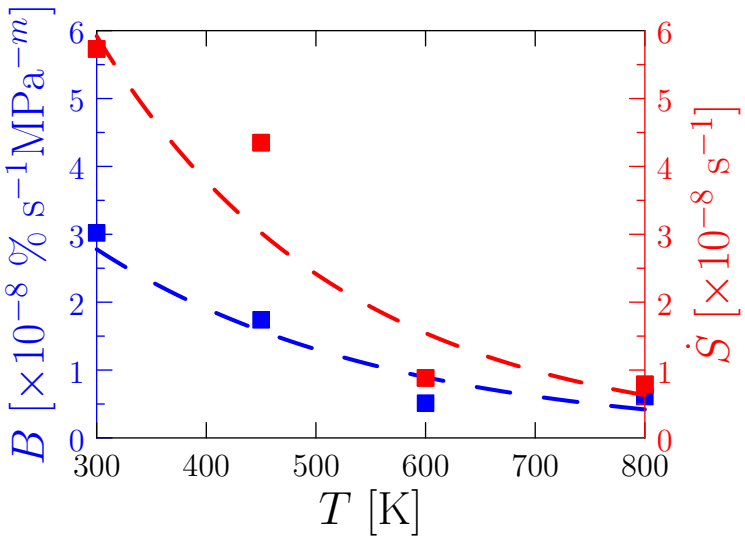

Figure 7.4: Temperature dependence of the creep compliance and the swelling rate. Their respective exponential fits are also plotted.

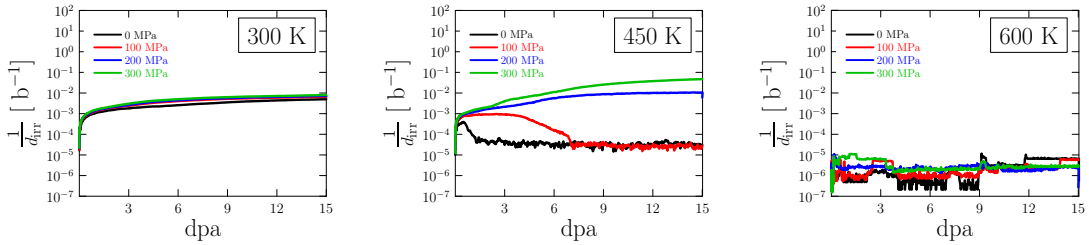

(a) (b) (c)

Figure 7.5: Evolution of inverse obstacle spacing with neutron dose at different temperatures and stresses (from five statistically independent runs). The results at 800 K are virtually the same as for 600 K and are omitted for clarity

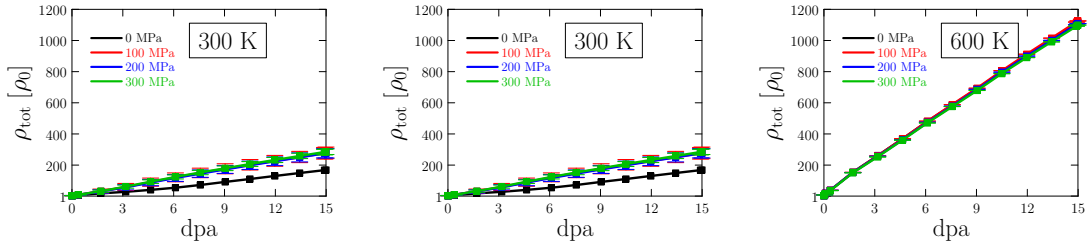

(a) (b) (c)

Figure 7.6: Evolution of the total dislocation density with neutron dose at different temperatures and stresses (from five statistically independent runs). The results at 800 K are virtually the same as for 600 K and are omitted for clarity

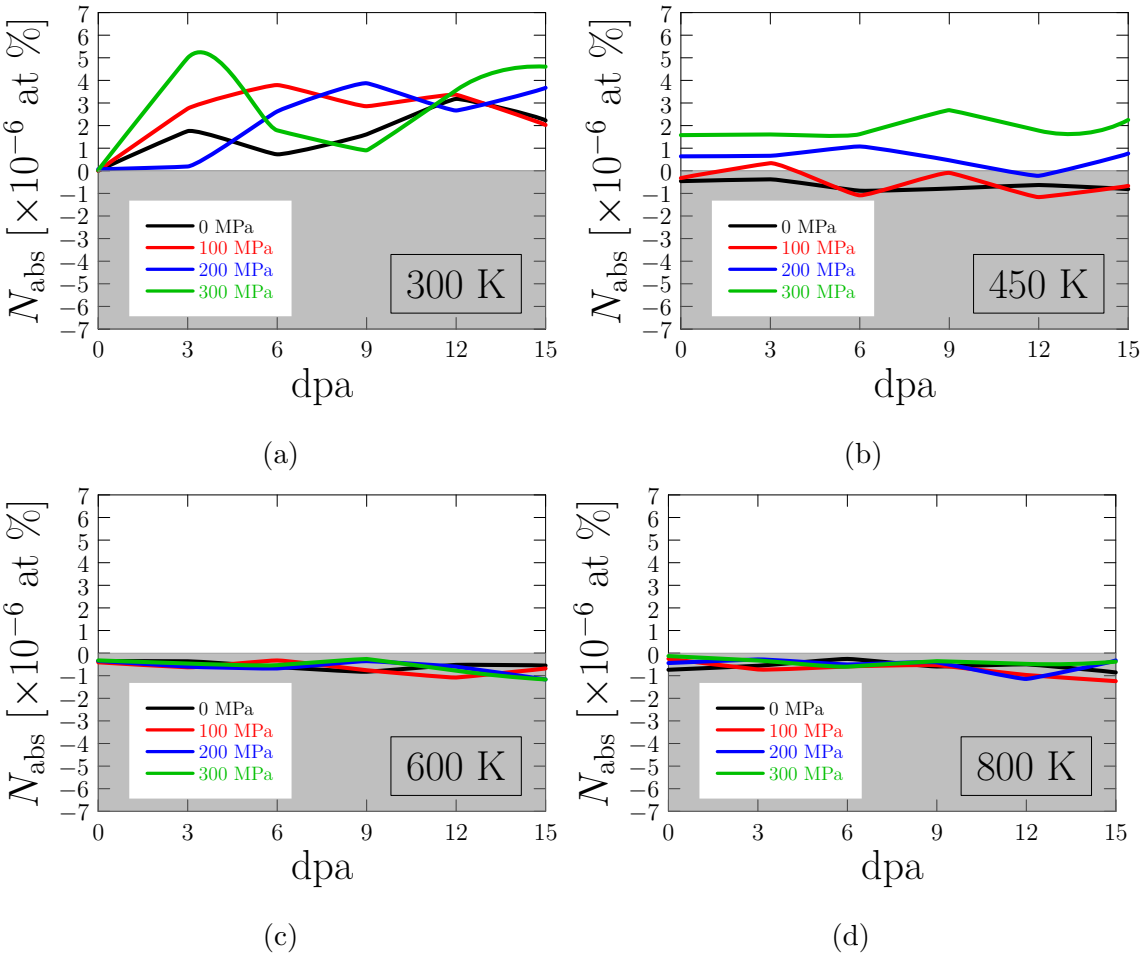

Figure 7.7: Atomic fraction of net absorbed point defects according to eq. (7.27). The plots are split into positive (clear) and negative (gray-shaded) regions.

CHAPTER 8

Conclusions

We finalize the thesis with our most important conclusions:

1. We have developed the SR-SCD model and used it to simulate hydrogen transport/accumulation in Zr-metal clad. This model accounts for a dynamic oxide/metal interface motion due to the time-dependent growth of the oxide scale. At the initial stage of corrosion, high concentrations of small hydride nuclei form across the entire metal clad was observed, which could possibly evolve into fine microstructure in the future stages.

2. We also used SR-SCD model to simulate a set of experiments involving sequences of ion-irradiations, hydrogen plasma exposure, and hydrogen thermal desorption of tungsten material. A thorough analysis to the simulated TDS result reveals that the thermal desorption spectra are broadly composed of three temperature regions: one below room temperature characterized by emissions from dislocations and grain boundaries, and intermediate one characterized by emissions from small overpressurized V-H clusters, and a high temperature one governed by release from large underpressurized bubbles. The study also shows that SAV formation mechanism significantly influences the hydrogen retention during exposure of tungsten to H plasmas.

3. We developed a coupled CP/SCD model by bidirectionally exchanging updated states of certain variables. Our simulation result of post-mortem tensile tests of tungsten material suggests multi GPa-level irradiation hardening associated with <5 dpa irradiations with 18-MeV self-ions for pre-irradiated samples, which is however in contrast to *in situ* tensile test results that shows weak irradiation hardening. This difference indicates that during irradiation, dislocation multiplication acts as potent defect accumulation inhibitor.

4. We developed a stochastic solver for crystal plasticity models based on the residence-time algorithm. This model strictly works for explicit problem and intrinsically gains numerical stability without the need of any extra procedures. By regarding and sampling plastic shear rates as reaction rates, the SCP model naturally breaks the symmetry of plastic slip, which could be used to study plastic localization phenomenon. Comparing to explicit deterministic CP algorithm, SCP model becomes more efficient at $T > 600$ K.

5. We decorated the coupled CP/SCD model, distinguishing edge and screw dislocation motions, and applied the it to simulate irradiation creep/swelling behavior of single-crystal iron under first wall DEMO conditions. The model accounts for previous theories such as absorption of interstitial loops (PAG) and the preferential absorption of SIA small clusters and single SIAs (SIPA) by dislocations. Our result finally provides new irradiation creep and swelling rate correlations in eqs. (7.41) and (7.42).

APPENDIX A

Slip systems in bcc crystals

Table A.1: Slip systems considered in this simulation [57]

α	Reference system	$\boldsymbol{s}^{\alpha}$	$\boldsymbol{n}^{\alpha}$
1	$[1\bar{1}1](011)$	$[1\bar{1}1]$	$[011]$
2	$[\bar{1}\bar{1}1](011)$	$[\bar{1}\bar{1}1]$	$[011]$
3	$[111](0\bar{1}1)$	$[111]$	$[0\bar{1}1]$
4	$[\bar{1}11](0\bar{1}1)$	$[\bar{1}11]$	$[0\bar{1}1]$
5	$[\bar{1}11](101)$	$[\bar{1}11]$	$[101]$
6	$[\bar{1}\bar{1}1](101)$	$[\bar{1}\bar{1}1]$	$[101]$
7	$[111](\bar{1}01)$	$[111]$	$[\bar{1}01]$
8	$[1\bar{1}1](\bar{1}01)$	$[1\bar{1}1]$	$[\bar{1}01]$
9	$[\bar{1}11](110)$	$[\bar{1}11]$	$[110]$
10	$[\bar{1}1\bar{1}](110)$	$[\bar{1}1\bar{1}]$	$[110]$
11	$[111](\bar{1}10)$	$[111]$	$[\bar{1}10]$
12	$[11\bar{1}](\bar{1}10)$	$[11\bar{1}]$	$[\bar{1}10]$

APPENDIX B

Latent hardening coefficients

Table B.1: Interaction coefficients $\xi_{\alpha\beta}$ for the 12 slip systems listed in Table A.1. The letter coding indicates 'A' : self; 'CP' coplanar; 'CL': collinear; 'O':orthogonal; 'G': glissile; 'S': sessile.

α	1	2	3	4	5	6	7	8	9	10	11	12
1	A											
2	CP	A										
3	S	S	A									
4	S	S	CP	A								
5	G	O	O	CL	A							
6	O	CL	G	O	CP	A						
7	O	G	CL	O	S	S	A					
8	CL	O	O	G	S	S	CP	A				
9	O	G	O	CL	CL	O	G	O	A			
10	CL	O	G	O	O	G	O	CL	CP	A		
11	G	O	CL	O	G	O	CL	O	S	S	A	
12	O	CL	O	G	O	CL	O	G	S	S	CP	A

Table B.2: Values of $\xi_{\alpha\beta}$ for latent hardening in bcc crystals [265]

Self	Coplanar	Collinear	Orthogonal	Glissile	Sessile
0.009	0.009	0.72	0.05	0.09	0.06

APPENDIX C

Binding energies of vacancy and hydrogen-vacancy clusters

Table C.1: Binding energies of monomers to I_n and V_n clusters used in the simulations. All data from ref. [32]. Values for $E^f(I_1)$ and $E^f(V_1)$ are 9.96 [340] and 3.23 eV, respectively [363].

Species	E_b [eV]
I_2	2.12
I_3	3.02
I_4	3.60
I_5	3.98
I_6	4.27
I_7	5.39
$n > 7$	$E^f(I_1) + \left(E^b(I_2) - E^f(I_1)\right) n^{2/3} - 1.71(n-1)^{2/3}$
V_2	-0.1
V_3	0.04
V_4	0.64
V_5	0.72
V_6	0.89
V_7	0.72
V_8	0.88
$n > 8$	$E_f(V_1) + \left(E^b(V_2) - E^f(V_1)\right) n^{2/3} - 1.71(n-1)^{2/3}$

Table C.2: (Left table) Binding energies of vacancy monomers from V_mH_n clusters used in this work (from refs. [218, 276]). The binding energies are given in terms of the H-to-V ratio of the cluster, $x = n/m$, and include a value for the emission of a vacancy and a different value for the emission of a hydrogen atom (indicated in each case). (Right table) Binding energies of H monomers to SIA-hydrogen clusters (values from ref. [218]).

	E^b [eV]
x	V_1
1	1.6
2	2.1
3	2.4
4	3.9
5	4.4
6	5.8
7	7.0
8	8.2
9	9.8
10	11.2
11	13.65
12	15.88
13	18.30
14	20.92
15	23.73

Cluster type	E^b_{H} [eV]
I_1H_1	0.67
I_1H_2	0.40
I_1H_3	0.22
I_1H_4	0.05
I_2H_1	0.57
I_2H_2	0.45
I_2H_3	0.22
I_2H_3	0.1
I_mH_n	$0.013m^4 - 0.44m^2 + m$

Table C.3: Binding energies of hydrogen monomers from V_mH_n clusters used in this work (from ref. [166]). The binding energies are given in terms of the H-to-V ratio of the cluster, $x = n/m$, and the cluster size, number of vacancies m. An empirical relation approximating the data was obtained using symbolic regression [93]: $E^b = 1.707 - \frac{0.507}{m^3} + \frac{0.1677x}{m^2} - 0.1699x - 8.58e^{-4}x^3 - 1.793e^{-3}mx^2$.

	E^b [eV]									
x	V_1	V_2	V_3	V_4	V_5	V_6	V_7	V_8	V_9	V_{10}
< 1			1.65284	1.64638	1.64638	1.64638	1.64638	1.64638	1.64638	1.64638
1	1.17486	1.41062	1.39447	1.52366	1.52366	1.52366	1.52366	1.52366	1.52366	1.52366
2	1.18455	1.37186	1.36218	1.38478	1.38478	1.38478	1.38478	1.38478	1.38478	1.38478
3	1.16194	1.29112	1.23945	1.21038	1.16194	1.16194	0.968161	0.968161	0.968161	0.968161
4	1.11349	0.939095	0.868043	0.829287	0.774384	0.774384	0.784073	0.784073	0.784073	0.784073
5	1.04244	0.774384	0.671036	0.619362	0.528932	0.528932	0.351303	0.351303	0.351303	0.351303
6	0.929406	0.567688	0.406206	0.299629	0.20274	0.20274	−0.00718592	−0.00718592	−0.00718592	−0.00718592
7	0.793761	0.293169	0.0703251	−0.0976155						
8	0.619362	−0.0459414								
9	0.399747									
10	0.141377									
11	−0.168667									

APPENDIX D

Numerical algorithm of the CP-SCD model for Chapter 5

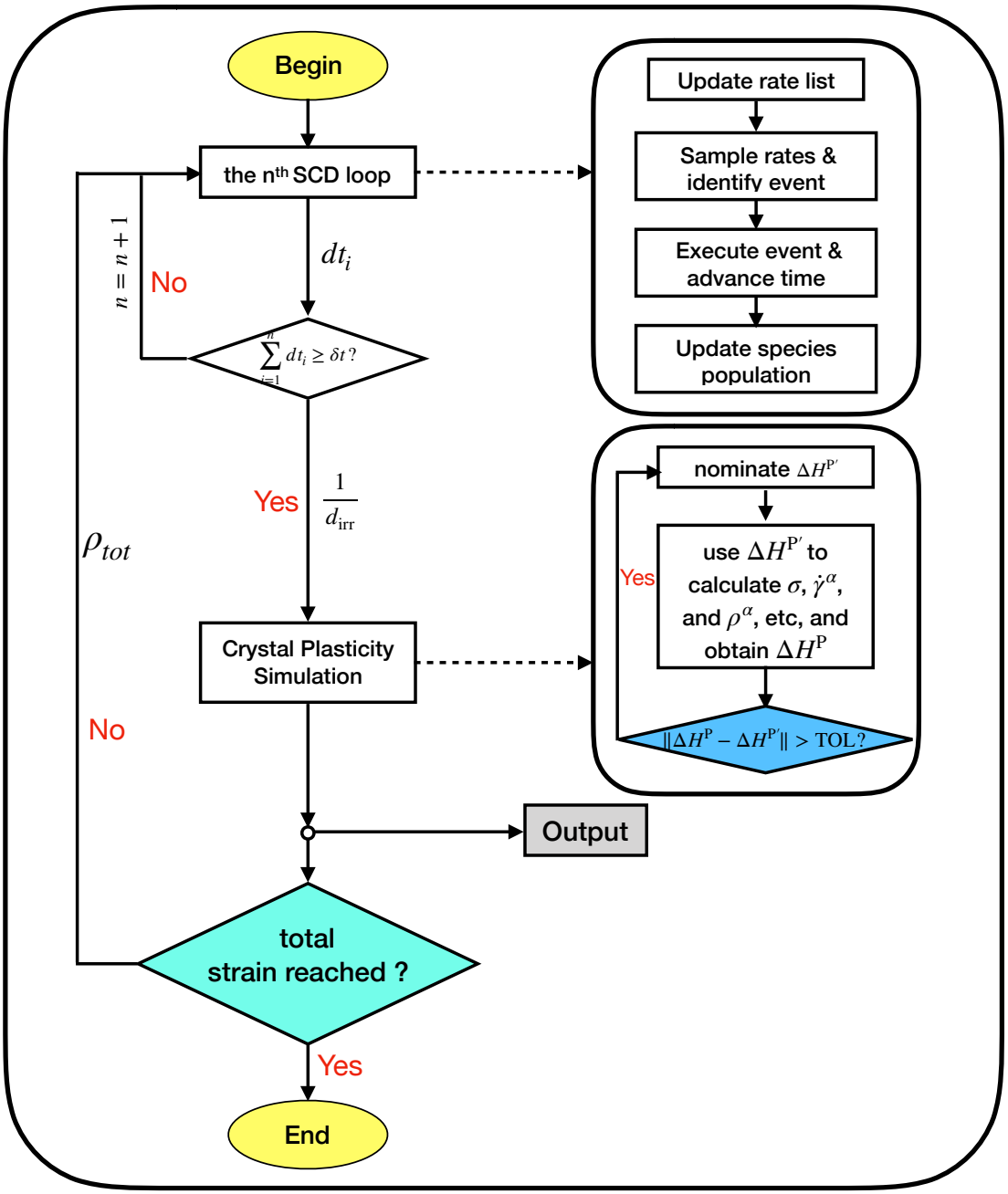

Figure D.1: Flowchart of the CP/SCD model.

Algorithm 2 Numerical procedure to solve the coupled CP-SCD model.

Initialize: $\dot{\boldsymbol{\varepsilon}}_0$, TOL, `maxiter`, t_{TOT}, δt, $t = \delta t$, $\{\rho^\alpha\} = \rho_0$, ρ_{tot}

while $(t < t_{\mathrm{TOT}})$ **do**

  Do: n steps of SCD until $(\delta t == \sum_{i=1}^{n} dt_i)$, send updated value L to CP

  Get: total strain increment $\Delta\boldsymbol{\varepsilon}_{\mathrm{t}} = \dot{\boldsymbol{\varepsilon}}_0 \delta t$

  Initialize: $\Delta\boldsymbol{H}^{\mathrm{P}'} = 0$, $\Delta\boldsymbol{H}^{\mathrm{P}} = \Delta\boldsymbol{\varepsilon}_{\mathrm{t}}$, `step` $= 1$

  while $\left(\|\Delta\boldsymbol{H}^{\mathrm{P}} - \Delta\boldsymbol{H}^{\mathrm{P}'}\|_1 > \mathrm{TOL}\right)$ **and** (`step` $\leqslant$ `maxiter`) **do**

    $\Delta\boldsymbol{H}^{\mathrm{P}} = \Delta\boldsymbol{H}^{\mathrm{P}'}$

    Get: elastic strain increment $\Delta\boldsymbol{\varepsilon}^{\mathrm{E}} = \Delta\boldsymbol{\varepsilon}_{\mathrm{t}} - \Delta\boldsymbol{H}^{\mathrm{P}}$

    Calculate: stress (tensor) increment $\Delta\boldsymbol{\sigma} = \mathbb{C} : \Delta\boldsymbol{\varepsilon}^{\mathrm{E}}$

    Update: stress tensor $\boldsymbol{\sigma} = \boldsymbol{\sigma} + \Delta\boldsymbol{\sigma}$

    for $\alpha = 1, N$ **do**

      Initialize: $\rho^\alpha_{\mathrm{int}} = 0$, $\Delta\rho^\alpha = 0$, $\rho^\alpha_f = 0$, $\Delta\tau^\alpha = 0$

      Calculate: modulus: $b = \|\boldsymbol{b}^\alpha\|$

      Get: slip direction $\boldsymbol{s}^\alpha = b^{-1}\boldsymbol{b}^\alpha$, plane normal $\boldsymbol{n}^\alpha$

      Calculate: resolved shear stress $\tau^\alpha_{\mathrm{RSS}} = \boldsymbol{s}^\alpha \cdot \boldsymbol{\sigma} \cdot \boldsymbol{n}^\alpha$

      for $\beta = 1, N$ **do**

        Calculate: forest dislocation density $\rho^\alpha_f = \rho^\alpha_f + \rho^\beta |\boldsymbol{s}^\beta \cdot \boldsymbol{n}^\alpha|$.

        Calculate: forest interaction density $\rho^\alpha_{\mathrm{int}} = \rho^\alpha_{\mathrm{int}} + \xi_{\alpha\beta}\rho^\beta$

      end for

      Get: forest hardening $\Delta\tau^\alpha_{\mathrm{int}} = \mu b\sqrt{\rho^\alpha_{\mathrm{int}}}$

      Calculate: $\lambda^\alpha = \left(\sqrt{\rho^\alpha_f} + \frac{1}{\delta_{\mathrm{irr}}}\right)^{-1}$ ← Receive δ_{irr} from SCD

      Get: defect hardening $\Delta\tau^\alpha_d = \frac{\mu b}{\delta_{\mathrm{irr}}}$

      if $(|\tau^\alpha_{\mathrm{RSS}}| > (\Delta\tau^\alpha_{\mathrm{int}} + \Delta\tau^\alpha_d))$ **then**

        Get: excess stress $\Delta\tau^\alpha = \tau^\alpha_{\mathrm{RSS}} - \mathrm{sgn}(\tau^\alpha_{\mathrm{RSS}})\,(\Delta\tau^\alpha_{\mathrm{int}} + \Delta\tau^\alpha_d)$

Algorithm 2 (continued)

Calculate: prefactor $v_0^\alpha = \mathrm{sgn}(\tau_{\mathrm{RSS}}^\alpha)\nu_0 \frac{h}{b}\left(\lambda^\alpha - w\right)$

Calculate: velocity $v^\alpha = v_0^\alpha \exp\left\{-\frac{\Delta H_0}{kT}\left(1 - \left|\frac{\Delta\tau^\alpha}{\sigma_P}\right|^p\right)^q\right\}$

Calculate: slip rate $\dot{\gamma}^\alpha = bv^\alpha\rho^\alpha$

Calculate: dislocation density change $\Delta\rho^\alpha = \frac{|\dot{\gamma}^\alpha|}{\lambda^\alpha}\left(1 - 2b\lambda^\alpha\rho^\alpha\right)\frac{\delta t}{b}$

Calculate: plastic slip $\delta\boldsymbol{H}^{\mathrm{P}} = |\dot{\gamma}^\alpha|\left(\boldsymbol{s}^\alpha \otimes \boldsymbol{n}^\alpha\right)\delta t$

Update: plastic strain increment $\Delta\boldsymbol{H}^{\mathrm{P}'} = \Delta\boldsymbol{H}^{\mathrm{P}'} + \delta\boldsymbol{H}^{\mathrm{P}}$

`step = step + 1`

end if

end for

end while

for $\alpha = 1, N$ **do**

Update: dislocation density $\rho^\alpha = \rho^\alpha + \Delta\rho^\alpha$

Calculate: $\rho_{\mathrm{tot}} = \rho_{\mathrm{tot}} + \rho^\alpha \rightarrow$ Pass ρ_{tot} to SCD and update reaction rates

end for

Send: transfer ρ_{tot} to SCD and update reaction rates

Update: $\boldsymbol{\varepsilon}_{\mathrm{t}} = \boldsymbol{\varepsilon}_{\mathrm{t}} + \Delta\boldsymbol{\varepsilon}_{\mathrm{t}}$

$\boldsymbol{\varepsilon}^{\mathrm{E}} = \boldsymbol{\varepsilon}^{\mathrm{E}} + \Delta\boldsymbol{\varepsilon}^{\mathrm{E}}$

$\boldsymbol{H}^{\mathrm{P}} = \boldsymbol{H}^{\mathrm{P}} + \Delta\boldsymbol{H}^{\mathrm{P}}$

Plot: $(\boldsymbol{\varepsilon}_{\mathrm{t}}, \boldsymbol{\sigma})$

$t = t + \delta t$

end while

APPENDIX E

Explicit deterministic CP algorithm for Chapter 6

Algorithm 3

Initialize: $\dot{\boldsymbol{\varepsilon}}_0$, T, TOL, `maxiter`, N, t_{TOT}, $t = 0$, δt, $\{\rho^\alpha\} = \rho_0$, d_g

Initialize: $\Delta\boldsymbol{\varepsilon}^{\mathrm{E}} = \dot{\boldsymbol{\varepsilon}}_0 \delta t$

while $(t < t_{\mathrm{TOT}})$ **do**

  Calculate: stress (tensor) increment $\Delta\boldsymbol{\sigma} = \mathbb{C} : \Delta\boldsymbol{\varepsilon}^{\mathrm{E}}$

  Update: stress tensor $\boldsymbol{\sigma} = \boldsymbol{\sigma} + \Delta\boldsymbol{\sigma}$

  Initialize: $\Delta\boldsymbol{\varepsilon}^{\mathrm{P}} = \mathbf{0}$

  for $\alpha = 1, N$ **do**

    Initialize: $\rho_f^\alpha = 0$

    Calculate: modulus: $b = \|\boldsymbol{b}^\alpha\|$

    Get: slip direction $\boldsymbol{s}^\alpha = b^{-1}\boldsymbol{b}^\alpha$, plane normal $\boldsymbol{n}^\alpha$

    Calculate: resolved shear stress $\tau_{\mathrm{RSS}}^\alpha = \boldsymbol{s}^\alpha \cdot \boldsymbol{\sigma} \cdot \boldsymbol{n}^\alpha$

    for $\beta = 1, N$ **do**

      Calculate: forest dislocation density $\rho_f^\alpha = \rho_f^\alpha + \xi_{\alpha\beta}\rho^\beta |\boldsymbol{s}^\beta \cdot \boldsymbol{n}^\alpha|$

      Calculate: forest dislocation hardening $g^\alpha = g^\alpha + \xi_{\alpha\beta}\rho^\beta |\boldsymbol{s}^\beta \cdot \boldsymbol{n}^\alpha|$

    end for

    Get: dislocation hardening $\tau_h^\alpha = \mu b \sqrt{g^\alpha + \xi_{\alpha\alpha}\rho^\alpha}$

    Calculate: $\lambda^\alpha = \left(\sqrt{\rho_f^\alpha} + \frac{1}{d_g}\right)^{-1}$

Algorithm 3 (continued)

if $((\lambda^\alpha - w > 0)$ **and** $(\tau^\alpha_{\mathrm{RSS}} - \tau^\alpha_h > 0))$ **then**

$v^\alpha_0 = \mathrm{sgn}(\tau^\alpha_{\mathrm{RSS}})\nu_0 \frac{h}{b} (\lambda^\alpha - w)$

$v^\alpha = v^\alpha_0 \exp\left\{-\frac{\Delta H_0}{kT}\left(1 - \left|\frac{\tau^\alpha_{\mathrm{RSS}} - \tau^\alpha_h}{\sigma_{\mathrm{P}}}\right|^p\right)^q\right\}$

else

$v^\alpha = 0$

end if

Calculate: $\Delta\boldsymbol{\varepsilon}^{\mathrm{P}} = \Delta\boldsymbol{\varepsilon}^{\mathrm{P}} + \rho^\alpha b v^\alpha (\boldsymbol{s}^\alpha \otimes \boldsymbol{n}^\alpha)\, \delta t$

end for

Update: $t = t + \delta t$

Update: $\Delta\boldsymbol{\varepsilon}^{\mathrm{E}} = \left(\dot{\boldsymbol{\varepsilon}}_0 \delta t - \Delta\boldsymbol{\varepsilon}^{\mathrm{P}}\right)$

Update: $\boldsymbol{\varepsilon}_{\mathrm{tot}} = \boldsymbol{\varepsilon}_{\mathrm{tot}} + \dot{\boldsymbol{\varepsilon}}_0 \delta t$

for $\beta = 1, N$ **do**

Update: $\rho^\beta = \rho^\beta + \frac{\left|\dot{\gamma}^\beta\right|}{\lambda^\beta}\left(1 - 2b\lambda^\beta \rho^\beta\right)\frac{\delta t}{b}$

end for

end while

APPENDIX F

Derivation of the climb-assisted edge dislocation velocity

As indicated in Section 7.2.1.2, when the excess stress $\Delta\tau^{\alpha}$ becomes too small, edge dislocations may undergo climb-assisted glide by bypassing slip obstacles via climb. As such, the *e*ffective glide velocity can be obtained as a composite of three steps: (1) unimpeded glide between obstacles, (2) defect-induced climb to a glide plane over the obstacle, and (3) glide past the obstacle. As shown schematically in Figure F.1, each one of these steps is defined by a characteristic distance, each taking a finite amount of time (for simplicity, here we drop the superscript α to refer to a specific slip system). Step (1) is governed by an obstacle spacing given by λ, defined as in eq. (7.18), and a time δt_0. Step (2) is defined by an obstacle bypass distance, Δ_{obs}, and a time δt_1. Finally, step (3) is characterized by (twice) Δ_{obs} and δt_2. The effective glide velocity is then obtained as:

$$\bar{v}_{\text{e}} = \frac{\lambda + 2\Delta_{\text{obs}}}{\delta t_0 + \delta t_1 + \delta t_2} \tag{F.1}$$

where $\delta t_0 = \lambda / v_{\text{e}}$, $\delta t_1 = \Delta_{\text{obs}} / v_{\text{climb}}$, and $\delta t_2 = 2\Delta_{\text{obs}} / v_{\text{e}}$, i.e.:

$$\bar{v}_{\text{e}} = \frac{\lambda + 2\Delta_{\text{obs}}}{\dfrac{\lambda}{v_{\text{e}}} + \dfrac{\Delta_{\text{obs}}}{v_{\text{climb}}} + \dfrac{2\Delta_{\text{obs}}}{v_{\text{e}}}} \tag{F.2}$$

Operating with this expression yields:

$$\bar{v}_{\mathrm{e}} = \frac{(\lambda + 2\Delta_{\mathrm{obs}})\, v_{\mathrm{e}} v_c}{v_{\mathrm{climb}}\,(\lambda + 2\Delta_{\mathrm{obs}}) + v_{\mathrm{e}}\Delta_{\mathrm{obs}}} \tag{F.3}$$

where v_{climb} is given by eq. (7.25) and v_{e} is now defined by the RSS, not the excess stress, as in eq. (7.16), since the dislocation segment taking a time δt_0 can now glide unimpeded in between obstacles. Substituting v_{e} with its definition in terms of the RSS, and re-introducing the superscript α, eq. (F.3) now reads:

$$\bar{v}_{\mathrm{e}}^{\alpha} = \frac{b\tau_{\mathrm{RSS}}^{\alpha}\,(\lambda^{\alpha} + 2\Delta_{\mathrm{obs}})\, v_{\mathrm{climb}}^{\alpha}}{\Gamma v_{\mathrm{climb}}^{\alpha}\,(\lambda^{\alpha} + 2\Delta_{\mathrm{obs}}) + b\tau_{\mathrm{RSS}}^{\alpha}\Delta_{\mathrm{obs}}} \tag{F.4}$$

where the superindex α has been again added. The above expression satisfies the condition that no edge dislocation glide is possible when the RSS is zero, yet shows that edge dislocations are capable of gliding through a field of obstacles even when the cutting stress $\Delta\tau^{\alpha}$ is larger than the RSS. Under the often valid assumption that $\delta t_1 \gg \delta t_0,\ \delta t_2$, the above equation simplifies to:

$$\bar{v}_{\mathrm{e}}^{\alpha} = v_{\mathrm{climb}}^{\alpha}\left(2 + \frac{\lambda^{\alpha}}{\Delta_{\mathrm{obs}}}\right) \tag{F.5}$$

In this work, we set Δ_{obs} to the arithmetic average between a dislocation screening distance equal to $2b$ and the effective size of the radius of the irradiated species, $\bar{r}$, given by eq. (7.24):

$$\Delta_{\mathrm{obs}} = b + \frac{\bar{r}}{2}$$

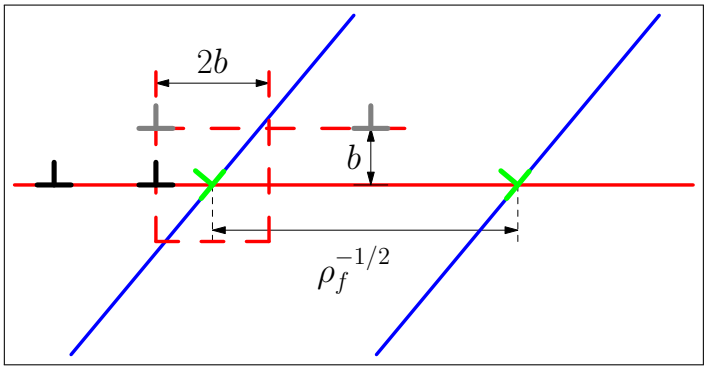

(a)

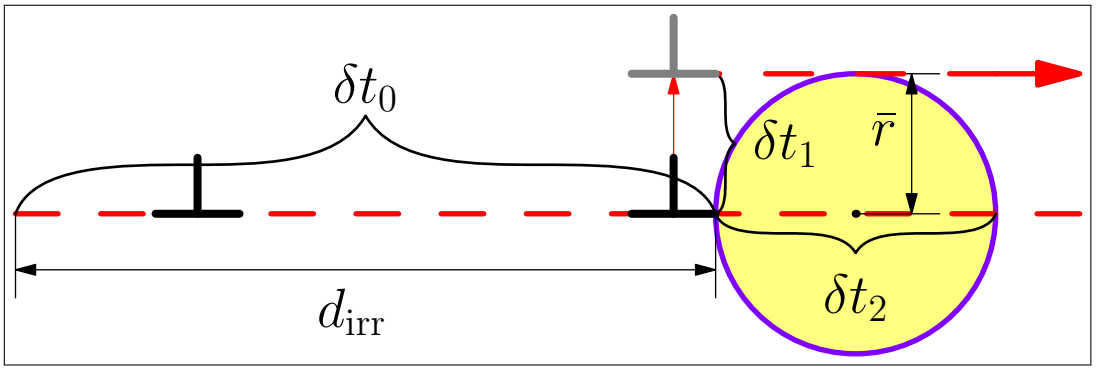

(b)

Figure F.1: Schematic diagram of an edge dislocation bypassing an obstacle by the climb-assisted glide mechanism. (a) Climb over forest dislocations. (b) Climb over irradiation obstacles. Both of these two scenarios are limiting cases of eq. (F.4) when $\lambda^\alpha = \left(\rho_f^\alpha\right)^{-1/2}$ and $\lambda^\alpha = d_{\text{irr}}$, respectively.

APPENDIX G

Numerical Algorithm for Chapter 7

Algorithm 4 Numerical procedure to solve the CP-SCD model.

Initialize: $\boldsymbol{\sigma}_0$, t_{TOT}, δt, $t = \delta t$, $\{\rho_e^\alpha\} = \{\rho_s^\alpha\} = \frac{1}{4}\rho_0$
Calculate: elastic strain $\boldsymbol{\varepsilon_e} = \mathbb{C}^{-1}\boldsymbol{\sigma_0}$
for $\alpha = 1, N$ **do**
    Calculate: modulus: $b = \|\boldsymbol{b}^\alpha\|$
    Get: slip direction $\boldsymbol{s}^\alpha = b^{-1}\boldsymbol{b}^\alpha$, plane normal $\boldsymbol{n}^\alpha$
    Calculate: resolved shear stress $\tau^\alpha_{\mathrm{RSS}} = \boldsymbol{s}^\alpha \cdot \boldsymbol{\sigma}_0 \cdot \boldsymbol{n}^\alpha$
end for
while $(t < t_{\mathrm{TOT}})$ **do**
    Initialize: $\Delta \boldsymbol{H}^{\mathrm{P}} = 0$, $\Delta\boldsymbol{\varepsilon}_{\mathrm{slip}} = 0$, $\Delta\boldsymbol{\varepsilon}_{\mathrm{climb}} = 0$
    for $\alpha = 1, N$ **do**
        Initialize: $\rho^\alpha_{\mathrm{int}} = 0$, $\Delta\rho^\alpha = 0$, $\rho^\alpha_f = 0$, $\Delta\tau^\alpha = 0$, $\rho_{tot} = 0$
        for $\kappa = 1, N$ **do**
            Calculate: forest dislocation density $\rho^\alpha_f = 2\sum_{\kappa\neq\alpha}\left(\rho^\kappa_{\mathrm{e}}\left|\boldsymbol{n}^\alpha \cdot (\boldsymbol{s}^\kappa \times \boldsymbol{n}^\kappa)\right| + \rho^\kappa_{\mathrm{s}}\left|\boldsymbol{n}^\alpha \cdot \boldsymbol{s}^\kappa\right|\right)$.
            Calculate: forest interaction density $\rho^\alpha_{\mathrm{int}} = \rho^\alpha_{\mathrm{int}} + 2\xi_{\alpha\kappa}\left(\rho^\kappa_e + \rho^\kappa_s\right)$
        end for
            Receive: d_{irr}, $\bar{r}$, $\left(N^{abs}_{\mathrm{V}} - N^{abs}_{\mathrm{SIA}}\right) \leftarrow$ SCD
        Get: forest hardening $\Delta\tau^\alpha_f = \mu b\sqrt{\rho^\alpha_{\mathrm{int}}}$
        Calculate: $\lambda^\alpha = \left(\frac{1}{d_g} + \sqrt{\rho^\alpha_f} + \frac{1}{d_{\mathrm{irr}}}\right)^{-1}$
        Get: defect hardening $\Delta\tau^\alpha_{\mathrm{irr}} = \frac{\mu b}{d_{\mathrm{irr}}}$
        Calculate: climb velocity: $v^\alpha_{\mathrm{climb}} = \left(\frac{N^{abs}_{\mathrm{V}} - N^{abs}_{\mathrm{SIA}}}{\Omega\ \rho_{\mathrm{tot}}}\right)\left(\frac{\Omega_a}{b\ \delta t}\right)\left(\frac{\rho^\alpha_{\mathrm{e}}}{\rho_{\mathrm{tot}}}\right)$
        if $\left(\left|\tau^\alpha_{\mathrm{RSS}}\right| > \left(\Delta\tau^\alpha_f + \Delta\tau^\alpha_{\mathrm{irr}}\right)\right)$ **then**
            Get: excess stress $\Delta\tau^\alpha = \tau^\alpha_{\mathrm{RSS}} - \mathrm{sgn}\left(\tau^\alpha_{\mathrm{RSS}}\right)\left(\Delta\tau^\alpha_f + \Delta\tau^\alpha_{\mathrm{irr}}\right)$
            Calculate: prefactor $v^\alpha_0 = \mathrm{sgn}\left(\tau^\alpha_{\mathrm{RSS}}\right)\frac{\nu_0 h}{b}\left(\lambda^\alpha - w\right)$
            if $\left(v^\alpha_0 > 0\right)$ **then**
                Calculate: slip velocity of screw dislocation $v^\alpha_s = v^\alpha_0 \exp\left\{-\frac{\Delta H_0}{kT}\left[1 - \left(\frac{\Delta\tau^\alpha}{\sigma_P}\right)^p\right]^q\right\}$
            else
                $v^\alpha_s = 0$
            end if
            Calculate: slip velocity of edge dislocation $v^\alpha_e = \mathrm{sgn}\left(\tau^\alpha_{\mathrm{RSS}}\right)\sup\left\{\frac{b\Delta\tau^\alpha}{B}, \frac{b\tau^\alpha_{\mathrm{RSS}}(d_{\mathrm{irr}}+2\bar{r})v^\alpha_{\mathrm{climb}}}{Bv^\alpha_{\mathrm{climb}}(d_{\mathrm{irr}}+2\bar{r}) + b\tau^\alpha_{\mathrm{RSS}}\bar{r}}\right\}$
        else
            $v^\alpha_s = 0$
            if $(\bar{r} > 0)$ **then**
                $v^\alpha_{\mathrm{e}} = \mathrm{sgn}\left(\tau^\alpha_{\mathrm{RSS}}\right)\frac{b\tau^\alpha_{\mathrm{RSS}}(d_{\mathrm{irr}}+2\bar{r})v^\alpha_{\mathrm{climb}}}{Bv^\alpha_{\mathrm{climb}}(d_{\mathrm{irr}}+2\bar{r}) + b\tau^\alpha_{\mathrm{RSS}}\bar{r}}$
            else
                $v^\alpha_{\mathrm{e}} = 0$
            end if
        end if

Algorithm 4 (continued)

Calculate: slip rate $\dot{\gamma}^{\alpha} = \left(\rho_e^{\alpha} v_e^{\alpha} + \rho_s^{\alpha} v_s^{\alpha}\right) b$

Calculate: edge dislocation density change $\Delta\rho_e^{\alpha} = \left[\frac{2\rho_s^{\alpha}|v_s^{\alpha}|}{\lambda^{\alpha}} - \left(\rho_{\mathrm{e}}^{\alpha}\right)^2 b \left(|v_{\mathrm{e}}^{\alpha}| + |v_{\mathrm{climb}}^{\alpha}|\right)\right] \delta t$

Calculate: screw dislocation density change $\Delta\rho_s^{\alpha} = \left[\frac{2\rho_e^{\alpha}|v_e^{\alpha}|}{\lambda^{\alpha}} - \left(\rho_{\mathrm{s}}^{\alpha}\right)^2 b \left|v_{\mathrm{s}}^{\alpha}\right|\right] \delta t$

Update: edge dislocation density $\rho_e^{\alpha} = \rho_e^{\alpha} + \Delta\rho_e^{\alpha}$

Update: screw dislocation density $\rho_s^{\alpha} = \rho_s^{\alpha} + \Delta\rho_s^{\alpha}$

Calculate: plastic slip $\Delta\boldsymbol{\varepsilon}_{\mathrm{slip}} = \left|\dot{\gamma}^{\alpha}\right| \left(\boldsymbol{s}^{\alpha} \otimes \boldsymbol{n}^{\alpha}\right) \delta t$

Calculate: climb rate $\dot{\beta}^{\alpha} = \rho_e^{\alpha} v_{\mathrm{climb}}^{\alpha} b$

Calculate: climb strain: $\Delta\boldsymbol{\varepsilon}_{\mathrm{climb}} = \left|\dot{\beta}^{\alpha}\right| \left(\boldsymbol{s}^{\alpha} \otimes \boldsymbol{s}^{\alpha}\right) \delta t$

Update: plastic strain increment $\Delta\boldsymbol{H}^{\mathrm{P}} = \Delta\boldsymbol{H}^{\mathrm{P}} + \left(\Delta\boldsymbol{\varepsilon}_{\mathrm{slip}} + \Delta\boldsymbol{\varepsilon}_{\mathrm{climb}}\right)$

Update: $\boldsymbol{\varepsilon}_{\mathrm{climb}} = \boldsymbol{\varepsilon}_{\mathrm{climb}} + \Delta\boldsymbol{\varepsilon}_{\mathrm{climb}}$

Calculate: $\rho_{\mathrm{tot}} = \rho_{tot} + 2\left(\rho_e^{\alpha} + \rho_s^{\alpha}\right)$

end for

Update: $\boldsymbol{\varepsilon}_{\mathrm{t}} = \boldsymbol{\varepsilon}_{\mathrm{t}} + \Delta\boldsymbol{H}^{\mathrm{P}}$

$\boldsymbol{H}^{\mathrm{P}} = \boldsymbol{H}^{\mathrm{P}} + \Delta\boldsymbol{H}^{\mathrm{P}}$

Pass: $\rho_{\mathrm{tot}} \rightarrow$ SCD

$t = t + \delta t$

end while

Bibliography

[1] *Review of theoretical conceptions on regimes of oxidation and hydrogen pickup in Zr-alloys.*

[2] Volumes published in this series. In J. FRIEDEL, editor, *Dislocations*, International Series of Monographs on Solid State Physics, page ii. Pergamon, 1964.

[3] Corrosion of zirconium alloys in nuclear power plants. Technical Report IAEA-TECDOC-684, International Atomic Energy Agency, 1993.

[4] *Chapter 11-Irradiation Creep*, pages 113–121. ASTM International, West Conshohocken, PA, 01 2001.

[5] A. Barbu *, C. S. Becquart, J.L. Bocquet, J. Dalla Torre, and C. Domain. Comparison between three complementary approaches to simulate large fluence irradiation: application to electron irradiation of thin foils. *Philosophical Magazine*, 85(4-7):541–547, 2005.

[6] RG Abernethy. Predicting the performance of tungsten in a fusion environment: a literature review. *Materials Science and Technology*, 33(4):388–399, 2017.

[7] GJ Ackland. Embrittlement and the bistable crystal structure of zirconium hydride. *Physical review letters*, 80(10):2233, 1998.

[8] V.Kh. Alimov and B.M.U. Scherzer. Deuterium retention and re-emission from tungsten materials. *Journal of Nuclear Materials*, 240(1):75 – 80, 1996.

[9] V.Kh. Alimov, B. Tyburska-Pschel, S. Lindig, Y. Hatano, M. Balden, J. Roth, K. Isobe, M. Matsuyama, and T. Yamanishi. Temperature dependence of surface morphology and deuterium retention in polycrystalline iter-grade tungsten exposed to low-energy, high-flux d plasma. *Journal of Nuclear Materials*, 420(1):519 – 524, 2012.

[10] TR Allen, RJM Konings, and AT Motta. 5.03 corrosion of zirconium alloys. *Comprehensive nuclear materials*, pages 49–68, 2012.

[11] L. Anand and M. Kothari. A computational procedure for rate-independent crystal plasticity. *Journal of the Mechanics and Physics of Solids*, 44(4):525 – 558, 1996.

[12] M Ando, Takashi Nozawa, Takanori Hirose, H Tanigawa, E Wakai, Roger E Stoller, and Janie Myers. Effect of helium on irradiation creep behavior of b-doped f82h irradiated in hfir. *Fusion Science and Technology*, 68(3):648–651, 2015.

[13] Anon. *Standard practice for neutron radiation damage simulation by charged-particle irradiation*. ASTM, United States, 1984.

[14] N. Aravas and E.C. Aifantis. On the geometry of slip and spin in finite plastic deformation. *International Journal of Plasticity*, 7(3):141–160, 1991.

[15] AS Argon and SR Maloof. Fracture of tungsten single crystals at low temperatures. *Acta Metallurgica*, 14(11):1463–1468, 1966.

[16] I.I. Arkhipov, S.L. Kanashenko, V.M. Sharapov, R.Kh. Zalavutdinov, and A.E. Gorodetsky. Deuterium trapping in ion-damaged tungsten single crystal. *Journal of Nuclear Materials*, 363-365:1168 – 1172, 2007. Plasma-Surface Interactions-17.

[17] DEJ Armstrong, X Yi, EA Marquis, and SG Roberts. Hardening of self ion implanted tungsten and tungsten 5-wt% rhenium. *Journal of Nuclear Materials*, 432(1-3):428–436, 2013.

[18] A Arsenlis and DM Parks. Crystallographic aspects of geometrically-necessary and statistically-stored dislocation density. *Acta materialia*, 47(5):1597–1611, 1999.

[19] Athanasios Arsenlis and David M. Parks. Modeling the evolution of crystallographic dislocation density in crystal plasticity. *Journal of the Mechanics and Physics of Solids*, 50(9):1979–2009, 2002.

[20] Athanasios Arsenlis, Moono Rhee, Gregg Hommes, Robert Cook, and Jaime Marian. A dislocation dynamics study of the transition from homogeneous to heterogeneous deformation in irradiated body-centered cubic iron. *Acta Materialia*, 60(9):3748–3757, 2012.

[21] Asghar Aryanfar, William Goddard III, and Jaime Marian. Constriction percolation model for coupled diffusion-reaction corrosion of zirconium in pwr. *Corrosion Science*, 158:108058, 2019.

[22] Asghar Aryanfar, John Thomas, Anton Van der Ven, Donghua Xu, Mostafa Youssef, Jing Yang, Bilge Yildiz, and Jaime Marian. Integrated computational

modeling of water side corrosion in zirconium metal clad under nominal lwr operating conditions. *JOM*, 68(11):2900–2911, 2016.

[23] R. J. Asaro. Crystal Plasticity. *Journal of Applied Mechanics*, 50(4b):921–934, 12 1983.

[24] Hesam Askari, Michael R Maughan, Niaz Abdolrahim, Dinakar Sagapuram, David F Bahr, and Hussein M Zbib. A stochastic crystal plasticity framework for deformation of micro-scale polycrystalline materials. *International Journal of Plasticity*, 68:21–33, 2015.

[25] C.R.F. Azevedo. A review on neutron-irradiation-induced hardening of metallic components. *Engineering Failure Analysis*, 18(8):1921 – 1942, 2011.

[26] D.J Bacon and Yu.N Osetsky. Multiscale modelling of radiation damage in metals: from defect generation to material properties. *Materials Science and Engineering: A*, 365(1):46 – 56, 2004. Multiscale Materials Modelling.

[27] Jacob Bair, Mohsen Asle Zaeem, and Michael Tonks. A review on hydride precipitation in zirconium alloys. *Journal of Nuclear Materials*, 466:12–20, 2015.

[28] M. Balden, V. Rohde, S. Lindig, A. Manhard, and K. Krieger. Blistering and re-deposition on tungsten exposed to asdex upgrade divertor plasma. *Journal of Nuclear Materials*, 438:S220 – S223, 2013. Proceedings of the 20th International Conference on Plasma-Surface Interactions in Controlled Fusion Devices.

[29] ATW Barrow, A Korinek, and MR Daymond. Evaluating zirconium–zirconium hydride interfacial strains by nano-beam electron diffraction. *Journal of Nuclear Materials*, 432(1-3):366–370, 2013.

[30] Nathan R Barton, Athanasios Arsenlis, and Jaime Marian. A polycrystal plasticity model of strain localization in irradiated iron. *Journal of the Mechanics and Physics of Solids*, 61(2):341–351, 2013.

[31] P Beardmore and D Hull. Deformation and fracture of tungsten single crystals. *Journal of the Less Common Metals*, 9(3):168–180, 1965.

[32] C. S. Becquart, C. Domain, U. Sarkar, A. DeBacker, and M. Hou. Microstructural evolution of irradiated tungsten: Ab initio parameterisation of an okmc model. *Journal of Nuclear Materials*, 403(1):75–88, 2010.

[33] C.S. Becquart, A. Barbu, J.L. Bocquet, M.J. Caturla, C. Domain, C.-C. Fu, S.I. Golubov, M. Hou, L. Malerba, C.J. Ortiz, A. Souidi, and R.E. Stoller. Modeling the long-term evolution of the primary damage in ferritic alloys using coarse-grained methods. *Journal of Nuclear Materials*, 406(1):39 – 54, 2010. FP6 IP PERFECT Project: Prediction of Irradiation Damage Effects in Reactor Components.

[34] CS Becquart, MF Barthe, and A De Backer. Modelling radiation damage and he production in tungsten. *Physica scripta*, 2011(T145):014048, 2011.

[35] VL Berdichevsky. Entropy and temperature of microstructure in crystal plasticity. *International Journal of Engineering Science*, 128:24–30, 2018.

[36] R. Betti and O. A. Hurricane. Inertial-confinement fusion with lasers. *Nature Physics*, 12(5):435–448, 2016.

[37] A Bhattacharya, E Meslin, J Henry, A Barbu, S Poissonnet, and B Décamps. Effect of chromium on void swelling in ion irradiated high purity fe–cr alloys. *Acta Materialia*, 108:241–251, 2016.

[38] Matthew S Blackmur, Michael Preuss, Joseph D Robson, Olivier Zanellato, Robert J Cernik, Fabienne Ribeiro, and Jérôme Andrieux. Strain evolution during hydride precipitation in zircaloy-4 observed with synchrotron x-ray diffraction. *Journal of Nuclear Materials*, 474:45–61, 2016.

[39] Matthew S Blackmur, JD Robson, M Preuss, Olivier Zanellato, RJ Cernik, S-Q Shi, Fabienne Ribeiro, and Jérôme Andrieux. Zirconium hydride precipitation kinetics in zircaloy-4 observed with synchrotron x-ray diffraction. *Journal of nuclear materials*, 464:160–169, 2015.

[40] M.S. Blackmur, J.D. Robson, M. Preuss, O. Zanellato, R.J. Cernik, S.-Q. Shi, F. Ribeiro, and J. Andrieux. Zirconium hydride precipitation kinetics in zircaloy-4 observed with synchrotron x-ray diffraction. *Journal of Nuclear Materials*, 464:160 – 169, 2015.

[41] Marline Blat and Didier Noel. Detrimental role of hydrogen on the corrosion rate of zirconium alloys. In *Zirconium in the Nuclear Industry: Eleventh International Symposium*. ASTM International, 1996.

[42] Joseph Bloch. The temperature-dependent changes of the kinetics and morphology of hydride formation in zirconium. *Journal of Alloys and Compounds*, 216(2):187 – 195, 1995.

[43] Jakob Blomqvist, Johan Olofsson, Anna-Maria Alvarez, and Christina Bjerkén. Structure and thermodynamical properties of zirconium hydrides from first-principle. In Jeremy T. Busby, Gabriel Ilevbare, and Peter L. Andresen, editors, *Proceedings of the 15th International Conference on Environmental Degradation of Materials in Nuclear Power Systems — Water Reactors*, pages 671–681, Cham, 2016. Springer International Publishing.

[44] Sophie Blondel, David E Bernholdt, Karl D Hammond, Lin Hu, Dimitrios Maroudas, and Brian D Wirth. Benchmarks and tests of a multidimensional cluster dynamics model of helium implantation in tungsten. *Fusion Science and Technology*, 71(1):84–92, 2017.

[45] Christoph Bohnert, Sabine M Weygand, Nicola J Schmitt, Ruth Schwaiger, and Oliver Kraft. Orientation dependence of the fracture behavior of single-crystal tungsten. *Procedia Materials Science*, 3:479–484, 2014.

[46] X. Bonnin, E. Hodille, N. Ning, C. Sang, and Ch. Grisolia. Rate equations modeling for hydrogen inventory studies during a real tokamak material thermal cycle. *Journal of Nuclear Materials*, 463:970 – 973, 2015. PLASMA-SURFACE INTERACTIONS 21.

[47] VA Borodin and PV Vladimirov. Diffusion coefficients and thermal stability of small helium–vacancy clusters in iron. *Journal of nuclear materials*, 362(2-3):161–166, 2007.

[48] Alfred B Bortz, Malvin H Kalos, and Joel L Lebowitz. A new algorithm for monte carlo simulation of ising spin systems. *Journal of Computational Physics*, 17(1):10–18, 1975.

[49] Philippe Bossis, Dominique Pecheur, Karine Hanifi, Joël Thomazet, and Martine Blat. Comparison of the high burn-up corrosion on m5 and low tin zircaloy-4. In *14th International Symposium on Zirconium in the Nuclear Industry*, volume 3, pages 494–525, 2006.

[50] Nikolai I Budylkin, Elena G Mironova, VM Chernov, VA Krasnoselov, SI Porollo, and Francis A Garner. Neutron-induced swelling and embrittlement of pure iron and pure nickel irradiated in the bn-350 and bor-60 fast reactors. *Journal of nuclear materials*, 375(3):359–364, 2008.

[51] R Bullough and MR Hayns. Irradiation-creep due to point defect absorption. *Journal of Nuclear Materials*, 57(3):348–352, 1975.

[52] GJC Carpenter. The dilatational misfit of zirconium hydrides precipitated in zirconium. *Journal of Nuclear Materials*, 48(3):264–266, 1973.

[53] Franois Cattant, Didier Crusset, and Damien Féron. Corrosion issues in nuclear industry today. *Materials Today*, 11(10):32 – 37, 2008.

[54] R.A. Causey, R. Doerner, H. Fraser, R.D. Kolasinski, J. Smugeresky, K. Umstadter, and R. Williams. Defects in tungsten responsible for molecular hydrogen isotope retention after exposure to low energy plasmas. *Journal of Nuclear Materials*, 390-391:717 – 720, 2009. Proceedings of the 18th International Conference on Plasma-Surface Interactions in Controlled Fusion Device.

[55] Rion A. Causey. Hydrogen isotope retention and recycling in fusion reactor plasma-facing components. *Journal of Nuclear Materials*, 300(2):91–117, 2002.

[56] Rion A. Causey, Donald F. Cowgill, and Robert H. Nilson. Review of the oxidation rate of zirconium alloys. Technical report, Sandia National Laboratories, 2005.

[57] David Cereceda, Martin Diehl, Franz Roters, Dierk Raabe, J. Manuel Perlado, and Jaime Marian. Unraveling the temperature dependence of the yield strength in single-crystal tungsten using atomistically-informed crystal plasticity calculations. *International Journal of Plasticity*, 78:242–265, 2016.

[58] K. S. Chan. An assessment of delayed hydride cracking in zirconium alloy cladding tubes under stress transients. *International Materials Reviews*, 58(6):349–373, 2013.

[59] Cheng Chen, Liping Guo, Yaxia Wei, Ziyang Xie, and Yunxiang Long. Effect of strengthening methods on the defect evolution under irradiations investigated with rate theory simulations. *Metals*, 9(7), 2019.

[60] Dandan Chen, Xinfu He, Genshen Chu, Xiao He, Lixia Jia, Zhaoshun Wang, Wen Yang, and Changjun Hu. An overview: multiscale simulation in understanding the radiation damage accumulation of reactor materials. *SIMULATION*, 0(0):0037549719880940, 0.

[61] Jiachao Chen and Wolfgang Hoffelner. Irradiation creep of oxide dispersion strengthened (ods) steels for advanced nuclear applications. *Journal of Nuclear Materials*, 392(2):360–363, 2009.

[62] Jiachao Chen, Peter Jung, Manuel A Pouchon, Tomislav Rebac, and Wolfgang Hoffelner. Irradiation creep and precipitation in a ferritic ods steel under helium implantation. *Journal of nuclear materials*, 373(1-3):22–27, 2008.

[63] Weidong Chen, Lijun Wang, and Shigang Lu. Influence of oxide layer on hydrogen desorption from zirconium hydride. *Journal of alloys and Compounds*, 469(1-2):142–145, 2009.

[64] I. I. Chernov, M. S. Staltsov, B. A. Kalin, and L. Yu. Guseva. Some problems of hydrogen in reactor structural materials: A review. *Inorganic Materials: Applied Research*, 8(5):643–650, Sep 2017.

[65] Jerome Chevalier, Laurent Gremillard, Anil V. Virkar, and David R. Clarke. The tetragonal-monoclinic transformation in zirconia: Lessons learned and future trends. *Journal of the American Ceramic Society*, 92(9):1901–1920, 2009.

[66] O.K. Chopra and A.S. Rao. A review of irradiation effects on lwr core internal materials neutron embrittlement. *Journal of Nuclear Materials*, 412(1):195 – 208, 2011.

[67] S Cierjacks, K Ehrlich, ET Cheng, H Conrads, and H Ullmaier. High-lntensity fast neutron sources and neutron fields for fusion technology and fusion materials research. *Nuclear Science and Engineering*, 106(2):99–113, 1990.

[68] Mahmut N Cinbiz, Donald A Koss, Arthur T Motta, Jun-Sang Park, and Jonathan D Almer. In situ synchrotron x-ray diffraction study of hydrides in zircaloy-4 during thermomechanical cycling. *Journal of Nuclear Materials*, 487:247–259, 2017.

[69] L. Ciupinski, O.V. Ogorodnikova, T. Plocinski, M. Andrzejczuk, M. Rasinski, M. Mayer, and K.J. Kurzydlowski. Tem observations of radiation damage in tungsten irradiated by 20mev w ions. *Nuclear Instruments and Methods in Physics Research Section B: Beam Interactions with Materials and Atoms*, 317:159 – 164, 2013. Proceedings of the 19th International Workshop on Inelastic Ion-Surface Collisions (IISC-19), Frauenchiemsee, Germany, 16-21 September 2012.

[70] John C Clayton. Out-of-pile nickel alloy-induced accelerated hydriding of zircaloy fasteners. In *Zirconium in the Nuclear Industry*. ASTM International, 1984.

[71] CE Coleman and D Hardie. The hydrogen embrittlement of α-zirconium?a review. *Journal of the Less Common Metals*, 11(3):168–185, 1966.

[72] Robert Comstock and Arthur T Motta. *Zirconium in the Nuclear Industry: 18th International Symposium*. ASTM International, 2018.

[73] J. B. Condon and T. Schober. Hydrogen bubbles in metals. *Journal of Nuclear Materials*, 207:1–24, 1993.

[74] Beatriz Cordero, Verónica Gómez, Ana E Platero-Prats, Marc Revés, Jorge Echeverría, Eduard Cremades, Flavia Barragán, and Santiago Alvarez. Covalent radii revisited. *Dalton Transactions*, (21):2832–2838, 2008.

[75] Adrien Couet, Arthur T Motta, A Ambard, and RJ Comstock. Oxide electronic conductivity and hydrogen pickup fraction in zr alloys. In *2014 Annual Meeting on Transactions of the American Nuclear Society and Embedded Topical Meeting: Nuclear Fuels and Structural Materials for the Next Generation Nuclear Reactors, NSFM*, pages 845–848, 2014.

[76] Adrien Couet, Arthur T. Motta, and Antoine Ambard. The coupled current charge compensation model for zirconium alloy fuel cladding oxidation: I. parabolic oxidation of zirconium alloys. *Corrosion Science*, 100:73 – 84, 2015.

[77] Adrien Couet, Arthur T. Motta, and Robert J. Comstock. Hydrogen pickup measurements in zirconium alloys: Relation to oxidation kinetics. *Journal of Nuclear Materials*, 451(1):1 – 13, 2014.

[78] Olivier Courty, Arthur T Motta, and Jason D Hales. Modeling and simulation of hydrogen behavior in zircaloy-4 fuel cladding. *Journal of Nuclear Materials*, 452(1-3):311–320, 2014.

[79] B Cox. Some thoughts on the mechanisms of in-reactor corrosion of zirconium alloys. *Journal of Nuclear materials*, 336(2):331–368, 2005.

[80] Brian Cox. Mechanisms of hydrogen absorption by zirconium alloys. Technical report, Atomic Energy of Canada Ltd., 1985.

[81] Alberto M Cuitino and Michael Ortiz. Computational modelling of single crystals. *Modelling and Simulation in Materials Science and Engineering*, 1(3):225, 1993.

[82] Hongsheng Dai. A review on the exact monte carlo simulation. In *Bayesian Inference on Complicated Data*. IntechOpen, 2019.

[83] Suchandrima Das. Recent advances in characterising irradiation damage in tungsten for fusion power. *SN Applied Sciences*, 1(12):1614, 2019.

[84] Suchandrima Das, Hongbing Yu, Kenichiro Mizohata, Edmund Tarleton, and Felix Hofmann. Modified deformation behaviour of self-ion irradiated tungsten: A combined nano-indentation, hr-ebsd and crystal plasticity study. *International Journal of Plasticity*, 135:102817, 2020.

[85] Suchandrima Das, Hongbing Yu, Edmund Tarleton, and Felix Hofmann. Hardening and strain localisation in helium-ion-implanted tungsten. *Scientific Reports*, 9(1):18354, 2019.

[86] Suchandrima Das, Hongbing Yu, Edmund Tarleton, and Felix Hofmann. Orientation-dependent indentation response of helium-implanted tungsten. *Applied Physics Letters*, 114(22):221905, 2019.

[87] Paul R Dawson. Computational crystal plasticity. *International journal of solids and structures*, 37(1-2):115–130, 2000.

[88] P. M. Derlet, D. Nguyen-Manh, and S. L. Dudarev. Multiscale modeling of crowdion and vacancy defects in body-centered-cubic transition metals. *Phys. Rev. B*, 76:054107, Aug 2007.

[89] PM Derlet and SL Dudarev. Microscopic structure of a heavily irradiated material. *Physical Review Materials*, 4(2):023605, 2020.

[90] Lucile Dezerald, David Rodney, Emmanuel Clouet, Lisa Ventelon, and François Willaime. Plastic anisotropy and dislocation trajectory in bcc metals. *Nature Communications*, 7(1):11695, 2016.

[91] C. Domain, R. Besson, and A. Legris. Atomic-scale ab-initio study of the zr-h system: I. bulk properties. *Acta Materialia*, 50(13):3513 – 3526, 2002.

[92] NE Dowling. *Mechanical behavior of materials*. Prentice-Hall, Englewood Cliffs, NJ, 1993.

[93] Renáta Dubčáková. Eureqa: software review. *Genetic programming and evolvable machines*, 12(2):173–178, 2011.

[94] SL Dudarev and Pui-Wai Ma. Elastic fields, dipole tensors, and interaction between self-interstitial atom defects in bcc transition metals. *Physical Review Materials*, 2(3):033602, 2018.

[95] M and-S Duesbery and V Vitek. Plastic anisotropy in bcc transition metals. *Acta Materialia*, 46(5):1481–1492, 1998.

[96] S Dumoulin, OS Hopperstad, and T Berstad. Investigation of integration algorithms for rate-dependent crystal plasticity using explicit finite element codes. *Computational Materials Science*, 46(4):785–799, 2009.

[97] Aaron Dunn, Rmi Dingreville, and Laurent Capolungo. Multi-scale simulation of radiation damage accumulation and subsequent hardening in neutron-irradiated-fe. *Modelling and Simulation in Materials Science and Engineering*, 24(1):015005, 2015.

[98] Aaron Dunn, Rmi Dingreville, Enrique Martnez, and Laurent Capolungo. Synchronous parallel spatially resolved stochastic cluster dynamics. *Computational Materials Science*, 120:43 – 52, 2016.

[99] Aaron Y. Dunn, Laurent Capolungo, Enrique Martinez, and Mohammed Cherkaoui. Spatially resolved stochastic cluster dynamics for radiation damage evolution in nanostructured metals. *Journal of Nuclear Materials*, 443(1):128 – 139, 2013.

[100] N Dupin, I Ansara, C Servant, C Toffolon, C Lemaignan, and J.C Brachet. A thermodynamic database for zirconium alloys. *Journal of Nuclear Materials*, 275(3):287 – 295, 1999.

[101] Amlan Dutta. Compressive deformation of fe nanopillar at high strain rate: Modalities of dislocation dynamics. *Acta Materialia*, 125:219–230, 2017.

[102] Karl Ehrlich. Irradiation creep and interrelation with swelling in austenitic stainless steels. *Journal of nuclear materials*, 100(1-3):149–166, 1981.

[103] Bernhard Eidel. Crystal plasticity finite-element analysis versus experimental results of pyramidal indentation into (0 0 1) fcc single crystal. *Acta Materialia*, 59(4):1761–1771, 2011.

[104] N. Eliaz, A. Shachar, B. Tal, and D. Eliezer. Characteristics of hydrogen embrittlement, stress corrosion cracking and tempered martensite embrittlement in high-strength steels. *Engineering Failure Analysis*, 9(2):167 – 184, 2002.

[105] C.E. Ells. Hydride precipitates in zirconium alloys (a review). *Journal of Nuclear Materials*, 28(2):129 – 151, 1968.

[106] C. A. English, B. L. Eyre, and J. Summers. Influence of irradiation temperature on self-ion damage in copper. *The Philosophical Magazine: A Journal of Theoretical Experimental and Applied Physics*, 34(4):603–614, 1976.

[107] J.H. Evans. Void swelling and irradiation-induced void shrinkage in neutron irradiated molybdenum and tzm. *Journal of Nuclear Materials*, 88(1):31 – 41, 1980.

[108] T. Faney and B. D. Wirth. Spatially dependent cluster dynamics modeling of microstructure evolution in low energy helium irradiated tungsten. *Modelling and Simulation in Materials Science and Engineering*, 22(6):065010, 2014.

[109] Xufei Fang, Arkadi Kreter, Marcin Rasinski, Christoph Kirchlechner, Steffen Brinckmann, Christian Linsmeier, and Gerhard Dehm. Hydrogen embrittlement of tungsten induced by deuterium plasma: Insights from nanoindentation tests. *Journal of Materials Research*, 33(20):35303536, 2018.

[110] P Feltham. A stochastic model of crystal plasticity. *Journal of Physics D: Applied Physics*, 6(17):2048, 1973.

[111] D. Féron. *Nuclear Corrosion Science and Engineering*. 10. Woodhead Publishing, 1 edition, 2012.

[112] V Fidleris. The irradiation creep and growth phenomena. *Journal of Nuclear Materials*, 159:22–42, 1988.

[113] M. W. Finnis and J. E. Sinclair. A simple empirical n-body potential for transition metals. *Philosophical Magazine A*, 50(1):45–55, 1984.

[114] V. Fohrmeister, G. Díaz, and J. Mosler. Classic crystal plasticity theory vs crystal plasticity theory based on strong discontinuities—theoretical and algorithmic aspects. *International Journal for Numerical Methods in Engineering*, 117(13):1283–1303, 2019.

[115] S Forest. Modeling slip, kink and shear banding in classical and generalized single crystal plasticity. *Acta materialia*, 46(9):3265–3281, 1998.

[116] Samuel Forest. Strain localization phenomena in generalized single crystal plasticity. *Journal of the Mechanical Behavior of Materials*, 11(1-3):45–50, 2000.

[117] Samuel Forest and MB Rubin. A rate-independent crystal plasticity model with a smooth elastic–plastic transition and no slip indeterminacy. *European Journal of Mechanics-A/Solids*, 55:278–288, 2016.

[118] P. Franciosi. The concepts of latent hardening and strain hardening in metallic single crystals. *Acta Metallurgica*, 33(9):1601 – 1612, 1985.

[119] P. Franciosi, L.T. Le, G. Monnet, C. Kahloun, and M.-H. Chavanne. Investigation of slip system activity in iron at room temperature by sem and afm in-situ tensile and compression tests of iron single crystals. *International Journal of Plasticity*, 65:226 – 249, 2015.

[120] David G Franklin and Ronald B Adamson. Implications of zircaloy creep and growth to light water reactor performance. *Journal of Nuclear Materials*, 159:12–21, 1988.

[121] R. Frauenfelder. Solution and diffusion of hydrogen in tungsten. *Journal of Vacuum Science and Technology*, 6(3):388–397, 1969.

[122] Chu-Chun Fu, Jacques Dalla Torre, François Willaime, Jean-Louis Bocquet, and Alain Barbu. Multiscale modelling of defect kinetics in irradiated iron. *Nature materials*, 4(1):68–74, 2005.

[123] Chu-Chun Fu and F Willaime. Ab initio study of helium in α- fe: Dissolution, migration, and clustering with vacancies. *Physical Review B*, 72(6):064117, 2005.

[124] Yuh Fukai. Formation of superabundant vacancies in m-h alloys and some of its consequences: a review. *Journal of Alloys and Compounds*, 356-357:263 – 269, 2003. Proceedings of the Eighth International Symposium on Metal-Hydrogen Systems, Fundamentals and Applications (MH2002).

[125] Yuh Fukai. *The metal-hydrogen system: basic bulk properties*, volume 21. Springer Science & Business Media, 2006.

[126] Yuk Fukai and Nobuyuki Ōkuma. Formation of superabundant vacancies in pd hydride under high hydrogen pressures. *Phys. Rev. Lett.*, 73:1640–1643, Sep 1994.

[127] M. Fukumoto, H. Kashiwagi, Y. Ohtsuka, Y. Ueda, M. Taniguchi, T. Inoue, K. Sakamoto, J. Yagyu, T. Arai, I. Takagi, and T. Kawamura. Deuterium

trapping in tungsten damaged by high-energy hydrogen ion irradiation. *Journal of Nuclear Materials*, 390-391:572 – 575, 2009. Proceedings of the 18th International Conference on Plasma-Surface Interactions in Controlled Fusion Device.

[128] RR Galimov and SB Goryachev. The sink strength of dislocation multipole and dislocation wall. *physica status solidi (b)*, 154(1):43–54, 1989.

[129] Jin Gao, Kiyohiro Yabuuchi, and Akihiko Kimura. Characterization of ordered dislocation loop raft in fe3+ irradiated pure iron at 300 c. *Journal of Nuclear Materials*, 511:304–311, 2018.

[130] L. Gao, A. Manhard, W. Jacob, U. von Toussaint, M. Balden, and K. Schmid. High-flux hydrogen irradiation-induced cracking of tungsten reproduced by low-flux plasma exposure. *Nuclear Fusion*, 59(5):056023, apr 2019.

[131] Crispin Gardiner. *Stochastic methods*, volume 4. Springer Berlin, 2009.

[132] Crispin W Gardiner et al. *Handbook of stochastic methods*, volume 3. springer Berlin, 1985.

[133] FA Garner and DS Gelles. Irradiation creep mechanisms: an experimental perspective. *Journal of Nuclear Materials*, 159:286–309, 1988.

[134] FA Garner and MB Toloczko. Irradiation creep and void swelling of austenitic stainless steels at low displacement rates in light water energy systems. *Journal of nuclear materials*, 251:252–261, 1997.

[135] FA Garner, MB Toloczko, and ML Grossbeck. The dependence of irradiation creep in austenitic alloys on displacement rate and helium to dpa ratio. *Journal of nuclear materials*, 258:1718–1724, 1998.

[136] L. M. Garrison, Y. Katoh, and N. A. P. Kiran Kumar. Mechanical properties of single-crystal tungsten irradiated in a mixed spectrum fission reactor. *Journal of Nuclear Materials*, 518:208–225, 2019.

[137] L. M. Garrison, F. W. Meyer, and M. E. Bannister. The influence of microstructure on deuterium retention in polycrystalline tungsten. *Fusion Science and Technology*, 72(4):574–580, 2017.

[138] F Garzarolli, H Seidel, R Tricot, and JP Gros. Oxide growth mechanism on zirconium alloys. In *Zirconium in the Nuclear Industry: Ninth International Symposium*. ASTM International, 1991.

[139] Yu.M. Gasparyan, O.V. Ogorodnikova, V.S. Efimov, A. Mednikov, E.D. Marenkov, A.A. Pisarev, S. Markelj, and I. Cadez. Thermal desorption from self-damaged tungsten exposed to deuterium atoms. *Journal of Nuclear Materials*, 463:1013 – 1016, 2015. PLASMA-SURFACE INTERACTIONS 21.

[140] MGD Geers, Maeva Cottura, Benoit Appolaire, Esteban P Busso, Samuel Forest, and Aurélien Villani. Coupled glide-climb diffusion-enhanced crystal plasticity. *Journal of the Mechanics and Physics of Solids*, 70:136–153, 2014.

[141] NM Ghoniem, JR Matthews, and RJ Amodeo. A dislocation model for creep in engineering materials. *Res Mechanica*, 29(3):197–219, 1990.

[142] N.M. Ghoniem and S. Sharafat. A numerical solution to the fokker-planck equation describing the evolution of the interstitial loop microstructure during irradiation. *Journal of Nuclear Materials*, 92(1):121 – 135, 1980.

[143] M. R. Gilbert, S. L. Dudarev, D. Nguyen-Manh, S. Zheng, L. W. Packer, and J. Ch Sublet. Neutron-induced dpa, transmutations, gas production, and helium embrittlement of fusion materials. *Journal of Nuclear Materials*, 442(1, Supplement 1):S755–S760, 2013.

[144] Mark R Gilbert, Jaime Marian, and J-Ch Sublet. Energy spectra of primary knock-on atoms under neutron irradiation. *Journal of nuclear materials*, 467:121–134, 2015.

[145] Daniel T Gillespie. A general method for numerically simulating the stochastic time evolution of coupled chemical reactions. *Journal of computational physics*, 22(4):403–434, 1976.

[146] Simone Giusepponi and Massimo Celino. The ideal tensile strength of tungsten and tungsten alloys by first-principles calculations. *Journal of Nuclear Materials*, 435(1):52 – 55, 2013.

[147] M. Grosse, M. Steinbrueck, E. Lehmann, and P. Vontobel. Kinetics of hydrogen absorption and release in zirconium alloys during steam oxidation. *Oxidation of Metals*, 70(3):149–162, Oct 2008.

[148] M Grosse, M Van Den Berg, C Goulet, and A Kaestner. In-situ investigation of hydrogen diffusion in zircaloy-4 by means of neutron radiography. In *Journal of Physics: Conference Series*, volume 340, page 012106. IOP Publishing, 2012.

[149] Earl A Gulbransen and Kenneth F Andrew. Diffusion of hydrogen and deuterium in high purity zirconium. *Journal of The Electrochemical Society*, 101(11):560–566, 1954.

[150] XH Guo, SQ Shi, QM Zhang, and XQ Ma. An elastoplastic phase-field model for the evolution of hydride precipitation in zirconium. part i: Smooth specimen. *Journal of Nuclear Materials*, 378(1):110–119, 2008.

[151] Morton E Gurtin. A finite-deformation, gradient theory of single-crystal plasticity with free energy dependent on densities of geometrically necessary dislocations. *International Journal of Plasticity*, 24(4):702–725, 2008.

[152] Morton E Gurtin, Lallit Anand, and Suvrat P Lele. Gradient single-crystal plasticity with free energy dependent on dislocation densities. *Journal of the Mechanics and Physics of Solids*, 55(9):1853–1878, 2007.

[153] Jemila Habainy, Yong Dai, Yongjoong Lee, and Srinivasan Iyengar. Mechanical properties of tungsten irradiated with high-energy protons and spallation neutrons. *Journal of Nuclear Materials*, 514:189–195, 2019.

[154] F. M. Haggag. *Effects Of Irradiation Temperature on Embrittlement of Nuclear Pressure Vessel Steels Effects of Radiation on Materials: Sixteenth International Symposium*. ASTM International, West Conshohocken, PA, 1994.

[155] Jack C Haley, Samuel A Briggs, Philip D Edmondson, Kumar Sridharan, Steve G Roberts, Sergio Lozano-Perez, and Kevin G Field. Dislocation loop evolution during in-situ ion irradiation of model fecral alloys. *Acta Materialia*, 136:390–401, 2017.

[156] FJ Harewood and PE McHugh. Comparison of the implicit and explicit finite element methods using crystal plasticity. *Computational Materials Science*, 39(2):481–494, 2007.

[157] Akira Hasegawa, Makoto Fukuda, Shuhei Nogami, and Kiyohiro Yabuuchi. Neutron irradiation effects on tungsten materials. *Fusion Engineering and Design*, 89(7-8):1568–1572, 2014.

[158] Howard L Heinisch, Fei Gao, and Richard J Kurtz. Atomic-scale modeling of interactions of helium, vacancies and helium–vacancy clusters with screw dislocations in alpha-iron. *Philosophical Magazine*, 90(7-8):885–895, 2010.

[159] K. Heinola and T. Ahlgren. Diffusion of hydrogen in bcc tungsten studied with first principle calculations. *Journal of Applied Physics*, 107(11):113531, 2010.

[160] Tae Wook Heo, Kimberly B Colas, Arthur T Motta, and Long-Qing Chen. A phase-field model for hydride formation in polycrystalline metals: Application to δ-hydride in zirconium alloys. *Acta Materialia*, 181:262–277, 2019.

[161] Brent J Heuser, J-L Lin, Changwoo Do, and Lilin He. Small-angle neutron scattering measurements of δ-phase deuteride (hydride) precipitates in zircaloy 4. *Journal of Applied Crystallography*, 51(3), 2018.

[162] Edward Hillner. Corrosion of zirconium-base alloys?an overview. In *Zirconium in the Nuclear Industry*. ASTM International, 1977.

[163] John P. Hirth. Effects of hydrogen on the properties of iron and steel. *Metallurgical Transactions A*, 11(6):861–890, Jun 1980.

[164] E.A. Hodille, A. Založnik, S. Markelj, T. Schwarz-Selinger, C.S. Becquart, R. Bisson, and C. Grisolia. Simulations of atomic deuterium exposure in self-damaged tungsten. *Nuclear Fusion*, 57(5):056002, mar 2017.

[165] Takamitsu Hoshihira, Teppei Otsuka, Ryusuke Wakabayashi, and Tetsuo Tanabe. Hydrogen behavior near surface regions in mo and w studied by tritium tracer technique. *Journal of Nuclear Materials*, 417(1):559–563, 2011.

[166] Jie Hou, Xiang-Shan Kong, Xuebang Wu, Jun Song, and C. S. Liu. Predictive model of hydrogen trapping and bubbling in nanovoids in bcc metals. *Nature Materials*, 18(8):833–839, 2019.

[167] Jing Hu, Junliang Liu, Sergio Lozano-Perez, Chris R.M. Grovenor, Mikael Christensen, Walter Wolf, Erich Wimmer, and Erik V. Mader. Hydrogen pickup during oxidation in aqueous environments: The role of nano-pores and nano-pipes in zirconium oxide films. *Acta Materialia*, 180:105 – 115, 2019.

[168] Xunxiang Hu, Takaaki Koyanagi, Makoto Fukuda, Yutai Katoh, Lance L. Snead, and Brian D. Wirth. Defect evolution in single crystalline tungsten following low temperature and low dose neutron irradiation. *Journal of Nuclear Materials*, 470:278 – 289, 2016.

[169] Xunxiang Hu, Takaaki Koyanagi, Makoto Fukuda, N. A. P. Kiran Kumar, Lance L. Snead, Brian D. Wirth, and Yutai Katoh. Irradiation hardening of

pure tungsten exposed to neutron irradiation. *Journal of Nuclear Materials*, 480:235–243, 2016.

[170] Xunxiang Hu, Donghua Xu, Thak Sang Byun, and Brian D. Wirth. Modeling of irradiation hardening of iron after low-dose and low-temperature neutron irradiation. *Modelling and Simulation in Materials Science and Engineering*, 22(6):065002, 2014.

[171] Chen-Hsi Huang, Mark R Gilbert, and Jaime Marian. Simulating irradiation hardening in tungsten under fast neutron irradiation including re production by transmutation. *Journal of Nuclear Materials*, 499:204–215, 2018.

[172] Peng Huang and Qian Yu. Dislocation multiplications in extremely small hexagonal-structured titanium nanopillars without dislocation starvation. *Scientific Reports*, 7(1):15890, 2017.

[173] Shu Huang and Jaime Marian. Rates of diffusion controlled reactions for one-dimensionally-moving species in 3d space. *Philosophical Magazine*, 99(20):2562–2583, 2019.

[174] Paul R Huebotter. Effects of metal swelling and creep on fast reactor design and performance. Technical report, Argonne National Lab., Ill., 1972.

[175] D. Hull, J. F. Byron, and F. W. Noble. Orientation dependence of yield in body-centered cubic metals. *Canadian Journal of Physics*, 45(2):1091–1099, 1967.

[176] T. Hwang, M. Fukuda, S. Nogami, A. Hasegawa, H. Usami, K. Yabuuchi, K. Ozawa, and H. Tanigawa. Effect of self-ion irradiation on hardening and microstructure of tungsten. *Nuclear Materials and Energy*, 9:430 – 435, 2016.

[177] T. Ikeda, T. Otsuka, and T. Tanabe. Application of tritium tracer technique to determination of hydrogen diffusion coefficients and permeation rate near room temperature for tungsten. *Fusion Science and Technology*, 60(4):1463–1466, 2011.

[178] Lise-Marie Imbert-Gerard, Elizabeth J. Paul, and Adelle M. Wright. An introduction to stellarators: From magnetic fields to symmetries and optimization, 2020.

[179] Adel Izadbakhsh, Kaan Inal, Raja K. Mishra, and Marek Niewczas. New crystal plasticity constitutive model for large strain deformation in single crystals of magnesium. *Computational Materials Science*, 50(7):2185 – 2202, 2011.

[180] Takahiro Izumi and Goroh Itoh. Thermal desorption spectroscopy study on the hydrogen trapping states in a pure aluminum. *MATERIALS TRANSACTIONS*, 52(2):130–134, 2011.

[181] A J. H. Donné. The european roadmap towards fusion electricity. *Philosophical transactions. Series A, Mathematical, physical, and engineering sciences*, 377, 03 2019.

[182] Patrick Jacques, Florence Lefebvre, and Clément Lemaignan. Deformation–corrosion interactions for zr alloys during i-scc crack initiation: part i: chemical contributions. *Journal of nuclear materials*, 264(3):239–248, 1999.

[183] Andrew T. Jennings and Julia R. Greer. Tensile deformation of electroplated copper nanopillars. *Philosophical Magazine*, 91(7-9):1108–1120, 2011.

[184] Zhengyi Jiang, Jingwei Zhao, and Haibo Xie. Chapter 5 - crystal plasticity theory. In Zhengyi Jiang, Jingwei Zhao, and Haibo Xie, editors, *Microforming Technology*, pages 87 – 108. Academic Press, 2017.

[185] Miaomiao Jin, Cody Permann, and Michael P Short. Breaking the power law: Multiscale simulations of self-ion irradiated tungsten. *Journal of Nuclear Materials*, 504:33–40, 2018.

[186] Donald F. Johnson and Emily A. Carter. Hydrogen in tungsten: Absorption, diffusion, vacancy trapping, and decohesion. *Journal of Materials Research*, 25(2):315–327, 2010.

[187] N. Juslin, P. Erhart, P. Traskelin, J. Nord, K. O. E. Henriksson, K. Nordlund, E. Salonen, and K. Albe. Analytical interatomic potential for modeling nonequilibrium processes in the w-c-h system. *Journal of Applied Physics*, 98(12):123520, 2005.

[188] S.R. Kalidindi. *Polycrystal Plasticity: Constitutive Modeling and Deformation Processing*. Massachusetts Institute of Technology, Department of Mechanical Engineering, 1992.

[189] Malvin H Kalos and Paula A Whitlock. *Monte carlo methods*. John Wiley & Sons, 2009.

[190] J. Kang, D.S. Wilkinson, M. Jain, J.D. Embury, A.J. Beaudoin, S. Kim, R. Mishira, and A.K. Sachdev. On the sequence of inhomogeneous deformation processes occurring during tensile deformation of strip cast aa5754. *Acta Materialia*, 54(1):209–218, 2006.

[191] Stefan Kapser, Martin Balden, Tiago Fiorini da Silva, Stefan Elgeti, Armin Manhard, Klaus Schmid, Thomas Schwarz-Selinger, and Udo von Toussaint. Influence of sub-surface damage evolution on low-energy-plasma-driven deuterium permeation through tungsten. *Nuclear Fusion*, 58(5):056027, apr 2018.

[192] JJ Kearns. Diffusion coefficient of hydrogen in alpha zirconium, zircaloy-2 and zircaloy-4. *Journal of Nuclear Materials*, 43(3):330–338, 1972.

[193] D Khatamian and FD Manchester. An ion beam study of hydrogen diffusion in oxides of zr and zr-nb (2.5 wt%): I. diffusion parameters for dense oxide. *Journal of Nuclear Materials*, 166(3):300–306, 1989.

[194] J. Knaster, A. Moeslang, and T. Muroga. Materials research for fusion. *Nature Physics*, 12(5):424–434, 2016.

[195] Marko Knezevic and Daniel J Savage. A high-performance computational framework for fast crystal plasticity simulations. *Computational materials science*, 83:101–106, 2014.

[196] U F Kocks. *Dislocations and Properties of Real Materials: Proceedings of the Conference to Celebrate the Fiftieth Anniversary of the Concept of Dislocation in Crystals*, volume 125. Maney Pub, 1985.

[197] UF Kocks. Independent slip systems in crystals. *Philosophical Magazine*, 10(104):187–193, 1964.

[198] U.F. Kocks and H. Mecking. Physics and phenomenology of strain hardening: the fcc case. *Progress in Materials Science*, 48(3):171 – 273, 2003.

[199] Aaron A. Kohnert, Brian D. Wirth, and Laurent Capolungo. Modeling microstructural evolution in irradiated materials with cluster dynamics methods: A review. *Computational Materials Science*, 149:442 – 459, 2018.

[200] A Kohyama, Y Kohno, K Asakura, M Yoshino, C Namba, and CR Eiholzer. Irradiation creep of low-activation ferritic steels in fftf/mota. *Journal of nuclear materials*, 212:751–754, 1994.

[201] Xiang-Shan Kong, Sheng Wang, Xuebang Wu, Yu-Wei You, C. S. Liu, Q. F. Fang, Jun-Ling Chen, and G. N. Luo. First-principles calculations of hydrogen solution and diffusion in tungsten: Temperature and defect-trapping effects. *Acta Materialia*, 84:426–435, 2015.

[202] Yaakov Kraftmakher. Equilibrium vacancies and thermophysical properties of metals. *Physics Reports*, 299(2):79 – 188, 1998.

[203] KV Mani Krishna, A Sain, I Samajdar, GK Dey, D Srivastava, S Neogy, R Tewari, and S Banerjee. Resistance to hydride formation in zirconium: An emerging possibility. *Acta materialia*, 54(18):4665–4675, 2006.

[204] F. Kroupa and P. B. Hirsch. Elastic interaction between prismatic dislocation loops and straight dislocations. *Discuss. Faraday Soc.*, 38:49–55, 1964.

[205] SN Kuchnicki, AM Cuitino, and RA Radovitzky. Efficient and robust constitutive integrators for single-crystal plasticity modeling. *International Journal of Plasticity*, 22(10):1988–2011, 2006.

[206] YE Kupriiyanova, VV Bryk, OV Borodin, AS Kalchenko, VN Voyevodin, GD Tolstolutskaya, and FA Garner. Use of double and triple-ion irradiation to study the influence of high levels of helium and hydrogen on void swelling of 8–12% cr ferritic-martensitic steels. *Journal of Nuclear Materials*, 468:264–273, 2016.

[207] Eiichi Kuramoto. Interaction between an edge dislocation and an interstitial atom under stress?fundamental process in sipa-creep? *Journal of Nuclear Materials*, 122(1-3):422–426, 1984.

[208] Lee D LaGrange, LJ Dykstra, John M Dixon, and Ulrich Merten. A study of the zirconium-hydrogen and zirconium-hydrogen–uranium systems between 600 and 800°. *The Journal of Physical Chemistry*, 63(12):2035–2041, 1959.

[209] A Lasa, JM Canik, S Blondel, TR Younkin, D Curreli, J Drobny, P Roth, M Cianciosa, W Elwasif, DL Green, et al. Multi-physics modeling of the long-term evolution of helium plasma exposed surfaces. *Physica Scripta*, 2020(T171):014041, 2020.

[210] Byeong-Joo Lee, M.I. Baskes, Hanchul Kim, and Yang Koo Cho. Second nearest-neighbor modified embedded atom method potentials for bcc transition metals. *Phys. Rev. B*, 64:184102, Oct 2001.

[211] EH Lee and DT Liu. Finite-strain elastic?plastic theory with application to plane-wave analysis. *Journal of applied physics*, 38(1):19–27, 1967.

[212] Hoon Lee, Kyung min Kim, Ju-Seong Kim, and Yong-Soo Kim. Effects of hydride precipitation on the mechanical property of cold worked zirconium alloys in fully recrystallized condition. *Nuclear Engineering and Technology*, 2019.

[213] A. W. Leonard. Edge-localized-modes in tokamaks. *Physics of Plasmas*, 21(9):090501, 2014.

[214] Richard LeSar. *Introduction to Computational Materials Science: Fundamentals to Applications*. Cambridge University Press, 2013.

[215] Hongwei Li and He Yang. An efficient parallel-operational explicit algorithm for taylor-type model of rate dependent crystal plasticity. *Computational materials science*, 54:255–265, 2012.

[216] Xiao-Chun Li, Xiaolin Shu, Yi-Nan Liu, F. Gao, and Guang-Hong Lu. Modified analytical interatomic potential for a w?h system with defects. *Journal of Nuclear Materials*, 408(1):12–17, 2011.

[217] Wang Li-Fang, Shu Xiaolin, Lu Guang-Hong, and Gao Fei. Embedded-atom method potential for modeling hydrogen and hydrogen-defect interaction in tungsten. *Journal of Physics: Condensed Matter*, 29(43):435401, 2017.

[218] Yu Yi Li Xiaochun, Liu Yinan and Shu Xiaolin Niu Guojian, Luo Guangnan. Molecular statics simulation of hydrogen defect interaction in tungsten. *Plasma Science and Technology*, 17, 2015.

[219] Leo Liberti and Sergei Kucherenko. Comparison of deterministic and stochastic approaches to global optimization. *International Transactions in Operational Research*, 12(3):263–285, 2005.

[220] Byung Hyuck Lim, Hyun Seon Hong, and Kyung Sub Lee. Measurements of hydrogen permeation and absorption in zirconium oxide scales. *Journal of nuclear materials*, 312(2-3):134–140, 2003.

[221] Mikaela Lindgren and Itai Panas. On the fate of hydrogen during zirconium oxidation by water: effect of oxygen dissolution in [small alpha]-zr. *RSC Adv.*, 4:11050–11058, 2014.

[222] Jochen Linke, Juan Du, Thorsten Loewenhoff, Gerald Pintsuk, Benjamin Spilker, Isabel Steudel, and Marius Wirtz. Challenges for plasma-facing components in nuclear fusion. *Matter and Radiation at Extremes*, 4(5):056201, 2019.

[223] Feng Liu, Zhongning Sun, Ming Ding, and Haozhi Bian. Research progress of hydrogen behaviors in nuclear power plant containment under severe accident conditions. *International Journal of Hydrogen Energy*, 46(73):36477–36502, 2021.

[224] Yi-Nan Liu, T. Ahlgren, L. Bukonte, K. Nordlund, Xiaolin Shu, Yi Yu, Xiao-Chun Li, and Guang-Hong Lu. Mechanism of vacancy formation induced by hydrogen in tungsten. *AIP Advances*, 3(12):122111, 2013.

[225] Yi-Nan Liu, Tiefeng Wu, Yi Yu, Xiao-Chun Li, Xiaolin Shu, and Guang-Hong Lu. Hydrogen diffusion in tungsten: A molecular dynamics study. *Journal of Nuclear Materials*, 455(1):676–680, 2014.

[226] Yue-Lin Liu, Zhen-Hong Dai, and Wei-Tian Wang. Influence of carbonvacancy interaction on carbon and vacancy diffusivity in tungsten. *Computational Materials Science*, 83:1–4, 2014.

[227] Yue-Lin Liu and Wenpu Shi. Investigating permeation and transport of h isotopes in tungsten by first-principles. *Fusion Engineering and Design*, 88(5):368–373, 2013.

[228] Yue-Lin Liu, Hong-Bo Zhou, Ying Zhang, Shuo Jin, and Guang-Hong Lu. The ideal tensile strength and deformation behavior of a tungsten single crystal. *Nuclear Instruments and Methods in Physics Research Section B: Beam Interactions with Materials and Atoms*, 267(18):3282 – 3285, 2009. Proceedings of the Ninth International Conference on Computer Simulation of Radiation Effects in Solids.

[229] Gang Lu and Efthimios Kaxiras. Hydrogen embrittlement of aluminum: The crucial role of vacancies. *Phys. Rev. Lett.*, 94:155501, Apr 2005.

[230] SC Lumley, RW Grimes, ST Murphy, PA Burr, Alexander Chroneos, PR Chard-Tuckey, and MR Wenman. The thermodynamics of hydride precipitation: The importance of entropy, enthalpy and disorder. *Acta Materialia*, 79:351–362, 2014.

[231] G.-N. Luo, W.M. Shu, and M. Nishi. Incident energy dependence of blistering at tungsten irradiated by low energy high flux deuterium plasma beams. *Journal of Nuclear Materials*, 347(1):111 – 117, 2005.

[232] XQ Ma, SQ Shi, CH Woo, and LQ Chen. The phase field model for hydrogen diffusion and γ-hydride precipitation in zirconium under non-uniformly applied stress. *Mechanics of Materials*, 38(1-2):3–10, 2006.

[233] H. Maier, T. Schwarz-Selinger, R. Neu, C. Garcia-Rosales, M. Balden, A. Calvo, T. Drbeck, A. Manhard, N. Ords, and T.F. Silva. Deuterium retention in tungsten based materials for fusion applications. *Nuclear Materials and Energy*, 18:245 – 249, 2019.

[234] L. Malerba. Molecular dynamics simulation of displacement cascades in -fe: A critical review. *Journal of Nuclear Materials*, 351(1):28 – 38, 2006. Proceedings of the Symposium on Microstructural Processes in Irradiated Materials.

[235] L. Malerba, M.C. Marinica, N. Anento, C. Bjrkas, H. Nguyen, C. Domain, F. Djurabekova, P. Olsson, K. Nordlund, A. Serra, D. Terentyev, F. Willaime, and C.S. Becquart. Comparison of empirical interatomic potentials for iron applied to radiation damage studies. *Journal of Nuclear Materials*, 406(1):19 – 38, 2010. FP6 IP PERFECT Project: Prediction of Irradiation Damage Effects in Reactor Components.

[236] A. Manhard, K. Schmid, M. Balden, and W. Jacob. Influence of the microstructure on the deuterium retention in tungsten. *Journal of Nuclear Materials*, 415(1, Supplement):S632 – S635, 2011. Proceedings of the 19th International Conference on Plasma-Surface Interactions in Controlled Fusion.

[237] Louis Kenneth Mansur. Irradiation creep by climb-enabled glide of dislocations resulting from preferred absorption of point defects. *Philosophical Magazine A*, 39(4):497–506, 1979.

[238] Jaime Marian, Charlotte S Becquart, Christophe Domain, Sergei L Dudarev, Mark R Gilbert, Richard J Kurtz, Daniel R Mason, Kai Nordlund, Andrea E Sand, Lance L Snead, et al. Recent advances in modeling and simulation of the exposure and response of tungsten to fusion energy conditions. *Nuclear Fusion*, 57(9):092008, 2017.

[239] Jaime Marian and Vasily V. Bulatov. Stochastic cluster dynamics method for simulations of multispecies irradiation damage accumulation. *Journal of Nuclear Materials*, 415(1):84–95, 2011.

[240] Jaime Marian, Tuan Hoang, Michael Fluss, and Luke L Hsiung. A review of helium–hydrogen synergistic effects in radiation damage observed in fusion energy steels and an interaction model to guide future understanding. *Journal of Nuclear Materials*, 462:409–421, 2015.

[241] Jaime Marian and Tuan L. Hoang. Modeling fast neutron irradiation damage accumulation in tungsten. *Journal of Nuclear Materials*, 429(1?3):293–297, 2012.

[242] M-C Marinica, Lisa Ventelon, M R Gilbert, L Proville, S L Dudarev, J Marian, G Bencteux, and F Willaime. Interatomic potentials for modelling radiation defects and dislocations in tungsten. *Journal of Physics: Condensed Matter*, 25(39):395502, 2013.

[243] G.P. Marino. Hydrogen supercharging in zircaloy. *Materials Science and Engineering*, 7(6):335 – 341, 1971.

[244] V. A. Markelov. Delayed hydride cracking of zirconium alloys: Appearance conditions and basic laws. *Russian Metallurgy (Metally)*, 2011(4):326, 2011.

[245] Dimitrios Maroudas, Sophie Blondel, Lin Hu, Karl D Hammond, and Brian D Wirth. Helium segregation on surfaces of plasma-exposed tungsten. *Journal of Physics: Condensed Matter*, 28(6):064004, jan 2016.

[246] Jonathan Marsh, You Sung Han, Devendra Verma, and Vikas Tomar. An investigation into plastic deformation of irradiated tungsten microstructure at elevated temperatures using the anand's viscoplastic model. *International Journal of Plasticity*, 74:127–140, 2015.

[247] Enrique Martínez, María José Caturla, and Jaime Marian. Dft-parameterized object kinetic monte carlo simulations of radiation damage. *Handbook of materials modeling: applications: current and emerging materials*, pages 2457–2488, 2020.

[248] Enrique Martínez, Jaime Marian, Malvin H Kalos, and José Manuel Perlado. Synchronous parallel kinetic monte carlo for continuum diffusion-reaction systems. *Journal of Computational Physics*, 227(8):3804–3823, 2008.

[249] Enrique Martínez, Paul R Monasterio, and Jaime Marian. Billion-atom synchronous parallel kinetic monte carlo simulations of critical 3d ising systems. *Journal of Computational Physics*, 230(4):1359–1369, 2011.

[250] Daniel R Mason, Andrea E Sand, and Sergei L Dudarev. Atomistic-object kinetic monte carlo simulations of irradiation damage in tungsten. *Modelling and Simulation in Materials Science and Engineering*, 27(5):055003, 2019.

[251] JR Matthews and MW Finnis. Irradiation creep models – an overview. *Journal of Nuclear Materials*, 159:257–285, 1988.

[252] Russell J. McDonald, Christos Efstathiou, and Peter Kurath. The Wavelike Plastic Deformation of Single Crystal Copper. *Journal of Engineering Materials and Technology*, 131(3), 06 2009.

[253] Glenn McRae, Christopher E. Coleman, and Brian W. Leitch. The first step for delayed hydride cracking in zirconium alloys. *Journal of Nuclear Materials*, 396:130–143, 2010.

[254] Sinisa Dj Mesarovic. Dislocation creep: climb and glide in the lattice continuum. *Crystals*, 7(8):243, 2017.

[255] Masanobu Miyake, Masayoshi Uno, and Shinsuke Yamanaka. On the zirconium–oxygen–hydrogen ternary system. *Journal of nuclear materials*, 270(1-2):233–241, 1999.

[256] JH Moon, PE Cantonwine, Ken R Anderson, S Karthikeyan, and MJ Mills. Characterization and modeling of creep mechanisms in zircaloy-4. *Journal of nuclear materials*, 353(3):177–189, 2006.

[257] Kazunori Morishita, Ryuichiro Sugano, and BD Wirth. Md and kmc modeling of the growth and shrinkage mechanisms of helium–vacancy clusters in fe. *Journal of nuclear materials*, 323(2-3):243–250, 2003.

[258] D Mosedale, GW Lewthwaite, and I Ramsay. Irradiation creep of fast reactor materials. In *Physical metallurgy of reactor fuel elements*. 1975.

[259] Arthur T. Motta, Laurent Capolungo, Long-Qing Chen, Mahmut Nedim Cinbiz, Mark R. Daymond, Donald A. Koss, Evrard Lacroix, Giovanni Pastore, Pierre-Clément A. Simon, Michael R. Tonks, Brian D. Wirth, and Mohammed A. Zikry. Hydrogen in zirconium alloys: A review. *Journal of Nuclear Materials*, 518:440 – 460, 2019.

[260] Arthur T Motta and Long-Qing Chen. Hydride formation in zirconium alloys. *JOM*, 64(12):1403–1408, 2012.

[261] Arthur T. Motta, Adrien Couet, and Robert J. Comstock. Corrosion of zirconium alloys used for nuclear fuel cladding. *Annual Review of Materials Research*, 45(1):311–343, 2015.

[262] Arthur T Motta, Aylin Yilmazbayhan, Marcelo J Gomes da Silva, Robert J Comstock, Gary S Was, Jeremy T Busby, Eric Gartner, Qunjia Peng, Yong Hwan Jeong, and Jeong Yong Park. Zirconium alloys for supercritical water reactor applications: Challenges and possibilities. *Journal of Nuclear Materials*, 371(1):61–75, 2007.

[263] M. Mrovec, R. Gröger, A. G. Bailey, D. Nguyen-Manh, C. Elsässer, and V. Vitek. Bond-order potential for simulations of extended defects in tungsten. *Phys. Rev. B*, 75:104119, Mar 2007.

[264] K Linga Murty. Creep studies for zircaloy life prediction in water reactors. *JOM*, 51(10):32–39, 1999.

[265] F. R. N. Nabarro. Dislocations in a simple cubic lattice. *Proceedings of the Physical Society*, 59(2):256–272, 1947.

[266] Giridhar Nandipati, Wahyu Setyawan, Howard L. Heinisch, Kenneth J. Roche, Richard J. Kurtz, and Brian D. Wirth. Displacement cascades and defect annealing in tungsten, part ii: Object kinetic monte carlo simulation of tungsten cascade aging. *Journal of Nuclear Materials*, 462:338 – 344, 2015.

[267] Sankar Narayanan, David L. McDowell, and Ting Zhu. Crystal plasticity model for bcc iron atomistically informed by kinetics of correlated kinkpair nucleation on screw dislocation. *Journal of the Mechanics and Physics of Solids*, 65:54–68, 2014.

[268] R. Nazarov, J. S. Majevadia, M. Patel, M. R. Wenman, D. S. Balint, J. Neugebauer, and A. P. Sutton. First-principles calculation of the elastic dipole tensor of a point defect: Application to hydrogen in α-zirconium. *Phys. Rev. B*, 94:241112, Dec 2016.

[269] I. M. Neklyudov, E. V. Sadanov, G. D. Tolstolutskaja, V. A. Ksenofontov, T. I. Mazilova, and I. M. Mikhailovskij. Interstitial atoms in tungsten: Interaction with free surface and in situ determination of formation energy. *Phys. Rev. B*, 78:115418, Sep 2008.

[270] Khanh Nguyen, Meijuan Zhang, Víctor Jesús Amores, Miguel A Sanz, and Francisco J Montáns. Computational modeling of dislocation slip mechanisms in crystal plasticity: A short review. *Crystals*, 11(1):42, 2021.

[271] FA Nichols. Theory of the creep of zircaloy during neutron irradiation. *Journal of Nuclear Materials*, 30(3):249–270, 1969.

[272] Kai Nordlund, Steven J. Zinkle, Andrea E. Sand, Fredric Granberg, Robert S. Averback, Roger E. Stoller, Tomoaki Suzudo, Lorenzo Malerba, Florian Banhart, William J. Weber, Francois Willaime, Sergei L. Dudarev, and David Simeone. Primary radiation damage: A review of current understanding and models. *Journal of Nuclear Materials*, 512:450 – 479, 2018.

[273] NA North, Ian Donald MacLeod, and C Pearson. *Corrosion of metals*. Butterworth-Heinemann, 1987.

[274] DO Northwood and U Kosasih. Hydrides and delayed hydrogen cracking in zirconium and its alloys. *International metals reviews*, 28(1):92–121, 1983.

[275] Takuji Oda, Deqiong Zhu, and Yoshiyuki Watanabe. Kinetic monte carlo simulation on influence of vacancy on hydrogen diffusivity in tungsten. *Journal of Nuclear Materials*, 467:439–447, 2015.

[276] Kazuhito Ohsawa, Fumihiro Nakamori, Yuji Hatano, and Masatake Yamaguchi. Thermodynamics of hydrogen-induced superabundant vacancy in tungsten. *Journal of Nuclear Materials*, 458:187–197, 2015.

[277] Maria Ann Okuniewski. *Irradiation-induced microstructural evolution and mechanical properties in iron with and without helium*. 2008.

[278] PAT Olsson, AR Massih, Jakob Blomqvist, A-M Alvarez Holston, and Christina Bjerkén. Ab initio thermodynamics of zirconium hydrides and deuterides. *Computational Materials Science*, 86:211–222, 2014.

[279] Fabien Onimus, Thomas Jourdan, Cheng Xu, Anne A. Campbell, and Malcolm Griffiths. *1.10 - Irradiation Creep in Materials*, pages 310–366. Elsevier, Oxford, 2020.

[280] EK Opperman, JL Straalsund, GL Wire, and RH Howell. Proton simulation of irradiation-induced creep. *Nuclear Technology*, 42(1):71–81, 1979.

[281] C. J. Ortiz, M. J. Caturla, C. C. Fu, and F. Willaime. He diffusion in irradiated $\alpha-$Fe: An ab-initio-based rate theory model. *Phys. Rev. B*, 75:100102, Mar 2007.

[282] M Ortiz and Egor Paul Popov. Accuracy and stability of integration algorithms for elastoplastic constitutive relations. *International journal for numerical methods in engineering*, 21(9):1561–1576, 1985.

[283] T. Otsuka, T. Hoshihira, and T. Tanabe. Visualization of hydrogen depth profile by means of tritium imaging plate technique: determination of hydrogen diffusion coefficient in pure tungsten. *Physica Scripta*, 2009(T138):014052, 2009.

[284] T P Chernyayeva and Artem Ostapov. Hydrogen in zirconium part 1. *Problems of Atomic Science and Technology*, 87, 07 2013.

[285] Anirban Patra and David L McDowell. Crystal plasticity-based constitutive modelling of irradiated bcc structures. *Philosophical Magazine*, 92(7):861–887, 2012.

[286] Anirban Patra, Ting Zhu, and David L McDowell. Constitutive equations for modeling non-schmid effects in single crystal bcc-fe at low and ambient temperatures. *International Journal of Plasticity*, 59:1–14, 2014.

[287] Giacomo Po, Yinan Cui, David Rivera, David Cereceda, Tom D. Swinburne, Jaime Marian, and Nasr Ghoniem. A phenomenological dislocation mobility law for bcc metals. *Acta Materialia*, 119:123–135, 2016.

[288] Michael Preuss. Zirconium cladding-the long way towards a mechanistic understanding of processing and performance. In *Proceedings of the second international conference on advances in nuclear materials: abstract booklet and souvenir*, 2011.

[289] Michael PREUSS, Joseph D ROBSON, Olivier ZANELLATO, Robert J CERNIK, Fabienne RIBEIRO, and Jérôme ANDRIEUX. Strain evolution during hydride precipitation in zircaloy-4 observed with synchrotron x-ray diffraction. 2016.

[290] Manfred P Puls. Review of the thermodynamic basis for models of delayed hydride cracking rate in zirconium alloys. *Journal of nuclear materials*, 393(2):350–367, 2009.

[291] Shi-Yao Qin, Shuo Jin, Lu Sun, Hong-Bo Zhou, Ying Zhang, and Guang-Hong Lu. Hydrogen assisted vacancy formation in tungsten: A first-principles investigation. *Journal of Nuclear Materials*, 465:135–141, 2015.

[292] K. D. Rasch, R. W. Siegel, and H. Schultz. Quenching and recovery investigations of vacancies in tungsten. *Philosophical Magazine A*, 41(1):91–117, 1980.

[293] P.A. Redhead. Thermal desorption of gases. *Vacuum*, 12(4):203 – 211, 1962.

[294] Xuehong Ren, Shaopu Yang, Wenzhao Zhao, and Guilin Wen. A crystal plasticity-based constitutive model for ratchetting of cyclic hardening polycrystalline metals. *International Journal of Dynamics and Control*, 8(4):1161–1168, 2020.

[295] Michael Reyes, Asghar Aryanfar, Sun Woong Baek, and Jaime Marian. Multilayer interface tracking model of zirconium clad oxidation. *Journal of Nuclear Materials*, 509:550–565, 2018.

[296] Abdallah Reza, Hongbing Yu, Kenichiro Mizohata, and Felix Hofmann. Thermal diffusivity degradation and point defect density in self-ion implanted tungsten. *Acta Materialia*, 193:270 – 279, 2020.

[297] Anthony D Rollett and UF Kocks. A review of the stages of work hardening. In *Solid State Phenomena*, volume 35, pages 1–18. Trans Tech Publ, 1993.

[298] Zhouwen Rong, Volker Mohles, David J Bacon*, and Yu N Osetsky. Dislocation dynamics modelling of dislocation–loop interactions in irradiated metals. *Philosophical Magazine*, 85(2-3):171–188, 2005.

[299] J.H. Root, W.M. Small, D. Khatamian, and O.T. Woo. Kinetics of the δ to γ zirconium hydride transformation in zr-2.5nb. *Acta Materialia*, 51(7):2041 – 2053, 2003.

[300] J.P. Roszell, J.W. Davis, and A.A. Haasz. Temperature dependence of deuterium retention mechanisms in tungsten. *Journal of Nuclear Materials*, 429(1):48 – 54, 2012.

[301] J.P. Roszell, A.A. Haasz, and J.W. Davis. D retention in w due to 10500ev d+ irradiation. *Journal of Nuclear Materials*, 415(1, Supplement):S641 – S644, 2011. Proceedings of the 19th International Conference on Plasma-Surface Interactions in Controlled Fusion.

[302] F. Roters, P. Eisenlohr, T.R. Bieler, and D. Raabe. *Crystal Plasticity Finite Element Methods: in Materials Science and Engineering*. Wiley, 2011.

[303] Franz Roters, Philip Eisenlohr, Luc Hantcherli, Denny Dharmawan Tjahjanto, Thomas R Bieler, and Dierk Raabe. Overview of constitutive laws, kinematics, homogenization and multiscale methods in crystal plasticity finite-element modeling: Theory, experiments, applications. *Acta Materialia*, 58(4):1152–1211, 2010.

[304] Arthur F Rowcliffe. Neutron irradiation facilities for fission and fusion reactor materials studies. *Nuclear Instruments and Methods in Physics Research Section A: Accelerators, Spectrometers, Detectors and Associated Equipment*, 249(1):26–33, 1986.

[305] Aleksandr RUSINOV, Mizuki SAKAMOTO, Hideki ZUSHI, Ryohei OHYAMA, Koichiro HONDA, Tetsuo TANABE, and Naoaki YOSHIDA. Deuterium retention in plasma sprayed tungsten exposed to low energy deuterium plasma. *Plasma and Fusion Research*, 8:1405004–1405004, 2013.

[306] Ho Jin Ryu, Yeon Soo Kim, and AM Yacout. Thermal creep modeling of ht9 steel for fast reactor applications. *Journal of nuclear materials*, 409(3):207–213, 2011.

[307] WOO SEOG RYU, DAE GYU PARK, UNG SUP SONG, JIN SEOK PARK, and SANG BOK AHN. Effects of irradiation on thermal conductivity of alloy 690 at low neutron fluence. *Nuclear Engineering and Technology*, 45(2):219 – 222, 2013.

[308] George P Sabol and Gerry D Moan. Zirconium in the nuclear industry: twelfth international symposium. ASTM, 2000.

[309] Shodai Sakurada, Yuki Uemura, Hiroe Fujita, Keisuke Azuma, Takeshi Toyama, Naoaki Yoshida, Tatsuya Hinoki, Sosuke Kondo, Yuji Hatano, Masashi Shimada, Dean Buchenauer, Takumi Chikada, and Yasuhisa Oya. Impact of annealing on deuterium retention behavior in damaged w. *Fusion Science and Technology*, 72(4):785–788, 2017.

[310] Maria Samaras. Multiscale modelling: the role of helium in iron. *Materials Today*, 12(11):46–53, 2009.

[311] E.J. Savino and C.N. Tomé. Irradiation creep by stress-induced preferential attraction due to anisotropic diffusion (sipa-ad). *Journal of Nuclear Materials*, 108-109:405–416, 1982.

[312] A Sawatzky. The diffusion and solubility of hydrogen in the alpha phase of zircaloy-2. *Journal of Nuclear Materials*, 2(1):62–68, 1960.

[313] Martin Schmidt-Baldassari. Numerical concepts for rate-independent single crystal plasticity. *Computer Methods in Applied Mechanics and Engineering*, 192(11-12):1261–1280, 2003.

[314] John Christopher Scully. *The fundamentals of corrosion. 2*. 1978.

[315] Santiago A Serebrinsky. Physical time scale in kinetic monte carlo simulations of continuous-time markov chains. *Physical Review E*, 83(3):037701, 2011.

[316] Varun Shah, JAW van Dommelen, and Marc GD Geers. Multi-scale microstructure evolution of tungsten under neutron and plasma loads. In *European Congress and exhibition on Advances Materials and Processes (EUROMAT 2019)*, 2019.

[317] Yasunari Shinohara, Hiroaki Abe, Takeo Iwai, Naoto Sekimura, Toshiya Kido, Hiroyuki Yamamoto, and Tomitsugu Taguchi. In situ tem observation of growth process of zirconium hydride in zircaloy-4 during hydrogen ion implantation. *Journal of nuclear science and technology*, 46(6):564–571, 2009.

[318] Amir Siddiq and Tamer El Sayed. A thermomechanical crystal plasticity constitutive model for ultrasonic consolidation. *Computational Materials Science*, 51(1):241 – 251, 2012.

[319] M. J. Simmonds, Y. Q. Wang, J. L. Barton, M. J. Baldwin, J. H. Yu, R. P. Doerner, and G. R. Tynan. Reduced deuterium retention in simultaneously damaged and annealed tungsten. *Journal of Nuclear Materials*, 494:67–71, 2017.

[320] M.J. Simmonds, T. Schwarz-Selinger, J.H. Yu, M.J. Baldwin, R.P. Doerner, and G.R. Tynan. Isolating the detrapping of deuterium in heavy ion damaged tungsten via partial thermal desorption. *Journal of Nuclear Materials*, 522:158 – 167, 2019.

[321] E. P. Simonen. Radiation effects on time-dependent deformation: Creep and growth. *Metallurgical Transactions A*, 21(4):1053–1063, 1990.

[322] BN Singh, AJE Foreman, and H Trinkaus. Radiation hardening revisited: role of intracascade clustering. *Journal of nuclear materials*, 249(2-3):103–115, 1997.

[323] Kulbir Singh, C Robertson, and AK Bhaduri. Assessing the irradiation defect induced changes using dislocation based crystal plasticity model for bcc materials. *Procedia Structural Integrity*, 5:294–301, 2017.

[324] Ram N Singh, Per Ståhle, Ali R Massih, and AA Shmakov. Temperature dependence of misfit strains of δ-hydrides of zirconium. *Journal of Alloys and Compounds*, 436(1-2):150–154, 2007.

[325] Ravi Kiran Siripurapu, Barbara Szpunar, and Jerzy A Szpunar. Molecular dynamics study of hydrogen in α-zirconium. *International Journal of Nuclear Energy*, 2014, 2014.

[326] Jan Škarohlíd, Petr Ashcheulov, Radek Škoda, Andrew Taylor, Radim Čtvrtlík, Jan Tomáštík, František Fendrych, Jaromír Kopeček, Vladimír Cháb, Stanislav Cichoň, et al. Nanocrystalline diamond protects zr cladding surface against oxygen and hydrogen uptake: Nuclear fuel durability enhancement. *Scientific reports*, 7(1):6469, 2017.

[327] Chris Llewellyn Smith and Steve Cowley. The path to fusion power. *Philosophical transactions. Series A, Mathematical, physical, and engineering sciences*, 368(1914):1091–1108, 2010.

[328] M. V. Smoluchowski. Drei Vortrage uber Diffusion, Brownsche Bewegung und Koagulation von Kolloidteilchen. *Zeitschrift fur Physik*, 17:557–585, January 1916.

[329] Mayumi Someno. Solubility and diffusion of hydrogen in zirconium. *Nippon Kinzoku Gakkaishi (Japan)*, 24, 1960.

[330] N. Soneda, S. Ishino, A. Takahashi, and K. Dohi. Modeling the microstructural evolution in bcc-fe during irradiation using kinetic monte carlo computer simulation. *Journal of Nuclear Materials*, 323(2):169 – 180, 2003. Proceedings of the Second IEA Fusion Materials Agreement Workshop on Modeling and Experimental Validation.

[331] J. M. Steichen. Tensile properties of neutron irradiated tzm and tungsten. *Journal of Nuclear Materials*, 60(1):13–19, 1976.

[332] M Steinbrück, J Birchley, AV Goryachev, M Grosse, TJ Haste, Z Hozer, AE Kisselev, VI Nalivaev, VP Semishkin, L Sepold, et al. Status of studies on high-temperature oxidation and quench behaviour of zircaloy-4 and e110 cladding alloys. *ERMSAR-2008, Nesseber, Bulgaria, Session S*, 2, 2008.

[333] Martin Steinbrück. Hydrogen absorption by zirconium alloys at high temperatures. *Journal of nuclear materials*, 334(1):58–64, 2004.

[334] R.E. Stoller, S.I. Golubov, C. Domain, and C.S. Becquart. Mean field rate theory and object kinetic monte carlo: A comparison of kinetic models. *Journal of Nuclear Materials*, 382(2):77 – 90, 2008. Microstructural Processes in Irradiated Materials.

[335] Roger E Stoller, Mychailo B Toloczko, Gary S Was, Alicia G Certain, Shyam Dwaraknath, and Frank A Garner. On the use of srim for computing radiation damage exposure. *Nuclear instruments and methods in physics research section B: beam interactions with materials and atoms*, 310:75–80, 2013.

[336] James Stubbins, Brent Heuser, Peter Hosemann, and Xiang Liu. Fundamental studies of irradiation-induced modifications in microstructural evolution and mechanical properties of advanced alloys. 4 2018.

[337] Alexander Stukowski, David Cereceda, Thomas D. Swinburne, and Jaime Marian. Thermally-activated non-schmid glide of screw dislocations in w using atomistically-informed kinetic monte carlo simulations. *International Journal of Plasticity*, 65:108–130, 2015.

[338] Peihao Sun, Yongqiang Wang, Mungo Frost, and Christopher Sch˙Characterization of defect clusters in ion-irradiated tungsten by x-ray diffuse scattering. *Journal of Nuclear Materials*, 510:322 – 330, 2018.

[339] M.P. Surh, J.B. Sturgeon, and W.G. Wolfer. Master equation and fokkerplanck methods for void nucleation and growth in irradiation swelling. *Journal of Nuclear Materials*, 325(1):44–52, 2004.

[340] T Suzudo, M Yamaguchi, and A Hasegawa. Stability and mobility of rhenium and osmium in tungsten: first principles study. *Modelling and Simulation in Materials Science and Engineering*, 22(7):075006, sep 2014.

[341] Shutaro Takeda and Richard Pearson. Nuclear fusion power plants. In Tolga Taner, editor, *Power Plants in the Industry*, chapter 6. IntechOpen, Rijeka, 2019.

[342] L. Tan, L.L. Snead, and Y. Katoh. Development of new generation reduced activation ferritic-martensitic steels for advanced fusion reactors. *Journal of Nuclear Materials*, 478:42–49, 2016.

[343] Neill Taylor, Sergio Ciattaglia, Helen Boyer, Dave Coombs, Xue Zhou Jin, Karine Liger, Juan Carlos Mora, Guido Mazzini, Tonio Pinna, and Egidijus Urbonavicius. Resolving safety issues for a demonstration fusion power plant. *Fusion Engineering and Design*, 124:1177 – 1180, 2017. Proceedings of the 29th Symposium on Fusion Technology (SOFT-29) Prague, Czech Republic, September 5-9, 2016.

[344] D. Terentyev, V. Dubinko, A. Bakaev, Y. Zayachuk, W. Van Renterghem, and P. Grigorev. Dislocations mediate hydrogen retention in tungsten. *Nuclear Fusion*, 54(4):042004, 2014.

[345] U Theis and H Wollenberger. Mobile interstitials produced by neutron irradiation in copper and aluminium. *Journal of Nuclear Materials*, 88(1):121–130, 1980.

[346] M.H.J. t'Hoen, M. Mayer, A.W. Kleyn, H. Schut, and P.A. Zeijlmans van Emmichoven. Reduced deuterium retention in self-damaged tungsten exposed to high-flux plasmas at high surface temperatures. *Nuclear Fusion*, 53(4):043003, mar 2013.

[347] M.H.J. t'Hoen, B. Tyburska-Päschel, K. Ertl, M. Mayer, J. Rapp, A.W. Kleyn, and P.A. Zeijlmans van Emmichoven. Saturation of deuterium retention in self-damaged tungsten exposed to high-flux plasmas. *Nuclear Fusion*, 52(2):023008, jan 2012.

[348] Veena Tikare. Simulation of hydride reorientation in zr-based claddings during dry storage. Technical report, Sandia National Lab.(SNL-NM), Albuquerque, NM (United States), 2013.

[349] Veena Tikare, Philippe F Weck, and John Anthony Mitchell. Modeling of hydride precipitation and re-orientation. Technical report, Sandia National Laboratories (SNL-NM), 2015.

[350] MB Toloczko, FA Garner, and CR Eiholzer. Irradiation creep and swelling of the us fusion heats of ht9 and 9cr-1mo to 208 dpa at ∼400 °c. *Journal of nuclear materials*, 212:604–607, 1994.

[351] MB Toloczko, FA Garner, and CR Eiholzer. Irradiation creep of various ferritic alloys irradiated at $\sim$ 400 °c in the pfr and fftf reactors. *Journal of nuclear materials*, 258:1163–1166, 1998.

[352] GD Tolstolutskaya, VV Ruzhytskiy, IE Kopanets, SA Karpov, VV Bryk, Victor N Voyevodin, and Francis A Garner. Displacement and helium-induced enhancement of hydrogen and deuterium retention in ion-irradiated 18cr10niti stainless steel. *Journal of nuclear materials*, 356(1-3):136–147, 2006.

[353] Hareesh Tummala, Laurent Capolungo, and Carlos N Tome. Quantifying the stress fields due to a delta-hydride precipitate in alpha-zr matrix. Technical report, Los Alamos National Lab.(LANL), Los Alamos, NM (United States), 2017.

[354] Marc Tupin, Frantz Martin, Caroline Bisor, Romain Verlet, Philippe Bossis, Jacques Chêne, François Jomard, Pascal Berger, Serge Pascal, and Nicolas Nuns. Hydrogen diffusion process in the oxides formed on zirconium alloys during corrosion in pressurized water reactor conditions. *Corrosion Science*, 116:1–13, 2017.

[355] PA Turner and CN Tomé. Self-consistent modeling of visco-elastic polycrystals: application to irradiation creep and growth. *Journal of the Mechanics and Physics of Solids*, 41(7):1191–1211, 1993.

[356] B. Tyburska, V.Kh. Alimov, O.V. Ogorodnikova, K. Schmid, and K. Ertl. Deuterium retention in self-damaged tungsten. *Journal of Nuclear Materials*, 395(1):150 – 155, 2009.

[357] K Une and S Ishimoto. Dissolution and precipitation behavior of hydrides in zircaloy-2 and high fe zircaloy. *Journal of nuclear materials*, 322(1):66–72, 2003.

[358] Katsumi Une. Kinetics of reaction of zirconium alloy with hydrogen. *Journal of the Less Common Metals*, 57(1):93 – 101, 1978.

[359] Pierre-Louis Valdenaire, Yann Le Bouar, Benoît Appolaire, and Alphonse Finel. Density-based crystal plasticity: From the discrete to the continuum. *Physical Review B*, 93(21):214111, 2016.

[360] Erik van der Giessen and Kenneth W Neale. Analysis of the inverse swift effect using a rate-sensitive polycrystal model. *Computer methods in applied mechanics and engineering*, 103(1-2):291–313, 1993.

[361] Erik van der Giessen, Peter A Schultz, Nicolas Bertin, Vasily V Bulatov, Wei Cai, Gábor Csányi, Stephen M Foiles, M G D Geers, Carlos González, Markus Htter, Woo Kyun Kim, Dennis M Kochmann, Javier LLorca, Ann E Mattsson, Jrg Rottler, Alexander Shluger, Ryan B Sills, Ingo Steinbach, Alejandro Strachan, and Ellad B Tadmor. Roadmap on multiscale materials modeling. *Modelling and Simulation in Materials Science and Engineering*, 28(4):043001, mar 2020.

[362] Clinton DeW Van Siclen. Derivation of the residence time for kinetic monte carlo simulations. *arXiv preprint arXiv:0712.2464*, 2007.

[363] Lisa Ventelon, F. Willaime, Chu-Chun Fu, M. Heran, and I. Ginoux. Ab initio investigation of radiation defects in tungsten: Structure of self-interstitials and specificity of di-vacancies compared to other bcc transition metals. *Journal of Nuclear Materials*, 425(1):16 – 21, 2012. Microstructure Properties of Irradiated Materials.

[364] P. Vizcaíno, J.R. Santisteban, M.A. Vicente Alvarez, A.D. Banchik, and J. Almer. Effect of crystallite orientation and external stress on hydride precipitation and dissolution in zr2.5 *Journal of Nuclear Materials*, 447(1):82 – 93, 2014.

[365] Arthur F. Voter. Introduction to the kinetic monte carlo method. In Kurt E. Sickafus, Eugene A. Kotomin, and Blas P. Uberuaga, editors, *Radiation Effects in Solids*, pages 1–23, Dordrecht, 2007. Springer Netherlands.

[366] W.R. Wampler and R.P. Doerner. The influence of displacement damage on deuterium retention in tungsten exposed to plasma. *Nuclear Fusion*, 49(11):115023, sep 2009.

[367] Eric Yiqing Wang. Comparison Between Deterministic and Stochastic Biological Simulation. Technical report, Uppsala University, Department of Mathematics, 2014.

[368] Li-Fang Wang, Xiaolin Shu, Guang-Hong Lu, and Fei Gao. Embedded-atom method potential for modeling hydrogen and hydrogen-defect interaction in tungsten. *Journal of Physics: Condensed Matter*, 29(43):435401, sep 2017.

[369] Siyang Wang, Finn Giuliani, and T Ben Britton. Microstructure and formation mechanisms of δ-hydrides in variable grain size zircaloy-4 studied by electron backscatter diffraction. *Acta Materialia*, 169:76–87, 2019.

[370] Wenmin Wang, J Roth, S Lindig, and C.H Wu. Blister formation of tungsten due to ion bombardment. *Journal of Nuclear Materials*, 299(2):124 – 131, 2001.

[371] Xing Wang, Ming-Jie Zheng, Izabela Szlufarska, and Dane Morgan. Continuum model for hydrogen pickup in zirconium alloys of lwr fuel cladding. *Journal of Applied Physics*, 121(13):135101, 2017.

[372] Yuanyuan Wang, Xin Sun, and Jijun Zhao. A mechanism-based quantitative multi-scale framework for investigating irradiation hardening of tungsten at low temperature. *Materials Science and Engineering: A*, 774:138941, 2020.

[373] Gary S Was. *Fundamentals of radiation materials science: metals and alloys*. Springer, 2016.

[374] Gary S. Was. *Irradiation Creep and Growth*, pages 735–791. Springer New York, New York, NY, 2017.

[375] G.S. Was and P.L. Andresen. 6 - irradiation assisted corrosion and stress corrosion cracking (iac/iascc) in nuclear reactor systems and components. In Damien Fron, editor, *Nuclear Corrosion Science and Engineering*, Woodhead Publishing Series in Energy, pages 131 – 185. Woodhead Publishing, 2012.

[376] Hideo Watanabe, Naoki Futagami, Shiori Naitou, and Naoaki Yoshida. Microstructure and thermal desorption of deuterium in heavy-ion-irradiated pure tungsten. *Journal of Nuclear Materials*, 455(1):51 – 55, 2014. Proceedings of the 16th International Conference on Fusion Reactor Materials (ICFRM-16).

[377] HE Weekes, D Dye, JE Proctor, DS Smith, C Simionescu, TJ Prior, and MR Wenman. The effect of pressure on hydrogen solubility in zircaloy-4. *arXiv preprint arXiv:1806.09657*, 2018.

[378] HE Weekes, NG Jones, TC Lindley, and D Dye. Hydride reorientation in zircaloy-4 examined by in situ synchrotron x-ray diffraction. *Journal of Nuclear Materials*, 478:32–41, 2016.

[379] J Weiss, W Ben Rhouma, T Richeton, Stéphanie Dechanel, F Louchet, and L Truskinovsky. From mild to wild fluctuations in crystal plasticity. *Physical review letters*, 114(10):105504, 2015.

[380] Wei Wen, A Kohnert, M Arul Kumar, Laurent Capolungo, and Carlos N Tomé. Mechanism-based modeling of thermal and irradiation creep behavior: An application to ferritic/martensitic ht9 steel. *International Journal of Plasticity*, 126:102633, 2020.

[381] E Dow Whitney. Kinetics and mechanism of the transition of metastable tetragonal to monoclinic zirconia. *Transactions of the Faraday Society*, 61:1991–2000, 1965.

[382] WG Wolfer. Correlation of radiation creep theory with experimental evidence. *Journal of Nuclear Materials*, 90(1-3):175–192, 1980.

[383] WG Wolfer and M Ashkin. Stress- induced diffusion of point defects to spherical sinks. *Journal of Applied Physics*, 46(2):547–557, 1975.

[384] WG Wolfer and M Ashkin. Diffusion of vacancies and interstitials to edge dislocations. *Journal of Applied Physics*, 47(3):791–800, 1976.

[385] WG Wolfer, JP Foster, and FA Garner. The interrelationship between swelling and irradiation creep. *Nuclear Technology*, 16(1):55–63, 1972.

[386] WG Wolfer, LK Mansur, and JA Sprague. Theory of swelling and irradiation creep. Technical report, Wisconsin Univ., Madison (USA). Dept. of Nuclear Engineering; Oak Ridge ?, 1977.

[387] C. H. Woo. Irradiation creep due to sipa- induced growth. *Philosophical Magazine A*, 42(4):551–558, 1980.

[388] CH Woo. Irradiation creep due to elastodiffusion. *Journal of Nuclear Materials*, 120(1):55–64, 1984.

[389] W. Xiao, G. N. Luo, and W. T. Geng. Threshold concentration for h blistering in defect free w. *Journal of Nuclear Materials*, 421(1):176–180, 2012.

[390] Xiazi Xiao, Dmitry Terentyev, Alexander Bakaev, Aleksandr Zinovev, Andrii Dubinko, and EE Zhurkin. Crystal plasticity finite element method simulation for the nano-indentation of plasma-exposed tungsten. *Journal of Nuclear Materials*, 518:334–341, 2019.

[391] Xiazi Xiao and Long Yu. A hardening model for the cross-sectional nanoindentation of ion-irradiated materials. *Journal of Nuclear Materials*, 511:220 – 230, 2018. Special Section on 18th International Conference on Fusion Reactor Materials.

[392] Donghua Xu and Hang Xiao. Cluster dynamics model for the hydride precipitation kinetics in zirconium cladding. In John H. Jackson, Denise Paraventi, and Michael Wright, editors, *Proceedings of the 18th International Conference*

on Environmental Degradation of Materials in Nuclear Power Systems – Water Reactors, pages 1759–1768, Cham, 2019. Springer International Publishing.

[393] H.Y. Xu, W. Liu, G.N. Luo, Y. Yuan, Y.Z. Jia, B.Q. Fu, and G. De Temmerman. Blistering on tungsten surface exposed to high flux deuterium plasma. *Journal of Nuclear Materials*, 471:51 – 58, 2016.

[394] L. Yang, Z.J. Bergstrom, and B.D. Wirth. Effect of interatomic potential on the energetics of hydrogen and helium-vacancy complexes in bulk, or near surfaces of tungsten. *Journal of Nuclear Materials*, 512:357 – 370, 2018.

[395] Xue Yang and Ahmed Hassanein. Kinetic monte carlo simulation of hydrogen diffusion on tungsten reconstructed (001) surface. *Fusion Engineering and Design*, 89(11):2545–2549, 2014.

[396] M.Y. Ye, H. Kanehara, S. Fukuta, N. Ohno, and S. Takamura. Blister formation on tungsten surface under low energy and high flux hydrogen plasma irradiation in nagdis-i. *Journal of Nuclear Materials*, 313-316:72 – 76, 2003. Plasma-Surface Interactions in Controlled Fusion Devices 15.

[397] Tomoyuki Yokota and Tetsuo Shiraga. Evaluation of hydrogen content trapped by vanadium precipitates in a steel. *ISIJ International*, 43(4):534–538, 2003.

[398] David John Young. *High temperature oxidation and corrosion of metals*, volume 1. Elsevier, 2008.

[399] Mostafa Youssef, Ming Yang, and Bilge Yildiz. Doping in the valley of hydrogen solubility: A route to designing hydrogen-resistant zirconium alloys. *Phys. Rev. Applied*, 5:014008, Jan 2016.

[400] J.H. Yu, M.J. Simmonds, M.J. Baldwin, and R.P. Doerner. Deuterium retention in re-solidified tungsten and beryllium. *Nuclear Materials and Energy*, 18:297 – 306, 2019.

[401] Qianran Yu, Sabyasachi Chatterjee, Kenneth J. Roche, Giacomo Po, and Jaime Marian. Coupling crystal plasticity and stochastic cluster dynamics models of irradiation damage in tungsten. *Modelling and Simulation in Materials Science and Engineering*, 2021.

[402] Qianran Yu, Enrique Martnez, Javier Segurado, and Jaime Marian. A stochastic solver based on the residence time algorithm for crystal plasticity models. *Computational Mechanics*, 2021.

[403] Qianran Yu, Michael Reyes, Nachiket Shah, and Jaime Marian. Kinetic model of incipient hydride formation in zr clad under dynamic oxide growth conditions. *Materials*, 13(5):1088, 2020.

[404] Qianran Yu, Michael J Simmonds, Russ Doerner, George R Tynan, Li Yang, Brian D Wirth, and Jaime Marian. Understanding hydrogen retention in damaged tungsten using experimentally-guided models of complex multispecies evolution. *Nuclear Fusion*, 60(9):096003, 2020.

[405] Shulin Yuan, Minsheng Huang, Yaxin Zhu, and Zhenhuan Li. A dislocation climb/glide coupled crystal plasticity constitutive model and its finite element implementation. *Mechanics of Materials*, 118:44–61, 2018.

[406] AS Zaimovskii. Zirconium alloys in nuclear power. *Atomic Energy*, 45(6):1165–1168, 1978.

[407] M. Zaiser, J. Schwerdtfeger, A.S. Schneider, C.P. Frick, B.G. Clark, P.A. Gruber, and E. Arzt. Strain bursts in plastically deforming molybdenum micro- and nanopillars. *Philosophical Magazine*, 88(30-32):3861–3874, 2008.

[408] Michael Zaiser, Paolo Moretti, and Haijan Chu. Stochastic crystal plasticity models with internal variables: application to slip channel formation in irradiated metals. *Advanced Engineering Materials*, 22(9):1901208, 2020.

[409] O Zanellato, M Preuss, J-Y Buffiere, F Ribeiro, A Steuwer, J Desquines, J Andrieux, and B Krebs. Synchrotron diffraction study of dissolution and precipitation kinetics of hydrides in zircaloy-4. *Journal of Nuclear Materials*, 420(1-3):537–547, 2012.

[410] Jixi Zhang and Yanyao Jiang. A Study of Inhomogeneous Plastic Deformation of 1045 Steel . *Journal of Engineering Materials and Technology*, 126(2):164–171, 03 2004.

[411] K. Zhang, O. S. Hopperstad, B. Holmedal, and S. Dumoulin. A robust and efficient substepping scheme for the explicit numerical integration of a rate-dependent crystal plasticity model. *International Journal for Numerical Methods in Engineering*, 99(4):239–262, 2014.

[412] Kai Zhang, Bjørn Holmedal, Stephane Dumoulin, and Odd Sture Hopperstad. An explicit integration scheme for hypo-elastic viscoplastic crystal plasticity. *Transactions of Nonferrous Metals Society of China*, 24(7):2401–2407, 2014.

[413] Liangzhe Zhang, Rémi Dingreville, Timothy Bartel, and Mark T Lusk. A stochastic approach to capture crystal plasticity. *International journal of plasticity*, 27(9):1432–1444, 2011.

[414] Meijuan Zhang, K. Nguyen, Javier Segurado, and Francisco J. Montns. A multiplicative finite strain crystal plasticity formulation based on additive elastic corrector rates: Theory and numerical implementation. *International Journal of Plasticity*, 137:102899, 2021.

[415] Mu-Hang Zhang, Xiao-Hong Shen, Lei He, and Ke-Shi Zhang. Application of differential entropy in characterizing the deformation inhomogeneity and life prediction of low-cycle fatigue of metals. *Materials*, 11(10):1917, 2018.

[416] ZX Zhang, DS Chen, WT Han, and A Kimura. Irradiation hardening in pure tungsten before and after recrystallization. *Fusion Engineering and Design*, 98:2103–2107, 2015.

[417] Z Zhao, M Blat-Yrieix, J Morniroli, A Legris, L Thuinet, Y Kihn, A Ambard, and L Legras. Characterization of zirconium hydrides and phase field approach to a mesoscopic-scale modeling of their precipitation. In *Zirconium in the Nuclear Industry: 15th International Symposium*. ASTM International, 2009.

[418] Z. ZHAO, J.-P. MORNIROLI, A. LEGRIS, A. AMBARD, Y. KHIN, L. LEGRAS, and M. BLAT-YRIEIX. Identification and characterization of a new zirconium hydride. *Journal of Microscopy*, 232(3):410–421, 2008.

[419] Zhe Zhao, Yonggang Li, Chuanguo Zhang, Guyue Pan, Panfei Tang, and Zhi Zeng. Effect of grain size on the behavior of hydrogen/helium retention in tungsten: a cluster dynamics modeling. *Nuclear Fusion*, 57(8):086020, jun 2017.

[420] Shanliang Zheng and Thomas N. Todd. Study of impacts on tritium breeding ratio of a fusion demo reactor. *Fusion Engineering and Design*, 98-99:1915 – 1918, 2015. Proceedings of the 28th Symposium On Fusion Technology (SOFT-28).

[421] Hong-Bo Zhou, Shuo Jin, Ying Zhang, Guang-Hong Lu, and Feng Liu. Anisotropic strain enhanced hydrogen solubility in bcc metals: The independence on the sign of strain. *Physical Review Letters*, 109(13):135502, 2012.

[422] Weihua Zhu, Rongshan Wang, Guogang Shu, Ping Wu, and Heming Xiao. First-principles study of different polymorphs of crystalline zirconium hydride. *The Journal of Physical Chemistry C*, 114(50):22361–22368, 2010.

[423] James F Ziegler, Matthias D Ziegler, and Jochen P Biersack. *Srim*. Cadence Design Systems, 2008.

[424] James F Ziegler, Matthias D Ziegler, and Jochen P Biersack. Srim–the stopping and range of ions in matter (2010). *Nuclear Instruments and Methods in Physics Research Section B: Beam Interactions with Materials and Atoms*, 268(11-12):1818–1823, 2010.

[425] Andrzej Zieliński and Sylwia Sobieszczyk. Hydrogen-enhanced degradation and oxide effects in zirconium alloys for nuclear applications. *International journal of hydrogen energy*, 36(14):8619–8629, 2011.

[426] M. Zucchetti, Z. Chen, L. El-Guebaly, V. Khripunov, B. Kolbasov, D. Maisonnier, Y. Someya, M. Subbotin, R. Testoni, and K. Tobita. Progress in international radioactive fusion waste studies. *Fusion Science and Technology*, 75(5):391–398, 2019.

[427] E Zuzek, JP Abriata, A San-Martin, and FD Manchester. The h-zr (hydrogen-zirconium) system. *Bulletin of alloy phase diagrams*, 11(4):385–395, 1990.